EBM Experimental Biology and Medicine

Volume 250 | Issue 5

Experimental Biology and Medicine

Editor-in-Chief

Nicola Conran
University of Campinas, Brazil

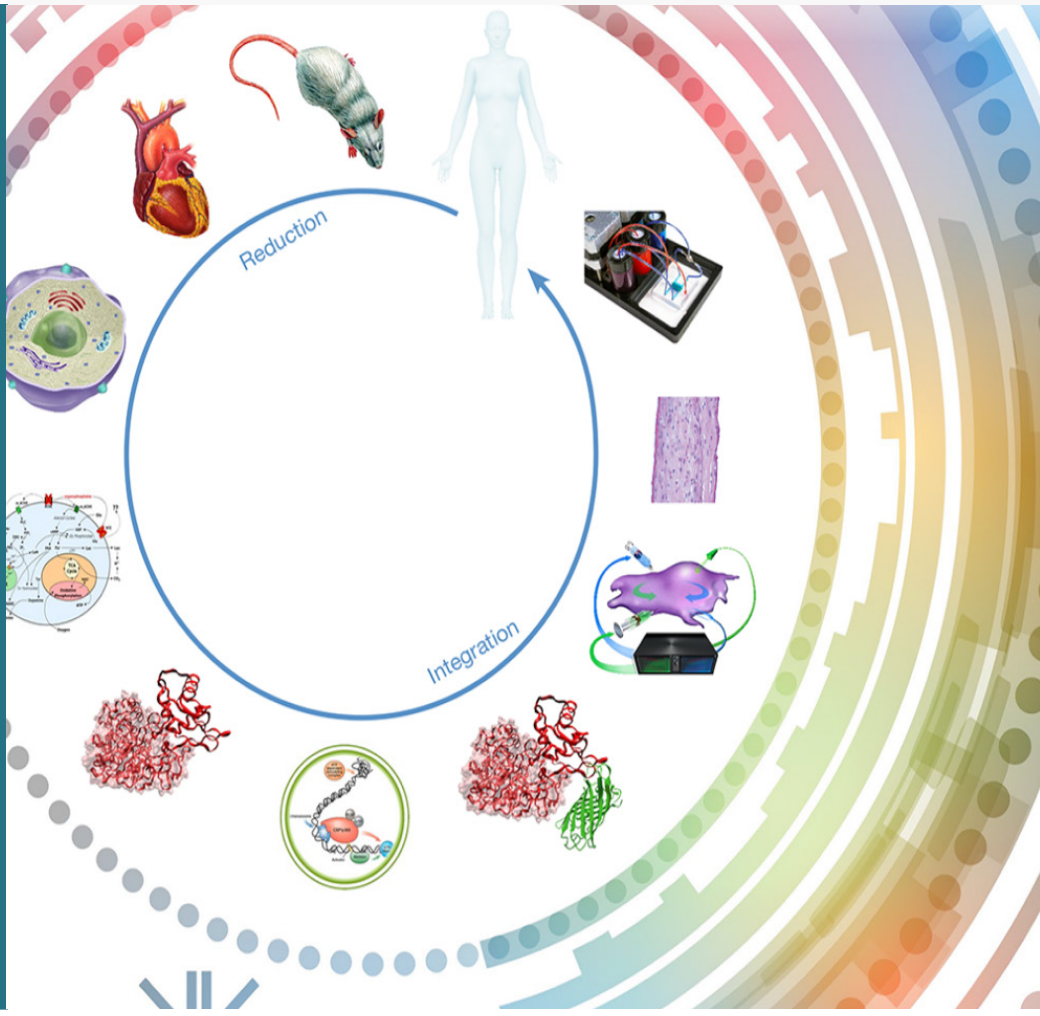

ISBN 978-2-8325-6516-2
DOI 10.3389/978-2-8325-6516-2

frontiers | Publishing Partnerships

EBM Experimental Biology and Medicine

SEBM Executive Council

Publication Committee

Society for Experimental Biology and Medicine
3220 N Street NW, #179
Washington DC 20007, USA
Executive Director – ed@sebm.org

www.sebm.org

EBM Experimental Biology and Medicine

Editorial Board

ISSN 1535-3699
ISBN 978-2-8325-6516-2
DOI 10.3389/978-2-8325-6516-2

EBM Experimental Biology and Medicine

2025 | Volume 250 | Issue 5 | ISSN 1535-3699

Table of contents

Physiology and Pathophysiology

Population Health

EBM Experimental Biology and Medicine

TYPE Original Research
PUBLISHED 29 May 2025
DOI 10.3389/ebm.2025.10523

OPEN ACCESS

*CORRESPONDENCE
Ming Guan,
guanming88@yahoo.com
Guojun Cao,
gjcao16@fudan.edu.cn

†These authors have contributed equally to this work

RECEIVED 09 February 2025
ACCEPTED 14 May 2025
PUBLISHED 29 May 2025

CITATION
Xiang J, Peng J, Xing Z, Ren G, Zhang H, Song X, Zhang B, Guan M and Cao G (2025) Potential supplementary tumor markers for liquid biopsy in non-small cell lung cancer.
Exp. Biol. Med. 250:10523.
doi: 10.3389/ebm.2025.10523

Potential supplementary tumor markers for liquid biopsy in non-small cell lung cancer

Jin Xiang[1†], Junyan Peng[2†], Zhifang Xing[1], Guoqiang Ren[3], Huating Zhang[1], Xiaodong Song[1], Bo Zhang[1], Ming Guan[1*] and Guojun Cao[1*]

[1]Department of Laboratory Medicine, Huashan Hospital, Shanghai Medical College, Fudan University, Shanghai, China, [2]Tendering Office, Huashan Hospital, Shanghai Medical College, Fudan University, Shanghai, China, [3]Department of Pathology, Huashan Hospital, Shanghai Medical College, Fudan University, Shanghai, China

The identification of epidermal growth factor receptor (EGFR) tyrosine kinase (TK) domain mutations in non-small cell lung cancer (NSCLC) patients is crucial for therapeutic decision-making and monitoring EGFR-tyrosine kinase inhibitor (TKI) resistance. Liquid biopsy has emerged as a promising alternative for patients ineligible for invasive tissue sampling. This study investigated the clinical utility of a novel chip-based digital PCR (dPCR) platform for detecting two important EGFR mutations - exon 19 deletions (19del) and threonine-methionine amino acid substitution at position 790 (T790M) - in serum samples, while exploring potential serum biomarkers for mutation prediction. The collection of 350 serum samples were conducted on patients diagnosed with NSCLC at Huashan Hospital between August 2023 and February 2024. Cell-free deoxyribonucleic acid (cfDNA) was extracted from serum and was analyzed for EGFR mutations using dPCR. The serum tumor marker levels were quantified. The dPCR assay demonstrated positive predictive values of 73.33% for 19del and 28.57% for T790M. Biomarker analysis revealed a carbohydrate antigen (CA) 199 cutoff of 11.75 U/mL (AUC = 0.707, 95% CI: 0.573–0.841, $P = 0.005$) for 19del detection, while progastrin-releasing peptide (ProGRP) showed a cutoff of 45.15 pg/mL (AUC = 0.628, 95% CI: 0.521–0.735, $P = 0.028$) for T790M identification. Variant rate exhibited significant positive correlations with biomarker concentrations: 19del variant rates significantly associated with CA125 levels ($r = 0.624$, $P = 0.010$), while T790M correlated with both carcinoembryonic antigen (CEA) ($r = 0.531$, $P = 0.004$) and ProGRP ($r = 0.395$, $P = 0.041$) in mutation-positive cohorts. These findings indicate that serum-based dPCR liquid biopsy demonstrates potential clinical utility as a supplementary approach to tissue biopsy for NSCLC genotyping. Notably, elevated serum tumor marker levels correlate with enhanced mutation detection rates in liquid biopsy, implying their potential supplementary value in prioritizing patients for molecular profiling.

KEYWORDS

digital PCR, liquid biopsy, tumor markers, EGFR mutation, non-small cell lung cancer

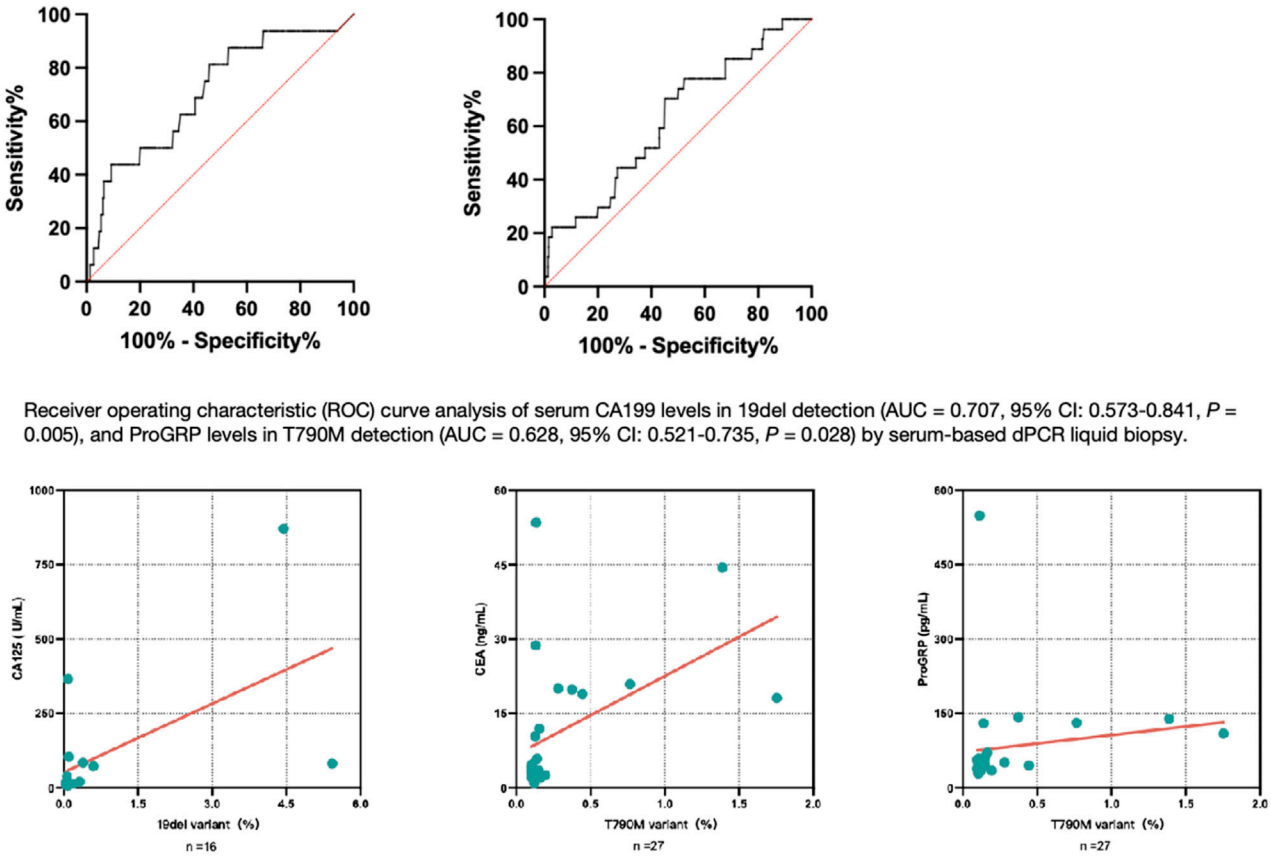

Receiver operating characteristic (ROC) curve analysis of serum CA199 levels in 19del detection (AUC = 0.707, 95% CI: 0.573-0.841, P = 0.005), and ProGRP levels in T790M detection (AUC = 0.628, 95% CI: 0.521-0.735, P = 0.028) by serum-based dPCR liquid biopsy.

Variant rate exhibited significant positive correlations with biomarker concentrations: 19del variant rates significantly associated with CA125 levels (r = 0.624, P = 0.010), while T790M correlated with both CEA (r = 0.531, P = 0.004) and ProGRP (r = 0.395, P = 0.041) in mutation-positive cohorts.

GRAPHICAL ABSTRACT

Impact statement

The dPCR liquid biopsy technique is bringing a ray of hope for NSCLCs who are unable to provide sufficient tissue samples for genotyping. However, its widespread clinical adoption faces persistent challenges. Our study verified the analytical performance of a new chip-based dPCR technique platform for quantifying two critical EGFR mutations (19del and T790M) in serum-derived cfDNA, and concurrently identified the potential serum biomarkers to optimize patient stratification for cost-effective molecular profiling. Key findings revealed that elevated serum CA199 and ProGRP levels demonstrated predictive utility for 19del and T790M mutations, respectively. Positive correlations were observed between the 19del variant rate and CA125 level, as well as between the T790M variant rate and CEA, ProGRP level.

Introduction

Lung cancer is the most common cancer type and leading cause of cancer-related deaths in China and worldwide [1]. NSCLC constitutes approximately 75%–80% of all lung cancer cases [2]. Because it is often asymptomatic in its early phases, most patients are diagnosed with NSCLC at an advanced stage with no possible surgical intervention, resulting in poor prognosis [3]. In oncogene-driven NSCLC, accurate molecular subtyping is the prerequisite for precision treatment. Mutations in the EGFR gene are one of the most common oncogenic driver mutations in non-squamous NSCLC, with a positive rate of 50% in East Asian populations [4]. For NSCLC tumors harboring EGFR mutations, especially in advanced patients, EGFR-TKI-based therapy has become the standard treatment approach. This has been shown to be superior to chemotherapy for improving patient survival and prognosis [5]. As one of the most important

and common EGFR mutations, 19del constitutes approximately 85% of all EGFR mutations together with exon 21 L858R point mutations. These alterations, often referred to as "classic" mutations, predicts good response to EGFR-TKIs [6]. However, more than 50% of patients receiving the first- or second-generation TKIs develop a point mutation in EGFR that results in T790M 9–14 months after treatment, leading to drug resistance [7]. Therefore, new therapeutic methods are needed for these NSCLC patients. Currently, EGFR gene mutation testing requires tumor tissue acquired by surgery or biopsy. However, the clinical application of tumor tissue biopsy is limited. Sampling is highly invasive and cannot be used for the dynamic monitoring of tumors during treatment and follow-up. Moreover, tumor tissue heterogeneity may lead to certain mutant genes not being detected in some patients. Liquid biopsy is expected to bring new hope as a non-invasive and highly sensitive approach for NSCLC treatment guidance and monitoring. This minimally invasive and rapid technique enables real-time decision-making in various clinical scenarios by isolating, detecting, and analyzing tumor-released nucleic acids circulating in body fluids [3, 8, 9]. Peripheral blood samples can properly represent the tumor origin and are easy to obtain, rendering them as optimal materials for liquid biopsy. Circulating cfDNA in the peripheral blood of tumor origin, called circulating tumor DNA (ctDNA), is tumor-specific and can be representative of the full tumor tissue composition. However, ctDNA accounts for less than 1% of cfDNA and is highly fragmented with a short half-life. The proportion of ctDNA decreases significantly in early tumors and after treatment responses [10]. Therefore, a highly sensitive detection method is crucial for clinical practice.

Technologies based on polymerase chain reaction (PCR), including super amplification refractory mutation system (super-ARMS), beads, emulsion, amplification, magnetics (BEAMing), and dPCR, are suitable for detecting known specific loci and can all be used to detect cfDNA. As the latest generation of PCR, dPCR assay builds upon traditional PCR amplification and fluorescent probe-based detection methods is able to provide precise and absolute quantification of cfDNA mutations with good analytical sensitivity [11]. The target concentration was calculated according to Poisson distribution by directly counting the partitions that contained fluorescent target molecules. Several studies have identified the utility of liquid biopsy in the identification of EGFR mutations and acquired resistance with good sensitivities for various blood-based biomarkers. However, the clinical application and promotion of liquid biopsy are faced with similar difficulties at present, which including differences in methodological sensitivity and specificity of the assay itself, economic factors and the difficulties in conducting experiments in some laboratories. Recent studies have focused on developing predictive models that leverage clinical, radiological, and laboratory characteristics to ascertain EGFR mutation status in NSCLC [12]. This study aimed to use a new chip-based dPCR technique platform for the quantification of circulating cfDNA targets (EGFR 19del and T790M) in NSCLC patient serum samples, and to find potential serum biomarkers which may help to screen beneficiary patients and improve the dPCR liquid biopsy detection efficiency.

Materials and methods

Patients and materials

In this study, serum samples were obtained from 350 patients diagnosed with NSCLC. All samples were sent to the Department of Laboratory Medicine of Huashan Hospital for immunological testing between August 2023 and February 2024. The patients' demographic and clinical data were retrospectively investigated from an electronic medical records system. The data included sex, age, pathological classification, disease stage, tissue gene status, and the process of EGFR-TKI treatment. At least 4.0 mL of venous blood from each patient was collected in BD Vacutainer ® SST™ blood collection tubes (Becton, Dickinson and Company, USA) with gel separators and silica coagulant. Sampling and centrifugation were performed according to standard operating procedures. Serum samples were included if they met the following criteria: obtained from a donor who was histopathologically diagnosed with NSCLC, had no obvious hemolysis and lipemia, and was no less than 1.0 mL in volume. The selected samples were collected and stored in 1.5 mL Eppendorf (EP) tubes at −80°C until use. All procedures were in accordance with the Helsinki Declaration. The protocol of the current study was reviewed and approved by Huashan Hospital Ethical Committee (2022-572) and informed written consent was obtained from all enrolled patients.

cfDNA extraction

Purified nucleic acids were extracted from 1.0 mL of thawed and higher-speed centrifuged serum using a High Pure Viral Nucleic Acid Large Volume Kit (column method, Cat. No. 05114403001, Roche Diagnostics, Mannheim, Germany) according to the manufacturer's instructions with an elution volume of 70 μL.

EGFR mutation detection with the dPCR assay

Under standard conditions, dPCR was performed using a Digital LightCycler® System (Roche Diagnostics GmbH) to separately amplify 19del and T790M of EGFR. A maximum of 37 μL serum cfDNA, 10 μL Digital LightCycler® 5× DNA Master Mix, 0.5 μL restriction enzyme (HaeIII), 2.5 μL Parameter-

Specific Reagents (PSR, containing premixed primers and probes), and PCR-grade water were added to the reaction mixture to a total volume of 50 μL. As recommended to enable a higher sensitivity for detecting the target sequences, the high sensitivity nanowell plate with approximately 20,000 partitions per reaction was used for a higher input volume per lane. With this nanowell plate, 45 μL of reaction mixture were added to each lane before loading and partitioning the plate.

The 19del mutation site was analyzed using two labeled probes: 1) a reference probe (HEX-labeled), which was designed to bind to the amplicon irrespective of mutation presence, and 2) an indel probe (FAM-labeled), which was designed to bind to the wild-type (WT) sequence but not to any of the mutated sequences. The assay allows the detection of 28 deletions in the EGFR exon 19 (with COSMIC IDs: COSM26038, COSM13550, COSM6223, COSM13552, COSM13551, COSM12385, COSM6225, COSM12728, COSM12678, COSM12386, COSM12416, COSM12367, COSM12384, COSM18427, COSM12422, COSM12419, COSM23571, COSM6220, COSM6218, COSM12382, COSM12383, COSM6254, COSM12403, COSM6255, COSM12387, COSM6210, COSM12369, COSM12370). The 19del-PCR reaction was performed using the following cycling conditions: stage 1: 50°C for 2 min; stage 2: 95°C for 2 min; stage 3: 40 cycles of 95°C for 15 s and 60°C for 30 s; stage 4: 40°C for 30 s. The T790M mutation site (COSMIC ID: COSM6240) was analyzed using two labeled probes binding competitively to the mutation site. The mutant probe is FAM-labeled and the WT probe is HEX-labeled. The T790M-PCR reaction was performed using the following cycling conditions: stage 1: 50°C for 2 min; stage 2: 95°C for 2 min; stage 3: 40 cycles of 95°C for 10 s and 58°C for 20 s; stage 4: 40°C for 30 s. Finally, the Digital LightCycler® Development Software was used to perform partition clustering and analyze the results. The 19del mutation results were analyzed using two-dimensional (2D) scatter plots and the T790M mutation results were analyzed using one-dimensional (1D) scatter plots. A sample was considered mutant-positive if its gene variant rate was above the corresponding cutoff (0.05% for 19del mutation and 0.10% for T790M mutation) as provided by the manufacturers.

Analytical performance verification of the dPCR assay

The sensitivity of the EGFR 19del and T790M dPCR systems were evaluated using simulation samples with gradient mutation loads (5%, 1%, 0.5%, 0.1%, 0.05%), which were generated by mixing a mutant plasmid and the WT plasmid that provided by the manufacturer at different proportions. Three replicates per batch were used for each mutation load. Samples with only genomic DNA (0% mutant) were also included as a control. Positive 19del simulation samples, positive T790M simulation samples, and genomic DNA samples from the peripheral blood of healthy individuals were used to test the specificity of the EGFR 19del and T790M dPCR systems.

Tumor marker quantification

The concentrations of tumor markers associated with lung cancer, including CEA, cytokeratin 19 fragment (Cy211), neuron specific enolase (NSE), ProGRP, squamous cell carcinoma antigen (SCCA), CA199, CA125, CA153, CA724, and alpha1-fetoprotein (AFP), in residual serum samples were analyzed by electrochemiluminescence immunoassays (ECLIAs) on a cobas® 8000 modular analyzer series e801 (Roche Diagnostics GmbH) following the manufacturer's instructions. The reference intervals of these 10 serological markers were <6.5 ng/mL, <3.3 ng/mL, <17 ng/mL, <69.2 pg/mL, <2.7 ng/mL, <37 U/mL, <35 U/mL, <25 U/mL, <8.2 U/mL, and <7 ng/mL, respectively.

Statistical analysis

Statistical analyses were performed using IBM SPSS Statistics Version 25.0 (IBM Corp., Armonk, NY, USA) and Microsoft Excel Version 2013 (Microsoft Corp., Redmond, WA, USA). The figures were generated using GraphPad Prism 9.2 (GraphPad Software Inc., La Jolla, CA, USA).

Data for continuous variables are presented as the median with interquartile range (IQR), while data for categorical variables are presented as numbers and percentages. Comparisons between groups were performed by applying the chi-squared test, McNemar test, or Mann-Whitney U test, with correlations being analyzed by applying the Spearman test. A two-sided P-value <0.05 was considered statistically significant. ROC curve analysis and the Youden index were used to determine the best cutoff value and obtain the corresponding sensitivity and specificity values.

Results

General characteristics of patients

In this study, the frequencies of EGFR 19del and T790M mutations in serum cfDNA from 350 NSCLC patients were determined. The clinical characteristics of the study participants are shown in Table 1. Among them, 217 patients were male and 133 were female. The median age was 63 (56–70) years, with 300 patients diagnosed with adenocarcinoma, 34 with squamous carcinoma, and 16 with other subtypes (including large cell carcinoma, sarcomatoid carcinoma, and poorly-

TABLE 1 Clinical characteristics of the EGFR mutant-positive and EGFR mutant-negative participants.

Features	dPCR- 19del		*p* value	dPCR- T790M		*p* value
	Negative (n = 331)	Positive (n = 19)		Negative (n = 322)	Positive (n = 28)	
Sex			0.71			0.80
Male, n	206	11		199	18	
Female, n	125	8		123	10	
Age, year, median (IQR)	63 (57–70)	63 (48–76)	0.92	64 (56–70)	61 (58–68)	0.61
Pathology			0.63			0.096
Adenocarcinoma, n	283	17		279	21	
Others, n	48	2		43	7	
Stage			**0.041**			0.34
I, n	18	0		18	0	
II, n	11	1		12	0	
III, n	21	5		23	3	
IV, n	186	11		178	19	
N/A, n	95	2		91	6	
EGFR-TKI therapy			**<0.001**			0.51
"First or second" generation TKIs, n	46	2		44	4	
"Third generation" TKIs, n	67	12		75	4	
Never, n	211	5		196	20	
N/A, n	7	0		7	0	

EGFR, epidermal growth factor receptor; dPCR, digital polymerase chain reaction; IQR, interquartile range; TKI, tyrosine kinase inhibitor; N/A, not available; first-generation TKIs, gefitinib, icotinib, erlotinib; second-generation TKIs, afatinib, dacomitinib; third-generation TKIs: osimertinib, almonertinib, vormetinib. Bold values indicate statistical significance ($p < 0.05$).

differentiated NSCLC). The numbers of cases with stage I, II, III, and IV disease were 18, 12, 26, and 197, respectively, with 97 cases not yet staged. Tissue molecular tests were performed on samples from 56.0% (196 of 350) of the patients. The re-biopsy rate was 19% (38 of 196). The median time interval between tissue biopsy and blood sampling was 16.5 (6–32) months. For NSCLC treatment, 127 patients underwent EGFR-TKI therapy for 17 (8–33) months. Among these cases, 48 patients started with a first- or second-generation EGFR-TKI, with 28 of them switching to a third-generation EGFR-TKI during later treatment. Additionally, 79 cases started their treatment with the third-generation EGFR-TKIs (instead of starting with first- or second-generation and then switching), 14 of whom were treated with a combination of more than one EGFR-TKI.

Performance of the dPCR assay in detecting EGFR 19del and T790M mutations

For the mutational analysis, firstly the quantitative performance of the dPCR assay was evaluated. The sensitivity values of different targets were evaluated by mutation load. The results suggested that the mutant allele detection was quantitative and linear, with the limit of detection for EGFR 19del and T790M mutations being 0.05% and 0.10% mutation load, respectively (Figure 1). The dPCR system amplified the target nucleic acid template specifically, as no non-specific amplification of the background DNA or other DNA with similar sequences was observed.

Next, the complete workflow was analyzed. EGFR 19del mutations were identified in 5.4% of the analyzed serum cfDNA samples (19 positives among 350 tested serum samples), while EGFR T790M mutations were observed in 8.0% of the cases (28 of 350). The maximum variant rate was 5.4239% for 19del and 1.7539% for T790M. Figure 2 shows an image of the dPCR nanowell plate after the partitioning and amplification procedures. The plate was processed using the Digital LightCycler® analysis algorithm. Furthermore, Figure 3 shows the 2D and 1D scatter plots for partition fluorescence and demonstrates the detection of each mutation in its corresponding channel. In the 2D scatter plots, the red partitions were double negative for HEX and FAM, the green partitions were double positive for HEX and FAM, the blue partitions were positive for only HEX, and the yellow partitions were positive for only FAM

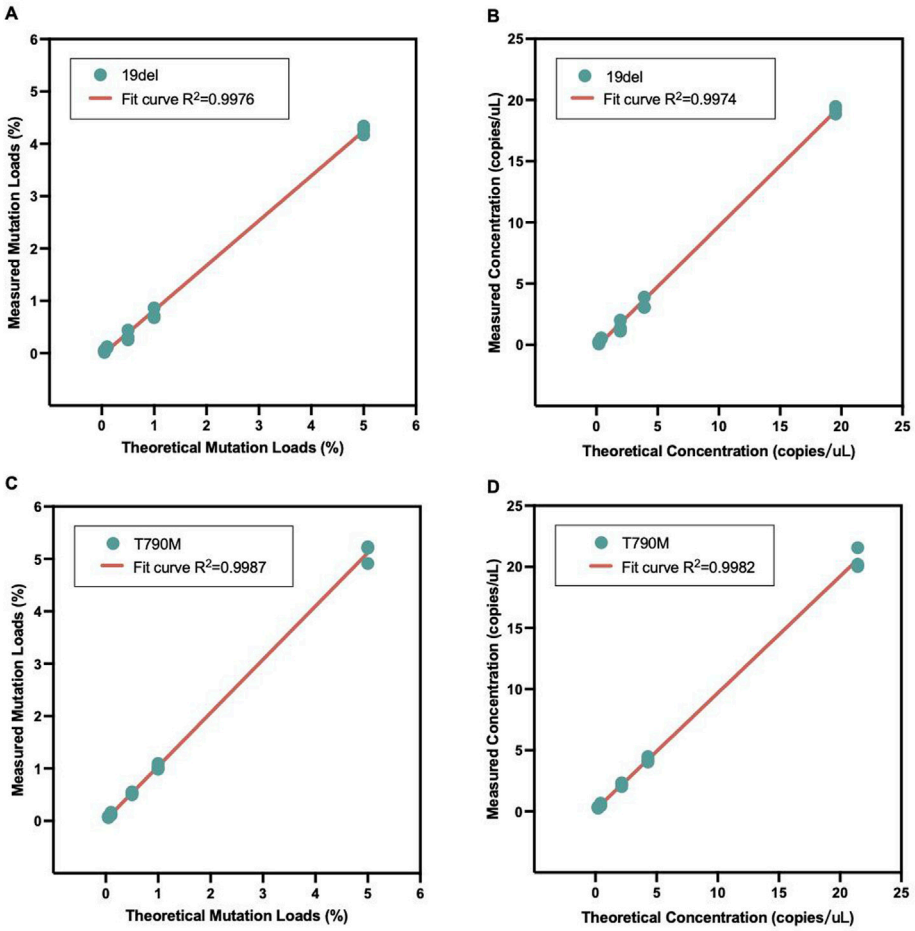

FIGURE 1
Sensitivity values of the digital polymerase chain reaction (dPCR) platform. The solid line represents the best fit line for mutation load data. The goodness of fit value (R squared) is shown in each figure panel. **(A)** Mutation load results for the EGFR 19del mutation. **(B)** Quantitative concentration results for 19del. **(C)** Mutation load results for the EGFR T790M mutation. **(D)** Quantitative concentration results for T790M.

but none were observed. In the 1D scatter plots, the red partitions were positive and blue partitions were negative for that channel. The dPCR assay also enabled quantitative detection of gene mutations. The median concentrations of the mutant and WT copies of the 19del-positive samples were 0.07 (0.03–0.56) copies/μL and 64.26 (42.17–147.65) copies/μL, respectively. These showed significant differences when compared with the 19del WT samples ($P < 0.001$, $P = 0.013$). For T790M, the median concentrations of variant and WT copies were 0.1225 (0.0805–0.1583) copies/μL and 87.8397 (67.6016–110.0498) copies/μL, respectively. Only the former was statistically significantly higher when compared with the T790M WT samples ($P < 0.001$, $P = 0.193$).

Table 1 also shows the clinical characteristics of the patients after they were categorized by their positive or negative status for the EGFR 19del and T790M mutations. Among the 19del mutant-positive patients, 58% (11 of 19) were male and 90% (17 of 19) were diagnosed with adenocarcinoma. The median age was 63 (48–76) years. A statistically significant effect of different disease stages on serum 19del mutation detection was observed

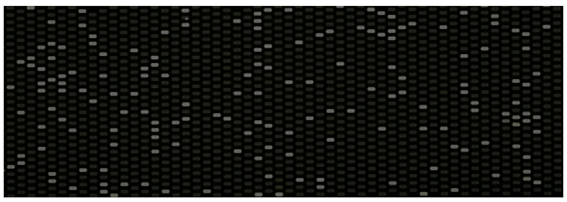

FIGURE 2
Image of the digital polymerase chain reaction (dPCR) nanowell plate after partitioning and amplification. Target-positive partitions are visible as discrete fluorescent wells against a background of non-fluorescent (target-negative) wells.

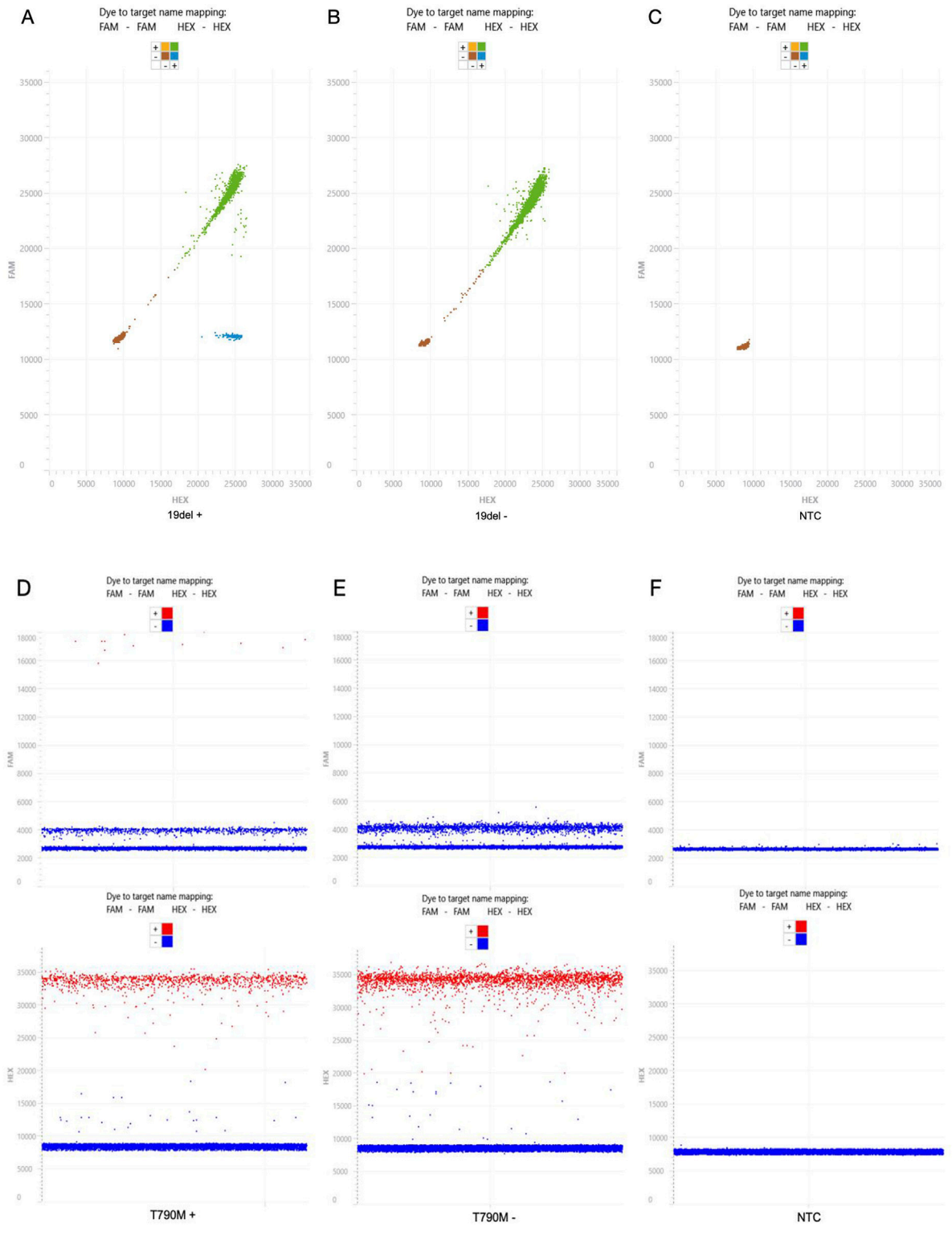

FIGURE 3
Two-dimensional (2D) and one-dimensional (1D) scatter plots of the positive, negative, and no template control (NTC) results of the EGFR 19del and T790M mutations using the digital polymerase chain reaction (dPCR) assay. The NTC samples were composed of only PCR-grade water. **(A)** 2D scatter plot of an exon 19del-positive sample, with a variant rate of 4.4467%, 2.9903 variant copies/μL, and 64.2565 wild-type (WT) copies/μL. **(B)** 2D

(*Continued*)

FIGURE 3 (Continued)
scatter plot of an exon 19del-negative sample, with a variant rate of 0%, 0 variant copies/μL, and 139.3881 WT copies/μL. **(C)** 2D scatter plot of the 19del NTC, with a variant rate of 0%, 0 variant copies/μL, and 0 WT copies/μL. **(D)** 1D scatter plots of a T790M-positive sample, with a variant rate of 1.39%, 1.0052 variant copies/μL, and 71.4508 WT copies/μL. **(E)** 1D scatter plots of a T790M-negative sample, with a variant rate of 0%, 0 variant copies/μL, and 97.4854 WT copies/μL. **(F)** 1D scatter plots of the T790M NTC, with a variant rate of 0%, 0 variant copies/μL, and 0 WT copies/μL.

(P = 0.041). The positive rate of serum 19del detection was highest in patients who used the third-generation EGFR-TKIs compared with those who never used them or received other generations of EGFR-TKI therapy (P < 0.001). According to the tissue biopsy results, three cases concurrently carried EGFR L858R mutations and one case carried a KRAS mutation in the corresponding tissue samples. Among the T790M mutant-positive patients, 64% (18 of 28) were male and 75% (21 of 28) were diagnosed with adenocarcinoma. The median age was 61 (58–68) years. The numbers of cases with EGFR L858R, 19del, ROS, KRAS, and TP53 mutations were 5, 2, 2, 2, and 1, respectively. There were another two cases with tissue biopsy test results showing no mutations.

Comparisons of liquid biopsy and tissue biopsy

Furthermore, to evaluate the consistency of the serum cfDNA gene status with tissue molecular test results, the data of the 196 cases that underwent tissue biopsy were investigated. Through tissue biopsy, 58% (114 of 196) of the patients were found to carry EGFR mutations, including thirty-two 19del cases, one T790M case, fifty-six L858R cases, four 19del-L858R co-occurrence cases, three 19del-T790M co-occurrence cases, nine T790M-L858R co-occurrence cases, and nine others. The positive rate of detection by tissue biopsy was much higher than that of liquid biopsy (19.9% vs. 7.6%, respectively, P < 0.001) for 19del. However, for T790M, it was slightly lower than that of liquid biopsy (6.6% vs. 7.1%, respectively, P = 1.00). The comparison of serum-based 19del analysis using dPCR and tissue testing revealed an overall agreement of 83.67% (164 of 196 cases), kappa = 0.334. The positive predictive value (PPV) was 73.33%. The positive agreement was 28.21% and the negative agreement was 97.45% (Table 2). More specifically, 11 cases were positive for the 19del mutation both in serum and tumor samples, while four cases were detected as mutant only in serum samples. All of the serum-positive-only cases were diagnosed with adenocarcinoma. Two of the patients underwent and benefited from EGFR-TKI therapy, as their previous genetic tests were positive for L858R. The comparison of serum-based T790M analysis using dPCR and tissue testing revealed an overall agreement of 90.31% (177 of 196 cases), kappa = 0.244. The PPV was 28.57%. The positive agreement was 30.77% and the negative agreement was 94.54% (Table 3). More specifically, four cases were positive for the T790M mutation both in serum and tumor samples, while 10 cases were detected as mutant only in serum samples. Three of these serum-positive-only cases underwent EGFR-TKI therapy for more than 20 months, with all of these patients showing disease progression before the drug was changed to osimertinib.

The correlations between serum EGFR 19del and T790M mutations by dPCR and serum tumor marker levels by ECLIAs

346 results of serum CY211, NSE, ProGRP, and CEA levels, 338 results of SCC levels, 309 results of CA199 and CA125 levels, 306 results of CA153 levels, 304 results of CA724 levels, and 298 results of AFP levels were finally obtained. The median CA199 concentration was approximately two-fold higher in the 19del-positive serum samples compared with the WT serum samples (21.2 vs. 11.0, respectively, P = 0.005). The median ProGRP concentration was significantly higher in the T790M-positive serum samples compared with the WT serum samples (51 vs. 46, respectively, P = 0.028) (Table 4).

ROC curve analysis was performed to obtain cutoff values of serum tumor marker concentrations that can predict EGFR mutation in serum liquid biopsy. For 19del, the CA199 cutoff value was 11.75 U/mL to reach the dPCR analytical sensitivity threshold of 0.05% mutant (P = 0.006), with an area under the ROC curve (AUC) value of 0.707 (95% confidence interval (CI): 0.573–0.841, P = 0.005) and a mutant positive rate of 8.78%. For T790M, the ProGRP cutoff value was 45.15 pg/mL to reach the dPCR analytical sensitivity of 0.10% mutant (P = 0.012), with an AUC value of 0.628 (95% CI: 0.521–0.735, P = 0.028) and a mutant positive rate of 11.11% (Figure 4).

Furthermore, a significant positive correlation was observed between the variant rate and CA125 concentration in 19del mutant-positive serum samples (r = 0.624, P = 0.010), while significant positive correlations were found between the variant rate and the CEA and ProGRP concentrations in T790M mutant-positive serum samples (r = 0.531, P = 0.004; r = 0.395, P = 0.041, respectively) (Figure 5).

The performance of serum genetic test results by dPCR for identifying disease progression

Table 5 shows the serum test results of EGFR 19del and T7910M mutations in patients with progressive disease and those

TABLE 2 Comparing EGFR 19del status detection using the dPCR assay in serum cfDNA with the tissue molecular test results included in patient medical records (n = 196).

Sample	Serum/dPCR		
	Negative	Positive	Total
Tissue/clinical			
Negative	153	4	157
Positive	28	11	39
Total	181	15	196

EGFR, epidermal growth factor receptor; dPCR, digital polymerase chain reaction; cfDNA, cell-free DNA.

TABLE 3 Comparing EGFR T790M status detection using the dPCR assay in serum cfDNA with the tissue molecular test results included in patient medical records (n = 196).

Sample	Serum/dPCR		
	Negative	Positive	Total
Tissue/clinical			
Negative	173	10	183
Positive	9	4	13
Total	182	14	196

EGFR, epidermal growth factor receptor; dPCR, digital polymerase chain reaction; cfDNA, cell-free DNA.

TABLE 4 Tumor marker levels of EGFR mutant-positive and EGFR mutant-negative samples.

Tests	dPCR- 19del		*p* value	dPCR-T790M		*p* value
	Negative	Positive		Negative	Positive	
CY211 (ng/mL) (n =346)	2.3 (1.6–4.3)	3.4 (2.1–5.3)	0.147	2.3 (1.6–4.6)	2.6 (2.0–3.7)	0.66
NSE (ng/mL) (n =346)	14.1 (11.9–17.0)	13 (10.7–20.3)	0.91	14.2 (12.1–17.1)	13.4 (11.3–15.6)	0.165
ProGRP (pg/mL) (n =346)	46.7 (35.7–59.2)	43.9 (36.9–58.4)	0.85	46 (35.7–58.5)	51 (45.2–71)	**0.028**
CEA (ng/mL) (n =346)	3.2 (1.8–9.96)	9.8 (2.09–140)	0.084	3.2 (1.8–10.0)	4.1 (2.9–18.9)	0.098
SCCA (ng/mL) (n =338)	1.2 (0.8–1.9)	1.15 (0.6–1.4)	0.115	1.2 (0.8–1.9)	1.2 (0.9–1.8)	0.91
CA199 (U/mL) (n =309)	11 (7.05–20.3)	21.2 (12.0–102.2)	**0.005**	11.1 (7.1–21)	14.9 (7.7–25.6)	0.41
CA125 (U/mL) (n =309)	15.7 (10.3–31.6)	21.7 (14.0–23.4)	0.059	15.8 (10.3–34)	16.5 (12.1–29)	0.70
CA153 (U/mL) (n =306)	15.1 (9.2–23.9)	15.9 (9.1–23.4)	0.77	15.1 (9.2–23)	19.2 (9.4–26.2)	0.45
CA724 (U/mL) (n =304)	2.8 (1.5–7.0)	2.7 (1.5–3.9)	1.00	2.8 (1.5–7.3)	2.6 (2–3.7)	0.50
AFP (ng/mL) (n =298)	3.2 (2.2–4.2)	2.5 (1.8–3.9)	0.164	3.2 (2.2–4.2)	2.9 (2.3–4.2)	1.00

EGFR, epidermal growth factor receptor; dPCR, digital polymerase chain reaction; Cy211, cytokeratin 19 fragment; NSE, neuron specific enolase; ProGRP, progastrin-releasing peptide; CEA, carcinoembryonic antigen; SCCA, squamous cell carcinoma antigen; CA199, carbohydrate antigen 199; CA125, carbohydrate antigen 125; CA153, carbohydrate antigen 153; CA724, carbohydrate antigen 724; AFP, alpha1-fetoprotein. Bold values indicate statistical significance ($p < 0.05$).

with stable disease after EGFR-TKI treatment. The EGFR T790M variant rates and copies of patients with progressive disease were significantly higher than those of patients with stable disease ($P = 0.031$, $P = 0.024$, respectively). ROC curve analysis showed that the AUC values were 0.6091 (95% CI: 0.5091–0.7091, $P = 0.036$ for the variant rate and 0.6135 (95% CI: 0.5129–0.7140, $P = 0.030$) for the variant copies. The Youden index values were 0.25 and 0.239, respectively. Additionally, the optimal cutoff values for the serum T790M variant rate and copies determined by ROC analysis were 0.0248% (with 64.2%

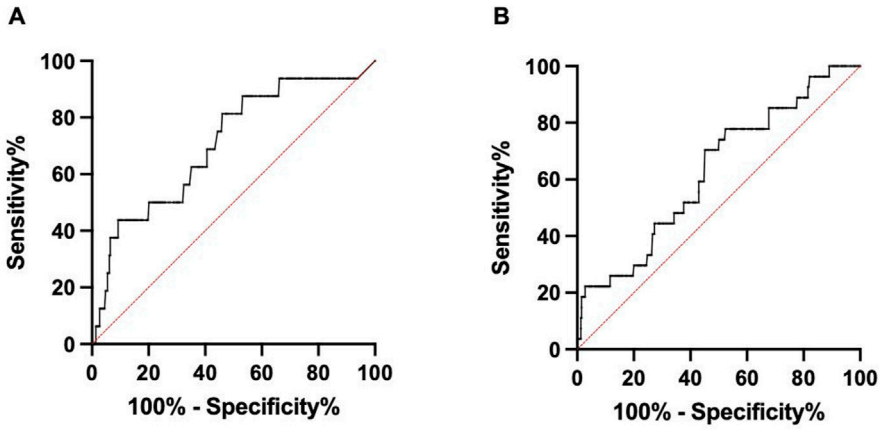

FIGURE 4
Receiver operating characteristic (ROC) curve analysis of serum tumor marker concentrations in EGFR mutation detection. **(A)** ROC curve of CA199 levels in 19del detection (AUC = 0.707, 95% CI: 0.573–0.841, *P* = 0.005). **(B)** ROC curve of ProGRP levels in T790M detection (AUC = 0.628, 95% CI: 0.521–0.735, *P* = 0.028).

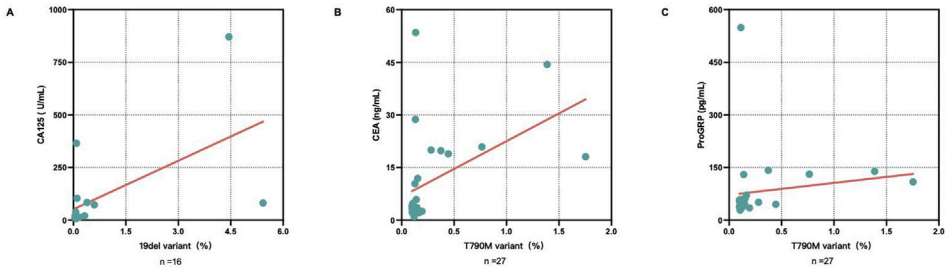

FIGURE 5
Correlations between the variant rates of epidermal growth factor receptor (EGFR)-mutant samples and serum tumor marker concentrations. **(A)** Positive correlation between the serum carbohydrate antigen 125 (CA125) levels and EGFR 19del variant rate (r = 0.624, *P* = 0.010). **(B)** Positive correlation between the serum carcinoembryonic antigen (CEA) levels and EGFR T790M variant rate (r = 0.531, *P* = 0.004). **(C)** Positive correlation between the serum progastrin-releasing peptide (ProGRP) levels and EGFR T790M variant rate (r = 0.395, *P* = 0.041).

sensitivity and 60.8% specificity) and 0.0247 copies/μL (with 60.4% sensitivity and 63.5% specificity).

Discussion

Compared with patients with WT EGFR, patients harboring EGFR TK domain mutations benefit more from EGFR-TKI therapy [2]. Accurate detection of EGFR mutations in NSCLC patients is therefore crucial for therapeutic stratification and longitudinal treatment monitoring. While tissue biopsy remains the diagnostic gold standard, its clinical utility is constrained by inherent limitations. In addition to its invasive nature, it provides only a static and spatially-limited assessment of the disease at the moment of the surgical procedure. Indeed, studies have shown that 27%–31% of NSCLC patients are unable to provide a biopsy sample suitable for EGFR mutation analysis at diagnosis or following disease progression [11]. This statistic increased to 70% for patients with locally advanced or metastatic disease at the time of NSCLC diagnosis [2]. Furthermore, a subset of patients with progressive disease decline repeat biopsies for molecular profiling despite clinical recommendations. In contrast, liquid biopsy offers a minimally invasive alternative enabling rapid, cost-effective, and real-time cancer longitudinal monitoring method that can capture tumor heterogeneity. Nevertheless, technical challenges persist in circulating cfDNA analysis due to its low concentration, genomic DNA contamination, and high fragmentation [13]. Additionally, inter-platform variability in dPCR methodologies - particularly regarding reference interval thresholds and gene

TABLE 5 The dPCR results of patients with progressive disease and stable disease after EGFR-TKI treatment.

EGFR mutations	PD (n = 53)	SD (n = 74)	*p* value
19del			
Variant rate (%)	0 (0–0.0272)	0 (0–0)	0.31
Variant (copies/μL)	0 (0–0.0266)	0 (0–0)	0.50
Wild type (copies/μL)	92.8651 (51.7457–179.8197)	84.1420 (44.9914–147.6963)	0.53
T790M			
Variant rate (%)	0.0446 (0–0.0683)	0.0147 (0–0.0555)	**0.031**
Variant (copies/μL)	0.0471 (0–0.0740)	0.0238 (0–0.0546)	**0.024**
Wild type (copies/μL)	72.8253 (43.4522–147.4915)	67.7830 (35.0735–121.2496)	0.41

dPCR, digital polymerase chain reaction; PD, progressive disease; SD, stable disease; EGFR-TKI, epidermal growth factor receptor tyrosine kinase inhibitor. Bold values indicate statistical significance ($p < 0.05$).

panel configurations - complicates result standardization across laboratories.

The data in this study described the performance characteristics of a novel dPCR assay platform for detecting EGFR 19del and T790M mutations in serum-derived cfDNA from NSCLC patients. This work demonstrated that the dPCR assay could achieve absolute quantification of mutant alleles according to Poisson distribution. The variant copy concentrations showed statistically significantly differences between EGFR mutant and WT samples. As was well known dPCR adopted the concept of "divide and conquer", which endowed it with excellent anti-interference ability. Based on the data provided, the dPCR method was found to be capable of detecting EGFR gene mutations in serum cfDNA samples that it could even detect gene mutations missed by tissue biopsy in some cases. However, the comparisons of gene status in serum cfDNA samples by dPCR assay and in tissue samples from patient clinical medical records suggested a rather high negative agreement and rather low positive agreement, which indicated that the assay was useful for ruling out mutations, but its sensitivity for detecting positives may be insufficient. The moderate performance of the current dPCR technology was indeed not as good as previously reported. In particular, further refinement might be necessary to improve the tests' low PPV in order to meet the clinical needs. It must be admitted that the differences in EGFR mutation detection capabilities between serum and tissue samples did exist that could not be ignored. There were several possible reasons for this. First, for the purpose of measuring multiple other cancer associated protein markers, we chose serum samples instead of the usual plasma samples for cfDNA extraction. The amount of ctDNA in each 1 mL serum sample was limited, with a potentially insufficient amount for dPCR amplification. Previous studies [14–17] have demonstrated that there are very low concentrations of cfDNA (1–5 ng/mL in healthy individuals and 5–1,500 ng/mL in cancer patients) and ctDNA (only a small fraction; <1% of the total cfDNA) in the bloodstream. Furthermore, the proportion of ctDNA present in a blood sample is related to the concordance of mutation profiles between tissue and blood. Insufficient materials could lead to false negative results. Second, the tissue and blood collection processes were not conducted at the same time in our study, and with long intervals. Jeffrey et al. [18] determined that a shorter time interval between tissue and blood collection was associated with increased concordance. As time goes by, secondary mutations and genotypic shifts might occur with recurrent tumors. This temporal genomic heterogeneity can have a substantial impact on the subsequent treatment outcomes [19].

Our study evaluated the potential relationship between serum biomarker levels and mutation detection in serum cfDNA by dPCR. Interestingly, we found that enhanced levels of certain tumor markers, specifically CA199 and ProGRP, could be potentially used as simple and practical clinical predictors of EGFR 19del and T790M mutation detection by dPCR liquid biopsy assay. Individuals with a serum CA199 level higher than 11.75 U/mL or ProGRP level higher than 45.15 pg/mL had an increased likelihood of EGFR mutation. However, the AUC values were below 0.8, which indicated that although the test can differentiate between mutation-positive and -negative cases to some extent, it might miss some positives or generate some false positives. On the other hand, significant positive correlations between serum CA125, CEA, and ProGRP levels and the variant rates in the EGFR mutant samples were observed. ProGRP is a tumor marker often used for the differential diagnosis of SCLC and NSCLC. Increasing ProGRP levels can help rule out NSCLC. Kudo et al. [20] reported that high ProGRP levels is also associated with neuroendocrine differentiation components of NSCLC. Kato et al. [21, 22] reported cases of NSCLC to SCLC transformation following EGFR-TKI treatment in patients whose ProGRP levels increased with disease progression. Our study further expanded the clinical application potential of this tumor marker. Serum tumor markers partly reflect the condition of ctDNA. A high proportion of ctDNA in the blood may enhance the mutation detection capability. Higher serum tumor marker levels were predictive of increased concordance in treatment-related genes

between paired tissue and plasma samples [17]. It was suggested that patients with higher serum CEA and CA199 levels had a significantly higher disease control rate and longer survival time with EGFR-TKI treatment [23].

It was suggested that for patients who underwent EGFR-TKI therapy, T790M mutation detection in serum had a predictive value of disease progression, even when the variant rate was lower than the corresponding cutoff value. More specifically, disease progression might present when the serum T790M variant rates or copies were higher than 0.0248% or 0.0247 copies/μL, respectively. The secondary EGFR T790M mutation constitutes the predominant acquired resistance mechanism to first- and second-generation TKIs [24]. The data indicated the clinical significance of mutation-negative results.

Our study indicated that the dPCR technology was indeed helpful in reducing the rate of missed diagnosis and was valuable for improving the level of clinical diagnosis, although the current effect was still not entirely satisfactory. There were certain limitations of this study that should be noted. First, this study was conducted in a single center, which resulted in a limited sample size and a possibility of bias. Thus, the results cannot truly reflect the dPCR assay performance for detecting EGFR 19del and T790M mutations among the population. Second, the low cfDNA concentration and high possibility of genomic DNA contamination in serum samples could result in an insufficient quantity of alleles for PCR amplification. Future studies that include an increased plasma volume and magnetic bead extraction method in place of the column method are needed to improve the cfDNA extraction efficiency. Third, the performance index data of the dPCR method, including sensitivity and specificity values, were difficult to accurately obtain because it was not feasible to perform tissue rebiopsy for further comparison. The moderate performance of the dPCR assay using serum suggested that further refinement or complementary markers might be necessary to improve the tests' PPV, especially in populations with lower mutation prevalence.

In conclusion, serum-based dPCR liquid biopsy assay demonstrates intermediate diagnostic capability for EGFR mutation monitoring. The assay should be reserved as an ancillary diagnostic tool in clinical scenarios characterized by contraindications to tissue biopsy or insufficient tumor material availability. Although further technical refinement is required to improve positive predictive performance, the assay is with good application value and prospects. Notably, its potential clinical utility lies in indicating possible disease transformation, oncogene drift or secondary mutations during longitudinal monitoring of NSCLC progression. To enhance practical implementation, combined detection of certain serum tumor markers emerges as a pragmatic triage strategy. This may facilitate the identification of subgroups most likely to benefit from EGFR testing, thereby improving the cost-effectiveness of precision oncology workflows through targeted patient stratification.

Author contributions

JX carried out the design of the study, performed the dPCR assay and drafted the manuscript. JP performed statistical analysis. ZX and GR collected clinical history and pathology workups. HZ performed the immunology analysis. XS and BZ collected the serum samples and helped to extract cfDNA. MG and GC conceived the study, participated in its design and coordination, and helped to draft the manuscript. All authors contributed to the article and approved the submitted version.

Data availability

The original contributions presented in the study are included in the article/supplementary material, further inquiries can be directed to the corresponding authors.

Ethics statement

The studies involving humans were approved by Huashan Hospital Ethical Committee (2022-572). The studies were conducted in accordance with the local legislation and institutional requirements. The participants provided their written informed consent to participate in this study.

Funding

The author(s) declare that financial support was received for the research and/or publication of this article. This study was funded by research grants from Shanghai "Rising Stars of Medical Talent" Youth Development Program, as well as Science and Technology Innovation Plan of Shanghai Science and Technology Commission (grant number 21Y11900600).

Conflict of interest

The author(s) declared no potential conflicts of interest with respect to the research, authorship, and/or publication of this article.

Generative AI statement

The author(s) declare that no Generative AI was used in the creation of this manuscript.

References

1. Qi J, Li M, Wang L, Hu Y, Liu W, Long Z, et al. National and subnational trends in cancer burden in China, 2005-20: an analysis of national mortality surveillance data. *The Lancet Public Health* (2023) **8**:e943–e955. doi:10.1016/s2468-2667(23)00211-6

2. da Cunha Santos G, Shepherd FA, Tsao MS. EGFR mutations and lung cancer. *Annu Rev Pathol* (2011) **6**:49–69. doi:10.1146/annurev-pathol-011110-130206

3. Franzi S, Seresini G, Borella P, Raviele PR, Bonitta G, Croci GA, et al. Liquid biopsy in non-small cell lung cancer: a meta-analysis of state-of-the-art and future perspectives. *Front Genet* (2023) **14**:1254839. doi:10.3389/fgene.2023.1254839

4. Gou LY, Wu YL. Prevalence of driver mutations in non-small-cell lung cancers in the People's Republic of China. *Lung Cancer (Auckland, N.Z.)* (2014) **5**:1–9. doi:10.2147/lctt.s40817

5. Ettinger DS, Wood DE, Aisner DL, Akerley W, Bauman JR, Bharat A, et al. Non-small cell lung cancer, version 3.2022, NCCN clinical practice guidelines in oncology. *J Natl Compr Cancer Netw* (2022) **20**:497–530. doi:10.6004/jnccn.2022.0025

6. Lu Z, Yi Y, Wang L, Luo Y, Luo D, Xiong L, et al. Non-small cell lung cancer cells with uncommon EGFR exon 19delins variants respond poorly to third-generation EGFR inhibitors. *Translational Oncol* (2024) **39**:101834. doi:10.1016/j.tranon.2023.101834

7. Kim C, Liu SV. First-line EGFR TKI therapy in non-small-cell lung cancer: looking back before leaping forward. *Ann Oncol* (2019) **30**:1852–5. doi:10.1093/annonc/mdz415

8. Casagrande GMS, Silva Md O, Reis RM, Leal LF. Liquid biopsy for lung cancer: up-to-date and perspectives for screening programs. *Int J Mol Sci* (2023) **24**:2505. doi:10.3390/ijms24032505

9. Bao H, Min L, Bu F, Wang S, Meng J. Recent advances of liquid biopsy: interdisciplinary strategies toward clinical decision-making. *Interdiscip Med* (2023) **1**:e20230021. doi:10.1002/inmd.20230021

10. Zhou Y, Shen L. Clinical application and challenges of liquid biopsy biomarkers in non-small cell lung cancer. *Lab Med* (2023) **38**:807–11. doi:10.3969/j.issn.1673-8640.2023.09.001

11. Normanno N, Denis MG, Thress KS, Ratcliffe M, Reck M. Guide to detecting epidermal growth factor receptor (EGFR) mutations in ctDNA of patients with advanced non-small-cell lung cancer. *Oncotarget* (2017) **8**:12501–16. doi:10.18632/oncotarget.13915

12. Hao J, Liu M, Zhou Z, Zhao C, Dai L, Ouyang S. Predicting epidermal growth factor receptor (EGFR) mutation status in non-small cell lung cancer (NSCLC) patients through logistic regression: a model incorporating clinical characteristics, computed tomography (CT) imaging features, and tumor marker levels. *PeerJ* (2024) **12**:e18618. doi:10.7717/peerj.18618

13. Martignano F. Cell-free DNA: an overview of sample types and isolation procedures. *Methods Mol Biol* (2019) **1909**:13–27. doi:10.1007/978-1-4939-8973-7_2

14. Merker JD, Oxnard GR, Compton C, Diehn M, Hurley P, Lazar AJ, et al. Circulating tumor DNA analysis in patients with cancer: American society of clinical oncology and college of American pathologists joint review. *J Clin Oncol* (2018) **36**:1631–41. doi:10.1200/jco.2017.76.8671

15. Diaz LA Jr, Bardelli A. Liquid biopsies: genotyping circulating tumor DNA. *J Clin Oncol.* (2014) **32**(6):579–586. doi:10.1200/JCO.2012.45.2011

16. Ranucci R. Cell-free DNA: applications in different diseases. *Methods Mol Biol* (2019) **1909**:3–12. doi:10.1007/978-1-4939-8973-7_1

17. Jiao XD, Ding LR, Zhang CT, Qin BD, Liu K, Jiang LP, et al. Serum tumor markers for the prediction of concordance between genomic profiles from liquid and tissue biopsy in patients with advanced lung adenocarcinoma. *Transl Lung Cancer Res* (2021) **10**:3236–50. doi:10.21037/tlcr-21-543

18. Thompson JC, Yee SS, Troxel AB, Savitch SL, Fan R, Balli D, et al. Detection of therapeutically targetable driver and resistance mutations in lung cancer patients by next-generation sequencing of cell-free circulating tumor DNA. *Clin Cancer Res* (2016) **22**:5772–82. doi:10.1158/1078-0432.ccr-16-1231

19. Fang Q, Wan X, D'Aiello A, Sun H, Gu W, Li Y, et al. Temporal genomic heterogeneity guiding individualized therapy in recurrent non-small cell lung cancer. *Front Oncol* (2023) **13**:1116809. doi:10.3389/fonc.2023.1116809

20. Kudo K, Ohyanagi F, Horiike A, Miyauchi E, Yanagitani N, Hoshi R, et al. Clinicopathological findings of non-small-cell lung cancer with high serum progastrin-releasing peptide concentrations. *Lung Cancer* (2011) **74**:401–4. doi:10.1016/j.lungcan.2011.03.019

21. Kato Y, Tanaka Y, Hino M, Gemma A. ProGRP as early predictive marker of non-small-cell lung cancer to small-cell lung cancer transformation after EGFR-TKI treatment. *Respir Med Case Rep* (2019) **27**:100837. doi:10.1016/j.rmcr.2019.100837

22. Watanabe S, Sone T, Matsui T, Yamamura K, Tani M, Okazaki A, et al. Transformation to small-cell lung cancer following treatment with EGFR tyrosine kinase inhibitors in a patient with lung adenocarcinoma. *Lung Cancer* (2013) **82**:370–2. doi:10.1016/j.lungcan.2013.06.003

23. Pan JB, Hou YH, Zhang GJ. Correlation between efficacy of the EGFR tyrosine kinase inhibitor and serum tumor markers in lung adenocarcinoma patients. *Clin Lab* (2014) **60**:1439–47. doi:10.7754/clin.lab.2013.131002

24. Ko B, Paucar D, Halmos B. EGFR T790M: revealing the secrets of a gatekeeper. *Lung Cancer Targets Ther* (2017) **8**:147–59. doi:10.2147/lctt.s117944

EBM Experimental Biology and Medicine

TYPE Original Research
PUBLISHED 29 May 2025
DOI 10.3389/ebm.2025.10520

OPEN ACCESS

*CORRESPONDENCE
Xi-Lan Yang,
xilanyang@njmu.edu.cn
Wei Gao,
drweig1984@outlook.com
Zheng-Kai Shen,
shenzhengkai@jscdc.cn

†These authors have contributed equally to this work

RECEIVED 07 February 2025
ACCEPTED 20 May 2025
PUBLISHED 29 May 2025

CITATION
Mao E-H, Bu Y-L, Liu Q-L, Xu J-S, Lu X, Yang X-L, Gao W and Shen Z-K (2025) Alcohol consumption may not be a risk factor for sarcopenia in the older adults. *Exp. Biol. Med.* 250:10520. doi: 10.3389/ebm.2025.10520

Alcohol consumption may not be a risk factor for sarcopenia in the older adults

En-Hui Mao[1†], Yun-Ling Bu[2†], Qiao-Ling Liu[3†], Jin-Shui Xu[4], Xiang Lu[5], Xi-Lan Yang[2*], Wei Gao[6*] and Zheng-Kai Shen[4*]

[1]Department of Endocrinology, Danyang Hospital of Traditional Medicine, Danyang, China, [2]Department of General Practice, The Fourth Affiliated Hospital of Nanjing Medical University, Nanjing, China, [3]Department of Geriatrics, The First People's Hospital of Lianyungang, Lianyungang, China, [4]Jiangsu Province Center for Disease Control and Prevention, Nanjing, China, [5]Department of Geriatrics, Sir Run Run Hospital, Nanjing Medical University, Nanjing, China, [6]Department of Geriatrics, Zhongda Hospital, School of Medicine, Southeast University, Nanjing, China

Abstract

The relationship between drinking and sarcopenia remains controversial. The aim of the present study was to investigate the association of alcohol drinking with sarcopenia in the older adults. A prospective study with 5244 Chinese community-dwelling older adults aged ≥65 years was performed. Sarcopenia was assessed by appendicular skeletal muscle mass index, grip strength, and gait speed. A quantitative questionnaire was used to obtain the information of alcohol drinking. After 4-year follow-up, our study showed that drinkers had lower incidence of sarcopenia than those non-drinkers (19.4% vs. 30.4%, $P < 0.001$ in males and 9.5% vs. 20.4%, $P = 0.004$ in females, respectively). Moreover, male drinkers had higher levels of muscle mass [median (IQR): 7.3 (6.7–7.9) kg/m^2 vs. 7.1 (6.5–7.7) kg/m^2, $P < 0.001$] grip strength [median (IQR): 31.1 (26.5–35.0) kg vs. 29.6 (24.8–38.8) kg, $P < 0.001$], and gait speed [median (IQR): 1.08 (0.98–1.17) m/s vs. 1.05 (0.94–1.15) m/s, $P < 0.001$] than those non-drinkers, while female drinkers had higher gait speed [median (IQR): 1.02 (0.94–1.11) m/s vs. 0.99 (0.89–1.09) m/s, $P = 0.031$] than those non-drinkers. Multivariate logistic regression showed that in older adults younger than 85 years, both interim drinking (RR = 0.60; 95%CI = 0.39–0.93; $P = 0.021$ for males; RR = 0.36; 95%CI = 0.13–0.90; $P = 0.035$ for females) and daily drinking (RR = 0.78; 95%CI = 0.61–0.99; $P = 0.045$ for males; RR = 0.34; 95%CI = 0.12–0.96; $P = 0.041$ for females) were correlated with decreased risk of sarcopenia even after adjustment for confounding factors. However, our dose-response analysis did not show any significant relationship between daily alcohol intake and the risk of sarcopenia as well as the components of sarcopenia. In conclusion, our results indicated that alcohol drinking may not be a risk factor for sarcopenia in the older adults. Further research will help to understand the underlying mechanism of the observed causal relationship.

KEYWORDS

alcohol, sarcopenia, older adults, community-dwelling, odds ratio

Impact statement

Although the possible role of alcohol consumption in sarcopenia has attracted increasing attention, the results of current studies remain controversial. Our prospective study provides a novel information that alcohol consumption may not be a risk factor for sarcopenia in a community-dwelling population of Chinese older adults. Specifically, alcohol consumption might have a potential protective effect against the risk of sarcopenia in older adults younger than 85 years old and those who were not underweight (BMI≥18.5 kg/m^2). However, heavy drinking has significant social burden in addition to human health and therefore is not recommended. Advices regarding the health effects of alcohol drinking on sarcopenia need to be further individualized according to the specific medical status.

Introduction

Sarcopenia has been identified as a novel geriatric disorder characterized by loss of muscle mass and muscle strength compromising with age [1]. The prevalence of sarcopenia in the older adult ranges from 6% to 12% worldwide [2], and 10.6%–38.8% in China [3–6]. Emerging evidence have linked sarcopenia with a variety of adverse outcomes including frailty, falls, fracture, morbidity and mortality, leading sarcopenia becomes a heavy burden and hotspot in the society of geriatrics [7].

Lifestyle is closely related to sarcopenia, among which drinking is one of the most modifiable behaviors [8]. Drinking is a traditional cultural behavior in China, with the drinking rate of 36.5% and 8.1% in aged male and female, respectively [9]. Although the possible role of alcohol consumption in sarcopenia has attracted increasing attention, the results of current studies remain controversial. Three studies based on Asian population suggested that alcohol drinking might be risk factor for sarcopenia [10–12], whereas another study did not found any correlation between alcohol consumption and sarcopenia [13]. Intriguingly, meta-analysis even indicated that alcohol intake might have protective effect on sarcopenia, especially in males [14, 15], while another recently published meta-analysis reported negative result [16]. The inconsistent results may attribute to the difference of diagnostic criteria for sarcopenia as well as the lack of the specificity of drinking information, such as drinking frequency and consumed alcohol volume. Therefore, the present study aimed to investigate the association of alcohol consumption with sarcopenia in a larger sample size with Chinese community-dwelling older adults.

Materials and methods

Study participants

This prospective study was based on participants from the National Basic Public Health Project in Yuetang Community Medical Center in Yangzhou, Jiangsu Province, China in 2020. Participants completed the general information questionnaire (including alcohol intake), physical examinations (including the collection of blood samples), and anthropometry information. A total of 5976 older adults aged ≥65 years were recruited. The exclusion criteria included: (1) unable to accomplish the specified actions (n = 173); (2) had a history of malignant tumors, dementia, mental disorders, severe cardiopulmonary dysfunction (New York Heart Association class III-IV) (n = 537); (3) With missing drinking information (n = 22). Finally, 5244 older adults were included in the follow-up study. This study was performed in accordance with the principles stated in the Declaration of Helsinki [17] and approved by the Ethics Committee of Sir Run Run Hospital, Nanjing Medical University (approval No. 2019-SR-S041). Written informed consent was obtained from each participant.

Assessment of alcohol consumption

Participants were classified as non-drinkers, interim drinkers (<7 days/week), and daily drinkers, as previously described [18]. For the daily drinkers, we further collected information about the type of alcohol (hard liquor, wine, beer) as well as the amount of intake, which was calculated in grams per day by multiplying the average frequency (times per day) by the amount of each beverage and its corresponding pure ethanol content (5 g ethanol for every 100 g of beer, 12 g ethanol for every 100 g of wine, and 40 g for every 100 g of hard liquor) [12].

Assessment of sarcopenia

The status of sarcopenia was assessed every year. Muscle mass was measured by bioelectrical impedance analysis (BIA) (Inbody S10; Inbody Korea Ltd., Korea). The height-adjusted appendicular skeletal muscle mass index (ASMI) was calculated as ASM (the sum of skeletal muscle in the arms and legs) divided by height squared in meters (ASM/height [2]). Low muscle mass was defined as an ASMI <7.0 kg/m^2 in men and <5.7 kg/m^2 in women [8]. Muscle strength was represented by grip strength measured using a dynamometer (CAMRY EH101, China). Low muscle strength was defined as handgrip strength <28 kg in men and <18 kg in women [8]. Gait speed on a 6-m test <1 m/s was defined as declined physical performance [8].

TABLE 1 Characteristics according to alcohol consumption at baseline.

Variables	Men				Women			
	Total (n = 2,603)	Non-drinker (n = 1,669)	Drinker (n = 934)	*P*	Total (n = 2,641)	Non-drinker (n = 2,525)	Drinker (n = 116)	*P*
Age, y	72 (69–76)	73 (69–78)	73 (68–77)	0.861	73 (69–77)	73 (69–77)	72 (69–76)	0.363
BMI, kg/m^2	23.5 ± 3.3	23.2 (20.9–25.6)	23.3 (20.5–25.6)	0.763	24.7 (22.4–27.2)	24.7 (22.4–27.3)	24.7 (22.5–26.7)	0.637
Waist-to-hip ratio	0.90 (0.87–0.94)	0.90 (0.86–0.94)	0.90 (0.87–0.93)	0.882	0.90 (0.86–0.94)	0.90 (0.86–0.94)	0.90 (0.87–0.93)	0.630
HGB, g/L	137 (128–144)	137 (126–142)	138 (127–144)	0.221	134 (127–139)	133 (127–139)	135 (129–142)	0.013
WBC, 10^9/L	5.4 (4.6–6.4)	5.4 (4.6–6.5)	5.4 (4.6–6.4)	0.486	5.3 (4.5–6.3)	5.4 (4.5–6.3)	5.2 (4.6–6.0)	0.652
PLT, 10^9/L	139 (110–171)	139 (109–170)	140 (110–171)	0.164	146 (116–181)	146 (115–181)	146 (116–182)	0.560
FBG, mmol/L	5.4 (5.1–5.9)	5.4 (5.1–5.9)	5.4 (5.1–5.9)	0.558	5.4 (5.1–6.0)	5.4 (5.1–6.0)	5.5 (5.2–5.9)	0.762
ALB, g/L	37.2 (35.6–43.2)	37.2 (35.3–43.9)	37.3 (35.4–43.5)	0.745	36.5 (34.2–41.2)	36.2 (33.8–43.1)	36.3 (33.4–42.8)	0.152
AST/ALT ratio	1.48 (1.15–1.92)	1.44 (1.13–1.86)	1.57 (1.21–2.00)	<0.001	1.53 (1.20–1.96)	1.52 (1.20–1.96)	1.56 (1.25–1.96)	0.479
TBIL, μmol/L	13.5 (10.6–17.7)	13.2 (10.4–17.2)	14.5 (11.0–19.0)	<0.001	11.8 (9.3–15.1)	11.8 (9.3–15.1)	11.8 (9.2–15.0)	0.780
Cr, μmol/L	64.1 (53.1–75.1)	64.2 (53.5–76.2)	64.1 (52.3–75.6)	0.110	62.5 (53.9–71.6)	62.6 (54.0–71.8)	62.1 (53.8–70.7)	0.413
BUN, mmol/L	5.3 (4.4–6.6)	5.3 (4.5–6.6)	5.4 (4.4–6.7)	0.683	5.3 (4.4–6.4)	5.3 (4.4–6.4)	5.5 (4.5–6.5)	0.184
TC, mmol/L	4.6 (4.1–5.2)	4.6 (4.1–5.1)	4.6 (4.2–5.0)	0.416	4.5 (4.1–5.1)	4.5 (4.0–5.1)	5.6 (4.1–5.3)	0.109
TG, mmol/L	1.1 (0.9–1.6)	1.1 (0.9–1.5)	1.1 (0.8–1.6)	0.775	1.2 (1.1–1.4)	1.2 (1.1–1.5)	1.2 (1.0–1.4)	0.813
LDL-C, mmol/L	1.93 (1.55–2.32)	1.93 (1.59–2.33)	1.92 (1.58–2.32)	0.245	2.18 (1.78–2.58)	2.17 (1.78–2.58)	2.25 (1.82–2.63)	0.304
ASMI, kg/m^2	7.7 (7.1–8.8)	7.6 (7.1–8.9)	7.7 (7.2–8.9)	0.823	6.1 (5.6–6.7)	6.2 (5.6–6.7)	6.1 (5.7–6.6)	0.954
Grip strength, kg	34.2 (32.3–38.3)	33.6 (31.8–39.8)	34.1 (32.5–40.0)	0.572	20.9 (18.0–23.8)	20.8 (18.0–23.8)	21.4 (19.2–23.5)	0.181
Gait speed, m/s	1.36 (1.06–1.56)	1.35 (1.04–1.65)	1.38 (1.03–1.77)	0.221	1.19 (1.09–1.29)	1.19 (1.09–1.30)	1.18 (1.04–1.30)	0.131

BMI, body mass index; ALB, albumin; ASMI, appendicular muscle mass index; HGB, hemoglobin; WBC, white blood cell; PLT, platelet; FBG, fasting blood glucose; AST, aspartate transaminase; ALT alanine transaminase; TBIL, total bilirubin; Cr, creatinine; BUN, blood urea nitrogen; TC, total cholesterol; TG, triglyceride; LDL-C, low-density lipoprotein cholesterol; HDL-C, high-density lipoprotein cholesterol.

Statistical analysis

Kolmogorov-Smirnov test was applied to test the normality of continuous variable. Non-normal data were represented as median and interquartile range (IQR), and compared by Mann-Whitney *U* test. Qualitative variables were represented as frequencies and compared by Pearson $\chi 2$ test. Logistic regression analyses were performed to identified the variables associated with the risk of sarcopenia. Odds ratios (ORs) and 95% confidence intervals (CIs) were calculated. Dose-response analysis was performed by the method described by Greenland and Orsini [19, 20]. The ORs that were the most confounding factors were adjusted and their 95% CIs were used to estimate log ORs and their standard errors (SEs). Linear regression was used to explore the dose-response relationship of every 1g increase in daily alcohol intake with the aspects of sarcopenia. Restricted cubic splines (four knots at fixed percentiles of 5%, 35%, 65%, and 95% of the distribution) were applied to evaluate potential nonlinear dose-response relationship between alcohol consumption and sarcopenia. All statistical analyses were performed by using SPSS 28.0 (IBM SPSS, Inc., USA). All analyses were two-sided and $P < 0.05$ was considered as statistical significance.

Results

Baseline characteristics

Among 5244 enrolled subjects, there were 1,050 older adults drank alcohol (20.0%) with 35.9% in males and 4.4% in females. As shown in Table 1, the male drinkers had higher levels of aspartate transaminase (AST)/alanine transaminase (ALT) ratio and total bilirubin (TBIL), whereas the female drinkers had higher levels of hemoglobin (HGB) at baseline ($P < 0.05$). By contrast, there were no significant differences in other clinical

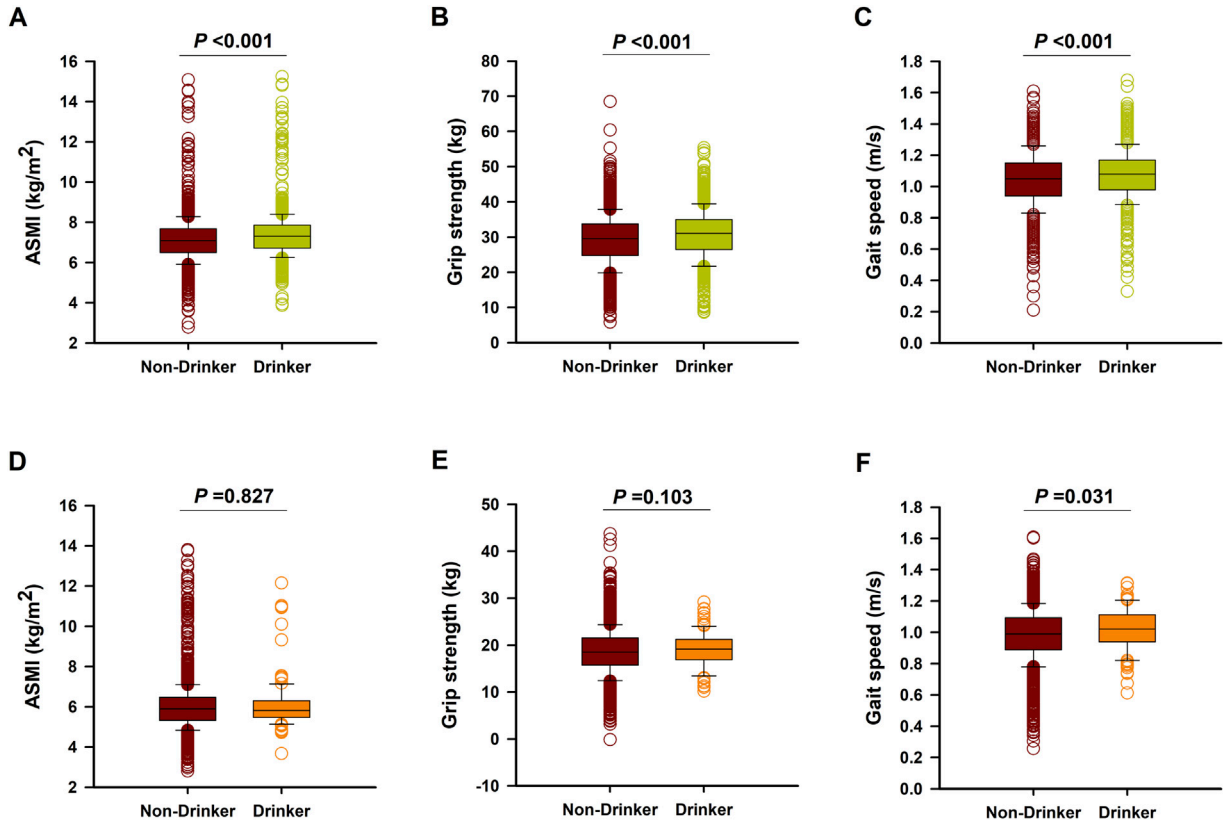

FIGURE 1
The levels of ASMI, grip strength, and gait speed in male **(A–C)** and Female **(D–F)** non-drinkers and drinkers after 4-years follow-up.

parameters as well as the ASMI, grip strength, and gait speed between drinks and non-drinkers at baseline ($P > 0.05$).

Association of alcohol consumption with sarcopenia

After a follow-up of 4 years, there were 691 aged males had sarcopenia (26.5%), with 184 patients in the drinking group and 507 patients in the non-drinking group. In addition, there were 527 aged females had sarcopenia (20.0%), with 11 patients in the drinking group and 516 patients in the non-drinking group. Interestingly, drinkers had a lower incidence of sarcopenia than those non-drinkers both in males (19.7% vs. 30.4%, $P < 0.001$) and females (9.5% vs. 20.4%, $P < 0.001$). Moreover, male drinkers also had higher levels of muscle mass [median (IQR): 7.3 (6.7–7.9) kg/m^2 vs. 7.1 (6.5–7.7) kg/m^2, $P < 0.001$], grip strength [median (IQR): 31.1 (26.5–35.0) kg vs. 29.6 (24.8–38.8) kg, $P < 0.001$], and gait speed [median (IQR): 1.08 (0.98–1.17) m/s vs. 1.05 (0.94–1.15) m/s, $P < 0.001$] than those non-drinkers (Figures 1A–C). By contrast, female drinkers had higher gait speed [median (IQR): 1.02 (0.94–1.11) m/s vs. 0.99 (0.89–1.09) m/s, $P = 0.031$], with no significant difference of muscle mass [median (IQR): 6.0 (5.2–6.4) kg/m^2 vs. 6.1 (5.2–6.7) kg/m^2, $P = 0.827$] and grip strength [median (IQR): 19.1 (18.3–21.0) kg vs. 18.6 (17.8–22.3) kg, $P = 0.103$] when compared to those female non-drinkers (Figures 1D–F).

Univariate logistic analysis indicated that the factors correlated with the risk of sarcopenia in males included age, low levels of body mass index (BMI), HGB, white blood counts (WBC), fasting blood glucose (FBG), TBIL, triglyceride (TG), and low-density lipoprotein cholesterol (LDL-C), but higher AST/ALT ratio and high-density lipoprotein cholesterol (HDL-C) (Table 2). Importantly, compared with non-drinkers, older men with interim drinking (RR = 0.56; 95%CI = 0.38–0.81; $P = 0.003$) and daily drinking (RR = 0.56; 95%CI = 0.46–0.69; $P < 0.001$) were less likely to have sarcopenia. For aged females, univariate logistic analysis indicated that the risks factors of sarcopenia included age, low levels of BMI, HGB, FBG, and TG, but higher AST/ALT ratio and HDL-C. Compared with non-drinkers, older women with daily drinking (RR = 0.35; 95%CI = 0.14–0.88; $P = 0.024$) were less likely to suffer from sarcopenia (Table 2). However, these protective effects of drinking on the incidence of sarcopenia were lost after adjustment for potential confounding factors (Table 3). Subgroup analysis suggested that

TABLE 2 Univariate logistic analysis for risk factors of sarcopenia in older adults.

Variables	Men			Women		
	β	OR (95%CI)	*P*	*β*	OR (95%CI)	*P*
Age	0.141	1.15 (1.13–1.17)	<0.001	0.143	1.15 (1.13–1.18)	<0.001
BMI	−0.264	0.77 (0.74–0.79)	<0.001	−0.296	0.74 (0.72–0.77)	<0.001
HGB	−0.035	0.97 (0.96–0.97)	<0.001	−0.028	0.97 (0.96–0.98)	<0.001
WBC	−0.090	0.91 (0.86–0.97)	0.003	−0.037	0.96 (0.90–1.03)	0.268
PLT	−0.001	1.00 (1.00–1.00)	0.302	−0.001	1.00 (1.00–1.00)	0.135
FBG	−0.098	0.91 (0.84–0.98)	0.013	−0.077	0.93 (0.86–0.99)	0.041
ALB	0.003	0.98 (0.97–1.03)	0.546	0.008	1.02 (0.98–1.05)	0.411
AST/ALT ratio	0.438	1.55 (1.38–1.74)	<0.001	0.645	1.91 (1.67–2.17)	<0.001
TBIL	−0.019	0.98 (0.97–0.99)	0.008	−0.009	0.99 (0.97–1.01)	0.340
Cr	0.001	1.00 (1.00–1.00)	0.617	0.003	1.00 (1.00–1.00)	0.261
BUN	0.034	1.03 (0.98–1.08)	0.143	0.063	1.07 (1.01–1.13)	0.029
TC	−0.058	0.94 (0.87–1.03)	0.170	0.011	1.01 (0.93–1.10)	0.790
TG	−0.339	0.71 (0.62–0.82)	<0.001	−0.241	0.79 (0.70–0.88)	<0.001
LDL-C	−0.159	0.85 (0.74–0.99)	0.036	−0.095	0.91 (0.78–1.06)	0.220
HDL-C	0.575	1.78 (1.42–2.23)	<0.001	0.868	2.38 (1.82–3.12)	<0.001
Alcohol consumption						
Non-drinker (64.12%)		1 (reference)			1 (reference)	
Interim drinker (7.07%)	−0.584	0.56 (0.38–0.81)	0.003	−0.741	0.48 (0.20–1.12)	0.089
Daily drinker (28.81%)	−0.574	0.56 (0.46–0.69)	<0.001	−1.057	0.35 (0.14–0.88)	0.024

OR, odds ratio; CI, confidence interval; BMI, body mass index; HGB, hemoglobin; WBC, white blood cell; PLT, platelet; FBG, fasting blood glucose; ALB, albumin; AST, aspartate transaminase; ALT alanine transaminase; TBIL, total bilirubin; Cr, creatinine; BUN, blood urea nitrogen; TC, total cholesterol; TG, triglyceride; LDL-C, low-density lipoprotein cholesterol; HDL-C, high-density lipoprotein cholesterol.

in the older adults with age <85 years old, both interim drinking (RR = 0.60; 95%CI = 0.39–0.93; $P = 0.021$ for males; RR = 0.36; 95%CI = 0.13–0.90; $P = 0.035$ for females) and daily drinking (RR = 0.78; 95%CI = 0.61–0.99; $P = 0.045$ for males; RR = 0.34; 95%CI = 0.12–0.96; $P = 0.041$ for females) were correlated with decreased risk of sarcopenia even after adjustment for confounding factors. Moreover, daily alcohol consumption (RR = 0.75; 95%CI = 0.58–0.95; $P = 0.019$) was also related to decreased risk of sarcopenia in aged males who were not underweight (BMI ≥18.5 kg/m^2) (Table 3).

Dose-response relationship between daily alcohol consumption and sarcopenia

We further analyzed the dose-response relationship between daily alcohol consumption and sarcopenia. Considering the small number of daily drinkers (n = 61) in the females, we only performed dose-response analysis in the male daily drinkers (n = 750). As shown in Figure 2, restricted cubic splines model indicated no nonlinear dose-response relationship between daily alcohol intake and risk of sarcopenia ($\chi2 = 1.76$, $P = 0.414$), low muscle mass ($\chi2 = 3.68$, $P = 0.159$), low grip strength ($\chi2 = 2.38$, $P = 0.304$), and low gait speed ($\chi2 = 0.55$, $P = 0.760$). Unfortunately, we did not find linear dose-response relationship between daily alcohol intake and the risk of sarcopenia ($P = 0.423$), as well as low muscle mass ($P = 0.297$), low grip strength ($P = 0.460$), and low gait speed ($P = 0.156$).

Discussion

Along with the population aging, sarcopenia has been getting more and more attention worldwide. Although various types of lifestyles have been linked to the etiology of sarcopenia [21]; however, the exact correlation between alcohol beverage consumption and sarcopenia remains controversial. Interestingly, we here showed that alcohol drinking might have a potential beneficial effect on the risk of sarcopenia in a community-dwelling population in Yangzhou city of older adults, especially in those younger than 85 years old. Further

TABLE 3 Multivariate logistic regression analyses for the association of alcohol consumption with sarcopenia.

Variables	Model 1			Model 2		
	β	OR (95%CI)	*p*	β	OR (95%CI)	*p*
Men						
Overall analyses						
Non-drinker (64.12%)		1 (reference)			1 (reference)	
Interim drinker (7.07%)	−0.283	0.75 (0.50–1.15)	0.187	−0.249	0.78 (0.51–1.19)	0.249
Daily drinker (28.81%)	−0.225	0.80 (0.63–1.01)	0.058	−0.150	0.86 (0.67–1.10)	0.236
Stratification analyses						
Age						
<85 years (n = 2,489)						
Non-drinker (63.08%)		1 (reference)			1 (reference)	
Interim drinker (7.15%)	−0.562	0.57 (0.38–0.87)	0.009	−0.504	0.60 (0.39–0.93)	0.021
Daily drinker (29.77%)	−0.383	0.68 (0.55–0.85)	0.001	−0.247	0.78 (0.61–0.99)	0.045
≥85 years (n = 114)						
Non-drinker (86.84%)		1 (reference)			1 (reference)	
Interim drinker (5.26%)	1.154	3.17 (0.30–33.57)	0.338	1.147	3.15 (0.18–54.19)	0.430
Daily drinker (7.89%)	−0.721	0.49 (0.11–2.20)	0.349	−1.109	0.33 (0.05–2.26)	0.259
BMI						
<18.5 kg/m^2 (n = 164)						
Non-drinker (81.71%)		1 (reference)			1 (reference)	
Interim drinker (4.27%)	−1.029	0.36 (0.07–1.79)	0.211	−1.240	0.29 (0.05–1.72)	0.172
Daily drinker (14.02%)	−0.553	0.58 (0.23–1.46)	0.245	−0.264	0.77 (0.24–2.44)	0.654
≥18.5 kg/m^2 (n = 2,439)						
Non-drinker (62.94%)		1 (reference)			1 (reference)	
Interim drinker (7.26%)	−0.221	0.80 (0.53–1.21)	0.296	−0.217	0.81 (0.53–1.23)	0.314
Daily drinker (29.81%)	−0.240	0.79 (0.63–0.99)	0.040	−0.294	0.75 (0.58–0.95)	0.019
Women						
Overall analyses						
Non-drinker (95.61%)		1 (reference)			1 (reference)	
Interim drinker (2.08%)	−0.935	0.39 (0.16–1.01)	0.057	−0.937	0.39 (0.15–1.01)	0.059
Daily drinker (2.31%)	−0.951	0.39 (0.14–1.04)	0.061	−0.886	0.41 (0.15–1.11)	0.080
Stratification analyses						
Age						
<85 years (n = 2,511)						
Non-drinker (95.58%)		1 (reference)			1 (reference)	
Interim drinker (2.07%)	−1.052	0.35 (0.12–0.99)	0.048	−1.022	0.36 (0.13–0.90)	0.035
Daily drinker (2.35%)	−1.135	0.32 (0.11–0.91)	0.033	−1.089	0.34 (0.12–0.96)	0.041
≥85 years (n = 130)						
Non-drinker (96.15%)		1 (reference)			1 (reference)	
Interim drinker (2.31%)	0.385	1.47 (0.13–16.93)	0.758	0.248	1.28 (0.09–18.10)	0.854
Daily drinker (1.54%)	−0.616	0.54 (0.03–9.00)	0.668	−0.443	0.64 (0.03–14.11)	0.779

(Continued on following page)

TABLE 3 (*Continued*) Multivariate logistic regression analyses for the association of alcohol consumption with sarcopenia.

Variables	Model 1			Model 2		
	β	OR (95%CI)	*p*	β	OR (95%CI)	*p*
BMI						
<18.5 kg/m^2 (n = 111)						
Never drinker (99.10%)	-	-	-	-	-	-
Interim drinker (0.90%)	-	-	-	-	-	-
Daily drinker (0.00%)	-	-	-	-	-	-
≥18.5 kg/m^2 (2,530)						
Never drinker (95.45%)		1 (reference)			1 (reference)	
Interim drinker (2.13%)	−0.701	0.50 (0.21–1.20)	0.120	−0.816	0.44 (0.18–1.09)	0.075
Daily drinker (2.41%)	−0.841	0.43 (0.17–1.12)	0.085	−0.855	0.43 (0.16–1.11)	0.080

OR, odds ratio; CI, confidence interval; BMI, body mass index.
Model 1: Adjusted for age (for overall analyses and BMI stratification analyses) or BMI (for overall analyses and age stratification analyses).
Model 2: Adjusted for age (for overall analyses and BMI stratification analyses) or BMI (for overall analyses and age stratification analyses), HGB, WBC, PLT, FBG, AST/ALT ratio, TBIL, Cr, BUN, TC, TG, LDL-C, and HDL-C.

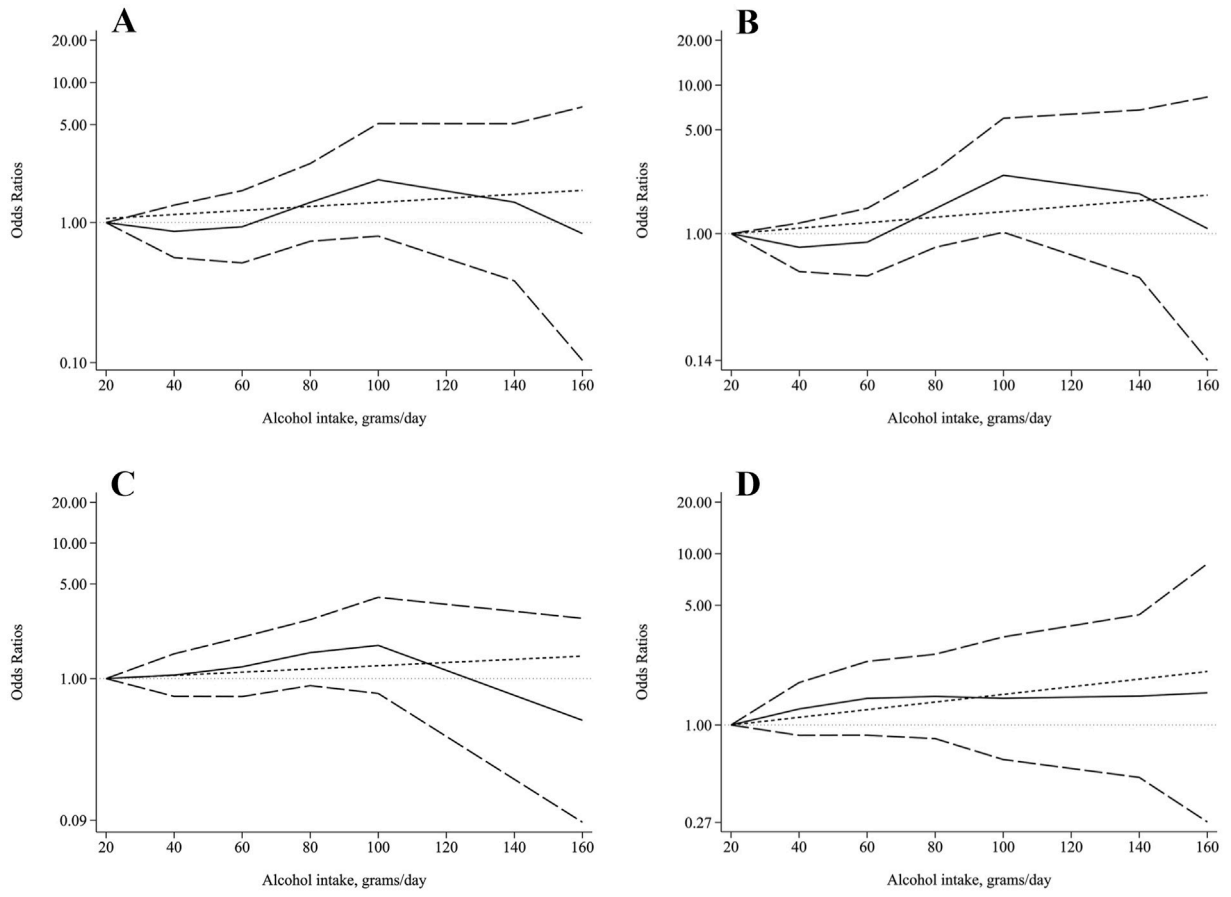

FIGURE 2
Dose-response relationship between alcohol intake and **(A)** sarcopenia, **(B)** low AMSI, **(C)** low grip strength, and **(D)** low gait speed. The solid line and the long dash line represent the ORs and its 95%CI. Short dash line represents the linear relationship. Linear and spline models were adjusted for age, BMI, HGB, WBC, PLT, FBG, AST/ALT ratio, TBIL, Cr, BUN, TC, TG, LDL-C, and HDL-C.

studies will be needed to identified the appropriate amount of alcohol consumption for the prevention of sarcopenia.

Alcohol consumption is growing globally and accounts for about 5.1% of the global burden of human diseases, especially cardiovascular disease and cancer [22–24]. Animal studies have demonstrated that alcohol can inhibit the synthesis of protein predominately in type II muscle fibers which in turn causes muscle atrophy [25–28]. Moreover, ethanol exposure also induces autophagy flux in C2C12 myotubes, which contributes to the pathogenesis of sarcopenia [26]. However, previous retrospective studies showed controversial results on the relationship between alcohol consumption and sarcopenia. Some studies found detrimental effects of alcohol on the risk of sarcopenia [10–12, 29, 30], whereas others reported negative results between two of them [31–34]. Although the different types of alcoholic beverages, the amount of consumption, as well as the different drinking patterns may affect the relationship between drinking and human diseases [35], the observed protective effects of alcohol intake on the risk of sarcopenia in our present study should be interpreted with caution. According to the dietary guidelines for Chinese residents, the recommended amount of alcohol intake should less than 25g/day [36]. Particularly, daily drinking was associated with lower risk of sarcopenia only in older adults younger than 85 years. This age difference in the relationship between alcohol consumption and sarcopenia may be attribute to the decreased alcohol intake along with aging [37]. Moreover, drinking pattern, such as whether the alcohol is taken at mealtimes [38], may also influence the effect of alcohol consumption on sarcopenia. Interestingly, a previous study showed that drinking with meals might be beneficial for decreasing the all-cause mortality [39]. However, we did not find a significant dose-response relationship between alcohol intake and sarcopenia. Considering that the individual dose was obtained by self-report, the limitation in measurement precision could obscure such a relationship. Therefore, further studies focused on different drinking pattern will help us to understand the potential health effects of alcohol on sarcopenia.

There are some potential explanations that may account for the protection effects against sarcopenia by alcohol consumption. Since malnutrition, especially with low BMI (<18.5 kg/cm^2), has been demonstrated as one of the most important risk factors for sarcopenia [7], the leading possibility might be related to the weight gain in alcohol consumers, especially in those daily drinkers [40]. However, considering that weight gain induced by alcohol consumption primarily due to an increase in fat mass, which often contributes to obesity, further studies are needed to confirm the association of drinking with the detailed amount of body composition. Another potential reason may be related the relatively positive life attitude of people who drink moderate amounts of alcohol [41]. In the present study, older adults with interim drinking also had a lower risk of sarcopenia. These people may have more social intercourse and exercise, both of which are important preventive measures for the management of sarcopenia [7]. Moreover, another study reported that alcohol consumption could also increase the level of HDL-C [42], which is inversely correlated with the risk of sarcopenia [43]. Sphingolipids level is also decreased in drinkers when compared to those non-drinkers [44]. As an important bioactive sphingolipid, previous studies have shown that ceramide can directly activate atypical PKC isoform protein kinase Cζ to induce endoplasmic reticulum stress and mitochondrial dysfunction [45], which play crucial roles in the pathogenesis of sarcopenia [46]. Therefore, moderate alcohol may play a protective role in skeletal muscle by depleting sphingolipids, especially ceramide. Nevertheless, further in-depth experiments are needed to investigate the explicit mechanism governing the effects of different types and amount of alcohol on the development of sarcopenia.

Several limitations should still be considered in the present study. Firstly, the information of alcohol consumption was self-reported, which may cause social desirability bias and recall error. Future prospective studies with an intervention of different amount of alcohol will help to determine the dose-dependent effects of alcohol consumption on the prevention of sarcopenia. Secondly, almost all the older adults in this study consumed liquor. The effects of different types of alcohol beverages such as wine, beer, sake, yellow rice, *etc.* on the risk of sarcopenia will need to be assessed. Thirdly, we cannot rule out the possibility of other potential confounding dietary factors, such as the nutritional status, physical activity, and socio-economic conditions as well as the consumption of tea, coffee, fruits, vitamins or other antioxidant substances.

Conclusion

In summary, our findings suggest that alcohol intake may not be a risk factor for the development of sarcopenia in this Yangzhou cohort. Instead, appropriate amount of alcohol consumption might be related to decreased risk of sarcopenia in older adults younger than 85 years. However, heavy drinking has significant social burden in addition to human health and therefore is not recommended. Advices regarding the health effects of alcohol drinking on sarcopenia need to be further individualized according to the specific medical status.

Author contributions

WG, Z-KS, and X-LY contributed to the conception and design of the study. E-HM, Y-LB, Q-LL, and J-SX contributed to data acquisition. Y-LB, E-HM, and Z-KS analyzed the data. E-HM and Y-LB drafted the manuscript. WG, Q-LL, and X-LY revised the manuscript. All authors contributed to the article and approved the submitted version.

Data availability

The raw data supporting the conclusions of this article will be made available by the authors, without undue reservation.

Ethics statement

The studies involving humans were approved by The Ethics Committee of Sir Run Run Hospital, Nanjing Medical University. The studies were conducted in accordance with the local legislation and institutional requirements. The participants provided their written informed consent to participate in this study.

Funding

The author(s) declare that financial support was received for the research and/or publication of this article. This work was supported by grants from the National Key Research and Development Plan of China (No. 2020YFC2008505 to XL), the National Natural Science Foundation of China (No. 81970217 to WG), and the Jiangsu Commission of Health (No. LKZ2023005 to WG, No. LKM2023004 to Z-KS), the project of Zhongda Hospital Affiliated to Southeast University for cultivating academic talent (No. CZXM-GSPRC22 to WG), the Zhongda Hospital Affiliated to Southeast University, Jiangsu Province High-Level Hospital Pairing Assistance Construction Funds (No. ZDLYG10 to WG), the Zhongda Hospital Affiliated to Southeast University, Jiangsu Province High-Level Hospital Construction Funds (No. GSP-LCYJFH17 to WG), China Heart House-Chinese Cardiovascular Association HX fund (No. 2022-CCA-HX-082 to WG), Bethune Charitable Foundation (No. 2024020185BA to WG).

Conflict of interest

The author(s) declared no potential conflicts of interest with respect to the research, authorship, and/or publication of this article.

Generative AI statement

The author(s) declare that no Generative AI was used in the creation of this manuscript.

References

1. Cruz-Jentoft AJ, Bahat G, Bauer J, Boirie Y, Bruyere O, Cederholm T, et al. Sarcopenia: revised European consensus on definition and diagnosis. *Age and Ageing* (2019) **48**:16–31. doi:10.1093/ageing/afy169

2. Shafiee G, Keshtkar A, Soltani A, Ahadi Z, Larijani B, Heshmat R. Prevalence of sarcopenia in the world: a systematic review and meta- analysis of general population studies. *J Diabetes Metab Disord* (2017) **16**:21. doi:10.1186/s40200-017-0302-x

3. Du Y, Wang X, Xie H, Zheng S, Wu X, Zhu X, et al. Sex differences in the prevalence and adverse outcomes of sarcopenia and sarcopenic obesity in community dwelling elderly in East China using the AWGS criteria. *BMC Endocr Disord* (2019) **19**:109. doi:10.1186/s12902-019-0432-x

4. Meng P, Hu YX, Fan L, Zhang Y, Zhang MX, Sun J, et al. Sarcopenia and sarcopenic obesity among men aged 80 years and older in Beijing: prevalence and its association with functional performance. *Geriatr and Gerontol Int* (2014) **14**(Suppl. 1):29–35. doi:10.1111/ggi.12211

5. Yang Q, Vijayakumar A, Kahn BB. Metabolites as regulators of insulin sensitivity and metabolism. *Nat Rev Mol Cel Biol* (2018) **19**:654–72. doi:10.1038/s41580-018-0044-8

6. Zeng Y, Hu X, Xie L, Han Z, Zuo Y, Yang M. The prevalence of sarcopenia in Chinese elderly nursing home residents: a comparison of 4 diagnostic criteria. *J Am Med Directors Assoc* (2018) **19**:690–5. doi:10.1016/j.jamda.2018.04.015

7. Cruz-Jentoft AJ, Sayer AA. Sarcopenia. *The Lancet* (2019) **393**:2636–46. doi:10.1016/s0140-6736(19)31138-9

8. Chen LK, Woo J, Assantachai P, Auyeung TW, Chou MY, Iijima K, et al. Asian working group for sarcopenia: 2019 consensus update on sarcopenia diagnosis and treatment. *J Am Med Directors Assoc* (2020) **21**:300–7.e2. doi:10.1016/j.jamda.2019.12.012

9. Yaru L, Jing W, Liyun Z, Zhihong W, Dongmei Y, Yuna H, et al. The drinking status and associated factors in adults in China *Chinese Journal of Epidemiology* (2018);**39**:898–903.

10. Gabat JAL, Faltado AL, Jr, Sedurante MB, Tee ML. Association of obesity and sarcopenia among adult Filipinos. *Osteoporos sarcopenia* (2018) **4**:109–13. doi:10.1016/j.afos.2018.08.001

11. Pang BWJ, Wee SL, Lau LK, Jabbar KA, Seah WT, Ng DHM, et al. Prevalence and associated factors of sarcopenia in Singaporean adults-the yishun study. *J Am Med Directors Assoc* (2021) **22**:885.e1–885.e10. doi:10.1016/j.jamda.2020.05.029

12. Zhai J, Ma B, Qin J, Lyu Q, Khatun P, Liang R, et al. Alcohol consumption patterns and the risk of sarcopenia: a population-based cross-sectional study among Chinese women and men from Henan province. *BMC public health* (2022) **22**:1894. doi:10.1186/s12889-022-14275-6

13. Hai S, Wang H, Cao L, Liu P, Zhou J, Yang Y, et al. Association between sarcopenia with lifestyle and family function among community-dwelling Chinese aged 60 years and older. *BMC Geriatr* (2017) **17**:187. doi:10.1186/s12877-017-0587-0

14. Steffl M, Bohannon RW, Petr M, Kohlikova E, Holmerova I. Alcohol consumption as a risk factor for sarcopenia - a meta-analysis. *BMC Geriatr* (2016) **16**:99. doi:10.1186/s12877-016-0270-x

15. Bu YL, Wang C, Zhao C, Lu X, Gao W. The association of alcohol consumption with the risk of sarcopenia: a dose-response meta-analysis. *The Am J Drug Alcohol Abuse* (2024) **50**:305–20. doi:10.1080/00952990.2023.2300049

16. Hong SH, Bae YJ. Association between alcohol consumption and the risk of sarcopenia: a systematic review and meta-analysis. *Nutrients* (2022) **14**:3266. doi:10.3390/nu14163266

17. Anonymous. Code of ethics on human experimentation adapted from the Helsinki declaration of the world medical association. *The Am J orthopsychiatry* (1968) **38**:589–90. doi:10.1111/j.1939-0025.1968.tb02426.x

18. Lau EM, Lynn HS, Woo JW, Kwok TC, Melton LJ, 3rd. Prevalence of and risk factors for sarcopenia in elderly Chinese men and women. *The Journals Gerontol Ser A: Biol Sci Med Sci* (2005) **60**:213–6. doi:10.1093/gerona/60.2.213

19. Greenland S, Longnecker MP. Methods for trend estimation from summarized dose-response data, with applications to meta-analysis. *Am J Epidemiol* (1992) **135**:1301–9. doi:10.1093/oxfordjournals.aje.a116237

20. Orsini N, Bellocco R, Greenland S. Generalized least squares for trend estimation of summarized dose-response data. *The Stata J Promoting Commun Stat Stata* (2006) **6**:40–57. doi:10.1177/1536867x0600600103

21. Gao Q, Hu K, Yan C, Zhao B, Mei F, Chen F, et al. Associated factors of sarcopenia in community-dwelling older adults: a systematic review and meta-analysis. *Nutrients* (2021) **13**:4291. doi:10.3390/nu13124291

22. Aberg F, Byrne CD, Pirola CJ, Mannisto V, Sookoian S. Alcohol consumption and metabolic syndrome: clinical and epidemiological impact on liver disease. *J Hepatol* (2023) **78**:191–206. doi:10.1016/j.jhep.2022.08.030

23. Monteiro MG. Alcohol consumption: overview of international trends. *Reference Module Biomed Sci* (2019). doi:10.1016/B978-0-12-801238-3.03186-X

24. Organization W. Global status report on noncommunicable diseases 2014 (2014);

25. Steiner JL, Lang CH. Alcohol impairs skeletal muscle protein synthesis and mTOR signaling in a time-dependent manner following electrically stimulated muscle contraction. *J Appl Physiol* (2014) **117**:1170–9. doi:10.1152/japplphysiol.00180.2014

26. Thapaliya S, Runkana A, McMullen MR, Nagy LE, McDonald C, Prasad SVN, et al. Alcohol-induced autophagy contributes to loss in skeletal muscle mass. *Autophagy* (2014) **10**:677–90. doi:10.4161/auto.27918

27. Lang CH, Frost RA, Svanberg E, Vary TC. IGF-I/IGFBP-3 ameliorates alterations in protein synthesis, eIF4E availability, and myostatin in alcohol-fed rats. *Am J Physiol Endocrinol Metab* (2004) **286**:E916–26. doi:10.1152/ajpendo.00554.2003

28. Lang CH, Pruznak AM, Nystrom GJ, Vary TC. Alcohol-induced decrease in muscle protein synthesis associated with increased binding of mTOR and raptor: comparable effects in young and mature rats. *Nutr and Metab* (2009) **6**:4. doi:10.1186/1743-7075-6-4

29. Prokopidis K, Witard OC. Understanding the role of smoking and chronic excess alcohol consumption on reduced caloric intake and the development of sarcopenia. *Nutr Res Rev* (2022) **35**:197–206. doi:10.1017/s0954422421000135

30. Fanelli Kuczmarski M, Mason MA, Beydoun MA, Allegro D, Zonderman AB, Evans MK. Dietary patterns and sarcopenia in an urban African American and White population in the United States. *J Nutr Gerontol Geriatr* (2013) **32**:291–316. doi:10.1080/21551197.2013.840255

31. Ko YC, Chie WC, Wu TY, Ho CY, Yu WR. A cross-sectional study about the relationship between physical activity and sarcopenia in Taiwanese older adults. *Scientific Rep* (2021) **11**:11488. doi:10.1038/s41598-021-90869-1

32. Daskalopoulou C, Wu YT, Pan W, Gine Vazquez I, Prince M, Prina M, et al. Factors related with sarcopenia and sarcopenic obesity among low- and middle-income settings: the 10/66 DRG study. *Scientific Rep* (2020) **10**:20453. doi:10.1038/s41598-020-76575-4

33. Castillo EM, Goodman-Gruen D, Kritz-Silverstein D, Morton DJ, Wingard DL, Barrett-Connor E. Sarcopenia in elderly men and women: the Rancho Bernardo study. *Am J Prev Med* (2003) **25**:226–31. doi:10.1016/s0749-3797(03)00197-1

34. Akune T, Muraki S, Oka H, Tanaka S, Kawaguchi H, Nakamura K, et al. Exercise habits during middle age are associated with lower prevalence of sarcopenia: the ROAD study. *Osteoporos Int* (2014) **25**:1081–8. doi:10.1007/s00198-013-2550-z

35. Hendriks HFJ. Alcohol and human health: what is the evidence? *Annu Rev Food Sci Technol* (2020) **11**:1–21. doi:10.1146/annurev-food-032519-051827

36. Wang SS, Lay S, Yu HN, Shen SR. Dietary guidelines for Chinese residents (2016): comments and comparisons. *J Zhejiang Univ Sci B* (2016) **17**:649–56. doi:10.1631/jzus.b1600341

37. Ferreira MP, Weems MK. Alcohol consumption by aging adults in the United States: health benefits and detriments. *J Am Diet Assoc* (2008) **108**:1668–76. doi:10.1016/j.jada.2008.07.011

38. Valencia-Martin JL, Galan I, Rodriguez-Artalejo F. The association between alcohol consumption patterns and adherence to food consumption guidelines. *Alcohol Clin Exp Res* (2011) **35**:2075–81. doi:10.1111/j.1530-0277.2011.01559.x

39. Trevisan M, Schisterman E, Mennotti A, Farchi G, Conti S. Drinking pattern and mortality:. *Ann Epidemiol* (2001) **11**:312–9. doi:10.1016/s1047-2797(00)00183-6

40. Traversy G, Chaput JP. Alcohol consumption and obesity: an update. *Curr Obes Rep* (2015) **4**:122–30. doi:10.1007/s13679-014-0129-4

41. French MT, Norton EC, Fang H, Maclean JC. Alcohol consumption and body weight. *Health Econ* (2010) **19**:814–32. doi:10.1002/hec.1521

42. Gaziano JM, Buring JE, Breslow JL, Goldhaber SZ, Rosner B, VanDenburgh M, et al. Moderate alcohol intake, increased levels of high-density lipoprotein and its subfractions, and decreased risk of myocardial infarction. *New Engl J Med* (1993) **329**:1829–34. doi:10.1056/nejm199312163292501

43. Damayanthi H, Moy FM, Abdullah KL, Dharmaratne SD. Health related quality of life and its associated factors among community-dwelling older people in Sri Lanka: a cross-sectional study. *Arch Gerontol Geriatr* (2018) **76**:215–20. doi:10.1016/j.archger.2018.03.009

44. Zhao X, Zhou R, Li H, Fan Y, Sun Y, Hu X, et al. The effects of moderate alcohol consumption on circulating metabolites and gut microbiota in patients with coronary artery disease. *Front Cardiovasc Med* (2021) **8**:767692. doi:10.3389/fcvm.2021.767692

45. Chavez JA, Summers SA. A ceramide-centric view of insulin resistance. *Cell Metab* (2012) **15**:585–94. doi:10.1016/j.cmet.2012.04.002

46. Hoogkamer W. Perception of gait asymmetry during split-belt walking. *Exerc Sport Sci Rev* (2017) **45**:34–40. doi:10.1249/jes.0000000000000094

EBM Experimental Biology and Medicine

TYPE Original Research
PUBLISHED 03 June 2025
DOI 10.3389/ebm.2025.10575

OPEN ACCESS

*CORRESPONDENCE
Abigail L. Pfaff,
abigail.pfaff@murdoch.edu.au

RECEIVED 12 March 2025
ACCEPTED 06 May 2025
PUBLISHED 03 June 2025

CITATION
Pfaff AL and Kõks S (2025) Retrotransposition-competent L1s are increased in the genomes of individuals with amyotrophic lateral sclerosis. *Exp. Biol. Med.* 250:10575. doi: 10.3389/ebm.2025.10575

Retrotransposition-competent L1s are increased in the genomes of individuals with amyotrophic lateral sclerosis

Abigail L. Pfaff[1,2]* and Sulev Kõks[1,2]

[1]Perron Institute for Neurological and Translational Science, Perth, WA, Australia, [2]Personalised Medicine Centre, Health Futures Institute, Murdoch University, Murdoch, WA, Australia

Abstract

An individual's genetics contributes to their risk of developing amyotrophic lateral sclerosis (ALS); however, there is still a large proportion of the heritability of ALS to be understood. Part of this missing heritability may lie in complex variants, such as the long interspersed element 1 (L1) retrotransposon, which have yet to be evaluated. The majority of L1 insertions in the human genome are no longer able to retrotranspose, but to date 279 retrotransposition-competent (RC) L1s have been reported. Many RC-L1s are polymorphic for their presence/absence; therefore, each individual will have a different number and complement of RC-L1s. These elements have been hypothesized to be involved in disease processes by multiple mechanisms such as somatic mutation by retrotransposition, the triggering of neuroinflammation and DNA damage. We hypothesize that L1s may influence disease development either through their effects on endogenous genes or through the properties that enable them to retrotranspose. Whole genome sequencing data from the New York Genome Center ALS consortium were used to characterize L1 variation identifying 2,803 polymorphic L1 elements and association analysis was performed in European individuals (ALS/ALS with other neurological disorder (ALSND) n = 2,653, controls n = 320). There were no individual L1 elements associated with disease, but we did identify a significant increase in the number of RC-L1s in ALS/ALSND genomes (p = 0.01) and the presence of ≥46 RC-L1s showed the most significant association (OR = 1.09 (1.02–1.16), p = 0.01) with disease. Analysis of individual L1s and their association with age at onset and survival identified one L1 whose presence was significantly associated with a lower age at onset (52.7 years) compared to homozygous absent individuals (59.2 years) (padj = 0.009). Our study has identified novel genetic factors for both disease risk and age at onset in ALS providing further evidence for the role of L1 retrotransposons in neurodegenerative diseases.

KEYWORDS

retrotransposons, L1, amyotrophic lateral sclerosis, neurodegeneration, genetics

Impact statement

This is the first study to assess genome-wide L1 variation in a large number of ALS and control genomes and to identify novel genetic factors involved in ALS risk and age at onset. ALS is a genetically heterogeneous disease with a large proportion of its heritability yet to be identified. Our study addressed this missing heritability by evaluating the presence/absence of the L1 retrotransposon and focusing on the subset of these elements that are still able to mobilize in the human genome. By understanding the mechanisms and risk factors that lead to ALS, new therapeutic targets can be identified for a disease with very limited treatment options.

Introduction

The long interspersed element-1 (L1) is the only autonomous family of retrotransposons in the human genome that contains elements currently able to mobilize and has played an important role in shaping the structure and function of the human genome [1]. L1s propagate through a "copy and paste" mechanism,

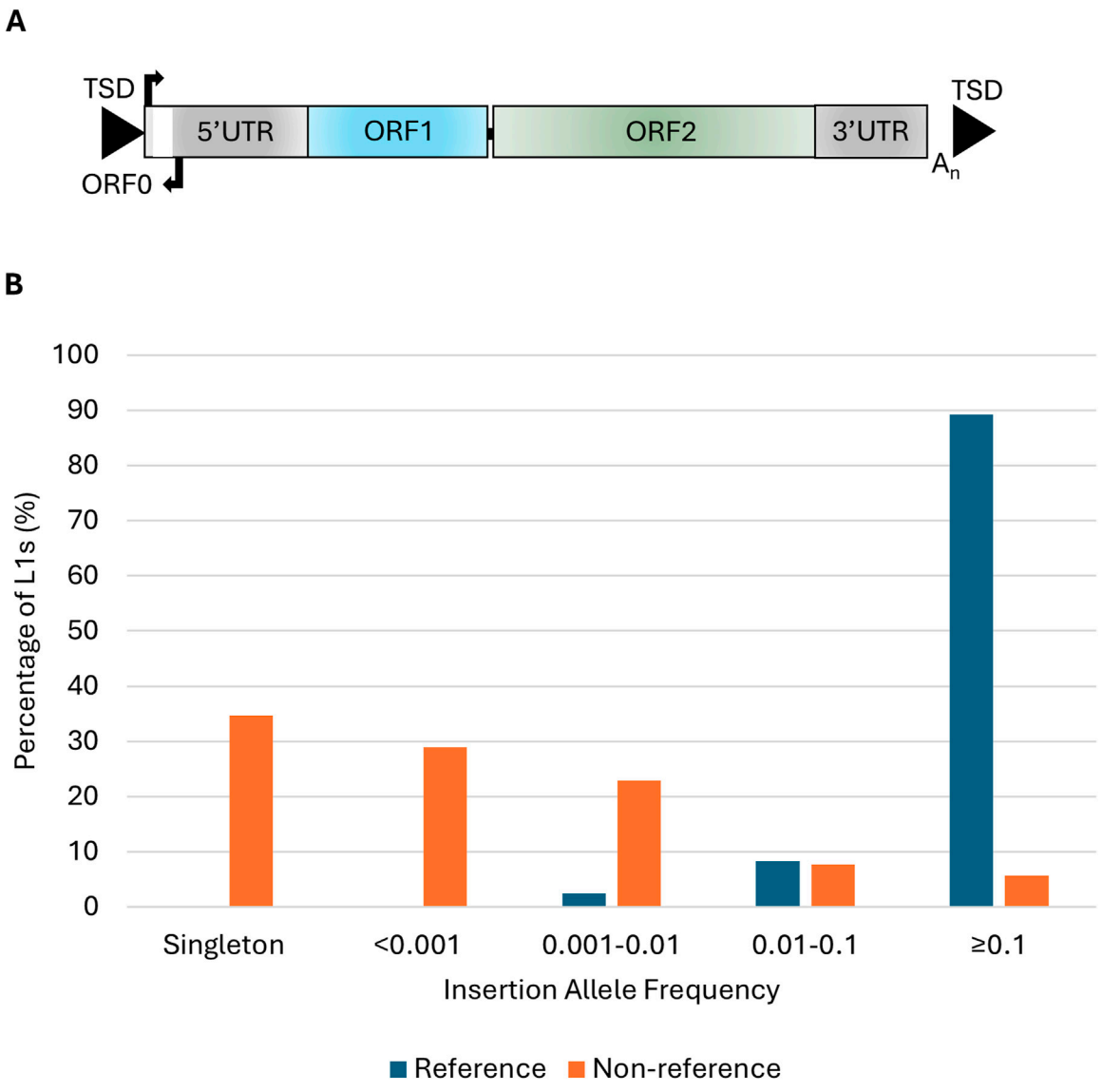

FIGURE 1
L1 structure and insertion allele frequencies of polymorphic L1s in the ALS consortium. **(A)** Schematic of a full-length L1 ~6 kb in length that consists of a 5′untranslated region (5′UTR) containing the endogenous L1 promoter and an antisense promoter, three open reading frames (ORF0, ORF1, and ORF2), and a 3′untranslated region (3′UTR) flanked by target site duplications (TSDs). **(B)** The insertion allele frequency of 205 reference and 2,598 non-reference L1s in the NYGC ALS consortium (n = 4,393).

termed target primed reverse transcription [2, 3], and mobilize the non-autonomous *Alu* and SINE-VNTR-Alu retrotransposons. The ongoing mobilization of L1s has led to genetic variation between individuals and can affect the function and expression of endogenous genes. There are at least 29 instances of disease caused by an L1 insertion, generally through loss-of-function mutations or aberrant splicing [4]. A full-length L1 element is ~6 kb in size, contains both a 5′ and 3′-untranslated region (UTR), three open reading frames (ORF0, ORF1, ORF2), a poly A tail at its 3′end, and is flanked by variable target site duplications (Figure 1A). The proteins encoded by ORF1, a ~40 kDa protein with RNA binding and chaperone activities, and ORF2, a ~150 kDa protein with endonuclease and reverse transcriptase activities, are required for retrotransposition [5–8]. Despite L1s contributing to 17% of the human genome and more than one million L1s annotated in hg38 only 146 L1s are full-length with intact ORFs [9]. The majority are unable to mobilize due to internal deletions or rearrangements, 5′ truncations and mutations in the ORFs encoding the proteins required for retrotransposition [10, 11].

The dysregulation and elevated expression of L1s, along with other families of retrotransposons, have been detected in several neurological conditions including the neurodegenerative disease amyotrophic lateral sclerosis (ALS) [12, 13]. ALS, the most common form of motor neuron disease (MND), is a progressive disease that is characterized by the loss of motor neurons in the brain and spinal cord and the life expectancy after diagnosis is 2–5 years [14]. It is a clinically and genetically heterogeneous condition, and the neurodegenerative mechanisms involved are not fully understood. Several processes have been shown to be altered or dysregulated in the disease, such as protein aggregation, axonal transport, oxidative stress, mitochondrial dysfunction, RNA processing and the expression of retrotransposable elements [12, 15]. Changes in the expression of multiple classes and families of retrotransposons have been identified in subsets of individuals with ALS [16, 17]. An increase in expression of several families of retrotransposons was identified in the frontal cortex of individuals with ALS who carried the C9ORF72 expansion when compared to those without the expansion and healthy controls [16]. Another study using machine learning identified three subtypes of ALS based on transcriptomic data from the frontal and motor cortices, one of which was characterized by the activation of retrotransposons and TAR DNA-binding protein 43 (TDP-43) dysfunction [17]. Cytoplasmic accumulation of TDP-43, encoded by the gene TARDBP, in which mutations can cause ALS, is a hallmark of the majority of ALS cases. There is evidence in human tissues and cell lines that TDP-43 binds to retrotransposon transcripts of different classes, which is thought to aid in the repression of these elements [18]. Heterochromatin formation over repetitive elements, including L1s, acts to suppress their expression, but loss of nuclear TDP-43 from neurons results in chromatin decondensation over L1 elements [19].

We hypothesize that polymorphic L1s may play a role in ALS development either through their effects on endogenous genes, such as loss-of-function mutations, or through properties that are inherent in their ability to mobilize. These include somatic mutation through retrotransposition, the triggering of neuroinflammation via the interferon pathway and DNA damage through the endonuclease activity of the ORF2 protein [13, 20]. The ability of specific L1s to retrotranspose can be detected using cellular retrotransposition assays and by tracing the source elements of both germline and somatic insertions using 3′transductions [21–23]. Retrotransposition-competent L1s (RC-L1s) annotated in the human reference genome and non-reference RC-L1s can be polymorphic for their presence or absence. Therefore, each individual will have a different number and complement of RC-L1s in their genome, which could potentially lead to differing levels of functional L1 mRNA.

To investigate the role of L1s in ALS we utilized whole genome sequencing from the New York Genome Center (NYGC) ALS consortium to characterize the landscape of polymorphic L1s in ALS and control genomes to evaluate their effects on ALS risk, age at onset, and survival. These analyses were performed for both individual L1 insertions and the total number of RC-L1s present. We identified an increased burden of RC-L1s, those still able to mobilize, in the genomes of individuals with ALS and a single L1 associated with a reduction in the age at onset of the disease.

Materials and methods

Genotyping of L1s using whole genome sequencing from the ALS consortium

Whole genome sequencing data in cram file format aligned to hg38 were obtained from the NYGC ALS consortium. The ALS consortium includes individuals with a range of diagnoses such as ALS spectrum MND (ALS), other MND, other neurological disorders (including Parkinson's disease and dementias) and ALS with other neurological disorders (ALSND) along with non-neurological controls (NNCs). The structural variant caller Delly[1], with default settings, was used to identify structural variants in a subset of individuals (n = 244) [24]. The structural variants from each individual were merged and those deletions that overlapped with reference L1s were extracted. This generated a list of reference L1s that were absent in at least one of the 244 individuals. This panel of

1 https://github.com/dellytools/delly

TABLE 1 Demographics of the NYGC ALS consortium cohort in which association analysis was performed.

Demographic		NNC (n = 320)	ALS/ALSND (n = 2,653)
Gender	Male	157 (49.1%)	1,594 (60.1%)
	Female	163 (50.9%)	1,059 (39.9%)
Age[a] Mean (min-max)		57.4 (17–90)	59.1 (12–90)

[a]For NNC age at collection (43 unknown) and ALS/ALSND age at symptom onset (159 unknown).

reference L1s was used in the second call step of Delly to generate genotypes for the entire ALS consortium cohort available (n = 4,393). Non-reference L1s were genotyped using Mobile Element Locator Tools (MELT version 2.2.2 in MELT-split mode) [22]. The L1 insertions detected were filtered to keep those supported by ≥2 split reads and an assessment score ≥3 and that had passed the filtering criteria performed by MELT. There were 210 reference and 2,649 non-reference polymorphic L1s identified in the ALS consortium cohort and after filtering for Hardy-Weinberg equilibrium ($p < 1 \times 10^{-6}$ in NNCs) 205 reference and 2,598 non-reference L1s remained.

Identification of retrotransposition competent L1s

RC-L1s were identified using published data on those L1s that displayed activity in a cellular retrotransposition assay or were identified as source elements for germline or somatic insertions using 3′ transduction events and details can be found in Pfaff et al [25]. The list of 198 RC-L1s from Pfaff et al has been extended using data from a more recent publication [26] and consists of 279 RC-L1s, 102 reference and 177 non-reference L1s.

Association, age at onset and survival analysis

Association analysis was performed on those individuals who were >90% European according to the ALS consortium metadata and those diagnosed with ALS-spectrum MND or ALS-spectrum MND with another neurological condition (n = 2,653) and compared to non-neurological controls (n = 320) (see Table 1 for demographics). Association analysis of 501 polymorphic L1s (minor allele frequency >0.01) with ALS was performed using logistic regression adjusted for age, sex and sequencing preparation in PLINK (v1.07) and p values were adjusted for multiple testing (Bonferroni correction). Of the polymorphic L1s genotyped in the NYGC ALS consortium 106 were retrotransposition competent and 93 of these were polymorphic in the European subset. The 3 RC-L1s located on the X chromosome were removed from further analysis so that men and women could be compared and 1 RC-L1s was filtered out because >5% of genotypes were missing. Only individuals with genotypes for all 89 RC-L1s were retained for analysis. Linear regression adjusted for sex, age and sequencing preparation was used to analyze the association between the total number of RC-L1s present and disease status. In addition, NNCs and individuals with ALS/ALSND were categorized based on the number of alleles with an RC-L1 present to analyze the association between the likelihood of having ALS/ALSND and a certain number of RC-L1s. Logistic regression adjusted for sex, age and sequencing preparation was performed on these RC-L1 groupings to determine if having more than a certain number of these defined elements was associated with ALS/ALSND. P values were adjusted for multiple testing using Bonferroni correction.

Age at onset analysis was performed using linear regression of age at onset on L1 genotype or RC-L1 number with sex, sequencing platform and site of onset as covariates and p values were adjusted for multiple testing (Bonferroni correction). Survival analysis was completed using the Cox proportional hazards model from the 'coxme' package in R with sex, sequencing platform, age at onset and site of onset as covariates and p values were adjusted for multiple testing (Bonferroni correction). Individuals in the ALS consortium dataset who were still alive were censored at their last follow-up.

L1s in ALS-associated loci

To identify polymorphic L1s from the ALS consortium located in ALS-associated loci the L1 coordinates were intersected with the coordinates of ALS-associated genes. The list of ALS associated genes was generated from the amyotrophic lateral sclerosis online database (ALSoD)[2] using those defined as definitive ALS genes or with strong evidence for their association.

2 https://alsod.ac.uk/

TABLE 2 Top 5 L1s significantly associated with ALS before correction.

L1 ID	Minor allele	MAF		OR (95% CI)	Unadj p value	Bonferroni p value
		NNCs	ALS/ALSND			
NRL1_20_43323466	P	0.431	0.371	0.76 (0.63–0.91)	0.003	1
NRL1_13_90973977	P	0.155	0.124	0.72 (0.57–0.92)	0.007	1
NRL1_20_29125080	P	0.025	0.014	0.46 (0.25–0.83)	0.011	1
NRL1_7_17055090	P	0.339	0.290	0.77 (0.64–0.94)	0.011	1
NRL1_10_89957889	P	0.081	0.105	1.54 (1.09–2.16)	0.013	1

Expression quantitative trait loci analysis in medial and lateral motor cortex

Matrix eQTL was used to calculate the L1 loci regulating the expression of transcript variants [27]. We used an additive linear model with covariates, age and sex, and FDR was used to correct multiple testing with only the results that remained significant after FDR correction (<0.05) reported here. Matrix eQTL also reports effect-size estimates as beta values or slope coefficients.

Results

The landscape of polymorphic L1s in the NYGC ALS consortium

In 4,393 whole genomes analyzed from the NYGC ALS consortium 205 reference and 2,598 non-reference L1s were identified as polymorphic for their presence/absence. The insertion allele frequencies (IAF) of the reference L1s were higher than those of the non-reference elements with 89.3% of the reference L1s having an IAF of ≥0.1 compared to 5.7% of the non-reference L1s (Figure 1B). The majority of L1 insertions were found in intergenic regions (59.5%) followed by 39.9% of the L1s found in introns. There were 3 (0.1%) L1 insertions located in exons, 2 (0.07%) in the 5′UTR and 12 (0.4%) in the 3′UTR of genes. The three exonic insertions were located in coding exons of the following genes *AASDH*, *HLA-DRB1* and *FSTL4*. The non-reference L1s located in the *AASDH* and *HLA-DRB1* genes were each found in a single individual diagnosed with ALS. The third exonic L1 is a common insertion (IAF = 0.77) found in the reference genome and the *FSTL4* transcript initiates from the antisense promoter of this L1 element. There were two L1 insertions located in the introns of ALS-associated genes *ERBB4* and *SCFD1* with IAF of 0.13 and 0.15 respectively in the ALS consortium, neither of which was associated with disease.

Association analysis was conducted on 501 L1 insertions (MAF >0.01) in the individuals of European descent in the ALS consortium as this formed the largest proportion of the cohort (Table 1 for demographics of this subset). There were 25 L1s associated with ALS/ALSND, but these did not survive correction for multiple testing (Supplementary Table S1). The top 5 L1s significantly associated with ALS/ALSND before correction are shown in Table 2. Age at onset analysis was performed identifying 31 associated L1s before correction with one L1 (NRL1_9_4265417) surviving correction for multiple testing (Supplementary Table S2). The presence of NRL1_9_4265417 was associated with a lower age at onset (est = -6.55, SE = 1.51, padj = 0.009). The average age at onset for individuals with the PA genotype was 52.7 years compared to 59.2 years for those with the AA genotype (Figure 2). NRL1_9_4265417 is a rare insertion with an IAF of 0.017 and located in intron 2 of the *GLIS3* gene. Survival analysis was performed identifying 26 associated L1s before correction for multiple testing (Supplementary Table S3), the top 5 of which are shown in Figure 3.

The number of RC-L1s is significantly increased in ALS/ALSND genomes

In the NYGC ALS consortium 106 RC-L1s, 34 reference and 72 non-reference, were identified as polymorphic for the presence or absence from the compiled list of 279 RC-L1s. In the European subset of the cohort 93 RC-L1s were polymorphic. Not all the RC-L1s were detected as variable in our cohort as some were fixed in the population or were very rare and may only be present in specific population groups. The number of present alleles of 89 of the polymorphic RC-L1s in the European individuals, those on the sex chromosomes and with missing genotypes >5% were removed, was significantly higher in the genomes of individuals with ALS/ALSND compared to NNCs (β = 0.40, p = 0.01). The number of alleles present in NNCs genomes ranged from 32 to 56 and in ALS/ALSND genomes from 30 to 63 and their distribution is shown in Figure 4A. The ALS/ALSND and NNC individuals were grouped into 6 different categories to determine whether having more than a certain number of RC-L1s present at the 89 loci was associated with disease. The presence of ≥45, ≥46 and ≥47 polymorphic RC-L1s

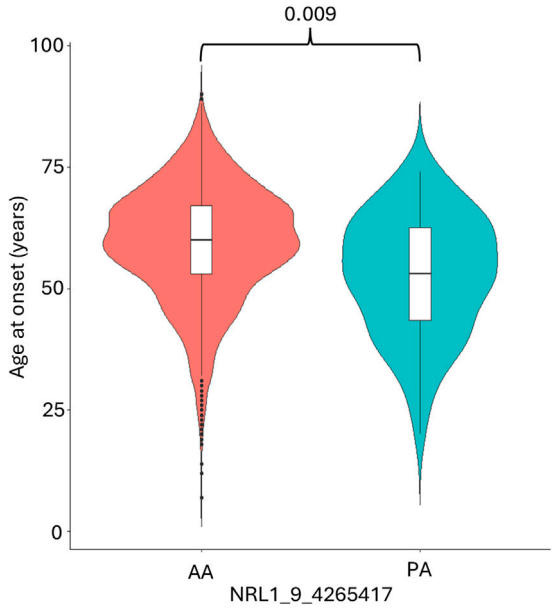

FIGURE 2
The presence of NRL1_9_4265417 is associated with a lower age at onset. The average age at onset of individuals diagnosed with ALS/ALSND was significantly lower in individuals with the PA genotype (52.7 years) compared to the AA genotype (59.2 years). PA n = 66 and AA n = 2,429.

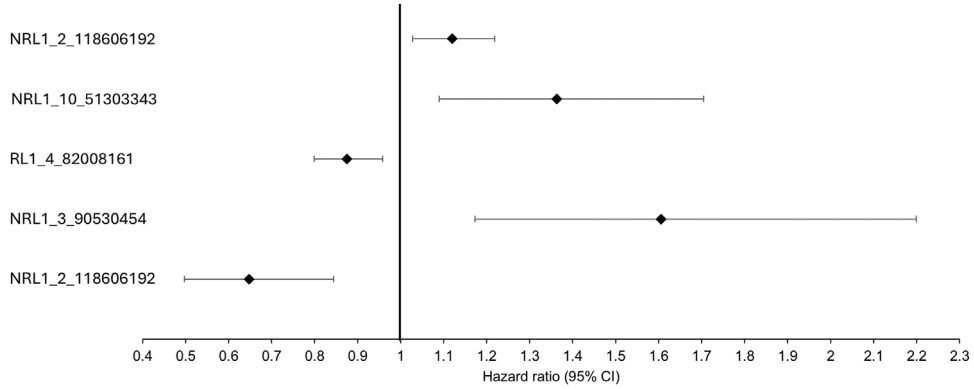

FIGURE 3
The top 5 most significant L1s associated with survival before correction. The black diamonds represent the hazard ratio and the black lines the 95% confidence intervals.

was significantly associated with ALS/ALSND (Figure 4B) and the percentage of individuals with a certain number of RC-L1s is shown in Figure 4C. The presence of ≥46 RC-L1s showed the most significant association (OR = 1.09 (1.02–1.16), p = 0.01) with 38.5% of NNCs having ≥46 compared to 46.5% of individuals with ALS/ALSND. The number of RC-L1s present in the genomes was not associated with age at onset or survival.

To determine whether the RC-L1s might influence ALS pathogenesis through effects on gene expression, an analysis was performed using genotypes of the 2,803 polymorphic L1s in this study and transcriptomic data from the medial and lateral motor cortex. This eQTL analysis identified 252 L1s that were significantly associated with expression changes of 395 different transcripts, but only 11 of these L1s were retrotransposition competent (Supplementary Table S4). The proportion of RC-L1s acting as eQTLs (4.4%) was not significantly different from the genome-wide proportion (3.8%) (Fisher's exact test p = 0.60) suggesting that they are not enriched as eQTLs over those L1s

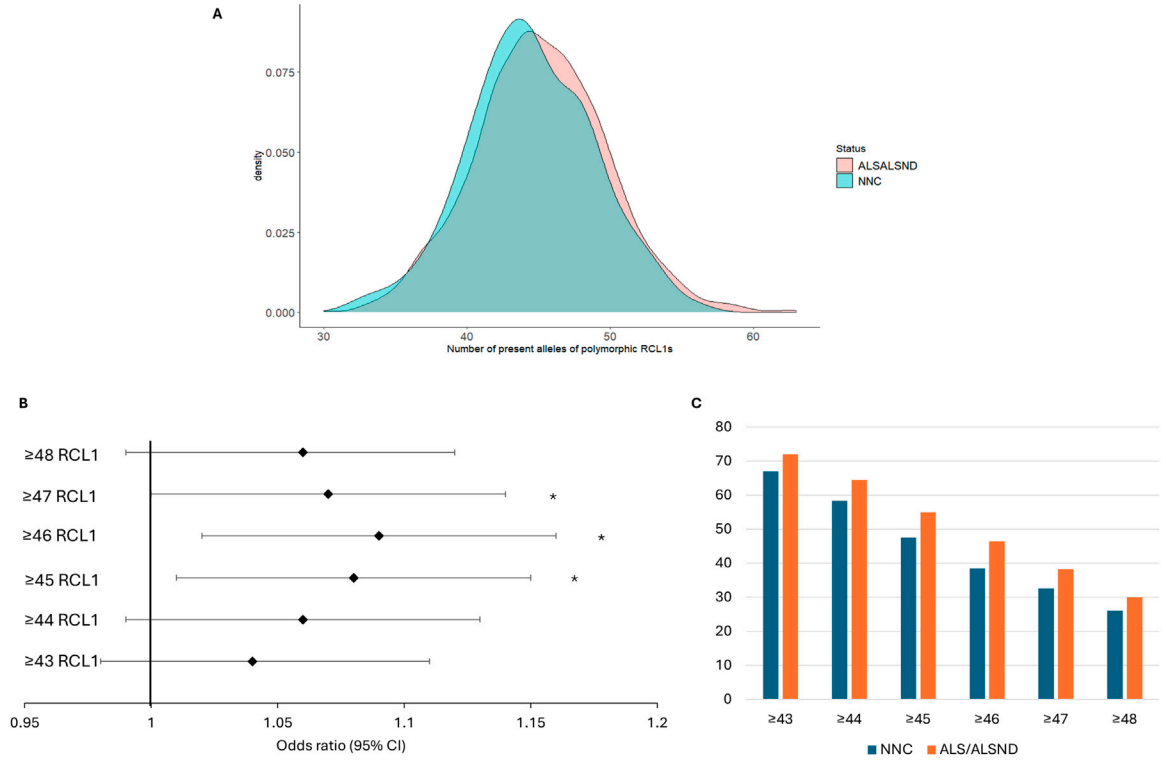

FIGURE 4
The total number of RC-L1s is increased in ALS/ALSND genomes. **(A)** The distribution of the total number of present alleles of 89 polymorphic RC-L1s in individuals diagnosed with ALS or ALSND compared to non-neurological controls (NNCs). **(B)** The forest plot represents the odds ratio of having ALS/ALSND based on an increasing number of polymorphic RC-L1s being present in an individual's genome. The likelihood of having ALS/ALSND was significantly associated with having ≥45, ≥46 and ≥47 present alleles of the polymorphic RC-L1. The black diamonds represent the odds ratio, and black lines the 95% confidence intervals. **(C)** The percentage of individuals with a given number of RC-L1 alleles present. NNCs n = 288, ALS/ALSND n = 2,420. *$p < 0.05$.

that are not able to retrotranspose. There were 25 transcripts whose expression was associated with the 11 RC-L1s and the majority (72%) were either pseudogenes or novel transcripts with limited functional information available. Genes whose expression was associated with the presence/absence of RC-L1s included zinc finger protein 367 (ZNF367), olfactory receptor family 5 subfamily K member 1 (OR5K1) and maturin (MTURN).

Discussion

Here we present data from a genome-wide analysis of polymorphic L1s using 4,393 whole genomes from the NYGC ALS consortium to identify novel genetic factors involved in ALS development and age at onset. ALS is a genetically heterogeneous disease with different patterns of inheritance and levels of gene penetrance with more than 30 genes associated with its development. The majority of large-scale studies have focused on single-nucleotide variants and suggest a heritability of 10–20%, which leaves 30–40% to be explained [28]. This missing heritability is likely to be found for other types of genetic variants and structural variants have already been associated with ALS [29]. Our study focused on polymorphic reference and non-reference L1s, evaluating their association with ALS as individual elements and in combination for those that can still mobilize within the human genome.

In the NYGC ALS consortium data 2,803 polymorphic L1s (205 reference and 2,598 non-reference) were identified. Association analysis performed on 501 L1s (MAF >0.01) did not identify individual L1s associated with disease after correction for multiple testing; however, when evaluating RC-L1s we identified an increased number of these elements in the genomes of individuals with ALS compared to controls. When analyzing the number of alleles present in 89 RC-L1s the total number of RC-L1s was higher in ALS/ALSND genomes (Figure 4A) and having ≥46 RC-L1s was most significantly associated with disease (Figures 4B,C). RC-L1s encode functional proteins that enable them to mobilize in the human genome and have the potential to generate somatic insertions, cause DNA damage and generate cytosolic RNA: DNA hybrids that activate the innate immune response and

affect normal cellular function [13, 20]. These features of RC-L1s that are inherent in their ability to retrotranspose are important factors in how they may contribute to neurodegeneration and neuroinflammation. An increased number of these elements present in a genome could lead to higher levels of functional mRNA in a cell when these elements are expressed and potentially greater effects. Elevated expression of retrotransposons, including L1s, in ALS has been reported by multiple studies and was often restricted to a subset of individuals [12, 16, 17]. Analysis of locus specific expression of reference L1 elements encoding intact proteins showed an overall decrease in expression in the brains of individuals with ALS, but in a small number of individuals with ALS this expression was massively increased, up to 25 times the average [30]. This study was limited to reference L1s and included all L1s encoding intact proteins (not specifically those with evidence of their ability to retrotranspose); therefore, evaluation of both reference and non-reference RC-L1s would provide important data regarding their expression profile in ALS.

Methylation of a CpG island located in the L1 5′UTR is involved in regulating L1 expression and a reduction in methylation could indicate which elements are most likely to be expressed. For example, the expression of a specific L1 located on chromosome 13 occurred alongside its hypomethylation during hESC neurodifferentiation and in adult tissues such as the hippocampus [31]. Changes in methylation of L1s may also be associated with disease states, for example L1s were differentially methylated in the prefrontal cortices of individuals with psychiatric disorders [32]. When analyzing a small number of highly active RC-L1s we identified a reduction in the methylation of selected RC-L1s in the motor cortex of individuals with ALS compared to healthy controls [33]. A global evaluation of RC-L1 methylation and expression in ALS could help identify those elements that are altered in the disease to refine the list of RC-L1s used in our analysis. For example, when analyzing the burden of RC-L1s in Parkinson's disease (PD) we identified an increased number of highly active RC-L1s in PD genomes rather than an increase in the presence of all RC-L1s [25].

Another potential mechanism by which RC-L1s may contribute to ALS pathogenesis is through their effects on endogenous gene expression. Transcriptomic analysis identified 252 L1s acting as eQTLs in either the medial or lateral motor cortex, of which 11 were RC-L1s affecting 25 different transcripts. The global association of RC-L1s as opposed to individual elements being linked to disease and the small number affecting gene expression suggest that it is their retrotransposition properties that are more likely to be involved in disease processes.

L1s, along with other retrotransposons, are therapeutic targets in a number of neurological conditions [34]. Reverse transcriptase inhibitors that target the L1 protein have been tested in a clinical trial for the neurodevelopmental disorder Aicardi-Goutieres syndrome [35, 36] and trials are currently underway in C9orf72 expansion positive individuals with ALS or frontotemporal dementia and in individuals with progressive supranuclear palsy. By analyzing RC-L1 variation and activity the aim would be to identify those individuals with ALS in whom L1s are contributing to disease development and who may benefit the most from these therapies targeting L1 activity.

We performed age at onset and survival analysis for both individual L1s and the burden of RC-L1s, identifying a single L1 (NRL1_9_4265417) whose presence was associated with a reduced age at onset (Figure 2). Age at onset of ALS is influenced by sex, family history and genetics [37]. Carriers of a Mendelian genetic variant have a lower age at onset and two recent age at onset GWAS have identified only two associated variants [28, 38, 39]. NRL1_9_4265417 is not in a known ALS-associated region and is located in intron 2 of the *GLIS3* gene, which is a transcriptional regulator and has been shown to modulate genes involved in autophagy and neuronal function [40]. Variants in *GLIS3* have also been associated with levels of tau and ptau in Alzheimer's disease [41]. Analysis of the functional consequences of this L1 insertion will be required to determine its effects and how it may act as a disease modifier.

This study has identified novel genetic factors for both disease risk and age at onset in ALS providing further evidence for the role of L1 retrotransposons in this neurodegenerative disease and their potential as a therapeutic target.

Author contributions

Conceptualization, AP and SK; methodology, AP and SK; formal analysis, AP; data interpretation, AP and SK; writing – original draft preparation, AP; writing – review and editing, SK All authors contributed to the article and approved the submitted version.

Data availability

The WGS sequencing analysed in this study from the ALS consortium were obtained upon application to the New York Genome Center and data requests can be made by completing a genetic data request form at ALSData@nygenome.org. https://www.nygenome.org/science-technology/collaborative-research.

Ethics statement

The studies involving humans were approved by Research ethics and integrity, Murdoch University (2020/040). The studies

were conducted in accordance with the local legislation and institutional requirements. The participants provided their written informed consent to participate in this study.

Funding

The author(s) declare that financial support was received for the research and/or publication of this article. AP and SK are funded by the MSWA and the Perron Institute for Neurological and Translational Science.

Acknowledgments

We would like to acknowledge the Target ALS Human Postmortem Tissue Core, the New York Genome Center for Genomics of Neurodegenerative Disease, the Amyotrophic Lateral Sclerosis Association and the TOW Foundation for the whole genome sequencing data used in this publication. This work was supported by resources provided by the Pawsey Supercomputing Centre with funding from the Australian Government and the Government of Western Australia.

Conflict of interest

The author(s) declared no potential conflicts of interest with respect to the research, authorship, and/or publication of this article.

Generative AI statement

The authors declare that no Generative AI was used in the creation of this manuscript.

Supplementary material

The Supplementary Material for this article can be found online at: https://www.ebm-journal.org/articles/10.3389/ebm.2025.10575/full#supplementary-material

References

1. Kazazian HH, Jr, Moran JV. Mobile DNA in health and disease. *N Engl J Med* (2017) **377**:361–70. doi:10.1056/nejmra1510092

2. Cost GJ, Feng Q, Jacquier A, Boeke JD. Human L1 element target-primed reverse transcription *in vitro*. *EMBO J* (2002) **21**:5899–910. doi:10.1093/emboj/cdf592

3. Luan DD, Korman MH, Jakubczak JL, Eickbush TH. Reverse transcription of R2Bm RNA is primed by a nick at the chromosomal target site: a mechanism for non-LTR retrotransposition. *Cell* (1993) **72**:595–605. doi:10.1016/0092-8674(93)90078-5

4. Hancks DC, Kazazian HH, Jr. Roles for retrotransposon insertions in human disease. *Mobile DNA* (2016) **7**:9. doi:10.1186/s13100-016-0065-9

5. Feng Q, Moran JV, Kazazian HH, Jr, Boeke JD. Human L1 retrotransposon encodes a conserved endonuclease required for retrotransposition. *Cell* (1996) **87**:905–16. doi:10.1016/s0092-8674(00)81997-2

6. Khazina E, Weichenrieder O. Non-LTR retrotransposons encode noncanonical RRM domains in their first open reading frame. *Proc Natl Acad Sci U S A* (2009) **106**:731–6. doi:10.1073/pnas.0809964106

7. Mathias SL, Scott AF, Kazazian HH, Jr, Boeke JD, Gabriel A. Reverse transcriptase encoded by a human transposable element. *Science* (1991) **254**:1808–10. doi:10.1126/science.1722352

8. Moran JV, Holmes SE, Naas TP, DeBerardinis RJ, Boeke JD, Kazazian HH, Jr. High frequency retrotransposition in cultured mammalian cells. *Cell* (1996) **87**:917–27. doi:10.1016/s0092-8674(00)81998-4

9. Penzkofer T, Jager M, Figlerowicz M, Badge R, Mundlos S, Robinson PN, et al. L1Base 2: more retrotransposition-active LINE-1s, more mammalian genomes. *Nucleic Acids Res* (2017) **45**:D68–D73. doi:10.1093/nar/gkw925

10. Lander ES, Linton LM, Birren B, Nusbaum C, Zody MC, Baldwin J, et al. Initial sequencing and analysis of the human genome. *Nature* (2001) **409**:860–921. doi:10.1038/35057062

11. Myers JS, Vincent BJ, Udall H, Watkins WS, Morrish TA, Kilroy GE, et al. A comprehensive analysis of recently integrated human Ta L1 elements. *The Am J Hum Genet* (2002) **71**:312–26. doi:10.1086/341718

12. Savage AL, Schumann GG, Breen G, Bubb VJ, Al-Chalabi A, Quinn JP. Retrotransposons in the development and progression of amyotrophic lateral sclerosis. *J Neurol Neurosurg Psychiatry* (2019) **90**:284–93. doi:10.1136/jnnp-2018-319210

13. Tam OH, Ostrow LW, Gale Hammell M. Diseases of the nERVous system: retrotransposon activity in neurodegenerative disease. *Mobile DNA* (2019) **10**:32. doi:10.1186/s13100-019-0176-1

14. Masrori P, Van Damme P. Amyotrophic lateral sclerosis: a clinical review. *Eur J Neurol* (2020) **27**:1918–29. doi:10.1111/ene.14393

15. van Es MA, Hardiman O, Chio A, Al-Chalabi A, Pasterkamp RJ, Veldink JH, et al. Amyotrophic lateral sclerosis. *The Lancet* (2017) **390**:2084–98. doi:10.1016/s0140-6736(17)31287-4

16. Prudencio M, Gonzales PK, Cook CN, Gendron TF, Daughrity LM, Song Y, et al. Repetitive element transcripts are elevated in the brain of C9orf72 ALS/FTLD patients. *Hum Mol Genet* (2017) **26**:3421–31. doi:10.1093/hmg/ddx233

17. Tam OH, Rozhkov NV, Shaw R, Kim D, Hubbard I, Fennessey S, et al. Postmortem cortex samples identify distinct molecular subtypes of ALS: retrotransposon activation, oxidative stress, and activated glia. *Cell Rep* (2019) **29**:1164–77.e5. doi:10.1016/j.celrep.2019.09.066

18. Li W, Jin Y, Prazak L, Hammell M, Dubnau J. Transposable elements in TDP-43-mediated neurodegenerative disorders. *PLoS One* (2012) **7**:e44099. doi:10.1371/journal.pone.0044099

19. Liu EY, Russ J, Cali CP, Phan JM, Amlie-Wolf A, Lee EB. Loss of nuclear TDP-43 is associated with decondensation of LINE retrotransposons. *Cell Rep* (2019) **27**:1409–21.e6. doi:10.1016/j.celrep.2019.04.003

20. Saleh A, Macia A, Muotri AR. Transposable elements, inflammation, and neurological disease. *Front Neurol* (2019) **10**:894. doi:10.3389/fneur.2019.00894

21. Brouha B, Schustak J, Badge RM, Lutz-Prigge S, Farley AH, Moran JV. Hot L1s account for the bulk of retrotransposition in the human population. *Proc Natl Acad Sci U S A* (2003) **100**:5280–5. doi:10.1073/pnas.0831042100

22. Gardner EJ, Lam VK, Harris DN, Chuang NT, Scott EC, Pittard WS, et al. The Mobile Element Locator Tool (MELT): population-scale mobile element discovery and biology. *Genome Res* (2017) **27**:1916–29. doi:10.1101/gr.218032.116

23. Rodriguez-Martin B, Alvarez EG, Baez-Ortega A, Zamora J, Supek F, Demeulemeester J, et al. Pan-cancer analysis of whole genomes identifies driver rearrangements promoted by LINE-1 retrotransposition. *Nat Genet* (2020) **52**:306–19. doi:10.1038/s41588-019-0562-0

24. Rausch T, Zichner T, Schlattl A, Stutz AM, Benes V, Korbel JO. DELLY: structural variant discovery by integrated paired-end and split-read analysis. *Bioinformatics* (2012) **28**:i333–i339. doi:10.1093/bioinformatics/bts378

25. Pfaff AL, Bubb VJ, Quinn JP, Koks S. An increased burden of highly active retrotransposition competent L1s is associated with Parkinson's disease risk and

progression in the PPMI cohort. *Int J Mol Sci* (2020) **21**:6562. doi:10.3390/ijms21186562

26. Nam CH, Youk J, Kim JY, Lim J, Park JW, Oh SA, et al. Widespread somatic L1 retrotransposition in normal colorectal epithelium. *Nature* (2023) **617**:540–7. doi:10.1038/s41586-023-06046-z

27. Shabalin AA. Matrix eQTL: ultra fast eQTL analysis via large matrix operations. *Bioinformatics* (2012) **28**:1353–8. doi:10.1093/bioinformatics/bts163

28. Al-Chalabi A, Andrews J, Farhan S. Recent advances in the genetics of familial and sporadic ALS. *Int Rev Neurobiol* (2024) **176**:49–74. doi:10.1016/bs.irn.2024.04.007

29. Al Khleifat A, Iacoangeli A, van Vugt J, Bowles H, Moisse M, Zwamborn RAJ, et al. Structural variation analysis of 6,500 whole genome sequences in amyotrophic lateral sclerosis. *NPJ Genom Med* (2022) **7**:8. doi:10.1038/s41525-021-00267-9

30. Pfaff AL, Bubb VJ, Quinn JP, Koks S. Locus specific reduction of L1 expression in the cortices of individuals with amyotrophic lateral sclerosis. *Mol Brain* (2022) **15**:25. doi:10.1186/s13041-022-00914-x

31. Sanchez-Luque FJ, Kempen MJHC, Gerdes P, Vargas-Landin DB, Richardson SR, Troskie RL, et al. LINE-1 evasion of epigenetic repression in humans. *Mol Cell* (2019) **75**:590–604 e12. doi:10.1016/j.molcel.2019.05.024

32. Watanabe R, Nakachi Y, Matsubara H, Ueda J, Ishii T, Ukai W, et al. Identification of epigenetically active L1 promoters in the human brain and their relationship with psychiatric disorders. *Neurosci Res* (2023) **195**:37–51. doi:10.1016/j.neures.2023.05.001

33. Savage AL, Lopez AI, Iacoangeli A, Bubb VJ, Smith B, Troakes C, et al. Frequency and methylation status of selected retrotransposition competent L1 loci in amyotrophic lateral sclerosis. *Mol Brain* (2020) **13**:154. doi:10.1186/s13041-020-00694-2

34. Eisenstein M. Startups probe hidden viruses in the 'dark genome' to treat disease. *Nat Biotechnol* (2024) **42**:539–41. doi:10.1038/s41587-024-02215-1

35. Crow YJ, Briggs TA, Eleftheriou D, Parida A, Battison C, Giddings A, et al. Reverse transcriptase inhibitors in Aicardi-Goutières syndrome: a crossover clinical trial. *Dev Med Child Neurol* (2025) **67**:750–7. doi:10.1111/dmcn.16199

36. Rice GI, Meyzer C, Bouazza N, Hully M, Boddaert N, Semeraro M, et al. Reverse-transcriptase inhibitors in the aicardi-goutieres syndrome. *N Engl J Med* (2018) **379**:2275–7. doi:10.1056/nejmc1810983

37. Chiò A, Moglia C, Canosa A, Manera U, D'Ovidio F, Vasta R, et al. ALS phenotype is influenced by age, sex, and genetics: a population-based study. *Neurology* (2020) **94**:e802–e810. doi:10.1212/wnl.0000000000008869

38. Li C, Lin J, Jiang Q, Yang T, Xiao Y, Huang J, et al. Genetic modifiers of age at onset for amyotrophic lateral sclerosis: a genome-wide association study. *Ann Neurol* (2023) **94**:933–41. doi:10.1002/ana.26752

39. Li C, Wei Q, Hou Y, Lin J, Ou R, Zhang L, et al. Genome-wide analyses identify NEAT1 as genetic modifier of age at onset of amyotrophic lateral sclerosis. *Mol Neurodegeneration* (2023) **18**:77. doi:10.1186/s13024-023-00669-6

40. Calderari S, Ria M, Gerard C, Nogueira TC, Villate O, Collins SC, et al. Molecular genetics of the transcription factor GLIS3 identifies its dual function in beta cells and neurons. *Genomics* (2018) **110**:98–111. doi:10.1016/j.ygeno.2017.09.001

41. Cruchaga C, Kauwe JS, Harari O, Jin SC, Cai Y, Karch CM, et al. GWAS of cerebrospinal fluid tau levels identifies risk variants for Alzheimer's disease. *Neuron* (2013) **78**:256–68. doi:10.1016/j.neuron.2013.02.026

EBM Experimental Biology and Medicine

TYPE Original Research
PUBLISHED 06 June 2025
DOI 10.3389/ebm.2025.10350

OPEN ACCESS

*CORRESPONDENCE
Abiola Isawumi,
isawumiabiola@gmail.com

RECEIVED 22 August 2024
ACCEPTED 30 April 2025
PUBLISHED 06 June 2025

CITATION
Abban MK, Ayerakwa EA and Isawumi A (2025) Biofilm and surface-motility profiles under polymyxin B stress in multidrug-resistant KAPE pathogens isolated from Ghanaian hospital ICUs. *Exp. Biol. Med.* 250:10350. doi: 10.3389/ebm.2025.10350

Biofilm and surface-motility profiles under polymyxin B stress in multidrug-resistant KAPE pathogens isolated from Ghanaian hospital ICUs

Molly K. Abban[1,2], Eunice Ampadubea Ayerakwa[1,2] and Abiola Isawumi[1,2]*

[1]West African Centre for Cell Biology of Infectious Pathogens, College of Basic and Applied Sciences, University of Ghana, Accra, Ghana, [2]Department of Biochemistry, Cell and Molecular Biology, College of Basic and Applied Sciences, University of Ghana, Accra, Ghana

Abstract

The threat of antimicrobial resistance in Ghana is increasing with the recent emergence of KAPE pathogens (*K. pneumoniae*, *A. baumannii*, *P. aeruginosa* and *Enterobacter* species) from the hospital environment. As opportunistic pathogens, KAPE leverage the formation of biofilms and swarms to survive stringent environmental conditions. As research continues to investigate approaches that bacteria employ to exacerbate infection, this study explored biofilm and swarm formation in MDR KAPE pathogens under polymyxin B stress emerging from Ghanaian hospitals. The antimicrobial susceptibility profile of KAPE pathogens to conventional antibiotics and polymyxin B was investigated via antibiotic disk diffusion and broth microdilution assays. Biofilm inhibition and eradication assays, swarm motility and a resazurin-based metabolic assay were used to profile bacterial phenotypic characteristics under polymyxin B stress. The strains exhibited resistance to the tested antibiotics with a high level of resistance to polymyxin B (PMB) (≥512 μg/mL). Additionally, the strains formed biofilms and bacterial swarms at 37°C. In the presence of PMB (≥512 μg/mL), KAPE pathogens formed swarms with no significant reduction in bacterial swarms at 1,048 μg/mL. Biofilm was observed for all strains with PMB neither inhibiting nor eradicating at high PMB (2048 μg/mL). Additionally, there were no significant differences in the phenotypic and antimicrobial susceptibility profiles of clinical and environmental KAPE pathogens from Ghanaian ICUs. Overall, the study established that clinical and environmental KAPE pathogens from Ghanaian ICUs exhibit adaptive phenotypic and

resistance characteristics that could potentially enhance bacterial survival during host colonization and infection. This could undermine treatment strategies and pose public health challenges in Ghana.

KEYWORDS

KAPE pathogens, polymyxin, biofilms, surface-motility, swarming

Impact statement

Critical priority bacterial pathogens pose serious public health challenges with increasing therapeutic failures. This is attributed to the development of survival mechanisms that facilitate antimicrobial resistance, host colonization and immune evasion. These mechanisms depend on the expression of diverse phenotypic traits including biofilm formation and surface-motility. Bacteria use biofilm and motility machinery to survive stringent environmental conditions, initiate virulence and persist in the presence of antibiotics. These traits contribute to the pathogenicity of bacteria and increase the burden of antimicrobial-resistant infections. This study examined biofilm-motility interplay as a mechanism of tolerance to polymyxin B.

Introduction

The hospital environment represents a model of microbial interaction because it plays a key role in disease pathogenesis. The interplay between humans and bacteria in the hospital environment threatens the safety of all hospital users, thereby increasing the frequency of hospital-acquired infections (HAIs) [1–3]. There is increased morbidity and mortality associated with HAIs [4] with ventilator-associated pneumonia (VAP), central line-associated bloodstream infections (CLABSI), catheter-associated urinary tract infections (CAUTI) and surgical site infections (SSI) being the predominant HAIs [5–7]. Incidence rates of HAIs (5.7%–19.1%) have been reported in developing countries including Ghana (8.2%) [3] with VAP, CLABSI and CAUTI being frequently reported [6–8]. Bacteria are the most commonly isolated pathogens and contribute to 87% of reported HAIs [5, 7, 9]. They survive in the hospital largely as commensals and opportunistic pathogens from normal human flora, immunocompromised patients and the general hospital environment. Globally, reported bacterial strains implicated in HAIs include *Pseudomonas aeruginosa, Acinetobacter baumannii*, members of the *Enterobacteriaceae* and *Staphylococcus aureus* [7, 10–12]. Of this group, Gram-negative bacteria represent a high risk to public health due to an increase in AMR [1, 7].

Gram-negative KAPE (*K. pneumoniae*, *A. baumannii*, *P. aeruginosa* and *Enterobacter* spp.) [1] or the friendly amendment ESCAPE [13] (*C. difficile*, *A. baumannii*, *P. aeruginosa* and Enterobacteriaceae), have been implicated in major bacterial infections and described as extremely critical with global precedence [14, 15]. They are ubiquitous and primarily associated with HAIs particularly among immunocompromised and critically ill patients [1, 6]. They have a tendency to circumvent lethal doses of antibiotics. These pathogens present with multidrug resistant, extensively drug-resistant or pan-drug-resistant phenotypes [16, 17] and infections resulting from these resistant Gram-negative pathogens have been associated with poorer patient outcomes than susceptible isolates [18]. The mechanisms employed by KAPE pathogens to display resistance and induce virulence include drug inactivation, modification of the target site, and reduction in drug permeability [19] and quorum sensing by utilizing surface-motility and biofilm development to promote resistant populations [20].

Swarming surface-motility and biofilm formation are hallmark survival mechanisms utilized by multidrug-resistant pathogens [21] during harsh, unfavorable conditions such as antibiotic treatment. Both processes allow for rapid colonization and establishment of infection with bacterial swarming enabling initial attachment of cells to surfaces including catheters to induce biofilm formation [22, 23]. These multicellular adaptations provide strains with mechanical and biochemical advantages, making it difficult to eliminate bacteria using conventional antibiotics [24]. In addition, swarming and biofilm-forming cells exhibit increased adaptive phenotypic resistance and tolerance due to innate and acquired resistance markers that promote AMR [25, 26]. Increased tolerance and resistance to conventional antibiotics lead to dependence on last-resort antibiotics such as carbapenems and polymyxins [21]. For antibiotics to disrupt and inhibit swarming and biofilm formation, higher antibiotic concentrations, combinations, or disruption of gene targets are required [26]. Although some studies report an inverse relationship between biofilm formation and swarm motility [27], the ability to form these coordinated multicellular behaviors particularly in MDR strains leads to increased virulence and pathogenicity [28–30].

There are few studies on how biofilm and motility, as phenotypic factors contribute to HAIs in Gram-negative bacteria in Ghana. Also, how these factors enhance the level of AMR, leading to reduced treatment options in the Ghanaian hospital setting, has not been fully explored. The majority of pathogens implicated in HAIs exhibit a tendency to colonize diverse surfaces via the formation of biofilms [29, 31] and surface swarm motility [21, 24]. In this study, we explored the

phenotypic characteristics of clinical and environmental Gram-negative KAPE, *Citrobacter* sp. and *E. coli* from ICUs of Ghanaian hospitals. Additionally, the interplay of surface-motility and biofilm profiles under polymyxin B as survival characteristics was explored.

Materials and methods

Bacterial strains and culture conditions

Archived Gram-negative bacterial strains of KAPE pathogens (obtained from air, fomites, and patients) from the ABISA™ bacterial culture library at the Department of Biochemistry, Cell and Molecular Biology, University of Ghana were used in this study (This study is part of a larger study approved by the Ghana Health Service: GHS-ERC01/02/17). Six environmental and six clinical strains associated with HAIs (*Klebsiella pneumoniae, Acinetobacter baumannii*, *Enterobacter* sp., *Citrobacter* sp. and *Pseudomonas aeruginosa*) were selected. Control strains were UK19 *E. coli* (ATCC 25922) for antimicrobial susceptibility testing, *Pseudomonas aeruginosa* (PS03) for biofilms and *Proteus mirabilis* (PT01) for swarm motility. Bacterial strains were recovered from a −80°C freezer and revived in Luria-Bertani broth (LB) (Invitrogen Life Tech, United States) at 37°C for 18 h with shaking at 60 rpm. Strains were refreshed in LB broth, streaked on MacConkey agar (Oxoid, England, CM0007B) and incubated at 37°C overnight.

AMR susceptibility profiles of strains

Fifteen standard commercial antibiotics including cloxacillin (5 µg), nitrofurantoin (200 µg), penicillin (15 µg), ampicillin (10 µg), nalidixic-acid (30 µg), ceftazidime (30 µg), chloramphenicol (50 µg), cefotaxime (10 µg), cefuroxime (30 µg), cotrimoxazole (25 µg), gentamycin (10 µg), tetracycline (30 µg), ceftriaxone (30 µg), erythromycin (15 µg) and flucloxacillin (10 µg) were used. Briefly, overnight bacterial culture was adjusted to 0.5 McFarland, seeded on sterile Mueller Hinton agar (Invitrogen life tech) plates and antibiotic discs were aseptically applied (incubation, 16–18 h at 37°C). The diameters of the zone of inhibition were recorded to the nearest millimeter (mm) and strains were classified as resistant, intermediate, or susceptible based on CLSI guidelines [32, 33]. The broth microdilution assay with polymyxin B (PMB) was conducted as previously described [34]. Briefly, PMB powder was prepared to a stock concentration of 12,000 µg/mL. Broth microdilution was performed with cation-adjusted Mueller Hinton broth in a range of two-fold dilutions (0.16–2,048 µg/mL) of PMB. One hundred microliters of PMB were transferred to 96-well plates and a final bacterial inoculum of 100 µL ($1–5 \times 10^5$ CFU/mL) was transferred to each well. The plates were incubated with shaking at 37°C for 18 h and the absorbance was read with a multimode microplate reader (Varioskan LUX Thermo Fisher Scientific). The minimum inhibitory concentration (MIC) was calculated as the percentage of OD < 10.

Bacterial surface-motility assay

The swarming motility assay was performed as described by Morales-Soto et al. [35] with a few modifications, with and without PMB. Nutrient agar (Oxoid) was prepared to a concentration of 0.5% (w/v). The media was cooled to 60°C, and 15 mL was transferred to 60 mm Petri dishes. The plates were left to air dry for 1 h. Each strain was cultured to log phase (OD_{600} 0.2–0.5~$1 \times 10^{5\text{-}6}$), harvested (5,000 rpm/5 min), and resuspended in double-distilled water. Five microliters of culture were spotted in the center of swarm media plates and incubated at 25°C, 37°C and 45°C for 24–72 h. Motility was assessed by measuring the diameter (mm) of the widest point of spread. For the swarm assay with PMB, nutrient agar plates were seeded with 512 µg/mL, 1,024 µg/mL and 2048 µg/mL PMB. Five microliters of bacterial culture at the log phase (OD_{600} 0.2–0.5), was spotted onto the center of the plates (25°C, 37°C, 45°C for 24–72 h). Biological and technical replicates were performed for each strain.

Biofilm assays

Biofilm formation was assayed with the capillary tube adherence method and the 96-well microtiter plates (MTP) adapted from O'Toole, 2011 [34]. Briefly, 200 µL and 2 mL overnight cultures normalized to OD_{600} 0.1 in LB broth were transferred to 96-well plates and capillary tubes respectively and incubated for 3–5 days at 37°C. Spent media were removed and the plates/tubes were washed three times with sterile distilled water to remove loosely adherent bacteria. Plates/tubes were air-dried for 30 min, stained with 0.1% (w/v) crystal violet solution, and incubated at room temperature for 30 min. Plates were washed with sterile distilled water, air-dried and quantitatively assessed with 200 µL of 96% (v/v) ethanol and absorbance was determined at 590 nm. The data were interpreted according to the cut-off value (ODc) adapted from Stepanović et al., [36]. The isolates were characterized as no biofilm producers when OD ≤ ODc, weak when ODc < OD ≤ 2ODc, moderate with 2ODc < OD ≤ 4ODc, and strong with OD > 4ODc, where OD represents the absorbance value. For the biofilm inhibition assay, the MIC established for the strains was used as the standard condition to determine the biofilm inhibitory concentration. Briefly, microtiter wells were seeded with 100 µL of standardized culture at log-phase (OD_{600} 0.2–0.5). 100 µl of PMB at 512 µg/mL, 1,024 µg/mL and 2048 µg/mL were transferred to the wells and incubated at 37°C for 5 days. The wells were washed and subjected to crystal violet staining to quantify biofilm products, and bacterial viability was confirmed with resazurin assay [38]. The Biofilm eradication assay was performed as previously described

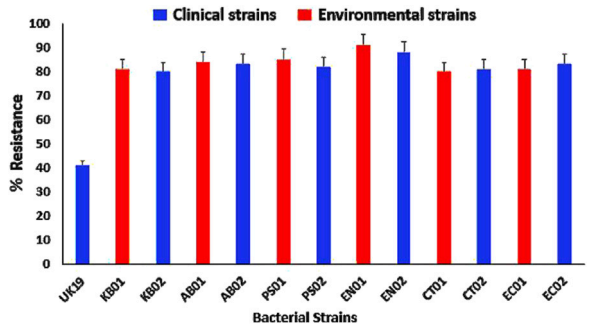

FIGURE 1
AMR profiles to conventional antibiotics relative to the UK19 *E. coli* control strain. (KB01, KB02) *K. pneumoniae*; (AB01, AB02) *A. baumannii*; (PS01, PS02) *P. aeruginosa*; (EN01, EN02) *Enterobacter* sp.; (CT01, CT02) *C. freundii*; (EC01, EC02) *E. coli*. Error bars indicate the percentage of resistance of the strains to the tested antibiotics.

[38]. Preformed biofilms were treated with 200 µL of PMB at 512 µg/mL, 1,024 µg/mL and 2048 µg/mL. Plates were incubated for 18–24 h at 37°C. Crystal violet and resazurin were used to quantify biofilm formation and determine the level of bacterial viability [38].

Statistical analysis

The data were expressed as mean ± standard deviation and analyzed using Microsoft Office Excel and GraphPad Prism 7.0 (GraphPad Software, Inc. CA, USA). One-way ANOVA and Dunnett's correction test were used to compare means between biofilm formation in strains relative to their untreated controls. Two-way ANOVA and Dunnett's multiple comparison test were used to compare means between swarming strains under the different treatment conditions and incubation times. For the metabolic assay, two-way ANOVA and Dunnett's multiple comparison were employed to compare controls (*Pseudomonas* sp. (PS03) and Negative control (PC)) to test strains. $P < 0.05$, statistically significant; ns ($P > 0.05$); *$P < 0.05$, **$P < 0.009$, ***$P = 0.001$, ****$P < 0.0001$.

Results

Strains are multidrug resistant with high levels of resistance to last-resort antibiotics

The strains were tested against 15 different antibiotics belonging to 8 classes (β-lactams, macrolides, aminoglycosides, nitrofurans, sulfonamides, phenicols, tetracyclines and quinolones). All the strains were highly resistant with at least 80% levels of AMR to the tested antibiotics (Figure 1). The strains were resistant to at least two of the eight classes of antibiotics, with different resistance patterns and a multiple antibiotic resistance index of ≥0.8 relative to 0.4 for the *E. coli* control strain (Supplementary) indicating high levels of resistance per the CLSI guidelines. All strains displayed high levels of resistance to PMB with a MIC of 512 µg/mL, which was above the CLSI breakpoint for resistance of ≤4 µg/mL (Supplementary).

Strains have strong biofilm phenotypes and swarm at high polymyxin B concentrations

Biofilm formation was observed in both clinical and environmental strains (Figure 2). 37°C for 24–72 h was the determined condition for strong biofilm formation. At 72 h, there was formation of mature biofilms with characteristic strong adherence to the walls of the tube and plate after crystal violet staining. The strains were categorized as negative, weak, moderate or strong based on the biofilm-forming index standard. The majority (66%) of the strains displayed a strong biofilm phenotype (Figure 2). Both clinical and environmental *K. pneumoniae*, *P. aeruginosa*. and *Enterobacter* sp. formed strong biofilms while environmental *Citrobacter* sp., clinical *A. baumannii* were weak biofilm formers. Clinical *Citrobacter* sp. and *E. coli* were moderate formers. In total, 63% of the environmental strains displayed a stronger biofilm phenotype compared to the clinical strains (37%).

Surface-motility, particularly swarming was determined by measuring the mean diameter of the swarms formed at 37°C (for 24, 48 and 72 h). Strains were described as non-motile with <5 mm diameter, 5 – 20 mm as intermediate and >20 mm as strong swarmers. For the majority of the strains, swarming was gradual while others showed a sharp increase in diameter after 24 h (Figure 3). Eight of the strains showed robust motility with diameters above 20 mm after 48 h (KB01, KB02, AB01, AB02, PS01, EN02, CT01, EC02). Clinical *P. aeruginosa* (PS02), *Citrobacter* sp. (CT02), environmental *E. coli* (EC01) and *Enterobacter* sp. (EN01) were intermediate swarmers. At 512 µg/mL, 1,024 µg/mL and 2048 µg/mL PMB, swarming was significantly reduced relative to the respective wild types (Figure 3). The majority of the strains exhibited an intermediate motility phenotype (5 – 20 mm) in the presence of PMB with strains of *K. pneumoniae* (KB02) and *A. baumannii* (AB01 and AB02) being inhibited at 1,024 and 2048 µg/mL, respectively (Figures 3B,C).

Strains formed biofilms in the presence of polymyxin B

At 512 µg/mL, 1,024 µg/mL and 2048 µg/mL PMB treatment, strains formed biofilms (Figure 4). There was no complete

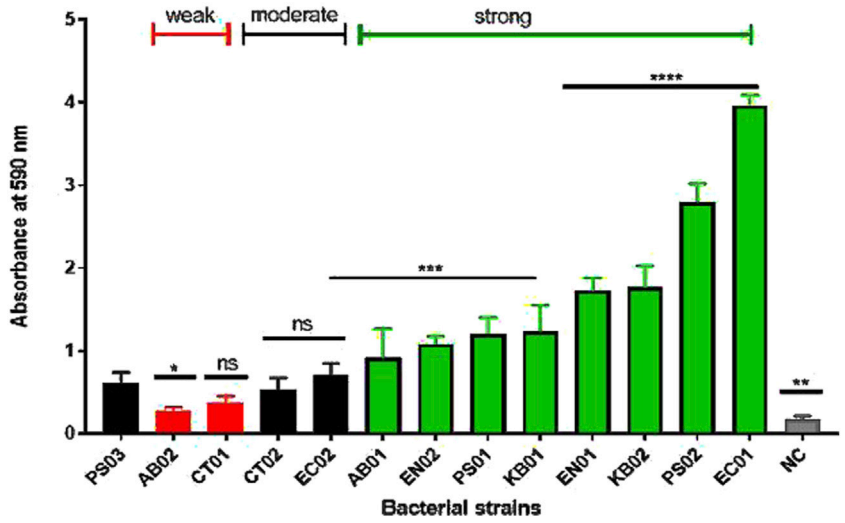

FIGURE 2
Biofilm profiles of clinical and environmental strains biofilm biomass was measured at 590 nm after 0.1% crystal violet staining. The relative biofilm produced for the strains was compared to PS03 (a biofilm-forming strain). The data are presented as mean ± standard deviation (n = 2), P < 0.05 statistically significant; *P < 0.05, **P < 0.005, ***P < 0.001, ***P < 0.0001; one-way ANOVA using Dunnett's correction for multiple comparisons.

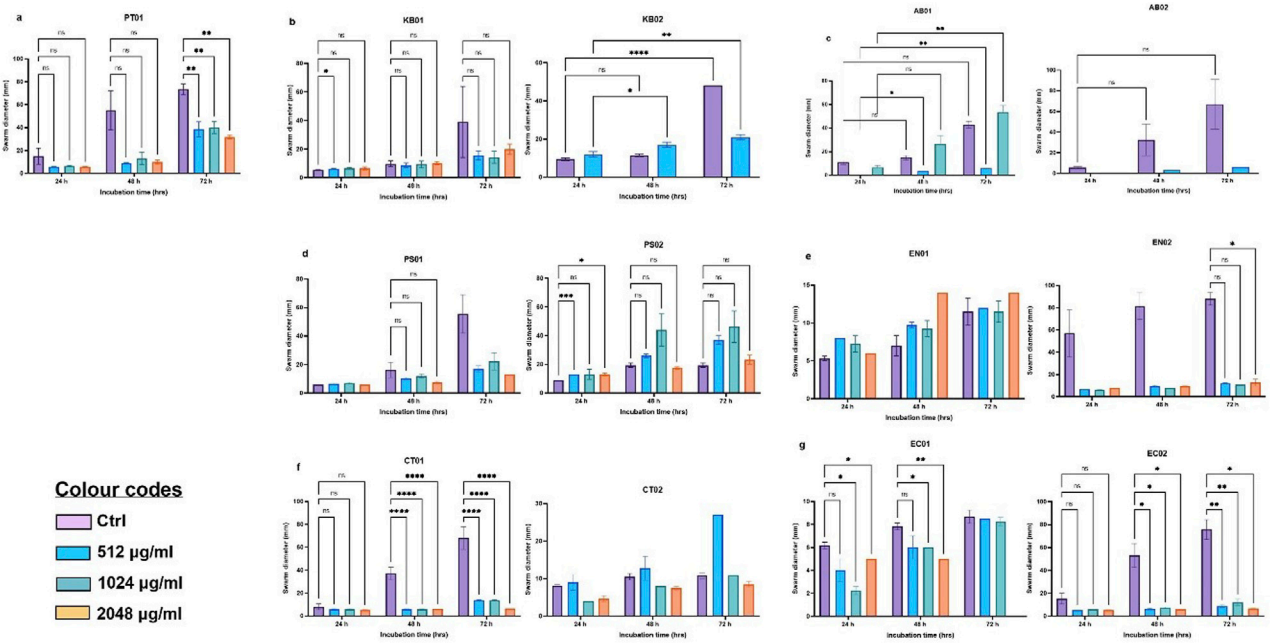

FIGURE 3
Swarm profile of clinical and environmental strains under PMB stress **(A)** PT01; **(B)** *K. pneumoniae* (KB01, KB02); **(C)** *A. baumannii* (AB01, AB02); **(D)** *P. aeruginosa* (PS01, PS02); **(E)** *Enterobacter* sp. (EN01, EN02); **(F)** *Citrobacter* sp. (CT01, CT02); **(G)** *E. coli* (EC01, EC02). The data are presented as mean ± standard deviation (n = 2) P < 0.05 statistically significant, *P < 0.05, **P < 0.005; two-way ANOVA with Dunnett's correction for multiple comparisons was used.

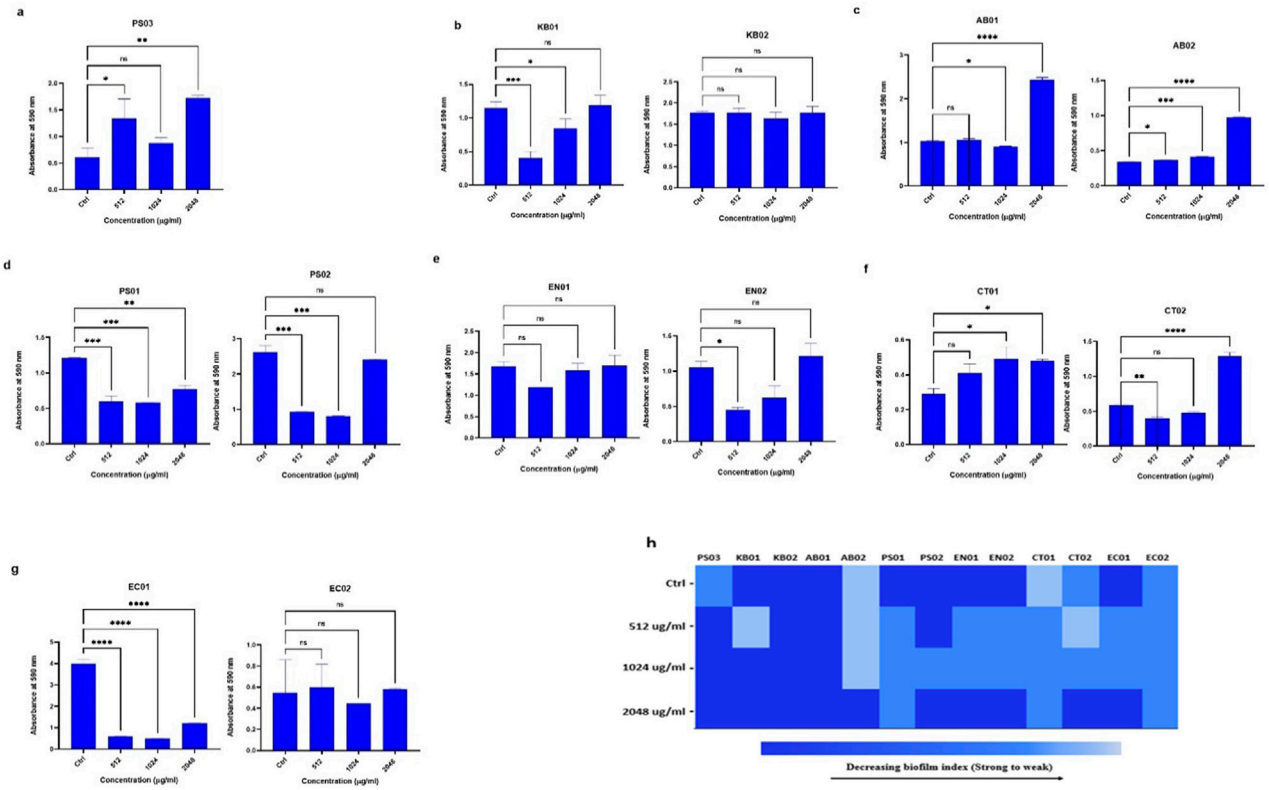

FIGURE 4
Assessment of biofilm inhibition in the presence of PMB **(A)** *Pseudomonas* sp. (PS03) **(B)** *K. pneumoniae* (KB01, KB02); **(C)** *A. baumannii* (AB01, AB02); **(D)** *P. aeruginosa* (PS01, PS02); **(E)** environmental and clinical strain of *Enterobacter* sp. (EN01, EN02); **(F)** *Citrobacter* sp. (CT01, CT02); **(G)** *E. coli* (EC01, EC02). **(H)** Heat map of biofilm index after PMB inhibition assay. Color codes represent weak, moderate and strong biofilms. The data are presented as mean ± standard deviation (n = 2) $P < 0.05$ statistically significant; *$P < 0.05$, **$P < 0.009$, ***$P < 0.001$; one-way ANOVA using Dunnett's correction for multiple comparisons.

inhibition and eradication of biofilm, but the degree of biofilm formed relative to the controls (without PMB) varied. There was an increase in biofilm biomass with increasing antibiotic concentration. For the determination of biofilm inhibition (Figure 4B), environmental *K. pneumoniae* (KB02) assumed a weak biofilm phenotype at 512 µg/mL relative to its strong phenotype in the absence of PMB. At 1,024 µg/mL and 2048 µg/mL, it formed strong biofilms. However, clinical *K. pneumoniae* formed strong biofilms at all PMB concentrations (Figure 4B), indicating no biofilm inhibition. The clinical *A. baumannii* strain formed a weak biofilm at 512–1024 µg/mL with a strong phenotype at 2048 µg/mL, while the environmental strain maintained a strong biofilm phenotype irrespective of PMB concentrations (Figure 4C). Biofilm formation in environmental *P. aeruginosa* was moderate at all antibiotic concentrations with the clinical strain displaying moderate biofilm formation at 1,024 µg/mL (Figure 4D). Environmental *Enterobacter* sp. was observed as a strong biofilm former under antibiotic pressure while the clinical strain displayed a moderate phenotype at 512 µg/mL and 1,024 µg/mL but a strong one at 2048 µg/mL (Figure 4E). The environmental *Citrobacter* sp. strain formed a weak biofilm in the absence of antibiotics, but showed a moderate biofilm phenotype at the three antibiotic concentrations (Figure 4F), while the clinical strain was observed as weak, moderate and strong at 512 µg/mL, 1,024 µg/mL and 2048 µg/mL respectively. In *E. coli*, the environmental strain (EC01) displayed a moderate phenotype at 512 µg/mL and 1,024 µg/mL, while the clinical strain (EC02) was observed as moderate at all the antibiotic concentrations (Figure 4G). Overall, the selected antibiotic concentrations did not inhibit biofilm formation, although some strains exhibited reduced biofilm (Figure 4H).

High concentrations of polymyxin B could not eradicate preformed biofilms

To determine the concentration of antibiotic needed to reduce preformed biofilm (Figure 5A), strains were challenged with PMB at MIC concentrations (512 µg/mL) (Figures 5A-G). In general, the

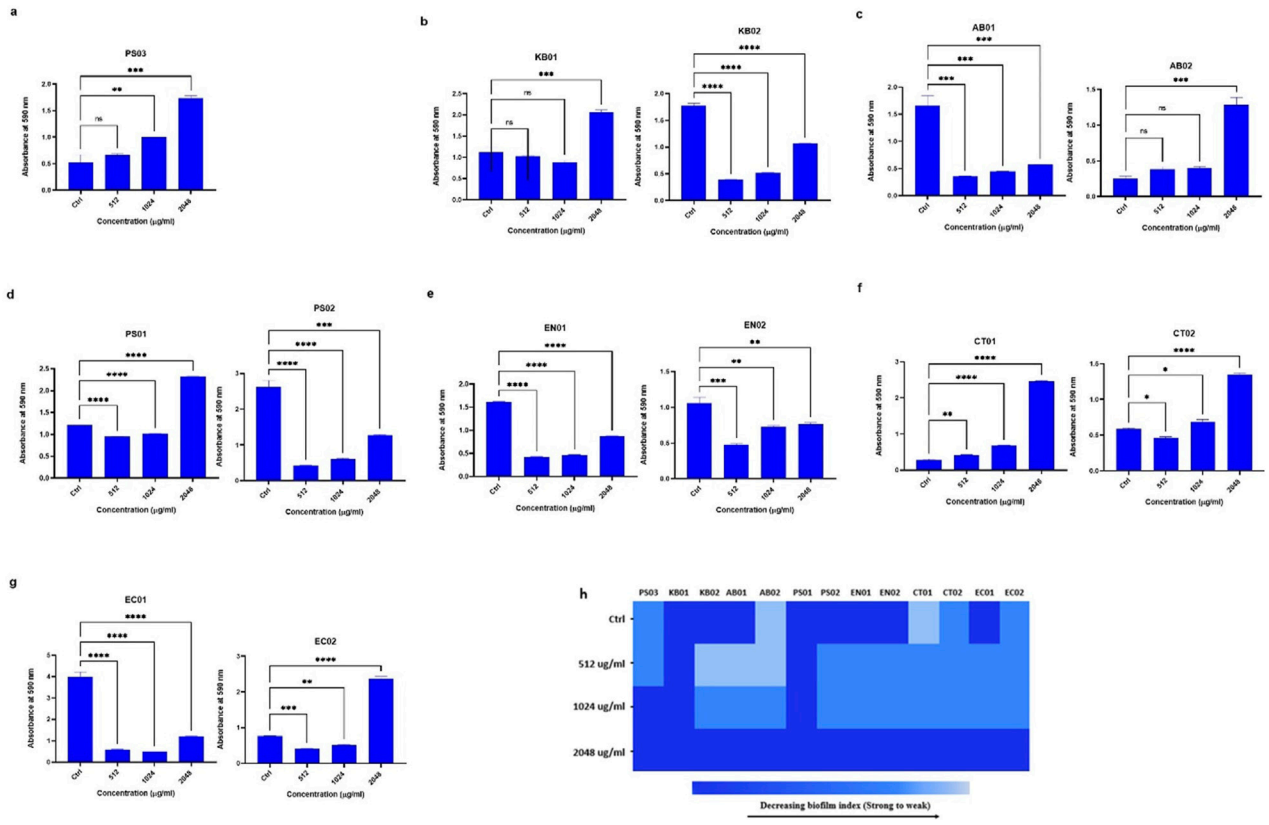

FIGURE 5
Assessment of biofilm eradication in the presence of PMB **(A)** *Pseudomonas* sp. **(B)** *K. pneumoniae* (KB01, KB02); **(C)** *A. baumannii* (AB01, AB02); **(D)** *P. aeruginosa* (PS01, PS02); **(E)** *Enterobacter* sp. (EN01, EN02); **(F)** *Citrobacter* sp. (CT01, CT02); **(G)** *E. coli* (EC01, EC02). **(H)** Heat map of biofilm index after PMB eradication assay. Color codes represent weak, moderate and strong biofilms. The data are presented as mean ± standard deviation (n = 2) $P < 0.05$ statistically significant; ns ($P > 0.05$); *$P < 0.05$, **$P < 0.009$, ***$P < 0.001$; one-way ANOVA using Dunnett's correction for multiple comparisons.

biofilm index of all the strains at 2048 µg/mL was strong, indicating that the antibiotic concentration did not eradicate the preformed biofilm (Figures 5B-G). At 1,024 µg/mL, the biofilm index ranged between moderate and strong (Figure 5C). At 512 µg/mL, there was a reduction in preformed biofilm from a strong index to a moderate index for the majority of the strains with clinical *K. pneumoniae* and *A. baumannii* (AB01 and AB02) assuming a weak phenotype (Figure 5B). In general, the degree of biofilm eradicated at 512 µg/mL was greater than at 1,024 µg/mL and 2048 µg/mL (Figure 5H).

Bacterial strains were viable after biofilm inhibition and eradication assay

The viability of the strains was inferred by employing a resazurin metabolic assay after inhibition and eradication assays. Strains were observed as metabolically active 24 h after incubation for the inhibition assay (Figure 6A) with some strains displaying metabolic activity 48 h after eradication (Supplementary – 48 h Metabolic Eradication). Relative fluorescence units (RFU) ranged from 1,500–2000, indicating a difference in strain reduction ability and viability of the cell population (MBIC). Some strains (KB01, PS02, EN02, and EC01) reduced resazurin more rapidly than others (KB02, EN01, CT02, and EC01); however, reduction was observed in all strains after biofilm formation and indication of strain viability (Figure 6A). For inhibition (MBIC), reduction/viability was higher at 1,024 µg/mL and 2048 µg/mL compared to 512 µg/mL for the majority of strains. There was no significant difference in the metabolic activity of the strains relative to the PS03, but there was a significant difference in cell viability after the inhibition assay relative to the negative control (NC). In the eradication assay (Figure 6B), the majority of the strains displayed low RFU levels at the 3 antibiotic concentrations. Although the reduction was low in MBEC (Figure 6B), relative to the negative control, a reduction was observed in all strains mainly at 48 h (Supplementary – 48 h Metabolic Eradication), indicating a degree of viability after antibiotic treatment.

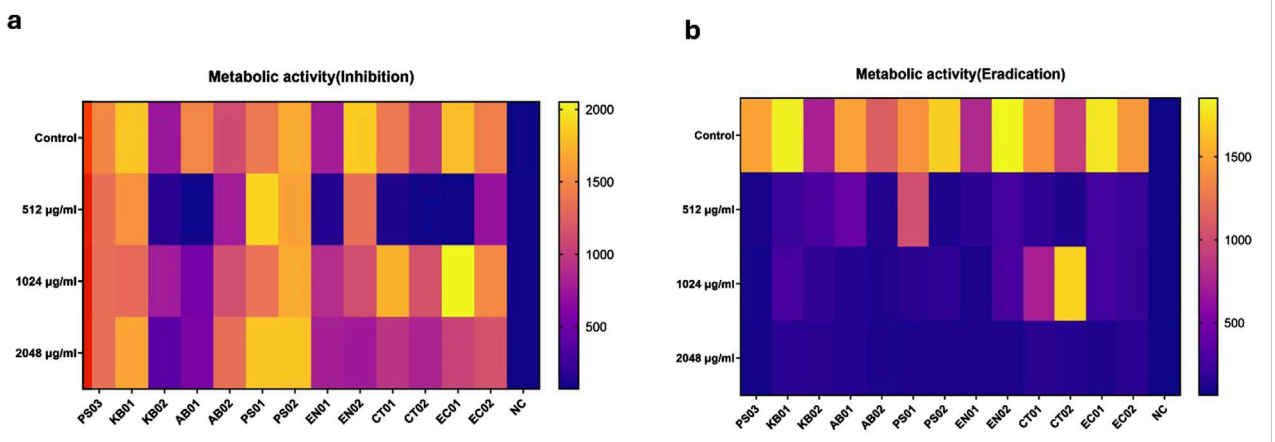

FIGURE 6
Metabolic activity of strains after PMB treatment at 24 h. MBIC and MBEC metabolic heatmap. The horizontal bar represents the degree of RFU measurement. Relative to controls (upper rows), each row panel represents treatment with PMB at 512 µg/mL, 1,024 µg/mL and 2048 µg/mL respectively. Two-way ANOVA with Dunnett's correction for multiple comparisons was used to compare metabolic activity between strains and controls. For the inhibition assay, there was a significant difference in metabolic activity of strains relative to NC ($p < 0.0028$) compared to PS03 ($p > 0.1$). For the eradication assay, no significant difference in the metabolic activity of strains relative to PS03 ($p > 0.05$) and NC ($p > 0.05$). $P < 0.05$ statistically significant; ns ($P > 0.05$); *$P < 0.05$, **$P < 0.009$, ***$P < 0.001$.

Discussion

This study characterized Gram-negative KAPE pathogens, *Citrobacter* spp. and *E. coli* from Ghanaian hospital environments and explored their phenotypic profiles (biofilm and swarm motility) under polymyxin B pressure. The clinical and environmental isolates displayed average (80%–85%) levels of AMR to the tested antibiotics. This raises concern as clinical isolates are expected to be more resistant than environmental isolates due to antibiotic exposure during treatment [39]. The resistance patterns exhibited by environmental isolates suggest that these strains have either acquired mobile genetic elements in the environment or have a tendency to adapt to environmental stress factors [40]. The MIC to polymyxin B was 512 µg/mL; seven times higher than the CLSI standard for AMR for *A. baumannii*, *P. aeruginosa* and *Enterobacter* spp. The presence of polymyxin-resistant strains in the hospital environment increases the risk of treatment failure during infection. The resistance pattern displayed to both conventional antibiotics and polymyxin B confers a multidrug-resistant phenotype to the strains. This relatively high level of resistance observed is particularly worrying in Ghana and adds to the growing reports of AMR observed globally [3, 41].

Surface-motility and biofilm formation can be described as complex adaptations associated with adaptive multidrug resistance, bacterial persistence, and virulence [21]. The colonization ability of the strains was analyzed *in vitro* by studying the biofilm-motility interplay. In this study, all strains exhibited surface movement on the semi-solid agar from the point of inoculation after 24 h. The degree of swarming was conditional, strain-specific and dependent on the ability of bacterial strains to generate and maintain moisture on the agar surface as described by Carabarin-Lima et al., 2016 and Lai et al., 2009 [26, 42]. *Proteus* sp. exhibited increasing swarming with increasing incubation times at 37°C. The majority of the strains displayed swarming to a lesser degree relative to the control (PT01); however, clinical strains of *A. baumannii*, *Enterobacter* sp., and *E. coli* and the environmental strain of *Citrobacter* sp. showed higher swarming ability after 48 h. Although some strains are classified as non-motile (*Klebsiella* sp. & *Acinetobacter* sp.), they have a tendency to display motility, which is evident as swarming on agar plates [42, 43]. It is possible that the halos observed on the agar plates for *Acinetobacter* sp. could employ twitching or surface-associated motility [44–46] and flagella-mediated motility for *Klebsiella* under certain defined conditions [42]. This is particularly important as motility is also characterized as a host invasion and evasion strategy. Motility regulation is often coupled to the expression of virulence determinants including the ability to invade diverse cell types, leading to persistent infections [44, 45]. The clinical relevance of surface-motility is particularly observed in acute infections, as it allows for rapid colonization and establishment of infection [46]. The incidence of HAIs is enhanced by the pathogenic tendencies of opportunistic KAPE pathogens.

The strains also exhibited swarming under polymyxin B pressure. Previous studies have reported higher AMR during bacterial swarming in *P. aeruginosa*, *S. marcescens* [26] and *S. enterica* [47]. As swarming is a multicellular coordinated behavior, cell density confers a protective layer to withstand

exposure to lethal concentrations of antibiotics [48, 49]. Death in a subpopulation of bacterial cells could enhance adaptive resistance in the surviving population [50] leading to reduced swarm diameter but persistent swarming; this is evident in the intermediate phenotype observed. Although both clinical and environmental strains displayed intermediate swarming and polymyxin B tolerance at 512, 1,024, 2048 μg/mL, surface-motility for *Klebsiella* (KB02) and *A. baumannii* (AB01 and AB02) was inhibited at higher concentrations, an indication of cell death. Overall, the presence of polymyxin B reduced the swarming ability of the strains but did not result in total cell death for the majority of strains relative to the *Proteus* sp. control. This suggests that surface-motility, particularly swarming could be a mechanism employed by bacteria to resist lethal concentrations of antibiotics, resulting in AMR and persistent infections in immunocompromised individuals in hospital settings [21].

We explored the ability of the strains to form biofilms following polymyxin B stress. Biofilm-associated bacteria can cause chronic infections that persist, unlike their planktonic counterparts, causing acute infections [51]. Biofilm formation can be suppressed through inhibition of the planktonic population, preventing initial adhesion, and removing established biofilm [52]. All strains were biofilm formers with some exhibiting higher degrees of biofilm biomass. Based on the biomass index, the majority of the strains (66%) were strong formers in the absence of antibiotics. Biofilm can be described as a stress-induced response to environmental factors such as exposure to antimicrobials to enable bacterial persistence during infection. The MIC of 512 μg/mL established for the planktonic cells did not inhibit biofilm formation even at 2048 μg/ml. A study of sub-MIC concentrations of antibiotics was reported to induce biofilm formation by a factor of 2 in *P. aeruginosa* [48], indicating that higher concentrations would induce even stronger biofilm phenotypes. In addition, Černohorská & Votava, [48] showed that strains of *P. aeruginosa*, *K. pneumoniae, A. baumannii* and *E. coli* exhibited enhanced survival and resistance in a biofilm population relative to the planktonic cells.

As a result of the difficulty in eradicating biofilms, some studies suggest increasing the antibiotic concentrations [52, 53]. In the eradication assay, the degree of biofilm was reduced at 512 μg/mL relative to the untreated control. Eradication did not result in complete clearance of the biofilm formed but in a moderation of the biofilm index, similar to reports that polymyxin B led to a reduction of preformed biofilm in *S. aureus*, *E. coli* [54] and *Pseudomonas* sp. [55]. Clearance of preformed biofilm cells is difficult, hence a multistep combination antibiotic treatment is required to efficiently reduce biofilm biomass in KAPE pathogens [56]. There was, however, strong biofilm formation in all strains at 2048 μg/mL, indicating the role of higher antibiotic concentration in inducing stronger biofilms and resistance [52]. When comparing the swarm and biofilm profiles, all strains that exhibited surface-motility formed biofilms at higher concentrations of polymyxin B. The robust swarming nature and the biofilm profile exhibited by the strains indicate a positive correlation between biofilm formation and swarming motility in our strains. Microbial biofilms and swarms pose a significant challenge in the hospital environment, as they influence antibiotic resistance phenotypes and enhance persistent infections in that setting.

To determine the viability of biofilm cells, a resazurin assay was adopted, in which metabolically active cells reduce blue non-fluorescent resazurin to pink and highly fluorescent resorufin [53]. The wild type reduction of the majority of the strains was above 1500 RFU relative to below 200 RFU for the negative control, indicating the presence of a viable number of active bacterial cells after biofilm development. During inhibition, fluorescence readings were above 500 RFU at 1,024 and 2048 μg/mL. Some studies have reported different metabolizing abilities of cells, such as *S. aureus,* which rapidly reduces resazurin compared to *P. aeruginosa* and *B. cenocepacia* [57]. The removal of the stress factor resulted in strains assuming a metabolically active phenotype; however, at 512 μg/mL, the majority of the strains displayed low metabolic activity at 24 h post-stress conditions. The reduction in biofilm at 512 μg/mL during inhibition corresponds to the reduction in cell viability observed at 512 μg/mL in the resazurin assay. Comparing the concentration of PMB at 512 and 1,024 μg/mL, sub-MIC concentrations of PMB could further reduce bacterial viability in a biofilm environment compared to increasing antibiotic concentration. In the eradication assay, a reduction of 500 RFU was recorded for the majority of the strains, which could indicate lower numbers of viable cells or dormancy after stress. Studies have reported low nutrient availability to bacterial cells in the deeper layers of a biofilm, leading to dormancy in this state with reversal of dormancy after stress removal [32]. Strains within a biofilm inhibition and eradication assay could be characterized as metabolically active and slow-growing strains, respectively. Metabolically active cells enhance biofilm formation and induce resistance phenotypes through the expression of diverse enzymes required for strain survival [58]. Additionally, preformed biofilms are characterized by slow-growing cells with reduced antibiotic efficacy due to biofilm biomass and reduced metabolic activity [58-61].

Conclusion

The clinical and environmental strains displayed appreciably similar growth and AMR patterns indicating that the strains could be described as multidrug resistant. The ability to form biofilm and display robust surface-motility, particularly under polymyxin B pressure indicates a greater ability to tolerate, resist and survive under high antibiotic pressure. Since polymyxin B did not significantly inhibit or reduce the degree of biofilm formed, the tendency for increased pathogenesis and virulence of infections during host colonization is possible. The presence of viable cells particularly during biofilm inhibition indicates a growing tolerance to antibiotics and therefore a need for

guided treatment options. The challenge of resistance coupled with the ability of strains to exhibit phenotypes corresponding to characteristics that enhance infection persistence in the hospital environment is challenging. These characteristics are particularly concerning, as environmental isolates exhibit similar phenotypes to clinical isolates. This poses a challenge to treatment outcomes and the subsequent spread of AMR in a closed environment such as the ICU. More worryingly, these strains are present in Ghanaian hospital environments, implying the need to intensify research into the mechanisms of AMR and explore possible therapeutic interventions.

Author contributions

AI and MA conceptualized and designed the study. AI, MA and EA investigated, interpreted and analyzed the data. AI and MA prepared the first draft of the manuscript. AI and MA revised the draft for important intellectual content. All authors contributed to the article and approved the submitted version.

Data availability

The datasets presented in the study are deposited in Harvard Dataverse as supplementary files and can be found here - https://doi.org/10.7910/DVN/JJUUKN.

Funding

The author(s) declare that financial support was received for the research and/or publication of this article. This work was supported by a WACCBIP-World Bank ACE fellowship (ACE02-WACCBIP: Awandare) and a DELTAS Africa grant (DEL-15-007: Awandare). The authors have no other relevant affiliations or financial involvement with any organization or entity with a financial interest in or financial conflict with the subject matter or materials discussed in the manuscript apart from those disclosed.

Acknowledgments

The authors would like to acknowledge the members and staff of the AMR Research Group (led by AI) at the West African Centre for Cell Biology of Infectious Pathogens (WACCBIP) and the Department of Biochemistry, Cell and Molecular Biology, University of Ghana for technical support.

Conflict of interest

The author(s) declared no potential conflicts of interest with respect to the research, authorship, and/or publication of this article.

References

1. Rice LB. Federal funding for the study of antimicrobial resistance in nosocomial pathogens: No ESKAPE. *The J Infect Dis* (2008) **197**(8):1079–81. doi:10.1086/533452

2. Abban MK, Ayerakwa EA, Mosi L, Isawumi A. The burden of hospital acquired infections and antimicrobial resistance. *Heliyon* (2023) **9**(10):e20561. doi:10.1016/j.heliyon.2023.e20561

3. Labi A-K, Obeng-Nkrumah N, Owusu E, Bjerrum S, Bediako-Bowan A, Sunkwa-Mills G, et al. Multi-centre point-prevalence survey of hospital-acquired infections in Ghana. *J Hosp Infect* (2019) **101**(1):60–8. doi:10.1016/j.jhin.2018.04.019

4. WHO. Report on the burden of endemic health care-associated infection worldwide clean care is safer care (2011). Available online at: www.who.int (Accessed August 5, 2020).

5. Khan HA, Baig FK, Mehboob R. Nosocomial infections: epidemiology, prevention, control and surveillance. *Asian Pac J Trop Biomed* (2017) **7**(5):478–82. doi:10.1016/j.apjtb.2017.01.019

6. Rosenthal VD, Yin R, Nercelles P, Rivera-Molina SE, Jyoti S, Dongol R, et al. International Nosocomial Infection Control Consortium (INICC) report of health care associated infections, data summary of 45 countries for 2015 to 2020, adult and pediatric units, device-associated module. *Am J Infect Control* (2024) **52**(9):1002–11. doi:10.1016/j.ajic.2023.12.019

7. Abubakar U, Amir O, Rodríguez-Baño J. Healthcare-associated infections in Africa: a systematic review and meta-analysis of point prevalence studies. *J Pharm Policy Pract* (2022) **15**(1):1–16. doi:10.1186/s40545-022-00500-5

8. Inada M, Ishikane M, Gia Binh N, Lan Huong M, Dao XC, Thi Phuong Thuy P, et al. The epidemiology of healthcare-associated bloodstream infection in an adult intensive care unit: a retrospective cohort study in a single tertiary care hospital in hanoi, vietnam. *Cureus* (2022) **14**(11):e31879. doi:10.7759/cureus.31879

9. Sydnor ERM, Perl TM. Hospital epidemiology and infection control in acute-care settings. *Clin Microbiol Rev* (2011) **24**(1):141–73. doi:10.1128/CMR.00027-10

10. World Health Organization. *ANTIMICROBIAL RESISTANCE global report on surveillance*.

11. Vincent JL, Rello J, Marshall J, Silva E, Anzueto A, Martin CD, et al. International study of the prevalence and outcomes of infection in intensive care units. *JAMA* (2009) **302**(21):2323–9. doi:10.1001/jama.2009.1754

12. Saleem Z, Godman B, Hassali MA, Hashmi FK, Azhar F, Rehman IU. Point prevalence surveys of health-care-associated infections: a systematic review. *Pathog Glob Health* (2019) **113**:191–205. doi:10.1080/20477724.2019.1632070

13. Peterson LR. Bad bugs, No drugs: No ESCAPE revisited. *Clin Infect Dis* (2009) **49**(6):992–3. doi:10.1086/605539

14. Tacconelli E, Carrara E, Savoldi A, Harbarth S, Mendelson M, Monnet DL, et al. Discovery, research, and development of new antibiotics: the WHO priority list of antibiotic-resistant bacteria and tuberculosis. *The Lancet Infect Dis* (2018) **18**(3):318–27. doi:10.1016/s1473-3099(17)30753-3

15. Breijyeh Z, Jubeh B, Karaman R. Resistance of gram-negative bacteria to current antibacterial agents and approaches to resolve it. *Molecules* (2020) **25**(6):1340. doi:10.3390/molecules25061340

16. Founou RC, Founou LL, Essack SY. Clinical and economic impact of antibiotic resistance in developing countries: a systematic review and meta-analysis. *PLoS One* (2017) **12**(12):e0189621. doi:10.1371/journal.pone.0189621

17. Basak S, Singh P, Rajurkar M. Multidrug resistant and extensively drug resistant bacteria: a study. *J Pathog* (2016) **2016**:1–5. doi:10.1155/2016/4065603

18. Morrill HJ, Pogue JM, Kaye KS, LaPlante KL. Treatment options for carbapenem-resistant Enterobacteriaceae infections. *Open Forum Infect Dis* (2015) **2**(2):ofv050. doi:10.1093/ofid/ofv050

19. Santajit S, Indrawattana N. Mechanisms of antimicrobial resistance in ESKAPE pathogens. *Biomed Res Int* (2016) **2016**:1–8. doi:10.1155/2016/2475067

20. Santajit S, Sookrung N, Indrawattana N. *Quorum* sensing in ESKAPE bugs: a target for combating antimicrobial resistance and bacterial virulence. *Biology (Basel)* (2022) **11**(10):1466. doi:10.3390/biology11101466

21. Coleman SR, Blimkie T, Falsafi R, Hancock REW. Multidrug adaptive resistance of *Pseudomonas aeruginosa* swarming cells. *Antimicrob Agents Chemother* (2020) **64**(3):e01999. doi:10.1128/aac.01999-19

22. Pratt LA, Kolter R. Genetic analysis of *Escherichia coli* biofilm formation: roles of flagella, motility, chemotaxis and type I pili. *Mol Microbiol* (1998) **30**(2):285–93. doi:10.1046/j.1365-2958.1998.01061.x

23. O'May C, Tufenkji N. The swarming motility of *Pseudomonas aeruginosa* is blocked by cranberry proanthocyanidins and other tannin-containing materials. *Appl Environ Microbiol* (2011) **77**(9):3061–7. doi:10.1128/aem.02677-10

24. Overhage J, Bains M, Brazas MD, Hancock REW. Swarming of *Pseudomonas aeruginosa* is a complex adaptation leading to increased production of virulence factors and antibiotic resistance. *J Bacteriol* (2008) **190**(8):2671–9. doi:10.1128/jb.01659-07

25. Olsen I. Biofilm-specific antibiotic tolerance and resistance. *Eur J Clin Microbiol Infect Dis* (2015) **34**(5):877–86. doi:10.1007/s10096-015-2323-z

26. Lai S, Tremblay J, Déziel E. Swarming motility: a multicellular behaviour conferring antimicrobial resistance. *Environ Microbiol* (2009) **11**(1):126–36. doi:10.1111/j.1462-2920.2008.01747.x

27. Caiazza NC, Merritt JH, Brothers KM, O'Toole GA. Inverse regulation of biofilm formation and swarming motility by *Pseudomonas aeruginosa* PA14. *J Bacteriol* (2007) **189**(9):3603–12. doi:10.1128/jb.01685-06

28. Rütschlin S, Böttcher T. Inhibitors of bacterial swarming behavior. *Chem – A Eur J* (2020) **26**(5):964–79. doi:10.1002/chem.201901961

29. Assefa M, Amare A. Biofilm-associated multi-drug resistance in hospital-acquired infections: a review. *Infect Drug Resist* (2022) **15**:5061–8. doi:10.2147/idr.s379502

30. Ruiz L, Domínguez MA, Ruiz N, Viñas M. Relationship between clinical and environmental isolates of *Pseudomonas aeruginosa* in a hospital setting. *Arch Med Res* (2004) **35**(3):251–7. doi:10.1016/j.arcmed.2004.02.005

31. Cangui-Panchi SP, Ñacato-Toapanta AL, Enríquez-Martínez LJ, Reyes J, Garzon-Chavez D, Machado A. Biofilm-forming microorganisms causing hospital-acquired infections from intravenous catheter: a systematic review. *Curr Res Microb Sci* (2022) **3**:100175. doi:10.1016/j.crmicr.2022.100175

32. CLSI. *Clsi m100-ED29: 2021 performance standards for antimicrobial susceptibility testing*. 30th ed. Vol. 40. Clsi (2020). p. 50–1.

33. Gooderham WJ, Bains M, McPhee JB, Wiegand I, Hancock REW. Induction by cationic antimicrobial peptides and involvement in intrinsic polymyxin and antimicrobial peptide resistance, biofilm formation, and swarming motility of PsrA in *Pseudomonas aeruginosa*. *J Bacteriol* (2008) **190**(16):5624–34. doi:10.1128/jb.00594-08

34. O'Toole GA. Microtiter dish biofilm formation assay. *J Vis Exp* (2011)(47):2437. doi:10.3791/2437

35. Morales-Soto N, Anyan ME, Mattingly AE, Madukoma CS, Harvey CW, Alber M, et al. Preparation, imaging, and quantification of bacterial surface motility assays. *J Vis Exp* (2015) **2015**(98):52338. doi:10.3791/52338

36. Stepanović S, Vuković D, Hola V, Bonaventura GDI, Djukić S, Ćirković I, et al. Quantification of biofilm in microtiter plates: overview of testing conditions and practical recommendations for assessment of biofilm production by staphylococci. *APMIS* (2007) **115**(8):891–9. doi:10.1111/j.1600-0463.2007.apm_630.x

37. Skogman ME, Vuorela PM, Fallarero A. A platform of anti-biofilm assays suited to the exploration of natural compound libraries. *J Vis Exp* (2016)(118):54829. doi:10.3791/54829

38. Cruz CD, Shah S, Tammela P. Defining conditions for biofilm inhibition and eradication assays for Gram-positive clinical reference strains. *BMC Microbiol* (2018) **18**(1):173–9. doi:10.1186/s12866-018-1321-6

39. Bengtsson-Palme J, Kristiansson E, Larsson DGJ. Environmental factors influencing the development and spread of antibiotic resistance. *FEMS Microbiol Rev* (2018) **42**(1):fux053–80. doi:10.1093/femsre/fux053

40. McCarter LL. Bacterial acrobatics on a surface: swirling packs, collisions, and reversals during swarming. *J Bacteriol* (2010) **192**(13):3246–8. doi:10.1128/jb.00434-10

41. Naghavi M, Vollset SE, Ikuta KS, Swetschinski LR, Gray AP, Wool EE, et al. Global burden of bacterial antimicrobial resistance 1990–2021: a systematic analysis with forecasts to 2050. *The Lancet* (2024) **404**(10459):1199–226. doi:10.1016/s0140-6736(24)01867-1

42. Carabarin-Lima A, León-Izurieta L, Rocha-Gracia RDC, Castañeda-Lucio M, Torres C, Gutiérrez-Cazarez Z, et al. First evidence of polar flagella in *Klebsiella pneumoniae* isolated from a patient with neonatal sepsis. *J Med Microbiol* (2016) **65**(8):729–37. doi:10.1099/jmm.0.000291

43. Kim W, Surette MG. Swarming populations of Salmonella represent a unique physiological state coupled to multiple mechanisms of antibiotic resistance. *Biol Proced Online* (2003) **5**(1):189–96. doi:10.1251/bpo61

44. Tipton KA, Dimitrova D, Rather PN. Phase-variable control of multiple phenotypes in Acinetobacter baumannii strain AB5075. *J Bacteriol* (2015) **197**(15):2593–9. doi:10.1128/jb.00188-15

45. Tipton KA, Rather PN. An ompRenvZ two-component system ortholog regulates phase variation, osmotic tolerance, motility, and virulence in Acinetobacter baumannii strain AB5075. *J Bacteriol* (2017) **199**(3):e00705. doi:10.1128/jb.00705-16

46. Jeong GJ, Khan F, Tabassum N, Kim YM. Motility of Acinetobacter baumannii: regulatory systems and controlling strategies. *Appl Microbiol Biotechnol* (2024) **108**(1):3–13. doi:10.1007/s00253-023-12975-6

47. Zegadło K, Gieroń M, Żarnowiec P, Durlik-Popińska K, Kręcisz B, Kaca W, et al. Bacterial motility and its role in skin and wound infections. *Int J Mol Sci* (2023) **24**(2):1707. doi:10.3390/ijms24021707

48. de Sousa T, Hébraud M, Alves O, Costa E, Maltez L, Pereira JE, et al. Study of antimicrobial resistance, biofilm formation, and motility of *Pseudomonas aeruginosa* derived from urine samples. *Microorganisms* (2023) **11**(5):1345. doi:10.3390/microorganisms11051345

49. Winstanley C, O'Brien S, Brockhurst MA. *Pseudomonas aeruginosa* evolutionary adaptation and diversification in cystic fibrosis chronic lung infections. *Trends Microbiol* (2016) **24**(5):327–37. doi:10.1016/j.tim.2016.01.008

50. Butler MT, Wang Q, Harshey RM. Cell density and mobility protect swarming bacteria against antibiotics. *Proc Natl Acad Sci* (2010) **107**(8):3776–81. doi:10.1073/pnas.0910934107

51. Černohorská L, Votava M. Determination of minimal regrowth concentration (MRC) in clinical isolates of various biofilm-forming bacteria. *Folia Microbiol (Praha)* (2004) **49**(1):75–8. doi:10.1007/bf02931650

52. Aka ST, Haji SH. Sub-MIC of antibiotics induced biofilm formation of *Pseudomonas aeruginosa* in the presence of chlorhexidine. *Braz J Microbiol* (2015) **46**(1):149–54. doi:10.1590/s1517-838246120140218

53. Field D, Seisling N, Cotter PD, Ross RP, Hill C. Synergistic nisin-polymyxin combinations for the control of pseudomonas biofilm formation. *Front Microbiol* (2016) **7**(OCT):1713. doi:10.3389/fmicb.2016.01713

54. Linares JF, Gustafsson I, Baquero F, Martinez JL. Antibiotics as intermicrobial signaling agents instead of weapons. *Proc Natl Acad Sci U S A* (2006) **103**(51):19484–9. doi:10.1073/pnas.0608949103

55. O'Brien J, Wilson I, Orton T, Pognan F. Investigation of the Alamar Blue (resazurin) fluorescent dye for the assessment of mammalian cell cytotoxicity. *Eur J Biochem* (2000) **267**(17):5421–6. doi:10.1046/j.1432-1327.2000.01606.x

56. Van den Driessche F, Rigole P, Brackman G, Coenye T. Optimization of resazurin-based viability staining for quantification of microbial biofilms. *J Microbiol Methods* (2014) **98**(1):31–4. doi:10.1016/j.mimet.2013.12.011

57. Jorge P, Grzywacz D, Kamysz W, Lourenço A, Pereira MO. Searching for new strategies against biofilm infections: colistin-AMP combinations against *Pseudomonas aeruginosa* and *Staphylococcus aureus* single- and double-species biofilms. *PLoS One* (2017) **12**(3):e0174654. doi:10.1371/journal.pone.0174654

58. Reffuveille F, de la Fuente-Núñez C, Mansour S, Hancock REW. A broad-spectrum antibiofilm peptide enhances antibiotic action against bacterial biofilms. *Antimicrob Agents Chemother* (2014) **58**(9):5363–71. doi:10.1128/aac.03163-14

59. Mah TFC, O'Toole GA. Mechanisms of biofilm resistance to antimicrobial agents. *Trends Microbiol* (2001) **9**:34–9. doi:10.1016/s0966-842x(00)01913-2

60. Werner E, Roe F, Bugnicourt A, Franklin MJ, Heydorn A, Molin S, et al. Stratified growth in *Pseudomonas aeruginosa* biofilms. *Appl Environ Microbiol* (2004) **70**(10):6188–96. doi:10.1128/aem.70.10.6188-6196.2004

61. Mirghani R, Saba T, Khaliq H, Mitchell J, Do L, Chambi L, et al. Biofilms: formation, drug resistance and alternatives to conventional approaches. *AIMS Microbiol* (2022) **8**(3):239–77. doi:10.3934/microbiol.2022019

EBM Experimental Biology and Medicine

TYPE Review
PUBLISHED 09 June 2025
DOI 10.3389/ebm.2025.10330

OPEN ACCESS

*CORRESPONDENCE
Peng Fu,
pfu@hust.edu.cn

RECEIVED 31 July 2024
ACCEPTED 14 May 2025
PUBLISHED 09 June 2025

CITATION
Zheng H, Zhang D, Xiang W, Gan Y, Peng Z, Wu Y and Fu P (2025) Deep brain stimulation for dystonia treatment in cerebral palsy: efficacy exploration. *Exp. Biol. Med.* 250:10330. doi: 10.3389/ebm.2025.10330

Deep brain stimulation for dystonia treatment in cerebral palsy: efficacy exploration

Haoyang Zheng[1], Duo Zhang[2], Wei Xiang[1], Yong Gan[3], Zesheng Peng[1], Yuyi Wu[1] and Peng Fu[1]*

[1]Department of Neurosurgery, Union Hospital, Tongji Medical College, Huazhong University of Science and Technology, Wuhan, China, [2]Department of Nursing, Tongji Hospital, Tongji Medical College, Huazhong University of Science and Technology, Wuhan, Hubei, China, [3]Department of Social Medicine and Health Management, School of Public Health, Tongji Medical College, Huazhong University of Science and Technology, Wuhan, China

Abstract

Dystonia, a challenging movement disorder, poses significant therapeutic challenges due to its resistance to treatment, resulting in both physical impairment and substantial mental distress, ultimately impacting overall quality of life. Cerebral palsy (CP) is a major non-genetic cause of secondary dystonia, characterized by diverse clinical presentations. This study aims to comprehensively evaluate the effectiveness of deep brain stimulation (DBS) as a therapeutic intervention for individuals with dystonic CP. We conducted a systematic analysis of studies assessing the safety and effectiveness of DBS, with a focus on its long-term outcomes [PROSPERO (Unique identifier: CRD42023399285)]. We examined factors that influence treatment response and proposed strategies to enhance patient quality of life. DBS, especially when targeting the basal ganglia or innovative targets, shows promise as a therapeutic approach for dystonic CP. While existing controlled studies confirm its safety and effectiveness, a thorough evaluation of long-term efficacy remains crucial. This research highlights the potential of DBS in improving the lives of individuals with dystonic CP, providing hope for further refinement, innovation, and broader clinical application of this therapeutic approach.

KEYWORDS

dystonia, cerebral palsy, deep brain stimulation, functional neurosurgery, movement disorders

Impact statement

This work is crucial to the field because dystonia, especially in the context of cerebral palsy (CP), presents significant therapeutic challenges due to its resistance to conventional treatments, leading to severe physical impairment and mental distress. Our study advances the field by providing a comprehensive evaluation of deep brain stimulation (DBS) as a therapeutic intervention for dystonic CP, emphasizing long-term outcomes. By systematically analyzing studies on the safety and effectiveness of DBS, and examining

factors influencing treatment response, this research introduces new insights into optimizing DBS for better patient outcomes. The findings suggest that DBS, particularly targeting the basal ganglia or innovative targets, holds significant promise in improving the quality of life for individuals with dystonic CP. This new information could guide further refinement and broader clinical application of DBS, potentially revolutionizing treatment strategies for dystonic CP and offering new hope to affected individuals.

Introduction

Dystonia is a movement disorder characterized by sustained or intermittent involuntary muscle contractions, which result in abnormal and repetitive movements or postures in affected individuals [1]. It is considered the third most common movement disorder, following Parkinson's disease and essential tremor, with an estimated overall prevalence of 601.1 per million [2]. Typically, dystonia is triggered or worsened by voluntary actions and is associated with overflow muscle activation. This disorder can present a range of challenges, including pain, depressive symptoms, anxiety, social stigmatization, and reduced self-esteem, ultimately leading to a compromised health-related quality of life [3]. Depending on its underlying cause, dystonia can manifest as primary, hereditary, or idiopathic, or it can occur as a secondary consequence of various neurological or systemic disorders [4].

Dystonia can be divided into two main subtypes based on clinical manifestations: motor dystonia and postural dystonia. Motor dystonia is characterized by abnormal muscle tension during movement, resulting in involuntary twitches and tremors across various body regions. These movements can occur intermittently or continuously and often worsen during voluntary actions, affecting motor function and causing dyskinesia. Motor dystonia includes a wide range of movement patterns, from focal (affecting a specific body part) to generalized (involving multiple body regions). Examples of motor dystonia include writer's cramp (focal hand dystonia), cervical dystonia (involving neck muscles), and generalized dystonia (affecting various body regions). Some forms of motor dystonia are specific to certain tasks, such as musician's dystonia when playing a musical instrument. On the other hand, postural dystonia is characterized by atypical and sustained postures without the repetitive muscle movements seen in motor dystonia. These postures are often involuntary and can cause discomfort and pain. They typically remain stable over time and occur in specific postures. Common examples of postural dystonia are camptocormia (forward bending of the trunk), Pisa syndrome (lateral bending of the trunk), and anterocollis (forward flexion of the neck). These postures become more pronounced when the individual tries to stand or walk. Postural dystonia significantly affects an individual's stability and balance, making it challenging to maintain an upright posture or engage in daily activities. In summary, both conditions have a significant impact on an individual's quality of life, requiring management strategies that may include physical therapy, medication, and other interventions tailored to the specific dystonic symptoms.

Cerebral palsy (CP) is the most common condition associated with dystonia in children, often resulting from brain injury due to complications of prematurity, stroke, or hypoxic-ischemic encephalopathy [5]. The incidence of CP was 1.77 per 1,000 live births, and it was commonly accompanied by other conditions such as seizures, communication disorders, hearing and visual impairments, and intellectual disabilities [6]. Dystonia significantly affects various aspects of well-being in the CP population, including motor function, emotional balance, and Health-Related Quality of Life (HRQoL). Many patients experience severe physical disabilities due to abnormal movements, posturing, and musculoskeletal deformities [7].

CP is the most common non-genetic condition associated with secondary dystonia, and its clinical management presents significant challenges [8]. The main goals in treating dystonia associated with CP are to reduce dystonic symptoms, improve functional capacity, relieve pain, and enhance overall care [9]. Traditional approaches, such as medication and physical therapies, often produce unsatisfactory results. On the other hand, deep brain stimulation (DBS) has emerged as a key intervention for cases that do not respond to medical treatment [10]. DBS improves dystonic symptoms by electrically modulating abnormal neuronal signals in the basal ganglia's output structure. This modulation has the potential to restore more effective signal transmission in the cortico-basal ganglia circuit, thereby reducing abnormal cortical excitability and normalizing synaptic plasticity in the motor cortex [11]. Recent studies have shown that DBS is significantly effective in myoclonus dystonia and tardive dystonia, which are types of primary dystonia [12]. However, the effectiveness of DBS in secondary dystonia is still being investigated and varies in different cases.

This review aims to provide a comprehensive evaluation of the impact of DBS surgery on the prognosis of functional adaptation in individuals with secondary dystonia associated with CP. In order to accomplish this, we have synthesized and analyzed the neurophysiological mechanisms, therapeutic effectiveness, factors influencing outcomes, and strategies for enhancing the results of DBS treatment in this particular group of patients.

Neurophysiological mechanisms of DBS in dystonia management

The general concept of DBS is that high-frequency stimulation modulates abnormal neural activity and trains it

into a pattern of normative behavior, with the possible mechanism being an inhibitory neuronal effect of the pulses on the somata. The inhibitory effect may manifest as a direct result of depolarization block, a phenomenon mediated by mechanisms that encompass sodium channel inactivation and augmentation of potassium currents. Furthermore, DBS may also increase and normalize signal output in the stimulated area by activating local axons [13]. Therefore, a thorough understanding of the neurophysiological basis of dystonia is essential for the development of DBS and new therapeutic approaches.

CP results from damage to the developing brain during pregnancy, birth, or early childhood. This damage affects important brain regions responsible for motor control, including the motor cortex, basal ganglia, cerebellum, and thalamus. Specific anatomic lesions are often found in CP, including diffuse cortical dysplasia and atrophic lobar sclerosis. These lesions can be observed as scattered scar-like marks resembling marbling within the cortex and basal nuclei. The regulation of normal muscle tone hinges on the dynamic balance between the inhibitory effect of descending cortical fibers and the facilitatory effect of peripheral afferent fibers. When brain injuries disrupt the descending cortical fiber tracts, this balance is disturbed. As a result, the inhibitory effect weakens, and the excitatory influence of peripheral afferent fibers becomes more prominent. Clinically, this disruption presents as spastic dyskinesia and postural anomalies.

In the past, dystonia was primarily believed to be caused by dysfunction in the basal ganglia. However, a new perspective suggests that other areas of the brain may also be involved. According to the emerging network model, dystonia can result from dysfunction in different parts of the brain network, dysfunction across multiple nodes, or abnormal communication between nodes [14]. The current evidence supports the idea that dystonia is a circuit disorder that affects the basal ganglia-thalamo-cortical and cerebello-thalamo-cortical pathways. This includes various regions such as the deep cerebellar nuclei, cerebellar cortex, pontine nuclei, basal ganglia, subthalamic nucleus, thalamus, and cerebral cortex [15].

The basal ganglia, a cluster of nuclei located deep within the brain, are widely acknowledged to play a pivotal role in the pathophysiology of dystonia arising from CP. In individuals with CP, damage to the basal ganglia leads to abnormal neuronal firing patterns and a compromised ability to inhibit unwanted movements. These nuclei are involved in various critical functions, including motor control, learning, cognition, motivation, emotion, and social behavior. The basal ganglia consist of the striatum, globus pallidus, subthalamic nucleus (STN), substantia nigra, and pedunculopontine nucleus (PPN). The cerebral cortex communicates with the basal ganglia through the corticostriatal pathway, which includes both the direct and indirect pathways [16]. The direct pathway projects from the striatum to the substantia nigra pars reticulata (SNr) and the globus pallidus interna (GPi), while the indirect pathway projects to SNr and GPi through the globus pallidus pars externa (GPe) and STN [17]. Additionally, there is growing evidence that cerebellar dysfunction may also contribute to the development of dystonia in CP. The cerebellum is involved in motor functions such as coordination, balance, and posture, as well as non-motor functions like language, social cognition, and emotion [18–21]. It has connections with the thalamus, vestibular nuclei, and inferior olive through monosynaptic projections. There are also polysynaptic short-latency connections between the cerebellum and key structures, including the basal ganglia [22]. This interconnectedness provides a basis for using DBS stimulation of the cerebellum in dystonia treatment, considering its anatomical and pathophysiological relationship with nuclei like the basal ganglia and thalamus.

Distinctions in the neurophysiological underpinnings of motor dystonia and postural dystonia are apparent. Motor dystonia primarily involves dysfunction within the basal ganglia, which plays a crucial role in motor regulation. Abnormalities in the basal ganglia can result in difficulties initiating and controlling voluntary movements. The connection between the basal ganglia and the cerebral cortex is essential for coordinating motor actions. The disrupted interaction between these regions is believed to contribute to the development of motor dystonia. On the other hand, postural dystonia focuses more on maintaining specific body positions rather than executing discrete movements. Postural dystonia often involves abnormalities in muscle tone regulation, leading to sustained muscle contractions and abnormal postures. In the case of postural dystonia, dysfunction of the direct pathway causes rigid hypertonia in childhood due to disinhibition of descending basal ganglia output [17]. Dysfunctions in the feedback loop between the sensory system, responsible for providing information about body position, and the motor system may have a stronger impact on postural dystonia. Although the cerebellum, located at the back of the brain, is not the primary area involved, abnormalities in this region can also contribute to postural dystonia. It is important to note that these are general descriptions, and there is a wide range of subtypes and variations within both motor and postural dystonia. Therefore, the specific causes and anatomical irregularities can vary considerably depending on the individual and the particular manifestation of dystonia they present.

The motor circuits involved in dystonia due to CP are highly complex and involve multiple regions within the brain. The basal ganglia, cerebellum, and cerebral cortex work together as an interconnected network, with the basal ganglia-to-cerebellum pathway playing a significant role in the manifestation of dystonic movements. Further research is needed to gain a better understanding of the underlying mechanisms and to develop effective therapeutic interventions for this condition.

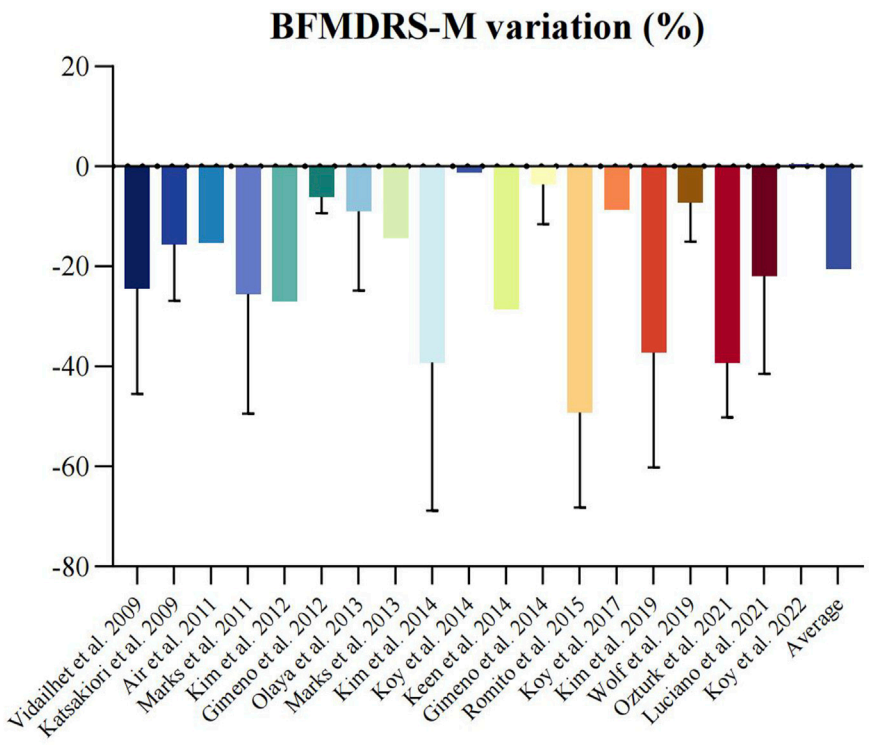

FIGURE 1
Forest plot of random effects meta-analysis of non-randomized studies reporting on dystonia before and after deep brain stimulation. Mean difference across studies reporting on BFMDRS-M scales.

Efficacy of DBS in treating dystonia in CP

A comprehensive literature review was performed using the Web of Science and PubMed database to identify relevant English-language articles published until 1 June 2024. The retrieval details have been registered at PROSPERO (CRD42023399285). Search terms included cerebral palsy, secondary dystonia, and deep brain stimulation. Supplementary Material S1 provides detailed criteria and statistical methods. Each article was meticulously scrutinized for patient-centric information. The clinical outcomes were commonly evaluated using the Burke-Fahn-Marsden Dystonia Rating Scale Movement (BFMDRS-M) score [23].

Twenty-one non-randomized studies [7, 24–43] assessed the efficacy of DBS using the BFMDRS-M scores. A meta-analysis of 19 studies [7, 24–40, 43] (n = 148) showed that DBS significantly improved dystonia due to CP (SMD 14.90; 95% CI 11.13 to 18.67; Figure 1). The mean BFMDRS-M score was 73.74 ± 25.23 before the procedure and 60.10 ± 29.06 after the procedure, indicating an overall improvement of 20.46% ($P < 0.001$). Except for the study by Koy et al., all studies reported the effectiveness of DBS in reducing motor symptoms of dystonia. However, the degree of improvement varied considerably across the studies, with a range of 1.23%–49.22% reduction in the BFMDRS-M score (Figure 2). While the overall effect observed in the forest plot supports a beneficial role for DBS in CP-associated dystonia, the heterogeneity among studies was not negligible (Chi-square $p = 0.01$, $I^2 = 46\%$). Although an I^2 value below 50% is often interpreted as low, in this context it may represent moderate heterogeneity. Potential sources of variability include differences in DBS implantation techniques, stimulation parameters, patient selection criteria, and outcome assessment methods. To account for this clinical and methodological variability, a random-effects model was employed in our meta-analysis. This approach provides a more conservative and robust estimate of treatment effect in the presence of heterogeneity, thereby strengthening the validity of the overall findings despite inter-study differences.

Three additional studies were evaluated but not included in the meta-analysis. Lin et al. reported a case of CP with severe dystonia in a 21-year-old female due to hypoxia at birth [42]. The patient did not benefit from GPi DBS surgery and was subsequently treated with high-frequency DBS on superior cerebellar peduncles (SCPs). After 6 months of follow-up, there was a reported improvement of 36.4% in the BFMDRS-M score (pre-operation = 93.5, post-operation = 59.5). Kim et al. conducted a study comparing bilateral GPi DBS with GPi DBS plus unilateral thalamotomy in 10 adult patients with CP [41].

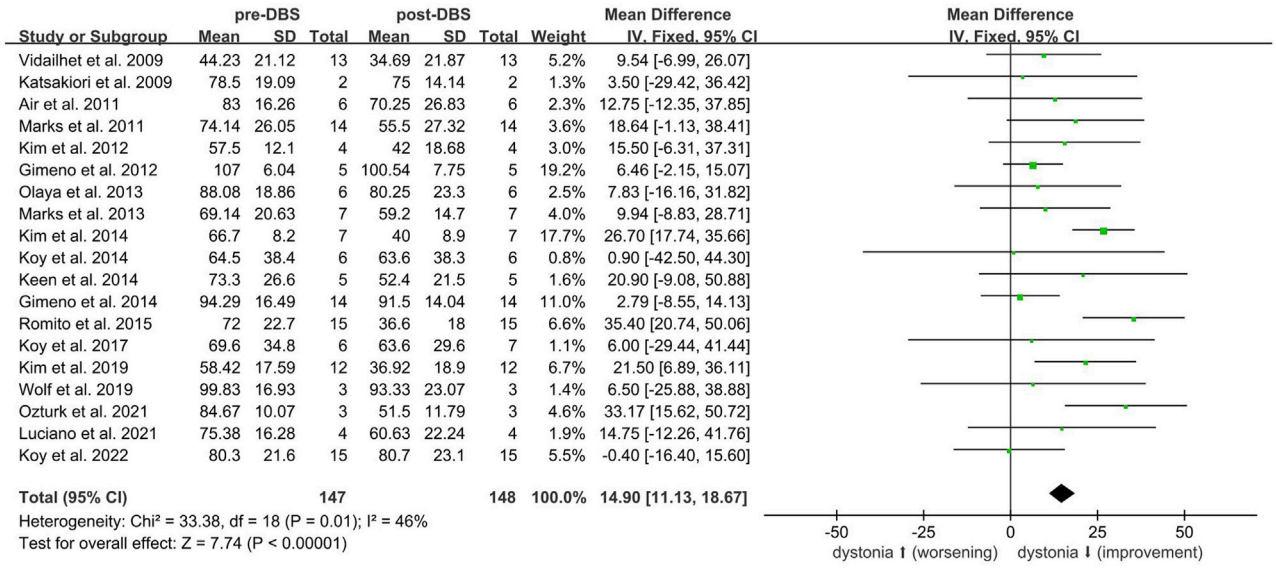

FIGURE 2
BFMRS-M scales variations in the individual studies on DBS in cerebral palsy. Negative values represent improvement. Standard error bars are showed.

The results did not show any significant improvement in the overall BFMDRS score between the two groups. Romina et al. reported a decrease in mean BFMDRS-M after 12 months of DBS implantation, but no change in individual patients [44]. Romina's study employed a within-subject design comparing pre- and post-operative outcomes without including an external control group, making it incompatible with the meta-analysis criteria. Galanda et al. reported positive improvements in posture and spasticity in CP patients through anterior cerebellar stimulation [45].

Factors influencing the efficacy of DBS

While patients with dystonia due to CP may potentially benefit from DBS, it is generally believed that the response to DBS treatment in CP patients with dystonia is not as favorable as in patients with idiopathic or genetic dystonia. This observation is particularly noteworthy considering the greater variability associated with acquired dystonia compared to its inherited or idiopathic counterparts [38, 46, 47]. The poorer response in patients with acquired dystonia is thought to be attributed to brain network damage, which limits the effectiveness of neuromodulation [48]. Therefore, there is a critical clinical need to identify prognosis and clinical predictors of surgical intervention for dystonia patients undergoing DBS in order to improve treatment outcomes.

Demographic criteria

In a recent meta-analysis, it was found that disease duration and age at surgery were weakly negatively associated with percent improvements in BFMDRS scores, as measured by the Pearson correlation coefficient. Through stepwise multiple regression analysis, only disease duration was identified as a significant predictor ($\beta = -0.165$, $P = 0.006$). This finding highlights the positive correlation between shorter disease duration and greater efficacy of DBS treatment. On the other hand, factors such as age at onset, follow-up period, and BFMDRS motor and disability scores at baseline were found to have no association with the clinical outcomes [49]. In contrast, Romina et al. suggested that the age of dystonia onset was related to DBS response, with less favorable results in early-onset forms [44]. Additionally, Isaias et al. found that disease duration and age at operation exhibited a significant negative correlation with DBS outcomes [50].

Structural brain lesions

The depiction of the brain on the preoperative magnetic resonance imaging (MRI) scan was an essential predictor for a favorable surgical response [47]. Researchers found a significant difference in Global Outcome Scale (GOS) scores between patients with normal and abnormal MRI scans, indicating that those with normal scans had a better prognosis. Elkaim et al. also emphasized that the presence of underlying brain pathology—whether inherited or acquired—is associated with

less favorable DBS outcomes in pediatric patients. In their analysis, brain pathologies such as pantothenate kinase-associated neurodegeneration, Lesch-Nyhan disease, and choreiform athetosis were discussed as examples of conditions linked to reduced therapeutic efficacy [51].

Target selection for DBS

The choice of target and the success of DBS treatment depend on the precise diagnosis, individual's condition, and expertise of the neurosurgical team. When selecting targets for DBS surgery to treat dystonia, the most commonly used nucleus is GPi. This nucleus is generally applicable to both primary and secondary dystonia [52]. As the principal output structure of the basal ganglia, the GPi primarily projects to the thalamus and midbrain, allowing it to control contralateral limb movement [53]. However, regulating all parts of the GPi and associated globus pallidus circuits can be challenging due to the large size and potential structural abnormalities of the GPi. This is particularly true for patients with perinatal injuries, such as those with CP [41]. As a result, alternative targets such as STN, ventral intermediate nucleus (Vim), ventralis oralis anterior (Voa), ventralis oralis posterior (Vop), and PPN have been proposed for CP patients with severe dystonia [31, 40, 54].

In a recent meta-analysis, patients who underwent GPi-DBS and STN-DBS showed significant improvements in movement symptoms, disability symptoms, 36-item Short Form Health Survey (SF-36) scores, and Beck Depression Inventory (BDI) scores [55]. Although the mean movement and disability scores were slightly higher in the STN group compared to the GPi group, the difference was not statistically significant. STN-DBS helps regulate abnormal activity patterns in the basal ganglia, leading to improved motor control. The STN is located upstream of the GPi in the motor circuit of the basal ganglia, suggesting that stimulation of the STN may be more effective than stimulation of GPi [52]. Schjerling et al. found that BFMDRS-M scores improved by 13.8 points with STN stimulation and 9.1 points with GPi stimulation after 6 months of follow-up ($p = 0.08$) [56]. Lin et al. also reported a significantly larger percentage improvement in the BFMDRS total movement score after 1 month of follow-up with STN-DBS (64%) compared to GPi-DBS (48%) ($p = 0.01$) [57]. Although the STN has shown promise as a potential target for DBS in certain movement disorders, its small size and deep anatomical location make accurate localization more challenging, especially in pediatric patients. Additionally, the STN has been less extensively investigated in this population, whereas the GPi remains the most well-established and commonly used target with a more robust evidence base supporting its efficacy.

The Voa and Vop serve as the principal outputs of the globus pallidus, receiving retroactive feedback from the motor cortex. Thalamic DBS intervenes in the tremor circuitry, reducing or eliminating tremors. In individuals with dystonia, the neuronal firing of the ventralis oralis occurs at the same frequency as the STN and GPi. These aberrant neuronal activities can be inhibited or modulated by DBS or lesioning [58]. Katsakiori et al. documented a favorable functional outcome in a patient with secondary dystonia who underwent Voa-DBS [27]. Additionally, Ghika et al. reported significant improvement in a patient with dystonia after systemic hypoxia who was treated with GPi and Voa stimulation, specifically after Voa-DBS surgery [59]. Previous studies have shown that around 83% of dystonic-related activity is located in the Vim region, which is likely associated with the upper limb [58]. Kim et al. demonstrated that patients who underwent GPi plus Vim DBS had significantly improved movement in the contralateral upper limb and better health-related quality of life compared to patients who underwent GPi surgery alone [31]. Dual-target DBS, particularly combining the thalamus with either the GPi or subthalamic nucleus, has shown superior efficacy in managing coexisting dystonia and tremor compared to single-target approaches. Previous study reported that Vim DBS provided an 85% tremor reduction but limited dystonia relief, while GPi DBS achieved 64% improvement in dystonia with only 40% tremor reduction [60]. Several patients required subsequent implantation of a second target (Vim or GPi) to manage residual symptoms, suggesting a complementary effect of these targets. Objective motion assessments further supported greater tremor control with combined stimulation compared to either target alone. These findings, though based on limited case series, highlight the potential of dual-target DBS to optimize outcomes in patients with complex movement disorders involving both tremor and dystonia.

The cerebellum has shown promise as a potential therapeutic target for individuals with CP. According to Dr. Ross Davis, 600 patients with CP have received cerebellar stimulation treatment, resulting in improvement for about two-thirds to three-quarters of the patients. Additionally, at least 50% of the patients experienced a reduction in spasticity of more than 20% [61]. A case study conducted by Stroud et al. also demonstrated significant benefits from cerebellar cortical stimulation, leading to a more than 50% decrease in BFMDRS-M scores for a patient with acquired dystonia [62]. Another study has reported four cases of cerebellar DBS with functional improvement that might be useful in the specific population of patients with dystonia [45]. Furthermore, DBS targeting the PPN shows promise in addressing locomotion and balance issues, potentially improving gait-related problems [54].

Stimulation programming

Stimulation programming in patients with CP showed significant heterogeneity. While there is no consensus on the optimal stimulation settings, several advanced programming approaches can potentially maximize clinical benefit [63]. A recent meta-analysis provided the average stimulation

parameters for STN-DBS for acquired dystonia, including an amplitude of 2.56 ± 0.73 V, pulse width of 100.61 ± 40.62 μs, and frequency of 143.79 ± 34.87 Hz [64]. Additionally, Magown et al. reported prevalent stimulation parameters for CP patients, with an amplitude of 3.0 V, frequency of 130 Hz, and pulse width of 120 μs. [65]. Moro et al. emphasized that frequency and amplitude were crucial factors in determining the clinical benefit of GPi-DBS [66]. In addition, the marginal effects of interleaving stimulation (a programming strategy that alternates stimulation between two sets of contacts to optimize therapeutic benefit) in reducing adverse effects and enhancing clinical outcomes were evident [67].

Follow-up and long-term care

Regular follow-up appointments with the healthcare team are important for monitoring progress, making any necessary adjustments to the stimulation parameters, and addressing any issues that may arise [68]. The overall success of DBS interventions is significantly influenced by the patient's psychological and emotional well-being, as well as the support system. Research studies have indicated that music, when used as a complementary form of therapy, can assist individuals with CP in overcoming emotional challenges and reducing levels of anxiety and pain [69]. After 30 min of intervention, the modified Yale preoperative anxiety scale for children's anxiety score of the music group was significantly lower than that of the control group ($t = 4.72$, $P = 0.00$).

Measures to improve the efficacy of DBS

Comprehensive patient assessment and appropriate patient selection

A thorough assessment is essential in confirming the diagnosis of dystonia and evaluating the severity, type, and distribution of symptoms. Motor dystonia is characterized by abnormal movements, often associated with dysfunction in the basal ganglia and cerebral cortex, which can result in difficulties initiating and controlling voluntary movements. On the other hand, postural dystonia primarily involves maintaining abnormal bodily positions, possibly due to irregular muscle tone and disrupted sensory feedback mechanisms, with potential involvement from the cerebellum. It is crucial to determine the specific type of dystonia exhibited by the patient. Candidates eligible for surgical intervention are those who have not responded adequately to other treatments, are medically suitable for surgery, and have realistic expectations regarding potential outcomes.

Advancements in imaging modalities

Most patients with dystonia do not have significant lesions on routine clinical imaging. However, the application of comprehensive imaging techniques such as positron emission tomography and MRI have revealed subtle quantitative abnormalities that are crucial for ensuring precise and safe electrode implantation [70]. With advancements in imaging modalities, diffusion tensor imaging (DTI) has become a valuable tool for visualizing white matter tracts formed by axonal projections of cortical and subcortical neurons *in vivo*. This allows for better optimization of DBS electrodes and stimulation paradigms, focusing on tract stimulation rather than deep brain nuclei introduction [71]. The White Matter Attenuated Inversion Recovery (WAIR) sequence is particularly useful in targeting the normally MRI-indistinguishable VIM, providing accurate preoperative planning, direct targeting, and anatomical analysis for DBS surgery [72]. Additionally, it is important to ensure that the electrodes reach the optimal depth for effective response to stimulation. Deviating more than 2 mm from the intended target can significantly impair treatment effectiveness or require higher stimulus energy, leading to intolerable adverse reactions [63]. Therefore, obtaining high-quality preoperative and intraoperative MRI images is crucial for optimizing the efficacy of DBS procedures.

Optimal target selection for DBS intervention

The determination of the optimal target for deep brain stimulation (DBS) for dystonia is dependent on a comprehensive assessment of individual cases. This assessment considers factors such as the specific type and distribution of dystonia, previous responses to medications and other treatments, unique patient attributes, and surgical expertise. The GPi is the primary target for dystonia, as it is involved in both motor and postural dystonia through basal ganglia pathways. By modulating activity in this region, DBS can improve motor control and reduce abnormal movements. STN is less frequently used for dystonia. However, existing literature suggests that it may be more effective in certain specific circumstances and should be considered accordingly. In cases of postural dystonia, especially when tremor is a significant component of the condition, targeting the thalamus, specifically the Vim, may be a relevant consideration.

Pharmacological administration

Besides DBS surgery to treat dystonia in patients with CP, there are various pharmacological management options that can be used in conjunction with surgical therapy. These options aim to preserve or restore function, relieve abnormal posture, and

minimize pain [73]. Despite Multiple medications have been evaluated, including oral baclofen, benzodiazepines, clonidine, gabapentin, levodopa, benzhexol, botulinum toxin, and intrathecal baclofen (ITB), the availability of high-quality evidence remains limited [74]. Currently, existing evidence does not strongly support the use of oral medications or botulinum toxin alone to effectively reduce dystonia in individuals with CP, likely due to the complex and multifactorial nature of dystonic pathophysiology. Among neurosurgical alternatives, ITB has shown promise, particularly in reducing spasticity and associated symptoms. ITB may be considered a secondary option for patients who do not experience adequate symptom control following DBS. However, due to the considerable heterogeneity in treatment response among patients with CP, these conclusions should be interpreted with caution. Further well-designed clinical trials are needed to clarify the optimal therapeutic approaches for this population.

Long-term DBS management

The programming of DBS can begin immediately after confirming the correct position of the DBS lead and ensuring there are no complications from the procedure. Alternatively, it can be initiated several weeks after surgery to address potential improvements related to the effects of lead insertion [75]. Despite the lack of consensus on the best stimulation parameters, it is highly recommended to take a systematic approach to optimize these settings [76]. Fine-tuning the parameters based on patient feedback and clinical assessment is an ongoing process. Real-time recording of neurophysiological biomarkers based on the patient's clinical status can be used to optimize stimulation parameters according to individual needs [77]. Specialized visualization software can estimate the volume of activated tissue and assist in programming by visualizing activation maps based on pre-defined target maps [78]. The response to DBS in patients with CP varies greatly, and dystonic symptoms often continue to progress and fluctuate during the follow-up period after DBS. Alongside the long-lasting effectiveness of DBS in treating dystonia, there have been cases of worsening symptoms and tolerance to treatment, necessitating staged or rescue DBS interventions. Post-surgery, intensive rehabilitation and physical therapy should be provided to help patients maximize their improved motor abilities. In the field of nursing, the phenomenological interview and theoretical tools of phenomenology are used to gain a deeper understanding of the lives of CP patients [79]. Caregivers should approach these interviews with an open and empathetic attitude, aiming to establish a foundation of trust with the interviewee. It is crucial for the caregiver to actively engage with the interviewee, encouraging them to provide detailed descriptions that are relevant to their experiences. The provision of comprehensive care, led by a multidisciplinary team including neurologists, neurosurgeons, neuropsychiatrists, nurses, and rehabilitation specialists, is crucial for delivering holistic care and achieving optimal outcomes. Therefore, the long-term management of DBS is a dynamic process that requires collaborative efforts between healthcare professionals, patients, and their caregivers.

Conclusion

DBS has proven to be an effective therapeutic intervention for dystonia in selected patients with CP. However, the clinical response to DBS can vary significantly depending on several factors, including disease duration, the presence of structural brain abnormalities, target site selection, stimulation programming, and the quality of long-term multidisciplinary care. Optimizing DBS outcomes requires continuous advancements in neuroimaging technologies, thorough patient selection and evaluation, tailored pharmacological management, and close collaboration between patients, caregivers, and healthcare professionals. A personalized, patient-centered approach—alongside regular assessment and adjustment—is essential to achieving the best possible clinical results. Promising innovations such as brain sensing, closed-loop DBS, and remote programming offer significant potential to further improve motor symptoms and enhance quality of life in CP patients. Nevertheless, to fully elucidate the therapeutic role of DBS in dystonic CP, further research is warranted. In particular, prospective cohort studies with large sample sizes conducted under standardized protocols and using a multidimensional assessment framework are needed to systematically evaluate the impact of DBS on both motor function and quality of life.

Author contributions

HZ and PF conceptualized and designed the study, made significant contributions to the drafting of the manuscript, and provided final approval to ensure the accuracy of the work. HZ and DZ conducted the research, while HZ, YG, and DZ were involved in the data analysis. WX, YW, and YG provided guidance to ensure the accuracy of the work. WX and PF supervised the entire research process. All authors contributed to the article and approved the submitted version.

Funding

The author(s) declare that financial support was received for the research and/or publication of this article. The research was supported by National Natural Science Foundation of China (82272884 and 82472953) and Natural Science Foundation of Hubei Province (2022CFBO49).

Conflict of interest

The author(s) declared no potential conflicts of interest with respect to the research, authorship, and/or publication of this article.

Supplementary material

The Supplementary Material for this article can be found online at: https://www.ebm-journal.org/articles/10.3389/ebm.2025.10330/full#supplementary-material

References

1. Albanese A, Bhatia K, Bressman SB, Delong MR, Fahn S, Fung VS, et al. Phenomenology and classification of dystonia: a consensus update. *Movement Disord* (2013) **28**:863–73. doi:10.1002/mds.25475

2. Dressler D, Altenmuller E, Giess R, Krauss JK, Adib Saberi F. The epidemiology of dystonia: the Hannover epidemiology study. *J Neurol* (2022) **269**:6483–93. doi:10.1007/s00415-022-11310-9

3. Tsuboi T, Wong JK, Okun MS, Ramirez-Zamora A. Quality of life outcomes after deep brain stimulation in dystonia: a systematic review. *Parkinsonism and Relat Disord* (2020) **70**:82–93. doi:10.1016/j.parkreldis.2019.11.016

4. Tai CH, Chou SC, Lin CH, Lee WT, Wu RM, Tseng SH. Long-term outcomes of idiopathic and acquired dystonia after pallidal deep brain stimulation: a case series. *World Neurosurg* (2022) **167**:E575–e582. doi:10.1016/j.wneu.2022.08.053

5. Pearson TS, Pons R. Movement disorders in children. *CONTINUUM: Lifelong Learn Neurol* (2019) **25**:1099–120. doi:10.1212/con.0000000000000756

6. Sellier E, Platt MJ, Andersen GL, Krägeloh-Mann I, De La Cruz J, Cans C, et al. Decreasing prevalence in cerebral palsy: a multi-site European population-based study, 1980 to 2003. *Developmental Med and Child Neurol* (2016) **58**:85–92. doi:10.1111/dmcn.12865

7. Koy A, Kühn AA, Huebl J, Schneider G-H, van Riesen AK, Eckenweiler M, et al. Quality of life after deep brain stimulation of pediatric patients with dyskinetic cerebral palsy: a prospective, single-arm, multicenter study with a subsequent randomized double-blind crossover (STIM-CP). *Movement Disord* (2022) **37**:799–811. doi:10.1002/mds.28898

8. Koy A, Hellmich M, Pauls KA, Marks W, Lin JP, Fricke O, et al. Effects of deep brain stimulation in dyskinetic cerebral palsy: a meta-analysis. *Movement Disord* (2013) **28**:647–54. doi:10.1002/mds.25339

9. Graham HK, Rosenbaum P, Paneth N, Dan B, Lin JP, Damiano DL, et al. Cerebral palsy. *Nat Rev Dis Primers* (2016) **2**:15082. doi:10.1038/nrdp.2015.82

10. Rodrigues FB, Duarte GS, Prescott D, Ferreira J, Costa J. Deep brain stimulation for dystonia. *Cochrane Database Syst Rev* (2019) **1**:CD012405. doi:10.1002/14651858.CD012405.pub2

11. Tisch S, Limousin P. Neurophysiological insights in dystonia and its response to deep brain stimulation treatment. *Exp Brain Res* (2020) **238**:1645–57. doi:10.1007/s00221-020-05833-8

12. Welter ML, Grabli D, Vidailhet M. Deep brain stimulation for hyperkinetics disorders: dystonia, tardive dyskinesia, and tics. *Curr Opin Neurol* (2010) **23**:420–5. doi:10.1097/wco.0b013e32833b7798

13. Miterko LN, Baker KB, Beckinghausen J, Bradnam LV, Cheng MY, Cooperrider J, et al. Consensus paper: experimental neurostimulation of the cerebellum. *Cerebellum* (2019) **18**:1064–97. doi:10.1007/s12311-019-01041-5

14. Neychev VK, Gross RE, Lehericy S, Hess EJ, Jinnah HA. The functional neuroanatomy of dystonia. *Neurobiol Dis* (2011) **42**:185–201. doi:10.1016/j.nbd.2011.01.026

15. Downs AM, Roman KM, Campbell SA, Pisani A, Hess EJ, Bonsi P. The neurobiological basis for novel experimental therapeutics in dystonia. *Neurobiol Dis* (2019) **130**:104526. doi:10.1016/j.nbd.2019.104526

16. Albin RL, Young AB, Penney JB. The functional anatomy of basal ganglia disorders. *Trends Neurosciences* (1989) **12**:366–75. doi:10.1016/0166-2236(89)90074-x

17. Nomura Y, Segawa M. Genetics and pathophysiology of primary dystonia with special emphasis on DYT1 and DYT5. *Semin Neurol* (2014) **34**:306–11. doi:10.1055/s-0034-1386768

18. Perciavalle V, Apps R, Bracha V, Delgado-Garcia JM, Gibson AR, Leggio M, et al. Consensus paper: current views on the role of cerebellar interpositus nucleus in movement control and emotion. *Cerebellum* (2013) **12**:738–57. doi:10.1007/s12311-013-0464-0

19. Lang EJ, Apps R, Bengtsson F, Cerminara NL, De Zeeuw CI, Ebner TJ, et al. The roles of the olivocerebellar pathway in motor learning and motor control. A consensus paper. *Cerebellum* (2017) **16**:230–52. doi:10.1007/s12311-016-0787-8

20. Koziol LF, Budding D, Andreasen N, D'Arrigo S, Bulgheroni S, Imamizu H, et al. Consensus paper: the cerebellum's role in movement and cognition. *Cerebellum* (2014) **13**:151–77. doi:10.1007/s12311-013-0511-x

21. Adamaszek M, D'Agata F, Ferrucci R, Habas C, Keulen S, Kirkby KC, et al. Consensus paper: cerebellum and emotion. *Cerebellum* (2017) **16**:552–76. doi:10.1007/s12311-016-0815-8

22. Chen CH, Fremont R, Arteaga-Bracho EE, Khodakhah K. Short latency cerebellar modulation of the basal ganglia. *Nat Neurosci* (2014) **17**:1767–75. doi:10.1038/nn.3868

23. Burke RE, Fahn S, Marsden CD, Bressman SB, Moskowitz C, Friedman J. Validity and reliability of a rating scale for the primary torsion dystonias. *Neurology* (1985) **35**:73–7. doi:10.1212/wnl.35.1.73

24. Air EL, Ostrem JL, Sanger TD, Starr PA. Deep brain stimulation in children: experience and technical pearls Clinical article. *J Neurosurgery-Pediatrics* (2011) **8**:566–74. doi:10.3171/2011.8.peds11153

25. Gimeno H, Tustin K, Lumsden D, Ashkan K, Selway R, Lin J-P. Evaluation of functional goal outcomes using the Canadian Occupational Performance Measure (COPM) following Deep Brain Stimulation (DBS) in childhood dystonia. *Eur J Paediatric Neurol* (2014) **18**:308–16. doi:10.1016/j.ejpn.2013.12.010

26. Gimeno H, Tustin K, Selway R, Lin J-P. Beyond the Burke-Fahn-Marsden Dystonia Rating Scale: deep brain stimulation in childhood secondary dystonia. *Eur J Paediatric Neurol* (2012) **16**:501–8. doi:10.1016/j.ejpn.2011.12.014

27. Katsakiori PF, Kefalopoulou Z, Markaki E, Paschali A, Ellul J, Kagadis GC, et al. Deep brain stimulation for secondary dystonia: results in 8 patients. *Acta Neurochirurgica* (2009) **151**:473–8. doi:10.1007/s00701-009-0281-x

28. Keen JR, Przekop A, Olaya JE, Zouros A, Hsu FPK. Deep brain stimulation for the treatment of childhood dystonic cerebral palsy. *J Neurosurgery-Pediatrics* (2014) **14**:585–93. doi:10.3171/2014.8.peds141

29. Kim AR, Chang JW, Chang WS, Park ES, Cho S-R. Two-year outcomes of deep brain stimulation in adults with cerebral palsy. *Ann Rehabil Med* (2014) **38**:209–17. doi:10.5535/arm.2014.38.2.209

30. Kim JH, Jung NY, Chang WS, Jung HH, Cho S-R, Chang JW. Intrathecal baclofen pump versus globus pallidus interna deep brain stimulation in adult patients with severe cerebral palsy. *World Neurosurg* (2019) **126**:E550–e556. doi:10.1016/j.wneu.2019.02.092

31. Kim JP, Chang WS, Cho S-R, Chang JW. The effect of bilateral globus pallidus internus deep brain stimulation plus ventralis oralis thalamotomy on patients with cerebral palsy. *Stereotactic Funct Neurosurg* (2012) **90**:292–9. doi:10.1159/000338093

32. Koy A, Pauls KAM, Flossdorf P, Becker J, Schönau E, Maarouf M, et al. Young adults with dyskinetic cerebral palsy improve subjectively on pallidal stimulation, but not in formal dystonia, gait, speech and swallowing testing. *Eur Neurol* (2014) **72**:340–8. doi:10.1159/000360984

33. Koy A, Weinsheimer M, Pauls KAM, Kuhn AA, Krause P, Huebl J, et al. German registry of paediatric deep brain stimulation in patients with childhood-onset dystonia (GEPESTIM). *Eur J Paediatric Neurol* (2017) **21**:136–46. doi:10.1016/j.ejpn.2016.05.023

34. Marks W, Bailey L, Reed M, Pomykal A, Mercer M, Macomber D, et al. Pallidal stimulation in children: comparison between cerebral palsy and DYT1 dystonia. *J Child Neurol* (2013) **28**:840–8. doi:10.1177/0883073813488674

35. Marks WA, Honeycutt J, Acosta F, Jr, Reed M, Bailey L, Pomykal A, et al. Dystonia due to cerebral palsy responds to deep brain stimulation of the globus pallidus internus. *Movement Disord* (2011) **26**:1748–51. doi:10.1002/mds.23723

36. Olaya JE, Christian E, Ferman D, Luc Q, Krieger MD, Sanger TD, et al. Deep brain stimulation in children and young adults with secondary dystonia: the Children's Hospital Los Angeles experience. *Neurosurg Focus* (2013) **35**:E7. doi:10.3171/2013.8.focus13300

37. Ozturk S, Temel Y, Aygun D, Kocabicak E. Deep brain stimulation of the globus pallidus internus for secondary dystonia: clinical cases and systematic review of the literature regarding the effectiveness of globus pallidus internus versus subthalamic nucleus. *World Neurosurg* (2021) **154**:E495–E508. doi:10.1016/j.wneu.2021.07.070

38. Romito LM, Zorzi G, Marras CE, Franzini A, Nardocci N, Albanese A. Pallidal stimulation for acquired dystonia due to cerebral palsy: beyond 5 years. *Eur J Neurol* (2015) **22**:426–U21. doi:10.1111/ene.12596

39. Vidailhet M, Yelnik J, Lagrange C, Fraix V, Grabli D, Thobois S, et al. Bilateral pallidal deep brain stimulation for the treatment of patients with dystonia-choreoathetosis cerebral palsy: a prospective pilot study. *The Lancet Neurol* (2009) **8**:709–17. doi:10.1016/s1474-4422(09)70151-6

40. Wolf ME, Blahak C, Saryyeva A, Schrader C, Krauss JK. Deep brain stimulation for dystonia-choreoathetosis in cerebral palsy: pallidal versus thalamic stimulation. *Parkinsonism and Relat Disord* (2019) **63**:209–12. doi:10.1016/j.parkreldis.2019.01.029

41. Kim JP, Chang WS, Chang JW. Treatment of secondary dystonia with a combined stereotactic procedure: long-term surgical outcomes. *Acta Neurochirurgica* (2011) **153**:2319–28. doi:10.1007/s00701-011-1147-6

42. Lin S, Zhang C, Li H, Wang Y, Wu Y, Wang T, et al. High frequency deep brain stimulation of superior cerebellar peduncles in a patient with cerebral palsy. *Tremor and Other Hyperkinetic Movements* (2020) **10**:38. doi:10.5334/tohm.551

43. San Luciano M, Robichaux-Viehoever A, Dodenhoff KA, Gittings ML, Viser AC, Racine CA, et al. Thalamic deep brain stimulation for acquired dystonia in children and young adults: a phase 1 clinical trial. *J Neurosurgery-Pediatrics* (2021) **27**:203–12. doi:10.3171/2020.7.peds20348

44. Mandarano R, Danieli A, Petacchi E, Di Pede C, Mondani M, Armellin MT, et al. Deep Brain Stimulation in childhood-onset dystonia due to brain pathology. A long-term study. *Eur J Paediatric Neurol* (2022) **37**:62–7. doi:10.1016/j.ejpn.2022.01.014

45. Galanda M, Horvath S. Stereotactic stimulation of the anterior lobe of the cerebellum in cerebral palsy from a suboccipital approach. *Acta Neurochirurgica Suppl* (2007) **97**:239–43. doi:10.1007/978-3-211-33081-4_27

46. Coubes P, Roubertie A, Vayssiere N, Hemm S, Echenne B. Treatment of DYT1-generalised dystonia by stimulation of the internal globus pallidus. *The Lancet* (2000) **355**:2220–1. doi:10.1016/s0140-6736(00)02410-7

47. Eltahawy HA, Saint-Cyr J, Giladi N, Lang AE, Lozano AM. Primary dystonia is more responsive than secondary dystonia to pallidal interventions: outcome after pallidotomy or pallidal deep brain stimulation. *Neurosurgery* (2004) **54**:613–21. doi:10.1227/01.neu.0000108643.94730.21

48. Tisch S. Deep brain stimulation in dystonia: factors contributing to variability in outcome in short and long term follow-up. *Curr Opin Neurol* (2022) **35**:510–7. doi:10.1097/wco.0000000000001072

49. Wang JJ, Tian H, Rao J, Xiong N, Yi DY, Liu XM, et al. Efficacy and safety of general anesthesia deep brain stimulation for dystonia: an individual patient data meta-analysis of 341 cases. *Neurol Sci* (2021) **42**:2661–71. doi:10.1007/s10072-021-05214-1

50. Isaias IU, Volkmann J, Kupsch A, Burgunder JM, Ostrem JL, Alterman RL, et al. Factors predicting protracted improvement after pallidal DBS for primary dystonia: the role of age and disease duration. *J Neurol* (2011) **258**:1469–76. doi:10.1007/s00415-011-5961-9

51. Elkaim LM, Alotaibi NM, Sigal A, Alotaibi HM, Lipsman N, Kalia SK, et al. Deep brain stimulation for pediatric dystonia: a meta-analysis with individual participant data. *Developmental Med and Child Neurol* (2019) **61**(49-+):49–56. doi:10.1111/dmcn.14063

52. Zhang JG, Zhang K, Wang ZC, Ge M, Ma Y. Deep brain stimulation in the treatment of secondary dystonia. *Chin Med J* (2006) **119**:2069–74. doi:10.1097/00029330-200612020-00008

53. DeLong MR, Crutcher MD, Georgopoulos AP. Primate globus pallidus and subthalamic nucleus: functional organization. *J Neurophysiol* (1985) **53**:530–43. doi:10.1152/jn.1985.53.2.530

54. Baumgartner AJ, Thompson JA, Kern DS, Ojemann SG. Novel targets in deep brain stimulation for movement disorders. *Neurosurg Rev* (2022) **45**:2593–613. doi:10.1007/s10143-022-01770-y

55. Fan H, Zheng Z, Yin Z, Zhang J, Lu G. Deep brain stimulation treating dystonia: a systematic review of targets, body distributions and etiology classifications. *Front Hum Neurosci* (2021) **15**:757579. doi:10.3389/fnhum.2021.757579

56. Schjerling L, Hjermind LE, Jespersen B, Madsen FF, Brennum J, Jensen SR, et al. A randomized double-blind crossover trial comparing subthalamic and pallidal deep brain stimulation for dystonia. *J Neurosurg* (2013) **119**:1537–45. doi:10.3171/2013.8.jns13844

57. Lin S, Wu Y, Li H, Zhang C, Wang T, Pan Y, et al. Deep brain stimulation of the globus pallidus internus versus the subthalamic nucleus in isolated dystonia. *J Neurosurg* (2020) **132**:721–32. doi:10.3171/2018.12.jns181927

58. Zhuang P, Li Y, Hallett M. Neuronal activity in the basal ganglia and thalamus in patients with dystonia. *Clin Neurophysiol* (2004) **115**:2542–57. doi:10.1016/j.clinph.2004.06.006

59. Ghika J, Villemure JG, Miklossy J, Temperli P, Pralong E, Christen–Zaech S, et al. Postanoxic generalized dystonia improved by bilateral Voa thalamic deep brain stimulation. *Neurology* (2002) **58**:311–3. doi:10.1212/wnl.58.2.311

60. Tsuboi T, Au KLK, Deeb W, Almeida L, Foote KD, Okun MS, et al. Motor outcomes and adverse effects of deep brain stimulation for dystonic tremor: a systematic review. *Parkinsonism and Relat Disord* (2020) **76**:32–41. doi:10.1016/j.parkreldis.2020.06.008

61. Davis R. Cerebellar stimulation for cerebral palsy spasticity, function, and seizures. *Arch Med Res* (2000) **31**:290–9. doi:10.1016/s0188-4409(00)00065-5

62. Stroud A, Tisch S, Jonker BP. Cerebellar cortex stimulation for acquired dystonia: a case report and review of its role in modern surgical practice. *Stereotactic Funct Neurosurg* (2022) **100**:321–30. doi:10.1159/000526072

63. Mulroy E, Vijiaratnam N, De Roquemaurel A, Bhatia KP, Zrinzo L, Foltynie T, et al. A practical guide to troubleshooting pallidal deep brain stimulation issues in patients with dystonia. *Parkinsonism and Relat Disord* (2021) **87**:142–54. doi:10.1016/j.parkreldis.2021.05.017

64. Wang Y, Zhang C, Sun B, Li D, Wu Y. Parameters for subthalamic deep brain stimulation in patients with dystonia: a systematic review. *J Neurol* (2022) **269**:197–204. doi:10.1007/s00415-020-10372-x

65. Magown P, Andrade RA, Soroceanu A, Kiss ZHT. Deep brain stimulation parameters for dystonia: a systematic review. *Parkinsonism and Relat Disord* (2018) **54**:9–16. doi:10.1016/j.parkreldis.2018.04.017

66. Moro E, Piboolnurak P, Arenovich T, Hung SW, Poon Y, Lozano AM. Pallidal stimulation in cervical dystonia: clinical implications of acute changes in stimulation parameters. *Eur J Neurol* (2009) **16**:506–12. doi:10.1111/j.1468-1331.2008.02520.x

67. Kern DS, Picillo M, Thompson JA, Sammartino F, di Biase L, Munhoz RP, et al. Interleaving stimulation in Parkinson's disease, tremor, and dystonia. *Stereotact Funct Neurosurg* (2018) **96**:379–91. doi:10.1159/000494983

68. Volonte MA, Clarizio G, Galantucci S, Scamarcia PG, Cardamone R, Barzaghi LR, et al. Long term follow-up in advanced Parkinson's disease treated with DBS of the subthalamic nucleus. *J Neurol* (2021) **268**:2821–30. doi:10.1007/s00415-021-10430-y

69. Yu H, Liu Y, Li S, Ma X. Effects of music on anxiety and pain in children with cerebral palsy receiving acupuncture: a randomized controlled trial. *Int J Nurs Stud* (2009) **46**:1423–30. doi:10.1016/j.ijnurstu.2009.05.007

70. Lahtinen M, Helander H, Vieira P, Uusimaa J, Katisko J. Starting a DBS service for children: it's not the latitude but the attitude - establishment of the paediatric DBS centre in Northern Finland. *Eur J Paediatric Neurol* (2022) **36**:107–14. doi:10.1016/j.ejpn.2021.12.003

71. Henderson JM. Connectomic surgery: diffusion tensor imaging (DTI) tractography as a targeting modality for surgical modulation of neural networks. *Front Integr Neurosci* (2012) **6**:15. doi:10.3389/fnint.2012.00015

72. Vassal F, Coste J, Derost P, Mendes V, Gabrillargues J, Nuti C, et al. Direct stereotactic targeting of the ventrointermediate nucleus of the thalamus based on anatomic 1.5-T MRI mapping with a white matter attenuated inversion recovery (WAIR) sequence. *Brain Stimulation* (2012) **5**:625–33. doi:10.1016/j.brs.2011.10.007

73. Koy A, Lin JP, Sanger TD, Marks WA, Mink JW, Timmermann L. Advances in management of movement disorders in children. *The Lancet Neurol* (2016) **15**:719–35. doi:10.1016/s1474-4422(16)00132-0

74. Bohn E, Goren K, Switzer L, Falck-Ytter Y, Fehlings D. Pharmacological and neurosurgical interventions for individuals with cerebral palsy and dystonia: a systematic review update and meta-analysis. *Developmental Med and Child Neurol* (2021) **63**:1038–50. doi:10.1111/dmcn.14874

75. Cif L, Coubes P. Historical developments in children's deep brain stimulation. *Eur J Paediatric Neurol* (2017) **21**:109–17. doi:10.1016/j.ejpn.2016.08.010

76. Kupsch A, Tagliati M, Vidailhet M, Aziz T, Krack P, Moro E, et al. Early postoperative management of DBS in dystonia: programming, response to stimulation, adverse events, medication changes, evaluations, and troubleshooting. *Movement Disord : official J Movement Disord Soc* (2011) **26 Suppl 1**(Suppl. 1):S37–53. doi:10.1002/mds.23624

77. Mahlknecht P, Limousin P, Foltynie T. Deep brain stimulation for movement disorders: update on recent discoveries and outlook on future developments. *J Neurol* (2015) **262**:2583–95. doi:10.1007/s00415-015-7790-8

78. Noecker AM, Mlakar J, Petersen MV, Griswold MA, McIntyre CC. Holographic visualization for stereotactic neurosurgery research. *Brain Stimul.* (2023) **16**:411–414. doi:10.1016/j.brs.2023.02.001

79. Zahavi D, Martiny KMM. Phenomenology in nursing studies: new perspectives. *Int J Nurs Stud* (2019) **93**:155–62. doi:10.1016/j.ijnurstu.2019.01.014

EBM Experimental Biology and Medicine

TYPE Original Research
PUBLISHED 19 May 2025
DOI 10.3389/ebm.2025.10356

OPEN ACCESS

*CORRESPONDENCE
Kim B. Pedersen,
kpeder@lsuhsc.edu

†These authors have contributed equally to this work

RECEIVED 26 August 2024
ACCEPTED 23 April 2025
PUBLISHED 19 May 2025

CITATION
Pedersen KB, Jelesijevic T, Morris TM, Melton SM, Henderson AS, Glenn JF, Davenport GJ, Ronis MJJ and Winsauer PJ (2025) Chronic administration of a cannabis-derived mixture at an antihyperalgesic dose does not significantly enhance hepatotoxicity or the development of metabolic dysfunction-associated steatohepatitis in male mice. *Exp. Biol. Med.* 250:10356. doi: 10.3389/ebm.2025.10356

Chronic administration of a cannabis-derived mixture at an antihyperalgesic dose does not significantly enhance hepatotoxicity or the development of metabolic dysfunction-associated steatohepatitis in male mice

Kim B. Pedersen[1*†], Tomislav Jelesijevic[2†], Tamara M. Morris[1], Sarah M. Melton[1], Ashley S. Henderson[1], John F. Glenn[3], Gregory J. Davenport[4], Martin J. J. Ronis[1] and Peter J. Winsauer[1]

[1]Department of Pharmacology and Experimental Therapeutics, Louisiana State University Health Sciences Center, New Orleans, LA, United States, [2]Department of Comparative Biomedical Sciences, Louisiana State University School of Veterinary Medicine, Baton Rouge, LA, United States, [3]MilMed R&D Consulting LLC, Brunswick, MD, United States, [4]Full Spectrum Omega Inc., Los Angeles, CA, United States

Abstract

Cannabis and cannabinoid mixtures have been linked to a variety of health benefits including pain mitigation, suppression of nausea produced by chemotherapeutic agents, anti-inflammatory effects, and effects on energy homeostasis, glucose, and lipid metabolism. The latter properties have led to the suggestion that these products could have therapeutic effects on the development of metabolic dysfunction-associated steatohepatitis (MASH) - a severe type of liver pathology in obese and diabetic patients. However, varying agonist and antagonistic properties of different cannabinoids on the endogenous cannabinoid system make prediction regarding hepatic effects and diet interactions difficult. The current study was designed to examine hepatic pathology following chronic administration of a cannabinoid mixture (NEPE14) at a dose equivalent to one previously demonstrating antihyperalgesic effects in rats. The effects of NEPE14 were investigated in a mouse model of MASH produced by feeding a Western diet rich in fat and simple sugars. After 24 weeks of NEPE14 administration, there was no hepatotoxicity in mice

receiving the control diet and no significant exacerbation of MASH in mice receiving the Western diet. In conclusion, no chronic liver toxicity was observed, but there was also no evidence for protection against MASH by this product.

KEYWORDS

cannabis, liver, Western diet, steatosis, metabolic dysfunction-associated steatohepatitis, MASH

Impact statement

Cannabinoid preparations are increasingly being used for medicinal purposes. Different cannabinoids were previously reported to promote or hinder steatosis of the liver. We evaluated a Non-Euphoric Phytocannabinoid Elixir #14 (NEPE14) at an antihyperalgesic dose for effects on liver pathology and on the development of metabolic dysfunction-associated steatohepatitis (MASH) in male mice. Chronic administration of NEPE14 caused neither amelioration nor worsening of hepatic toxicity, steatosis or inflammation in mice fed a Western diet for 24 weeks.

Introduction

Medical and recreational use of cannabis and cannabinoid products have increased dramatically as a result of legalization in many states in the US. The most prominent and well characterized phytochemicals in cannabis are delta-9-tetrahydrocannabinol (THC) and cannabidiol (CBD). However, cannabis contains many other potentially bioactive cannabinoids, alkaloids, flavonoids, and terpenoids [1]. The endocannabinoid system, involving signaling through the arachidonic acid-derived ligands anandamide and 2-arachidonylglycerol and cannabinoid receptors 1 and 2 (CB1 and CB2 encoded by genes *CNR1* and *CNR2*) are involved in the regulation of many neuronal systems, immune responses, and energy balance [2–4]. However, research into the potential beneficial or harmful effects of exogenous cannabinoids and other cannabis components has historically been limited until recently due to their registration as Schedule 1 substances by the Drug Enforcement Administration (DEA). Although they remain Schedule 1 substances to date, various state legally-approved medical marijuana programs (MMPs) have allowed for increased focus on these substances' medical uses. For instance, in addition to the known psychopharmacological and behavioral effects of cannabis, there is evidence from pre-clinical studies and clinical trials that various formulations with individual or multiple cannabis constituents can have anti-inflammatory effects on inflammatory bowel disease, potential anti-obesity effects, and possible protective effects against fatty liver disease [4].

Regarding the latter, the epidemiological and animal studies are inconclusive [4–6]. Both CB1 and CB2 receptors are expressed in liver and have a variety of effects on lipid and glucose homeostasis, insulin sensitivity and development of hepatic steatosis [4, 7]. In general, CB1 agonists induce steatosis via increases in *de novo* fatty acid synthesis and increased expression of lipogenic enzymes, whereas CB2 agonists increase steatosis by increasing expression of CB1 receptors [4]. Cannabinoid receptor antagonists are antisteatotic [4, 5]. Given that THC is a partial agonist it could be predicted to be steatotic. Conversely, CBD can decrease CB1 activation and is anti-inflammatory, which would suggest it to be both anti-steatotic and protective against fatty liver disease [4]. However, predictions about the effects of cannabis and cannabis-derived mixtures on steatosis and progression of fatty liver disease are complicated by the entourage effects of the many different cannabinoids and other phytochemicals in cannabis, and by the potential development of tolerance after chronic use [4–6]. Several studies have observed reduced steatosis in cannabis users [5] and a cross-sectional study found a 43% reduction in the incidence of non-alcoholic steatohepatitis (NASH) in chronic cannabis users [4]. These studies contrast with other studies that have observed no significant effects [5, 7]. Pre-clinical studies with CBD and hemp seed oil have demonstrated anti-steatotic, anti-inflammatory, and antioxidant effects in liver models of Non-Alcoholic Fatty Liver Disease (NAFLD) [8–10]. Phase 2 randomized control trials with CBD showed no significant benefit (Jazz Pharmaceuticals. A Randomized, Partially-blind, Placebo-controlled, Pilot, Dose-ranging Study To Assess The Effect Of Cannabidiol (CBD) On Liver Fat Levels In Subjects With Fatty Liver Disease. 2018.[1]).

NAFLD is a common and increasingly prevalent metabolic disorder [11]. The Western style dietary pattern with fast-food consumption is associated with increased frequency liver steatosis and liver disease [12, 13]. In light of the inconsistent data in the current literature and possible entourage effects of cannabinoids other than THC and CBD [1], the current study was designed to determine the chronic effects of a proprietary cannabis-derived mixture, Non-Euphoric Phytocannabinoid Elixir #14 (NEPE14), at an antihyperalgesic dose on liver pathology [14] and on development of metabolic dysfunction-associated steatohepatitis (MASH) in response to feeding a Western diet.

1 https://clinicaltrials.gov/study/NCT01284634

TABLE 1 Weight-to-volume assessments for specific cannabinoids identified in the batch of NEPE14 used for this experiment.

Non-euphoric phytocannabinoid elixir 14 (NEPE14)		
Batch #009		
Constituent cannabinoids	mg/mL	LOD/LOQ (mg/mL)
Δ9-THC	0.174	0.0001/0.0005
THCA	0.020	0.0001/0.0002
CBD	0.004	0.0001/0.0004
CBDA	0.016	0.0001/0.001
CBC	0.002	0.0001/0.0004
CBCA	0.0015	0.0001/0.0006
Δ8-THC	0.001	0.0003/0.0008
THCV	0.001	0.0001/0.0004
CBG	0.001	0.0001/0.0002
CBGA	0.001	0.0001/0.0003
CBN	0.001	0.0001/0.0003

The cannabinoids listed were identified by high performance liquid chromatography with diode-array detection (HPLC-DAD). Limit of Detection (LOD) refers to the lowest amount detectable, where Limit of Quantification (LOQ) refers to the lowest amount of an analyte in a sample that can be determined quantitatively with suitable precision/accuracy. The "A" after a cannabinoid, such as THCA, refers to the acid form of the cannabinoid.

Materials and methods

NEPE 14

Non-Euphoric Phytocannabinoid Elixir #14 (NEPE14) is a proprietary cannabis-derived whole-plant botanical formulation supplied by Full Spectrum Omega Therapeutics, Inc. (Adelanto, CA). It is a mixture of extracts from the Cannabis sativa plant, hemp (hempseed oil) and marijuana (proprietary extract process), and the final product contains less than 0.3% Δ^9–THC. The concentrations of the major phytocannabinoids are shown in Table 1. A certificate of analysis (COA) with the levels shown in Table 1 was provided for NEPE14 by SC Laboratories California LLC (Santa Cruz, CA). The regulatory compliance testing as reflected in the COA showed no measurable levels of pesticides, mycotoxins, microbes, residual solvents, or heavy metals.

Animals

Male C57Bl/6J mice were purchased from the Jackson Laboratory and housed two per cage. At 16 weeks of age, cages were randomized to receive a high-fat Western diet or a low-fat control diet *ad libitum*. The Western diet was AIN-76A (no. 5342 from TestDiet (Richmond, IN) supplemented with 21.3 g/L fructose and 18.9 g/L glucose in the drinking water, a diet previously developed by Krishnan et al. to produce fibrosing MASH with high fidelity to the human condition [15]. The control diet was AIN-93G (no. 5TJS) from TestDiet with normal drinking water. For each diet, mice in half the cages received NEPE14 and mice in the other half received corn oil provided daily at a volume of 1 μL/g body weight into the cheek pouch at 1,500 ± 90 min providing 0.23 μg of major cannabinoids per g body weight, of which 78% is Δ^9–THC. This dose of NEPE14 was similar to the lowest antihyperalgesic volume used in a previous study [14]. There were 10 mice per experimental group. At 40 weeks of age, mice were sacrificed by CO_2 asphyxiation after an overnight fast with collection of serum and tissues. The Institutional Animal Care and Use Committee (IACUC) of LSU Health Sciences Center approved the animal experiments.

Serum parameters

Alanine transaminase (ALT), aspartate aminotransferase (AST), triglycerides, cholesterol and insulin were determined by kits ab105134 (Abcam), MET-5127 (Cell Biolabs, Inc.), #10010303 (Cayman), #10007640 (Cayman) and ab277390 (Abcam), respectively. Glucose was measured with kit ab65333 (Abcam) in serum after deproteinization with 10 kDa spin columns ab93349 (Abcam). HOMA-IR was calculated from the fasted insulin and glucose levels.

TABLE 2 qRT-PCR primers.

Target	Gene	Forward primer	Reverse primer
18S rRNA		CGGACAGGATTGACAGATTG	CAAATCGCTCCACCAACTAA
COL1A1	*Col1a1*	CTGACGCATGGCCAAGAAGA	ATACCTCGGGTTTCCACGTC
αSMA	*Acta2*	GTGGCTATTCCTTCGTGACTAC	GAGCTACATAGCACAGCTTCTC
TNFα	*Tnf*	TTCTATGGCCCAGACCCTCA	CACTTGGTGGTTTGCTACGA
IL-6	*Il6*	CTTCACAAGTCGGAGGCTTAAT	GCAAGTGCATCATCGTTGTTC
IFN-γ	*Ifng*	ATCGGCTGACCTAGAGAAGA	AGCCAAGATGCAGTGTGTAG
B220	*Ptprc*	CCCTTCTTCTGCCTCAAAGT	CACCTGGATGATATGTGGTCTC
CD3E	*Cd3e*	GACGATGCCGAGAACATTGA	GCTTCTGAGGCAGCTCTTG
CYBB	*Cybb*	AGAGTCGGGATTTCTGACCG	GCCCCCTTCAGGGTTCTTGAT
CB2	*Cnr2*	GCTGACAAATGACACCCAGT	AGCCGTTGGTCACTTCTGTC
CD36	*Cd36*	GCAAAACGACTGCAGGTCAA	CACCAATGGTCCCAGTCTCA
FATP1	*Fatp1*	GTCCGCAATGAGTTCACCCT	GCTTGACGACTGCCTTGACT

Liver pathology

The left liver lobe was fixed for 3 days in alcoholic formalin made of 0.2 L 37% formaldehyde, 1.2 L 100% ethanol and 0.6 L H_2O followed by storage in 10% neutral buffered formalin. H&E-stained slides were scored by a board-certified veterinary anatomic pathologist blinded to the treatment groups for steatosis and inflammatory foci. Microsteatosis and macrosteatosis were graded separately for the periportal, midzonal and centrilobular zones with scores of 0, 1, 2 and 3 if steatosis was present in <5%, 5%–33%, 33%–66% and >66%, respectively, of the hepatocytes. Overall microsteatosis and macrosteatosis scores were the averages for the three zones. The total steatosis score was the average of the microsteatosis and macrosteatosis scores. Inflammatory foci were counted in six fields with a ×10 objective. Fibrosis was assessed after picrosirius red (PSR) staining. PSR stains collagen red and most other cellular components yellow. Liver parenchyma PSR (red) staining was quantified by the same ImageJ settings (threshold 50 for green image in a RGB stack) from four images from each mouse. The images were acquired by an Olympus BX43 microscope with DP28 camera. Liver triglycerides were determined from 87.5 to 100 mg flash-frozen liver tissue using the kit #10010303 (Cayman) and a TissueLyser II instrument (Qiagen, Hilden, Germany).

Immunohistochemistry

Five-micrometer-thick tissue liver sections were deparaffinized and rehydrated. Heat-mediated antigen retrieval was achieved in a pressure cooker at a temperature of 115–118°C and a pressure of 10.2–11.6 psi for 10 min. After blocking with Invitrogen eBioscience IHC/ICC blocking buffer–high protein (Fisher Scientific #50-184-85), slides were incubated with rabbit anti-CD3e (Fisher Scientific #PIMA535204) at a 1:1,000 dilution or rat anti-CD19 (Life Technologies #14-0194-80) at a 1:300 dilution primary antibodies. Alkaline phosphatase-conjugated goat anti-rabbit and rabbit anti-rat antibodies (Fisher Scientific #A18874 and # A18918, respectively) were added to the slides at a 1:500 dilution. Slides were incubated with a Vulcan Fast Red Chromagen kit (Fisher Scientific #50-828-59) for 10 min, washed with distilled water and counterstained with Harris hematoxylin (ThermoFisher Scientific #1859352). Slides were dehydrated and cover-slipped with Mounting Medium (ThermoFisher Scientific #1859351). The images were acquired using an Olympus BX43 microscope with an Olympus DP28 color camera.

QRT-PCR

The left part of the medial liver lobe was immersed in RNAProtect overnight at 4°C, followed by storage at −80°C until RNA extraction. RNA was extracted from 20 to 30 mg liver tissue using a TissueLyser II instrument and an RNAeasy Plus Mini Kit (Qiagen). RNA concentration was determined by absorbance at 260 nm on a NanoDrop spectrophotometer, and the quality assessed on a TapeStation 2200 instrument (Agilent Technologies, Santa Clara, CA). All RNA extracts were of high quality with RNA Integrity Numbers (RIN) between 8.9 and 9.6. Assays were run with Power SYBR Green RNA-to-CT 1-step kit reagents (Thermo Fisher Scientific, Waltham, MA) on a LightCycler 480 II (Roche, Indianapolis, IN). Primers are listed in Table 2. Targets were normalized to the amount of total RNA with each reaction containing 0.5 ng RNA for 18S rRNA and 5 ng RNA for all other targets.

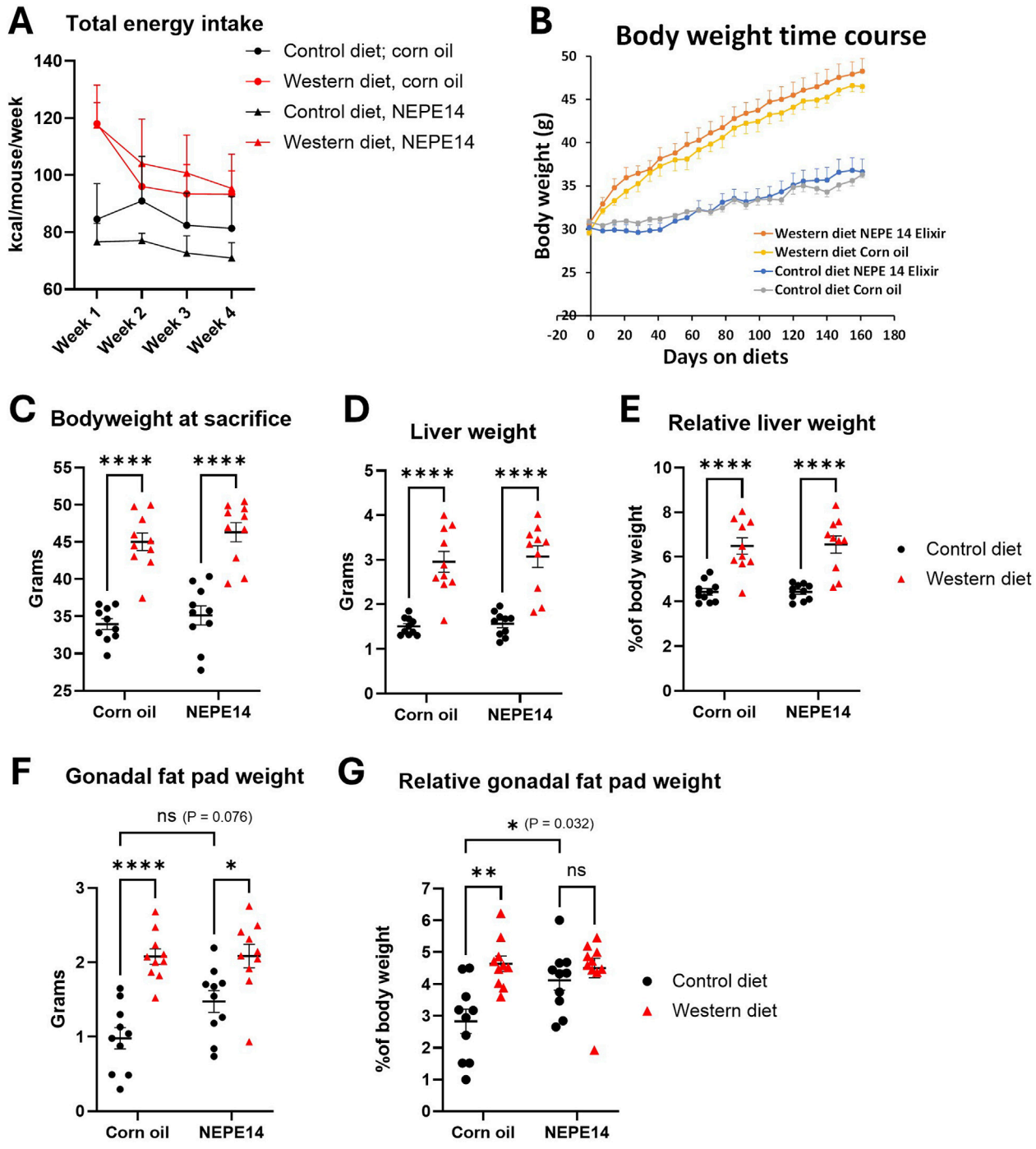

FIGURE 1
The Western diet promotes obesity. Mice were fed either a control diet or a Western diet and administered daily with corn oil or with NEPE14 for a dosage of 0.23 µg cannabinoids per Gram of body weight. **(A)** The total energy intake from pelleted food, drinking water with glucose and fructose, and corn oil/NEPE14 treatment in the first four weeks of the experiment was calculated. N = 5 cages per group with two mice per cage. **(B)** Time course of body weight; N = 10 mice per group. At sacrifice, body weight **(C)**, liver weight **(D)**, relative liver weight **(E)**, gonadal fat pad weight **(F)** and relative gonadal fat pad weight **(G)** were determined. ns: not significant. *, **, ****: $P < 0.05$, 0.01, 0.0001 for post-hoc comparisons after two-way ANOVA with Tukey's adjustment.

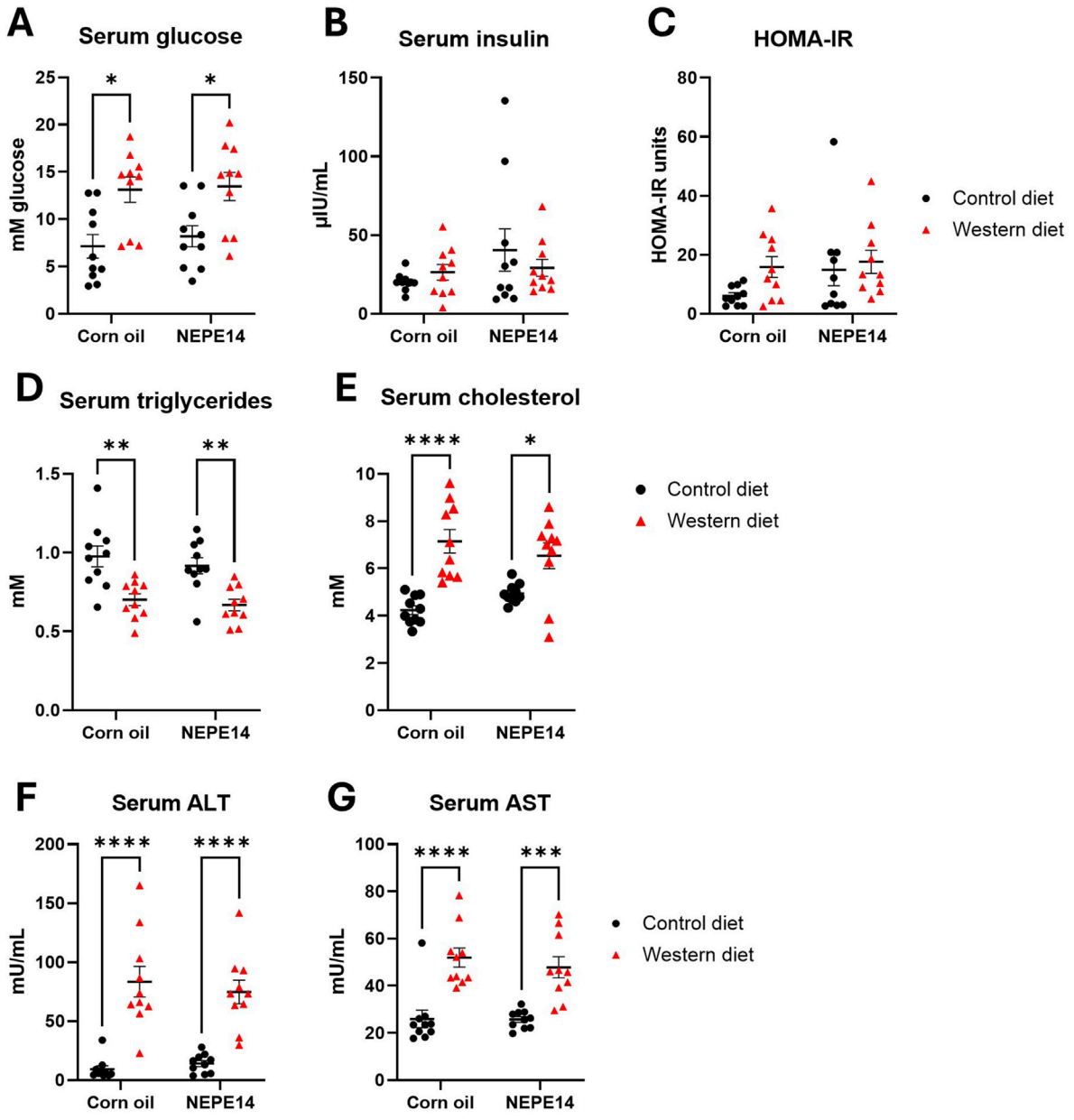

FIGURE 2
Serum parameters. Blood drawn from mice fasted overnight was used to determine serum glucose **(A)**, insulin **(B)**, HOMA-IR **(C)**, triglycerides **(D)**, cholesterol **(E)**, alanine transaminase (ALT) **(F)**, and aspartate aminotransferase (AST) **(G)**. *, **, ****: $P < 0.05$, 0.01, 0.0001 for post-hoc comparisons after two-way ANOVA with Tukey's adjustment.

Statistics

When considered appropriate, data were analyzed by an analysis of variance (ANOVA) with comparisons of means with Tukey's adjustment. For qRT-PCR data, two-way ANOVA was conducted of cycle threshold (C_T) values with conversion to linear scale for figure presentation. For liver pathology scores, non-parametric Kruskal-Wallis tests were conducted with Dunn's test for comparison of rank means. Incidence data were analyzed by pair-wise Fisher's exact test. Effects and differences were considered statistically significant for test probabilities $P < 0.05$. Statistical analyses were conducted with GraphPad Prism 10.2.0. Unless otherwise stated, figures show means and standard error of means in addition to individual measurements.

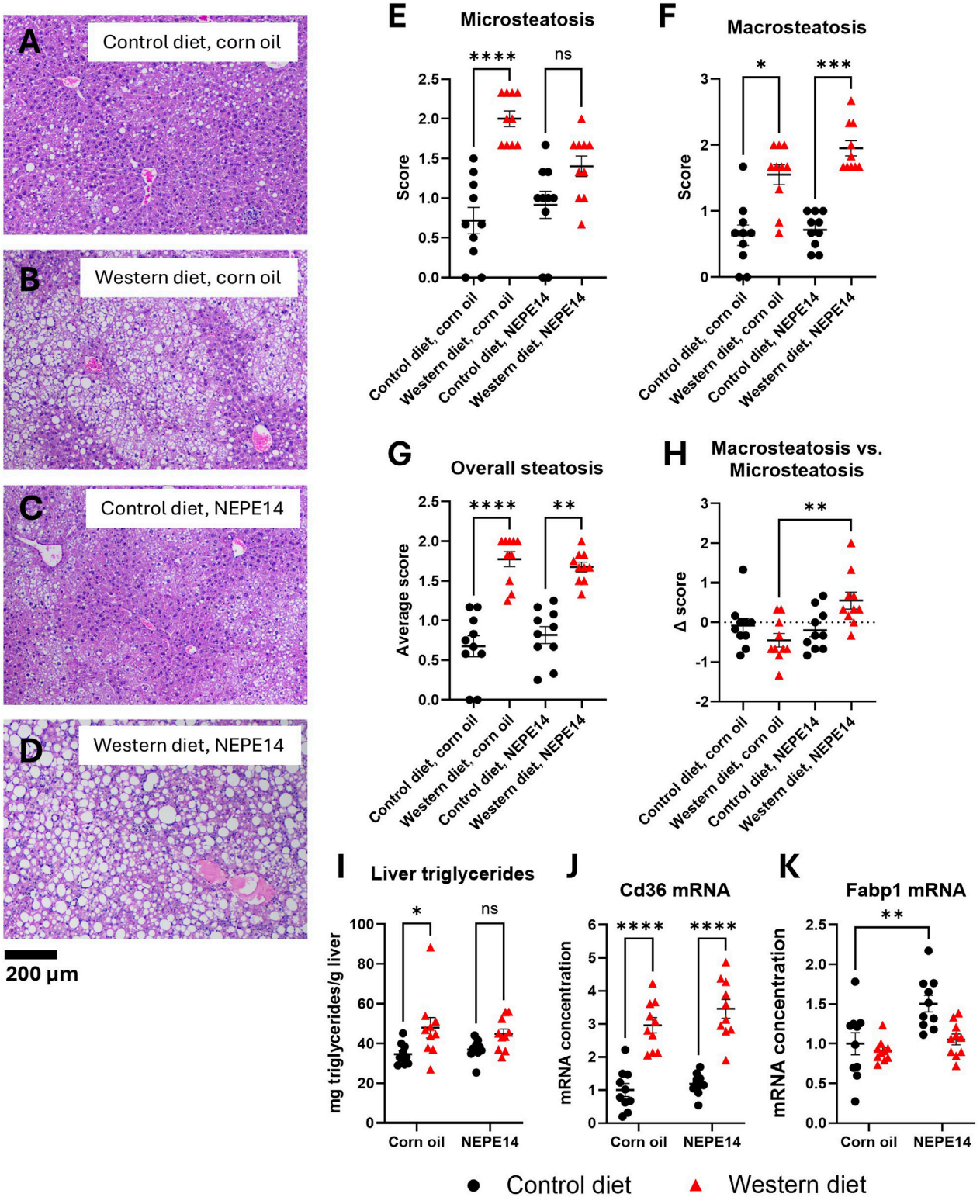

FIGURE 3
The Western diet promotes liver steatosis. Examples of H&E stained liver sections from each of the four treatment groups **(A–D)**. The livers were scored for microsteatosis **(E)**, macrosteatosis **(F)**, overall steatosis **(G)** and difference (Δ score) in macrosteatosis and microsteatosis scores **(H)**. *, **, ***, ****: $P < 0.05$, 0.01, 0.001, 0.0001 for post-hoc comparisons after Kruskal-Wallis test with Dunn's test. **(I)** Liver triglyceride content was determined. ns: not significant. *: $P < 0.05$ for post-hoc comparisons after two-way ANOVA with Tukey's adjustment. Hepatic concentrations of

(*Continued*)

FIGURE 3 (Continued)
Cd36 mRNA **(J)** and Fabp1 mRNA **(K)** were determined and scaled to a value of 1 for the mean of the control diet + corn oil group. **, ****: P < 0.01, 0.0001 for post-hoc comparisons after two-way ANOVA with Tukey's adjustment.

Results

The Western diet increases body, liver, and fat mass

The daily dosage of NEPE14 (1 μL/g body weight/day) provided 0.23 μg of quantified cannabinoids per Gram of body weight, of which 78% was Δ^9–THC (Table 1). The mean intake for each experimental group was monitored for the first four weeks. The average energy intake in kcal was higher for the Western diet than control diet, with no indication that NEPE14 significantly increased intake (Figure 1A). Body weights increased faster for mice fed the Western diet than mice fed the control diet (Figure 1B). At sacrifice, mice given the Western diet had significantly higher body weights than mice given the control diet with no significant effect of the corn oil/NEPE14 administration and no significant interaction between these factors (Figure 1C). With the Western diet, the liver weights and liver weights relative to body weights were significantly increased (Figures 1D,E) with no significant effects of NEPE14. The gonadal fat pad weight was likewise increased for mice fed the Western diet with no significant effect of NEPE14 (Figure 1F). Relative to body weight, NEPE14-treated mice had significantly increased relative gonadal fat pad weight when fed the control diet, but not the Western diet, with a significant (P = 0.032) interaction between diet and NEPE14 administration (Figure 1G).

The Western diet promotes hyperglycemia, dyslipidemia, and hepatic injury

Mice fed the Western diet had significantly higher fasting glucose than mice fed the control diet (Figure 2A), while there were no significant effects for serum insulin or the HOMA-IR parameter for insulin resistance (Figures 2B,C). The Western diet further led to decreased levels of serum triglycerides and increased levels of total serum cholesterol (Figures 2D,E). Mice fed the Western diet also had significantly increased concentrations of ALT and AST, indicative of liver damage (Figures 2F,G). There were no significant effects of the corn oil/NEPE14 treatment and no significant interactions between diet or NEPE14 administration for any of these serum parameters.

The Western diet promotes a liver phenotype consistent with metabolic dysfunction-associated steatohepatitis (MASH)

Livers from mice fed the Western diet tended to show a higher degree of steatosis than livers from mice fed the control diet (Figures 3A–D). The index of microsteatosis was significantly increased by the Western diet in mice treated with corn oil, while an index of macrosteatosis was significantly increased by the Western diet for both treatment groups (Figures 3E,F). The combined score of micro- and macrosteatosis was significantly increased by the Western diet (Figure 3G). To assess the degree of macrosteatosis relative to microsteatosis, we calculated the difference between the macrosteatosis and microsteatosis score (delta score). For mice fed the Western diet, this parameter was significantly increased (P = 0.005) by NEPE14 administration (Figure 3H). We further determined that the amount of liver triglycerides per Gram of liver tissue was significantly increased by the Western diet (P = 0.002 for main effect of diet) (Figure 3I). Thus, during intake of the Western diet, NEPE14 seems to shift storage of hepatic triglycerides towards macrosteatosis without alteration of the total amount of stored triglycerides.

CD36 is a fatty acid translocase with a possible role in pathogenesis of NAFLD. Hepatic expression of CD36 tends to be elevated in conditions of NAFLD, and CD36 overexpression can promote lipogenesis and steatosis [16, 17]. We observed that the concentration of Cd36 mRNA was significantly higher in mice fed the Western diet than in mice fed the control diet with no clear effect of NEPE14 (Figure 3J). Fatty acid binding protein 1 (FATP1) is an abundant hepatocyte protein that is important for intracellular fatty acid trafficking and protection from lipotoxicity of free fatty acids [18, 19]. In at least some cohorts of humans with steatosis and in some mouse models of NAFLD, hepatic expression of FATP1 is diminished. FATP1 also binds cannabinoids, including THC and CBD, which plays a role in hepatic detoxification of cannabinoids [20, 21]. We observed a small, but significant, upregulation of Fabp1 mRNA by NEPE14 administration in mice fed the control diet (Figure 3K).

Collagen was stained red with picrosirius red (PSR), and the sections were counterstained with hematoxylin. Hematoxylin stains nuclei and their nucleoli, generating a small amount of background signal. An image from each group is presented in Figures 4A–D. At sacrifice, upon macroscopic examination, three

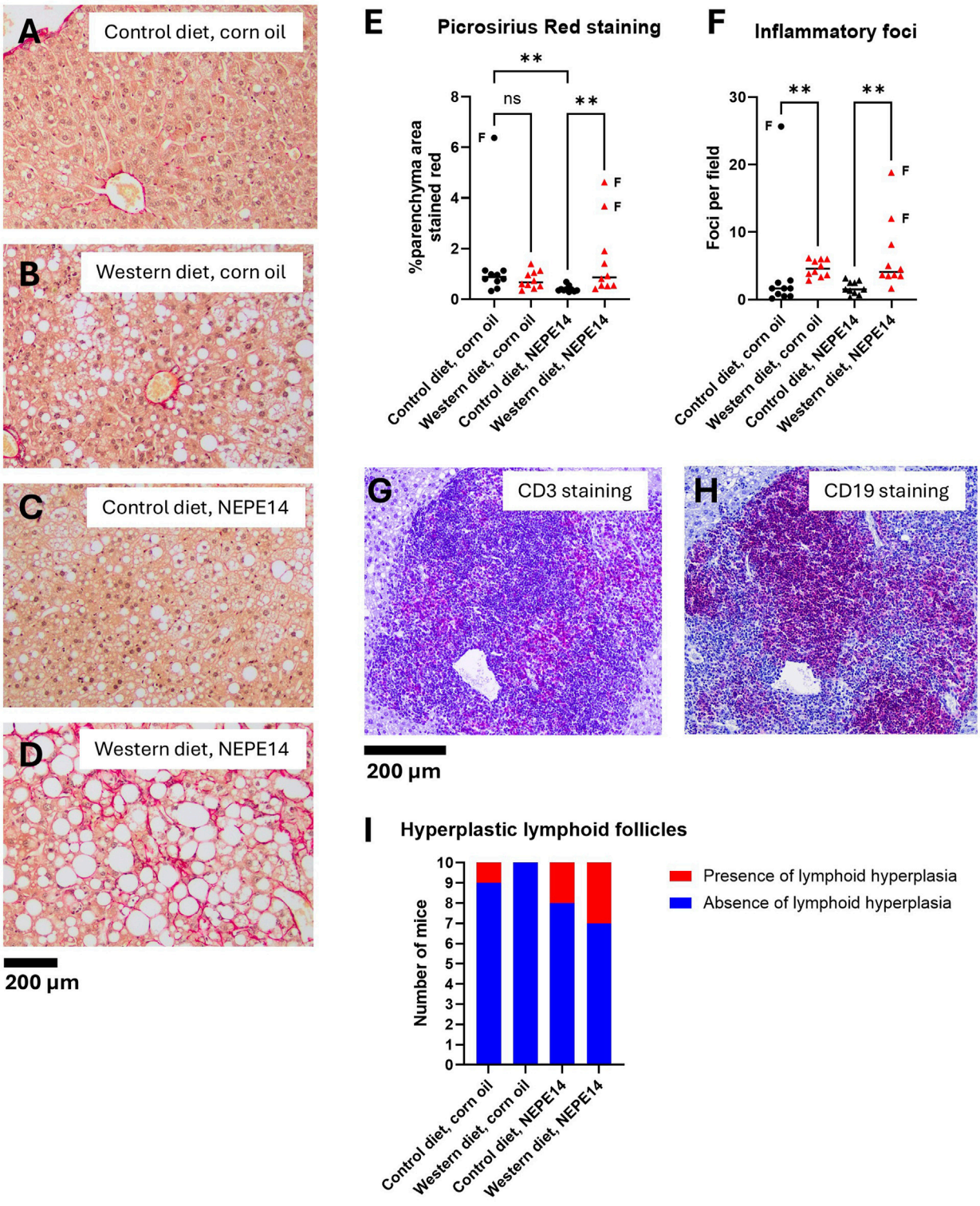

FIGURE 4
The Western diet promotes liver inflammation. Examples of liver sections stained with picrosirius red from each of the four treatment groups **(A–D)**. The sample in **(D)** was taken from one of the mice with a stiff, fibrotic liver. **(E)** Quantification of parenchymal PSR stained area. **(F)** Counting of inflammatory foci from H&E stained liver sections. In panels **E** and **F**, the horizontal lines indicate medians. The data points indicated by letter "F" are from stiff, fibrotic livers. ns: not significant. **: $P < 0.01$ for post-hoc comparisons after Kruskal-Wallis test with Dunn's test. **(G,H)** An example of

(*Continued*)

FIGURE 4 (Continued)
immunohistochemistry of a hyperplastic lymphoid follicle from a mouse fed the control diet and exposed to NEPE14 with the red-purple color demonstrating the occurrence of both CD3e-positive **(G)** and CD19-positive cells **(H)**. **(I)** Incidence of mice with hyperplastic lymphoid follicles observed in H&E stained liver sections.

mice had stiff, fibrotic livers. Two of these were mice that were fed the Western diet and received NEPE14, while the third was fed the control diet and administered corn oil. The three livers found to be highly fibrotic at sacrifice showed the highest degree of parenchymal PSR staining (Figures 4D,E). The Western diet led to significantly increased staining with picrosirius red in mice administered NEPE14 ($P < 0.05$). However, this increase was largely due to the two out of ten livers that were highly fibrotic (Figure 4E). In addition, there was a significant decrease in PSR staining produced by NEPE14 administration in mice fed the control diet, even though the staining intensity was already low in nine of the corn oil-administered mice.

The number of foci with inflammatory cells was significantly increased in mice fed the Western diet (Figure 4F). In some of the livers, there were one to three, small to medium size hyperplastic lymphoid follicles containing both CD3 positive (T-lineage cells) and CD19 positive (B-lineage cells) (Figures 4G,H). The incidence was higher in mice administered NEPE14 (Figure 4I), but this was not statistically significant ($P = 0.18$ by Fisher's exact test). In addition, there were three incidental findings in mice without hyperplastic lymphoid follicles: 1) a large pancreatic cyst in a mouse that received the Western diet and corn oil; 2) a hyperplastic nodule with a focus of cellular alteration in a mouse with a fibrotic liver that received the Western diet and NEPE14; and 3) a hepatocellular adenoma and moderate bile duct hyperplasia in a mouse with a fibrotic liver that received the control diet and corn oil (data not shown).

PSR staining provides a measure of collagen accumulation over time. To get a snapshot of collagen production at the time of sacrifice, we measured expression of mRNA for collagen 1a1 (Col1a1) and for alpha smooth muscle actin (αSMA) which is a marker of stellate cell activation. Concentrations of Col1a1 and αSMA mRNA were increased to the same degree by the Western diet ($P < 0.05$) in both the control and NEPE14 groups (Figure 5), suggesting activation of stellate cells promoting fibrosis. A key feature of steatohepatitis is enhanced inflammation. In addition to counting inflammatory foci (Figure 4F), we assessed the inflammatory milieu by determining expression of mRNAs for proinflammatory cytokines TNFα, IL-6 and interferon-γ that are upregulated in conditions of steatohepatitis [22–24]. We further measured B220 as a marker of B-cells; CD3e as a marker of T-cells; and the catalytic subunit CYBB of NOX2 that is a marker of Kupffer cells and other phagocytic cells with a role in the immune response. The Western diet led to significantly increased expression of mRNAs for TNFα, IL-6, B220, CD3e and CYBB ($P < 0.0001$, $P = 0.015$, $P = 0.001$, $P = 0.0001$, and $P < 0.0001$, respectively, for the main effects of diet) consistent with an enhanced inflammatory state (Figure 5). There were no significant effects of NEPE14 and no significant interactions between diet and chronic NEPE14 administration for any of these parameters. Finally, as receptors for phytocannabinoids, we explored expression of CB1 and CB2 receptors (expressed from genes *Cnr1* and *Cnr2*), and TRPV1 receptors. Likely due to low expression, we could not design robust qRT-PCR assays for Cnr1 and Trpv1 mRNA. Expression of Cnr2 mRNA was induced by the Western diet, with no significant effects of NEPE14 (Figure 5).

Discussion

In agreement with Krishnan et al. [15], chronic consumption of a Western diet rich in fat and simple sugars resulted in development of obesity and liver pathology consistent with fibrosing metabolic dysfunction-associated steatohepatitis (MASH) in male C57BL/6 mice. Furthermore, serum glucose and cholesterol were elevated in both studies. There were a small number of differences with the current study. We did not observe any significant increase in serum insulin, which may be due to the length of time between removal of the diet and sacrifice, which was 6 h in Krishnan et al. [15] and an overnight fast in the current study. We further observed a significant decrease in serum triglycerides, consistent with other studies of rodents fed a Western diet [25]. Feeding mice with the Western diet also promoted traits of the liver associated with development of MASH such as increased liver weight, increased liver steatosis, increased infiltration of inflammatory cells, and increased expression of profibrotic and proinflammatory genes. NEPE14, a cannabis-derived whole-plant botanical formulation has previously been shown to have significant antihyperalgesic effects when administered either intraperitoneally or at the current dose via the cheek pouch [14]. Given potential entourage effects between the different cannabinoid ingredients and other phytochemicals present in NEPE14, it was difficult to predict what effects chronic administration would have on energy utilization, glucose and lipid homeostasis, and liver pathology. The only significant effect of NEPE14 on body composition was a significant increase in relative adipose tissue weight in mice fed the control diet. This

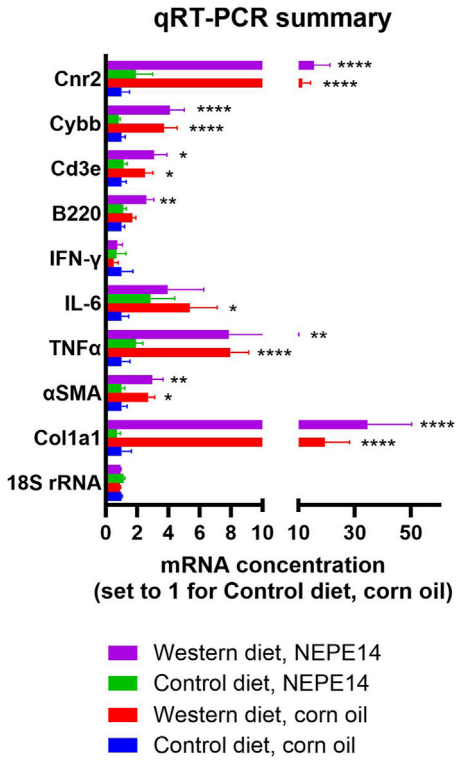

FIGURE 5
Hepatic mRNA expression. qRT-PCR was conducted for 18S rRNA as a house keeping gene, genes involved in fibrosis (Co1a1 and αSMA), genes involved in inflammation (TNFα, IL-6, IFN-γ, B220, CD3e and Cybb), and the gene encoding cannabinoid receptor 2 (Cnr2). N = 10 mice per experimental group. *, **, ****: $P < 0.05$, 0.01, 0.0001 for post-hoc comparisons after two-way ANOVA with Tukey's adjustment.

contrasts with previous studies showing weight loss and improved adiposity in animals administered delta-9-THC chronically [4]. For mice fed the control diet, administration of NEPE14 did not cause overt liver pathology, indicating a lack of hepatotoxicity associated with this particular phytocannabinoid mixture. Decreased PSR staining and increased expression of Fatp1 mRNA in mice administered NEPE14 could be beneficial effects, although that would need to be substantiated in future studies. For mice fed the Western diet, no significant differences were observed in the development of overall MASH pathology or gene expression with or without co-administration of NEPE14. However, there were some subtle differences related to the nature of hepatic fat accumulation. A significant shift in lipid droplet size toward macrosteatosis was observed after NEPE14 administration, suggesting a change in lipid packaging, but overall levels of steatosis and triglyceride accumulation were similar between the two groups that received the Western-style diet.

Limitations of the current study include using only male mice and only one volume of NEPE14. Future studies that include female mice and higher doses may be important, as females have been shown to be more sensitive than males to the antinociceptive effects of cannabinoids. In one study, for example, CB1 and CB2 antagonists were used to demonstrate that while both the acute antinociceptive and motoric effects of Δ9-THC were produced via activation of CB1 receptors, the CB1 antagonist rimonabant was up to 10 times more potent in female than male rats and the antagonism of the Δ9-THC-induced antinociception was greater than the antagonism for the motor impairment [26].

The occurrence of stiff, fibrotic livers in three mice, especially for a mouse on the control diet that was administered corn oil, was unexpected and contributes to the likelihood that these findings were idiopathic. Nevertheless, these livers also showed the highest degree of bridging and intralobular fibrosis by picrosirius red staining and the highest number of inflammatory foci. While we did not substantiate mRNA expression data with data on protein levels, it was remarkable that the mice with these livers also had the highest expression of mRNA for COL1A1, TNFα, IFN-γ, CD3E and CYBB within their respective experimental groups (data not shown), demonstrating an enhanced inflammatory state. The focus of cellular alterations found in the fibrotic liver of a mouse that received the Western diet and NEPE14, as well as the hepatocellular adenoma found in the fibrotic liver of a mouse that received the control diet and corn oil, could not be directly tied to a particular diet or substance administered due to the inconsistent occurrence of these pathological findings across the experimental groups. Interestingly, the role of endogenous cannabinoids on hematopoietic cell proliferation, differentiation, and migration has been found to be both positive and negative. For example, most fatty acid ethanolamides such as anandamide inhibit migration, whereas most fatty acid glyceryl esters stimulate migration [27]. The role of the cannabinoid receptors in these effects has also been difficult to establish as experiments with both CB1 and CB2 receptor antagonists indicated that the effects of 2-arachidonyl glycerol on cell migration were receptor dependent, but the effects of anandamide on cell migration were receptor independent.

Hepatic lymphoid hyperplasia was another unexpected finding. In humans, hepatic reactive lymphoid hyperplasia is a rare, but apparently benign condition [28]. While we cannot exclude the possibility of NEPE14 stimulating lymphoid hyperplasia, the incidence in NEPE14-administered mice was not significantly higher than in mice administered the corn oil control. There are reports of NEPE14 increasing lymphocyte counts in response to total body irradiation combined with skin wounding [29]; however, associating this type of bone marrow clonogenicity solely with NEPE administration would be difficult without further studies because NAFLD alone can

increase lymphocyte counts [30]. These data would also contrast with data demonstrating that cannabinoids often decrease lymphocyte counts. In one study, for instance, both purified delta-9-tetrahydrocannabinol (THC) and cannabidiol (CBD), along with THC- and CBD-enriched cannabis extracts, reduced activated lymphocyte proliferation in a murine bone marrow transplantation (BMT) model [31]. This study was also able to show that THC, but not CBD, produced this effect through CB2 receptors using splenocytes from CB2 knockout mice in a succinyl ester (CFSE)-labeled lymphocyte proliferation model. Another notable finding from this study was the effect of THC alone on lymphocyte proliferation, as it was eliminated in splenocytes lacking CB2 receptors, but was only less potent after the THC-enriched extract - suggesting that other constituents of the extract might also be responsible for limiting lymphocyte proliferation.

In conclusion, a Western diet for 24 weeks resulted in the development of obesity and liver pathology consistent with fibrosing metabolic dysfunction-associated steatohepatitis (MASH) in male C57BL/6 mice administered either corn oil or the cannabis-derived mixture NEPE14. The relative absence of an effect with NEPE14 in mice fed the Western diet indicated it did not worsen hepatotoxicity at a volume previously shown to have significant antihyperalgesic effects for pain management. It did, however, increase hepatic macrosteatosis compared to microsteatosis over this time period in mice fed the Western diet and produce small increases in relative adiposity in mice fed the control diet. Thus, NEPE14 administration neither significantly reduced nor enhanced development of MASH in response to a Western diet in this mouse model.

Author contributions

KP: Investigation, Methodology, Formal Analysis, Data curation, Visualization, Writing – Original draft, Writing – review and editing. TJ: Investigation, Data curation, Methodology, Visualization, Writing – review and editing. TM: Investigation, Methodology, Writing – review and editing. SM: Investigation, Methodology, Writing – review and editing. AH: Investigation, Methodology, Writing – review and editing. JG: Conceptualization, Resources, Writing – review and editing. GD: Resources, Writing – review and editing, MR: Conceptualization, Data curation, Writing – Original draft, review and editing. PW: Conceptualization, Data Curation, Funding acquisition, Writing – review and editing. All authors contributed to the article and approved the submitted version.

Data availability

The original contributions presented in the study are included in the article, further inquiries can be directed to the corresponding author.

Ethics statement

The animal study was approved by The Institutional Animal Care and Use Committee (IACUC) of LSU Health Sciences Center, New Orleans. The study was conducted in accordance with the local legislation and institutional requirements.

Funding

The author(s) declare that financial support was received for the research and/or publication of this article. The authors declare that this study received funding from Full Spectrum Omega Inc. The funder had the following involvement with the study: Conceptualization, providing NEPE14 for the study, and reviewing and editing the manuscript.

Acknowledgments

NEPE14 products from Full Spectrum Omega Inc. are the invention of Richard Brumfield Jr. and manufactured by La India Inc. and regulated under California Medicinal and Adult Use Cannabis Regulation and Safety Act (MAUCRSA) License #CDPH-10002445 (16169 Beaver Rd., Adelanto CA 92301) distributed by Beaver Freight Inc. MAUCRSA License #C11-0000037-LIC (16169 Beaver Rd., Adelanto CA 92301) and shipped by Jet Room Inc. MAUCRSA License #C10-0000057-LIC (17499 Adelanto Rd., Adelanto, CA 92301), LSU Health New Orleans contract #110300185A. We would like to thank Rahim Musa for his technical assistance in completing these experiments.

Conflict of interest

JG is a scientific program consultant to Full Spectrum Omega, Inc. GD is President of Full Spectrum Omega, Inc.

The remaining author(s) declared no potential conflicts of interest with respect to the research, authorship, and/or publication of this article.

References

1. Mechoulam R, Hanuš LO, Pertwee R, Howlett AC. Early phytocannabinoid chemistry to endocannabinoids and beyond. *Nat Rev Neurosci* (2014) **15**:757–64. doi:10.1038/nrn3811

2. Osei-Hyiaman D, DePetrillo M, Pacher P, Liu J, Radaeva S, Bátkai S, et al. Endocannabinoid activation at hepatic CB1 receptors stimulates fatty acid synthesis and contributes to diet-induced obesity. *J Clin Invest* (2005) **115**:1298–305. doi:10.1172/jci23057

3. Bergholm R, Sevastianova K, Santos A, Kotronen A, Urjansson M, Hakkarainen A, et al. CB1 blockade-induced weight loss over 48 weeks decreases liver fat in proportion to weight loss in humans. *Int J Obes* (2013) **37**:699–703. doi:10.1038/ijo.2012.116

4. Gotfried J, Naftali T, Schey R. Role of cannabis and its derivatives in gastrointestinal and hepatic disease. *Gastroenterology* (2020) **159**:62–80. doi:10.1053/j.gastro.2020.03.087

5. Dibba P, Li AA, Cholankeril G, Ali Khan M, Kim D, Ahmed A. Potential mechanisms influencing the inverse relationship between cannabis and nonalcoholic fatty liver disease: a commentary. *Nutr Metab Insights* (2019) **12**:1178638819847480. doi:10.1177/1178638819847480

6. Barré T, Di Marzo V, Marcellin F, Burra P, Carrieri P. Expanding research on cannabis-based medicines for liver steatosis: a low-risk high-reward way out of the present deadlock? *Cannabis Cannabinoid Res* (2023) **8**:5–11. doi:10.1089/can.2022.0014

7. Pertwee RG. The diverse CB1 and CB2 receptor pharmacology of three plant cannabinoids: Δ9-tetrahydrocannabinol, cannabidiol and Δ9-tetrahydrocannabivarin. *Br J Pharmacol* (2008) **153**:199–215. doi:10.1038/sj.bjp.0707442

8. Ribeiro A, Ferraz-de-Paula V, Pinheiro ML, Vitoretti LB, Mariano-Souza DP, Quinteiro-Filho WM, et al. Cannabidiol, a non-psychotropic plant-derived cannabinoid, decreases inflammation in a murine model of acute lung injury: role for the adenosine A2A receptor. *Eur J Pharmacol* (2012) **678**:78–85. doi:10.1016/j.ejphar.2011.12.043

9. Zurier RB, Burstein SH. Cannabinoids, inflammation, and fibrosis. *The FASEB J* (2016) **30**:3682–9. doi:10.1096/fj.201600646r

10. Gong M, Lu H, Li L, Feng M, Zou Z. Integration of transcriptomics and metabonomics revealed the protective effects of hemp seed oil against methionine–choline-deficient diet-induced non-alcoholic steatohepatitis in mice. *Food and Funct* (2023) **14**:2096–111. doi:10.1039/d2fo03054c

11. Younossi Z, Anstee QM, Marietti M, Hardy T, Henry L, Eslam M, et al. Global burden of NAFLD and NASH: trends, predictions, risk factors and prevention. *Nat Rev Gastroenterol and Hepatol* (2018) **15**:11–20. doi:10.1038/nrgastro.2017.109

12. Guo W, Ge X, Lu J, Xu X, Gao J, Wang Q, et al. Diet and risk of non-alcoholic fatty liver disease, cirrhosis, and liver cancer: a large prospective cohort study in UK biobank. *Nutrients* (2022) **14**:5335. doi:10.3390/nu14245335

13. Kardashian A, Dodge JL, Terrault NA. Quantifying the negative impact of fast-food consumption on liver steatosis among United States adults with diabetes and obesity. *Clin Gastroenterol Hepatol* (2023) **21**:3176–8.e3. doi:10.1016/j.cgh.2022.11.040

14. Morris T, Cucinello-Ragland JA, Marks TJ, Prevost K, Glenn JF, Davenport GJ, et al. Distinct antinociceptive and conditioned behavioral effects are produced by individual cannabinoids and a cannabis-derived mixture. *Pharmacol Biochem Behav* (2024) **235**:173692. doi:10.1016/j.pbb.2023.173692

15. Krishnan A, Abdullah TS, Mounajjed T, Hartono S, McConico A, White T, et al. A longitudinal study of whole body, tissue, and cellular physiology in a mouse model of fibrosing NASH with high fidelity to the human condition. *Am J Physiology-Gastrointestinal Liver Physiol* (2017) **312**:G666–G680. doi:10.1152/ajpgi.00213.2016

16. Rada P, González-Rodríguez Á, García-Monzón C, Valverde ÁM. Understanding lipotoxicity in NAFLD pathogenesis: is CD36 a key driver? *Cell Death and Dis* (2020) **11**:802. doi:10.1038/s41419-020-03003-w

17. Zeng H, Qin H, Liao M, Zheng E, Luo X, Xiao A, et al. CD36 promotes *de novo* lipogenesis in hepatocytes through INSIG2-dependent SREBP1 processing. *Mol Metab* (2022) **57**:101428. doi:10.1016/j.molmet.2021.101428

18. Wang G, Bonkovsky HL, de Lemos A, Burczynski FJ. Recent insights into the biological functions of liver fatty acid binding protein 1. *J Lipid Res* (2015) **56**:2238–47. doi:10.1194/jlr.r056705

19. Guzmán C, Benet M, Pisonero-Vaquero S, Moya M, García-Mediavilla MV, Martínez-Chantar ML, et al. The human liver fatty acid binding protein (FABP1) gene is activated by FOXA1 and PPARα; and repressed by C/EBPα: implications in FABP1 down-regulation in nonalcoholic fatty liver disease. *Biochim Biophys Acta (Bba) - Mol Cell Biol Lipids* (2013) **1831**:803–18. doi:10.1016/j.bbalip.2012.12.014

20. Huang H, McIntosh AL, Martin GG, Landrock D, Chung S, Landrock KK, et al. FABP1: a novel hepatic endocannabinoid and cannabinoid binding protein. *Biochemistry* (2016) **55**:5243–55. doi:10.1021/acs.biochem.6b00446

21. Elmes MW, Prentis LE, McGoldrick LL, Giuliano CJ, Sweeney JM, Joseph OM, et al. FABP1 controls hepatic transport and biotransformation of Δ(9)-THC. *Sci Rep* (2019) **9**:7588. doi:10.1038/s41598-019-44108-3

22. Li J, Chen Q, Yi J, Lan X, Lu K, Du X, et al. IFN-γ contributes to the hepatic inflammation in HFD-induced nonalcoholic steatohepatitis by STAT1β/TLR2 signaling pathway. *Mol Immunol* (2021) **134**:118–28. doi:10.1016/j.molimm.2021.03.005

23. Dong T, Li J, Liu Y, Zhou S, Wei X, Hua H, et al. Roles of immune dysregulation in MASLD. *Biomed and Pharmacother* (2024) **170**:116069. doi:10.1016/j.biopha.2023.116069

24. Shearn CT, Pulliam CF, Pedersen K, Meredith K, Mercer KE, Saba LM, et al. Knockout of the Gsta4 gene in male mice leads to an altered pattern of hepatic protein carbonylation and enhanced inflammation following chronic consumption of an ethanol diet. *Alcohol Clin Exp Res* (2018) **42**:1192–205. doi:10.1111/acer.13766

25. St-Amand R, Ngo Sock ÉT, Quinn S, Lavoie J-M, St-Pierre DH. Two weeks of western diet disrupts liver molecular markers of cholesterol metabolism in rats. *Lipids Health Dis* (2020) **19**:192. doi:10.1186/s12944-020-01351-2

26. Craft RM, Wakley AA, Tsutsui KT, Laggart JD. Sex differences in cannabinoid 1 vs. Cannabinoid 2 receptor-selective antagonism of antinociception produced by Δ^9-tetrahydrocannabinol and CP55,940 in the rat. *The J Pharmacol Exp Ther* (2012) **340**:787–800. doi:10.1124/jpet.111.188540

27. Patinkin D, Milman G, Breuer A, Fride E, Mechoulam R. Endocannabinoids as positive or negative factors in hematopoietic cell migration and differentiation. *Eur J Pharmacol* (2008) **595**:1–6. doi:10.1016/j.ejphar.2008.05.002

28. Zheng YC, Xie FC, Kang K, Shi Y, Mao YL, Sang XT, et al. Hepatobiliary case report and literature review of hepatic reactive lymphoid hyperplasia with positive anti-smooth muscle antibody and anti-nuclear antibody tests. *Transl Cancer Res* (2019) **8**:1001–5. doi:10.21037/tcr.2019.05.32

29. Wang L, Lin B, Zhai M, Cui W, Li X, Hull L, et al. Oral NEPE14 mitigates skin wound combined radiation injury-induced hematopoietic impairment in mice. *Radiat Res Soc 67th Annu Int Meet* (2021).

30. Cairoli V, De Matteo E, Rios D, Lezama C, Galoppo M, Casciato P, et al. Hepatic lymphocytes involved in the pathogenesis of pediatric and adult non-alcoholic fatty liver disease. *Sci Rep* (2021) **11**:5129. doi:10.1038/s41598-021-84674-z

31. Khuja I, Yekhtin Z, Or R, Almogi-Hazan O. Cannabinoids reduce inflammation but inhibit lymphocyte recovery in murine models of bone marrow transplantation. *Int J Mol Sci* (2019) **20**:668. doi:10.3390/ijms20030668

EBM Experimental Biology and Medicine

TYPE Brief Communication
PUBLISHED 23 May 2025
DOI 10.3389/ebm.2025.10448

OPEN ACCESS

*CORRESPONDENCE
Etienne Hebert-Chatelain,
etienne.hebert.chatelain@umoncton.ca

RECEIVED 26 November 2024
ACCEPTED 06 May 2025
PUBLISHED 23 May 2025

CITATION
Al-Younis I, Martín-Jiménez R, Khan M, Baussan Y, Jose C, Thibeault Y and Hebert-Chatelain E (2025) N-acetyl-L-cysteine improves mitochondrial and oxidative defects in the acadian variant of fanconi syndrome.
Exp. Biol. Med. 250:10448.
doi: 10.3389/ebm.2025.10448

N-acetyl-L-cysteine improves mitochondrial and oxidative defects in the acadian variant of fanconi syndrome

Inas Al-Younis[1,2], Rebeca Martín-Jiménez[1,2], Mehtab Khan[1,2], Yann Baussan[1,2], Caroline Jose[3], Yves Thibeault[4] and Etienne Hebert-Chatelain[1,2]*

[1]Canada Research Chair in Mitochondrial Signaling and Physiopathology, Moncton, NB, Canada, [2]Department of Biology, Université de Moncton, Moncton, NB, Canada, [3]Vitalité Health Network, Moncton, NB, Canada, [4]Department of Nephrology, G.-L.-Dumont University Hospital Center, Moncton, NB, Canada

Abstract

The Acadian variant of Fanconi Syndrome (AVFS) is a rare genetic disorder characterized by renal deficiencies. AVFS is caused by a mutation to *NDUFAF6* encoding a complex I assembly factor, and leading to metabolic alterations. We confirmed that fibroblasts derived from AVFS patients have lower complex I activity, mitochondrial membrane potential and cellular respiration. These mitochondrial defects were accompanied by higher levels of 8-hydroxy-2′deoxyguanosine, malondialdehyde and carbonyl, which are markers of oxidative damage to DNA, lipids and proteins, respectively. Thus, we hypothesized that the antioxidant N-Acetyl-L-cysteine (NAC) would reduce oxidative stress and mitochondrial defects in AVFS fibroblasts. Treatment with NAC during 5 days partially restored complex I activity, mitochondrial membrane potential and cellular respiration in AVFS fibroblasts. NAC also prevented oxidative damage in AVFS fibroblasts. This work shows for the first time that the physiopathology of AVFS includes high oxidative stress. It also reveals that NAC and other antioxidant-based strategies might represent an effective pharmacological treatment for AVFS.

KEYWORDS

mitochondrial disease, antioxidant, oxidative stress, kidney disease, rare disease

Impact Statement

The Acadian variant of Fanconi Syndrome is a rare mitochondrial disease for which there is no treatment. This work identifies oxidative stress as the most important mechanism in this disorder. It also suggests that the antioxidant NAC might be useful for the treatment of patients with this syndrome. This work will be of high interest for both fundamental biologists and clinicians.

Introduction

The Acadian variant of Fanconi Syndrome (AVFS) is a rare autosomal recessive genetic disorder characterized by defects in proximal tubular reabsorption and chronic kidney disease [1–3]. AVFS has only been reported in the Acadian population, who are descendants of the first French settlers on the East Coast of Canada. AVFS systematically progresses to end-stage renal disease and eventually requires kidney replacement therapy [2, 3]. AVFS has also been associated with other clinical features, namely pulmonary interstitial fibrosis and retinal blindness in some patients [2].

A non-coding mutation in NADH: ubiquinone oxidoreductase complex assembly factor 6 (NDUFAF6) has been reported as the cause of AVFS [1]. This mutation causes abnormal splicing of the *NDUFAF6* mRNA, which impairs the assembly of complex I (CI) of the electron transport system within mitochondria, leading to dysfunctional oxidative phosphorylation (OXPHOS) [1, 4]. OXPHOS is performed by a series of enzymatic complexes (CI to IV) which transfer high-energy electrons to O_2 to create an electrochemical gradient across the inner mitochondrial membrane. This gradient then feeds the ATP synthase to generate ATP [5, 6]. Incomplete reduction of O_2 during OXPHOS can lead to reactive oxygen species (ROS) such as the superoxide anion [6]. ROS can damage cellular structures and high ROS levels are associated with numerous pathological conditions, including renal diseases [7]. Thus, CI is a major entry point for electrons in OXPHOS and its dysfunction significantly increases ROS production [8]. This suggests that the mutation of NDUFAF6 could trigger high oxidative damage which would lead to the clinical symptoms of AVFS.

In this study, we hypothesized that N-Acetyl-L-cysteine (NAC), a well-known antioxidant, would alleviate AVFS symptoms. To address this, NAC was applied to fibroblasts derived from AVFS patients, in which we examined mitochondrial deficiencies and oxidative damage. The data obtained show that AVFS fibroblasts have high levels of oxidative damage which can be reduced by NAC. This work thus demonstrates for the first time the role of oxidative damage in AVFS and the potential of NAC as a pharmacological treatment in this syndrome.

Materials and methods

All procedures were approved by the *Comité d'éthique de la recherche (CÉR) du Réseau de santé Vitalité* (#101701_2023) and the *Comité d'éthique de la recherche avec les êtres humains de l'université de Moncton* (#2223-067).

Fibroblasts culture

Control fibroblasts were obtained from ATCC (ref. PCS-201-012). Fibroblasts from patient 1 were generated by T. Mracek (Cezch Academy of Science) and fibroblasts of patient 2 were generated at the University of Moncton. Control and patient 1 fibroblasts were used to be able to compare our data to the original work on AVFS published in 2016 [1]. The patients did not present pulmonary interstitial fibrosis at the time of the study. Information about the patients has to remain confidential considering the low number of known patients with AVFS. Patients provided written informed consent for the use of their skin biopsies.

To generate culture of fibroblasts from patients, skin biopsies were minced and then transferred in petri dish with Dulbecco's modified Eagle's medium (DMEM) containing 4.5 g L^{-1} glucose, 2 mM glutamine, 1 mM pyruvate, 20% (v/v) of fetal bovine serum (FBS), 100 units*mL^{-1} penicillin and 100 g*mL^{-1} streptomycin. All primary fibroblasts were maintained at 37°C in 5% CO_2 and 95% humidity in the same culture medium.

Chemicals

NAC (ref. A8199, Sigma-Aldrich) was first dissolved in distilled water and then in the culture medium at a concentration of 1 mM. Cells were treated for 5 days before analyses.

Oxidative stress markers

For lipid oxidation, malondialdehyde (MDA) levels were assessed using the lipid peroxidation MDA assay kit (ref. AB233471, Abcam) with some modifications. Briefly, after cell lysis and protein normalization, thiobarbituric acid (TBA) was added to samples during 1 h at 95°C. MDA levels were detected by fluorescence using Synergy H1 microplate reader (Biotek Instrument). For protein oxidative damage, carbonyl levels were determined using the protein carbonyl content assay kit (ref. MAK094, Sigma Aldrich) following manufacturer's instructions. DNA oxidative damage were determined by measuring the 8-OHdG levels by ELISA (ref. ab201734, Abcam) following manufacturer's instructions.

Complex I activity

For complex I activity, fibroblasts were harvested and protein levels were quantified. For each condition, 100 µg of protein was used in the assay as described previously [9].

Mitochondrial membrane potential

Cells were harvested and centrifuged at 1,000*g for 5 min. Cells were then washed twice with phosphate buffered saline

(pH 7.2). Cells were then incubated with 200 nM of tetramethylrhodamine methyl ester (TMRM, Ref. T668, ThermoFisher) and incubated for 30 min at 37°C in cell media. As of control, all cells were also pre-incubated with 5 μM of FCCP during 5 min at 37°C to verify that the TMRM was FCCP-sensitive. TMRM labeling was then measured using Attune cytometer (Invitrogen).

Cellular respiration

Oxygen consumption rates (OCR) were measured using the Oxygraph-2k Oroboros system (Innsbruck, Austria), as previously described [10–12]. Briefly, cell respiration was determined at 37°C with 2 × 10^6 intact cells in 2 mL chambers. Three different states of OCR cells were measured: (i) basal respiration, (ii) leak respiration after injection of oligomycin (2 μg mL^{-1}), and (iii) uncoupled respiration after injection of FCCP (2.5 μM).

SDS-PAGE and immunoblotting

SDS-PAGE was performed as described previously [11, 12]. Proteins were extracted in buffer containing 62.5 mM Tris–HCl, pH 6.8; 10% (v/v) glycerol, 2% (w/v) sodium dodecyl sulfate (SDS), 0.5% bromophenol blue, 2.5% (v/v) β-mercapto-ethanol) and boiled at 95°C during 5 min. Proteins were then separated at 200 V during 60 min, using 10 or 12% polyacrylamide gel containing 0.35% (V/V) of 2,2,2-trichloroethanol for total protein staining, as previously described [13].

After electrophoresis, proteins were transferred to polyvinylidene difluoride (PVDF) membranes. Membranes were blocked for 1 h in 50 mM Tris–Cl, pH 7.6; 150 mM NaCl, 0.1% Tween, containing 5% BSA or 5% skimmed milk. PVDF membranes were incubated with primary antibodies overnight at 4°C. Protein immunodetection was performed using primary antibodies directed against NDUFA9 (ab14713, Abcam), NDUFAF6 (sc-17091, Santa Cruz), SDHA (ab14715, Abcam), UQCRC2 (ab14742, Abcam), TOM20 (sc-17764, Santa Cruz). Then, PVDF membranes were incubated for 1 h with appropriate peroxidase-conjugated antibodies. Finally, immunoblots were visualized by chemiluminescence using the ChemiDoc Touch imaging system (Biorad, USA).

Statistical analyses

Data are presented as mean ± SEM and were statistically analyzed using one-way or two-way ANOVA followed by Tukey *post hoc* test with GraphPad Prism 9. In figures, the datapoints correspond to experiments conducted independently on different days. The results of *post hoc* tests are shown with letters: datapoints with different letters are statistically different ($p < 0.05$) whereas datapoints with the same letters are not statistically different ($p > 0.05$). For instance, a datapoint labelled with the letter a is statistically different from datapoints marked with the letters b or bc, whereas it is not statistically different from datapoints labelled with the letters a or ab.

Results

We first compared the mitochondrial physiology in fibroblasts from control and AVFS patients. The control and patient 1 fibroblasts are the same cells analyzed in the original work on AVFS [1], whereas the fibroblasts of patient 2 were generated for this study. We characterized the molecular defects associated with the syndrome. AVFS is caused by a mutation in the CI assembly factor NDUFAF6, reducing the levels of the NDUFAF6 protein, thereby impairing complex I assembly and activity [1]. To confirm this, we compared levels of different mitochondrial proteins between fibroblasts derived from one control and two AVFS patients by immunoblotting. The data obtained show reduced levels of NDUFAF6 and of the complex I subunit NDUFA9 (Figure 1A). However, levels of CII subunit SDHA, CIII subunit UQRCRC2, and TOM20 were similar between control and AVFS fibroblasts (Figure 1A), confirming that AVFS specifically involves CI deficiencies and is not linked to a global reduction of mitochondrial mass, as previously reported [1].

In parallel to decreased levels of CI-related proteins (Figure 1A), we also observed reduced enzymatic activity of CI in AVFS fibroblasts (Figure 1B). To evaluate the impact on OXPHOS, we then measured mitochondrial membrane potential and oxygen consumption. Labeling with the mitochondrial membrane potential-dependent dye TMRM showed that AVFS fibroblasts have altered OXPHOS as compared to the control fibroblasts (Figure 1C). Similarly, OCR of 3 different respiratory states were also decreased in AVFS fibroblasts (Figure 1D). These data confirm the presence of mitochondrial dysfunction in AVFS fibroblasts, as observed previously [1].

Alterations in CI assembly and activity are a major cause of oxidative stress [8]. To address whether the AVFS-related CI deficiencies result in higher oxidative damage, we examined levels of 8-hydroxy-2′deoxyguanosine (8-OHdG), malondialdehyde (MDA), and carbonyl, which are well-known biomarkers for oxidative damage to DNA, lipids and proteins, respectively. Strikingly, levels of 8-OHdG, MDA and carbonyl were all increased in AVFS fibroblasts (Figures 1E–G). These findings indicate that AVFS involves oxidative stress.

We hypothesized that a treatment with an antioxidant, such as NAC, would alleviate the mitochondrial and oxidative alterations observed in AVFS fibroblasts. To address this, fibroblasts were treated with NAC (1 mM) for 5 days. This treatment had no effect on TMRM fluorescence and MDA levels in control fibroblasts

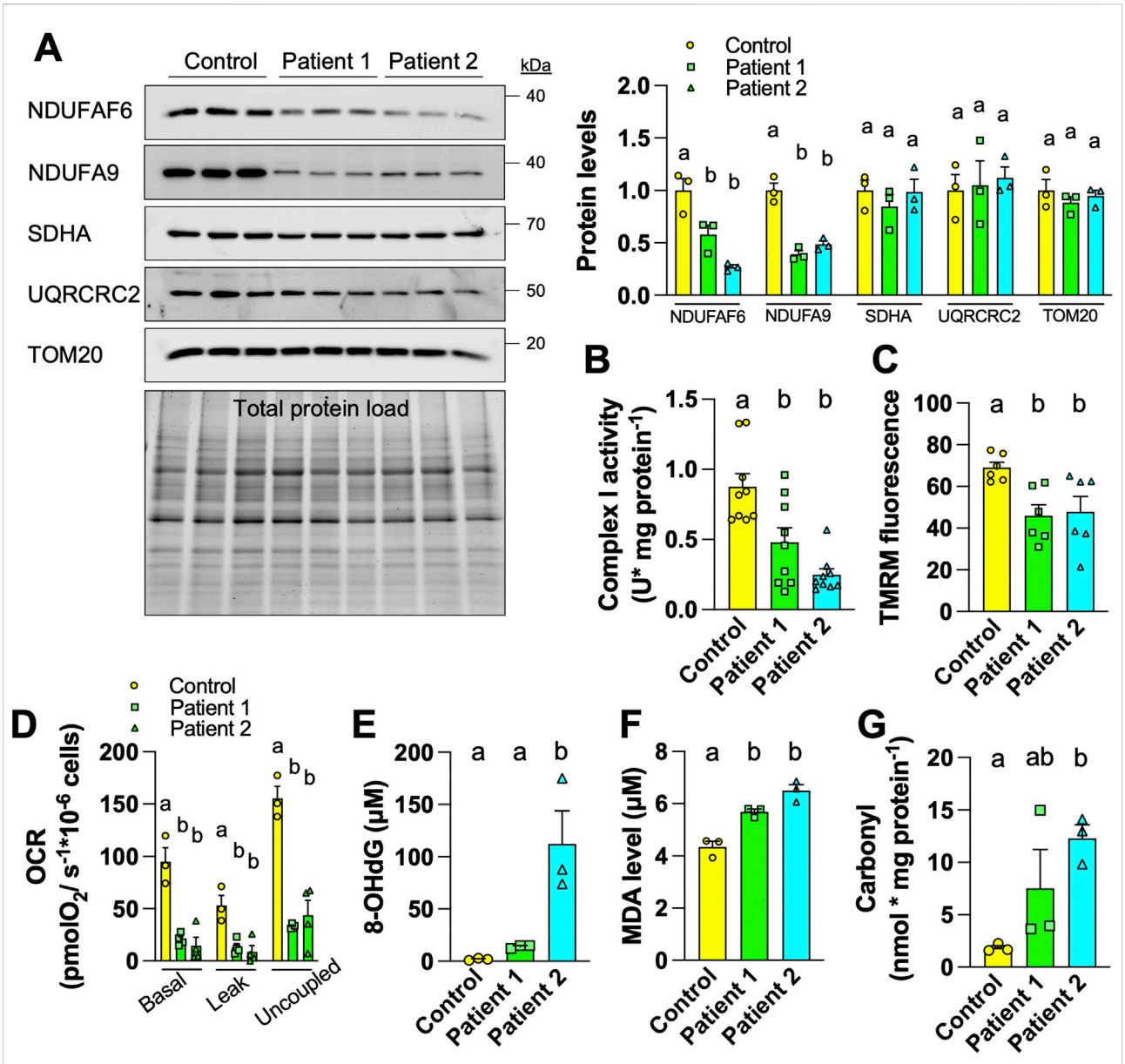

FIGURE 1
Fibroblasts derived from Acadian variant of Fanconi syndrome (AVFS) patients have mitochondrial deficits and oxidative damage. **(A)** Immunoblotting and quantification of mitochondrial proteins in fibroblasts derived from control or AVFS patients showing lower levels of NDUFAF6 and the complex I subunit NDUFA9 but not of SDHA, UQRCRC2 and TOM20. **(B)** The enzymatic activity of complex I is decreased in AVFS fibroblasts (n = 9). **(C)** Fluorescence of the mitochondrial membrane potential-dependent TMRM is decreased in AVFS fibroblasts (n = 6). **(D)** Oxygen consumption rates (OCR) at different respiratory states indicating lower mitochondrial metabolism in AVFS fibroblasts (n = 3-4). **(E–G)** Levels of **(E)** 8-hydroxy-2′-deoxyguanosine (8-OHdG), **(F)** malondialdehyde (MDA) and **(G)** carbonyl, which indicate oxidative damage on DNA, lipid and protein, respectively, are increased in AVFS fibroblasts (n = 3). Data are presented as mean +- SEM. Data with different letters are statistically different, as measured by one way ANOVA followed by post-hoc Tukey test.

(Figures 2A,B). Treatment of AVFS fibroblasts with NAC did not rescue NDUFAF6 levels (Figure 2C), but almost completely restored CI activity (Figure 2D) and mitochondrial membrane potential (Figure 2E). The NAC treatment fully rescued basal and leak OCR, but partially rescued uncoupled respiration in AVFS fibroblasts (Figure 2F). Levels of 8-OHdG were partially restored, whereas levels of MDA and carbonyl were completely restored in AVFS fibroblasts treated with NAC (Figures 2G–I). These findings indicate that the treatment with NAC is sufficient to reverse most of the oxidative damage induced by AVFS, and restore, at least partly, the mitochondrial deficiencies in fibroblasts derived from patients.

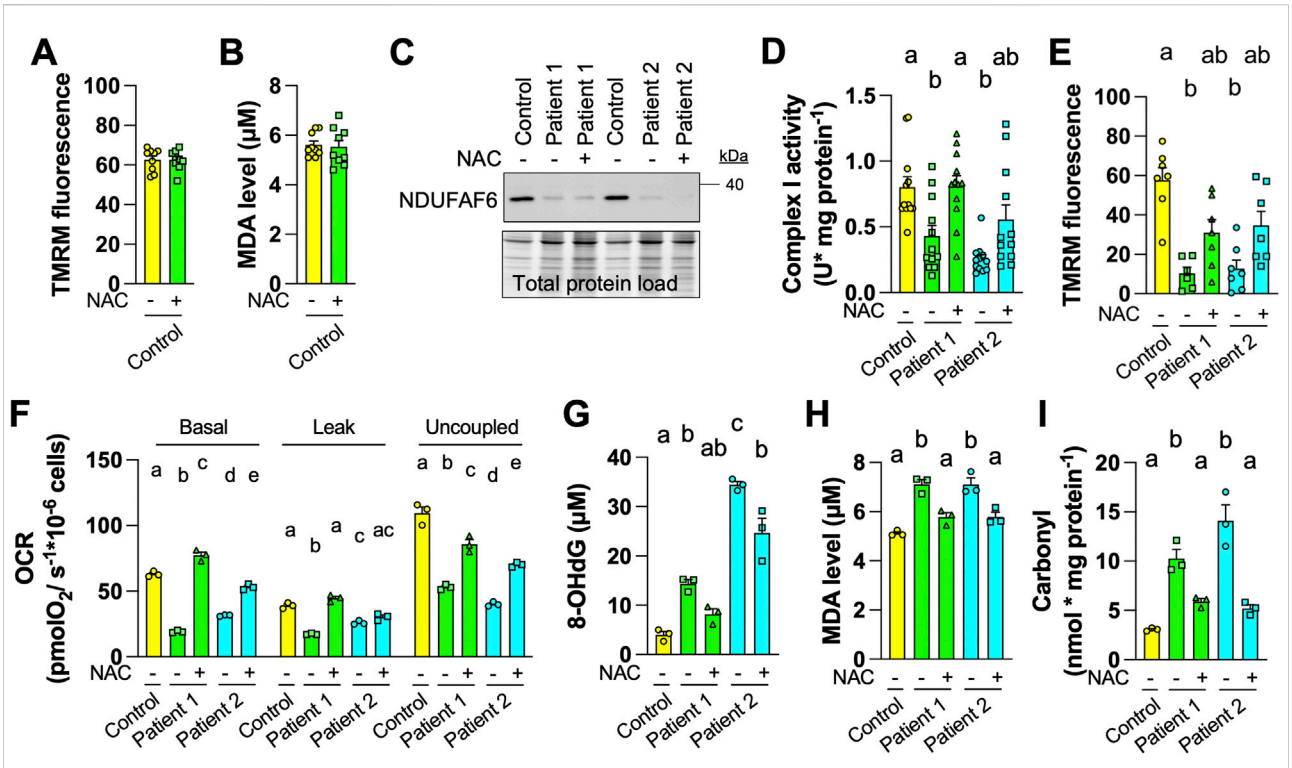

FIGURE 2
Treatment with the antioxidant N-Acetyl-L-cysteine (NAC) reverses oxidative damage in fibroblasts derived from Acadian variant of Fanconi syndrome (AVFS) patients. **(A)** TMRM fluorescence in control fibroblasts do not change after treatment with NAC (1 mM, 5 days, n = 9). **(B)** MDA levels in control fibroblasts do not change after treatment with NAC (n = 9). **(C)** Representative immunoblotting (n = 3) of NDUFAF6 in control and AVFS fibroblasts with vehicle or NAC, showing that NAC does not rescue levels of NDUFAF6. **(D)** The enzymatic activity of complex I is partly rescued in AVFS fibroblasts upon treatment with NAC (n = 12). **(E)** TMRM fluorescence is partly rescued in AVFS fibroblasts treated with NAC (n = 6-7). **(F)** Oxygen consumption rates (OCR) at different respiratory states are partly rescued upon treatment with NAC (n = 3) **(G–I)** Levels of **(G)** 8-hydroxy-2′-deoxyguanosine (8-OHdG), **(H)** malondialdehyde (MDA) and **(I)** carbonyl, which indicate that oxidative damage on DNA, lipid and protein, respectively, are partly rescued in AVFS fibroblasts treated with NAC (n = 3). Data are presented as mean +- SEM. Data with different letters are statistically different, as measured by one way ANOVA followed by post-hoc Tukey test.

Discussion

The aim of this work was to examine whether fibroblasts from AVFS patients have higher oxidative stress and test the potential beneficial effect of the antioxidant NAC to rescue the cellular and molecular defects linked to AVFS. Our findings demonstrate that AVFS fibroblasts from two different patients have higher levels of oxidative damage than control fibroblasts. Our findings also indicate that treatment with NAC can rescue the mitochondrial dysfunction and the oxidative damage associated to AVFS. This work suggests that NAC might be considered as promising treatment for AVFS.

NAC is a derivative of the amino acid cysteine and its antioxidant effect originates from its ability to promote the concentration of glutathione, an important thiol compound regulating redox potential within cells [14]. NAC is considered as a safe and inexpensive dietary supplement with limited side-effects, and is available over-the-counter in several countries [14]. It has received FDA approval for treatment of hepatotoxic dose of acetominophen [14]. NAC was also approved more recently for conditions with abnormal mucus secretion, including pneumonia and bronchitis [14]. NAC is used as short- and long-term treatment in several diseases related to both acute and chronic kidney impairments. For instance, short-term NAC treatment has been used in contrast-induced acute kidney injury, a condition in which kidney function is acutely altered after intravascular administration of iodinated contrast media for imaging purposes [15]. However, no global positive effects of NAC have been observed in this condition [16]. This could be due to the low bioavailability of the antioxidant upon oral administration [17–20]. However, various types of treatment with NAC appears to improve eGFR and reduce cardiovascular events in chronic kidney disease (CDK) [15]. For instance, patients with CDK treated with a chronic NAC regimen (600 mg of NAC orally twice daily during 3 years) had improved eGFR as compared to non-NAC users [19]. Overall, this suggest that chronic regimen with NAC could improve the renal function of AVFS patients.

Our findings suggest that oxidative stress is an important component within the physiopathology of AVFS since the most part of cellular defects in AVFS were rescued by NAC. For instance, the CI activity was almost completely rescued by

NAC, indicating that the CI enzymatic alterations caused by the AVFS-related mutation of NDUFAF6 are likely a consequence of oxidative damage on CI itself. Although this work is the first to report increased oxidative damage in AVFS, oxidative stress is commonly observed in mitochondrial diseases and other pathologies involving secondary mitochondrial dysfunctions, including neurodegenerative diseases [21]. In turn, NAC has been used to reverse oxidative stress in several pathological conditions related to mitochondrial dysfunctions [22–24]. For instance, it has been shown that NAC decreases levels of ROS and improve ATP production as well as mitochondrial membrane potential in fibroblasts derived from patients with different mitochondrial diseases [24]. NAC also delays the progression of motor deficits and improves mitochondrial functions in the R6/1 mouse models of Huntington's disease [25]. Overall, NAC improves mitochondrial function in cellular and animal models of various disorders involving mitochondrial dysfunction. However, this work is the first to demonstrate that NAC can be beneficial in AVFS patients.

It will be important to examine whether the positive effects of NAC observed in AVFS fibroblasts can be translated in patients. Indeed, fibroblasts from patients might not perfectly mimic the renal and lung cell types affected in AVFS since mitochondrial physiology varies across tissue and cell types [26–29]. Our findings could also be biased by the comparison with control fibroblasts obtained from ATCC, which potentially introduced variability due to differences in donor age, sex, and genetic background. Thus, the physiopathology of AVFS and the effect of NAC or other antioxidants should also be examined in patient-derived renal cells.

In conclusion, NAC represents a promising option for the treatment of AVFS since it rescued oxidative damage and mitochondrial dysfunction of AVFS fibroblasts. More studies should explore the potential beneficial effect of NAC and other antioxidant-based strategies in AVFS patients.

Author contributions

IA-Y, RM-J, MK, and YB performed experiments and analyzed data; CJ, YT, and EH-C planned the project; EH-C supervised the project; IA-Y, CJ, and EH-C wrote the manuscript. All authors contributed to the article and approved the submitted version.

References

1. Hartmannová H, Piherová L, Tauchmannová K, Kidd K, Acott PD, Crocker JFS, et al. Acadian variant of Fanconi syndrome is caused by mitochondrial respiratory chain complex I deficiency due to a non-coding mutation in complex I assembly factor NDUFAF6. *Hum Mol Genet* (2016) **25**:4062–79. doi:10.1093/hmg/ddw245

2. Wornell P, Crocker J, Wade A, Dixon J, Acott P. An Acadian variant of Fanconi syndrome. *Pediatr Nephrol* (2007) **22**:1711–5. doi:10.1007/s00467-007-0553-8

3. Crocker JF, McDonald AT, Wade AW, Acott PD. The acadian variant of fanconi's syndrome 1643. *Pediatr Res* (1997) **41**:276. doi:10.1203/00006450-199704001-01662

4. Zhang K, Li Z, Jaiswal M, Bayat V, Xiong B, Sandoval H, et al. The C8ORF38 homologue Sicily is a cytosolic chaperone for a mitochondrial complex I subunit. *J Cell Biol* (2013) **200**:807–20. doi:10.1083/jcb.201208033

Data availability

The raw data supporting the conclusions of this article will be made available by the authors, without undue reservation.

Ethics statement

The studies involving humans were approved by Comité d'éthique de la recherche (CÉR) du Réseau de santé Vitalité. The studies were conducted in accordance with the local legislation and institutional requirements. The participants provided their written informed consent to participate in this study.

Funding

The author(s) declare that financial support was received for the research and/or publication of this article. EH-C and YT received funding from DUO (Centre de formation médicale du Nouveau-Brunswick). EH-C also received funding from Canada Research Chair, CFI, ResearchNB and NBIF.

Acknowledgments

We are grateful to T. Mracek and P. Pecina (Cezch Academy of Science) for providing control and patient 1 fibroblasts. We also acknowledge M. Leblanc from G.-L.-Dumont University Hospital Center for preparing skin biopsies of patient 2.

Conflict of interest

The author(s) declared no potential conflicts of interest with respect to the research, authorship, and/or publication of this article.

Generative AI statement

The authors declare that no Generative AI was used in the creation of this manuscript.

5. Mitchell P, Moyle J. Chemiosmotic hypothesis of oxidative phosphorylation. *Nature* (1967) **213**:137–9. doi:10.1038/213137a0

6. Brand MD, Nicholls DG. Assessing mitochondrial dysfunction in cells. *Biochem J* (2011) **435**:297–312. doi:10.1042/bj20110162

7. Coughlan MT, Sharma K. Challenging the dogma of mitochondrial reactive oxygen species overproduction in diabetic kidney disease. *Kidney Int* (2016) **90**: 272–9. doi:10.1016/j.kint.2016.02.043

8. Hirst J, King MS, Pryde KR. The production of reactive oxygen species by complex I. *Biochem Soc Trans* (2008) **36**:976–80. doi:10.1042/bst0360976

9. Pollard AK, Craig EL, Chakrabarti L. Mitochondrial complex 1 activity measured by spectrophotometry is reduced across all brain regions in ageing and more specifically in neurodegeneration. *PLoS One* (2016) **11**:e0157405. doi:10.1371/journal.pone.0157405

10. Guedouari H, Daigle T, Scorrano L, Hebert-Chatelain E. Sirtuin 5 protects mitochondria from fragmentation and degradation during starvation. *Biochim Biophys Acta (Bba) - Mol Cell Res* (2017) **1864**:169–76. doi:10.1016/j.bbamcr.2016.10.015

11. Djeungoue-Petga M-A, Lurette O, Jean S, Hamel-Côté G, Martín-Jiménez R, Bou M, et al. Intramitochondrial Src kinase links mitochondrial dysfunctions and aggressiveness of breast cancer cells. *Cell Death Dis* (2019) **10**:940–15. doi:10.1038/s41419-019-2134-8

12. Lurette O, Guedouari H, Morris JL, Martín-Jiménez R, Robichaud JP, Hamel-Côté G, et al. Mitochondrial matrix-localized Src kinase regulates mitochondrial morphology. *Cell Mol Life Sci* (2022) **79**(6):327. doi:10.1007/s00018-022-04325-y

13. Ladner CL, Yang J, Turner RJ, Edwards RA. Visible fluorescent detection of proteins in polyacrylamide gels without staining. *Anal Biochem* (2004) **326**:13–20. doi:10.1016/j.ab.2003.10.047

14. Tenório MCd. S, Graciliano NG, Moura FA, Oliveira ACMd., Goulart MOF, Goulart MOF. N-acetylcysteine (NAC): impacts on human health. *Antioxidants* (2021) **10**:967. doi:10.3390/antiox10060967

15. Hernández-Cruz EY, Aparicio-Trejo OE, Hammami FA, Bar-Shalom D, Tepel M, Pedraza-Chaverri J, et al. N-Acetylcysteine in kidney disease: molecular mechanisms, pharmacokinetics, and clinical effectiveness. *Kidney Int Rep* (2024) **9**: 2883–903. doi:10.1016/j.ekir.2024.07.020

16. ACT Investigators*. Acetylcysteine for prevention of renal outcomes in patients undergoing coronary and peripheral vascular angiography. *Circulation* (2011) **124**:1250–9. doi:10.1161/circulationaha.111.038943

17. Borgström L, Kågedal B, Paulsen O. Pharmacokinetics of N-acetylcysteine in man. *Eur J Clin Pharmacol* (1986) **31**:217–22. doi:10.1007/bf00606662

18. Olsson B, Johansson M, Gabrielsson J, Bolme P. Pharmacokinetics and bioavailability of reduced and oxidized N-acetylcysteine. *Eur J Clin Pharmacol* (1988) **34**:77–82. doi:10.1007/bf01061422

19. Chiu A-H, Wang C-J, Lin Y-L, Wang C-L, Chiang T-I. N-acetylcysteine alleviates the progression of chronic kidney disease: a three-year cohort study. *Medicina (Mex.)* (2023) **59**:1983. doi:10.3390/medicina59111983

20. Holdiness MR. Clinical pharmacokinetics of N-acetylcysteine. *Clin Pharmacokinet* (1991) **20**:123–34. doi:10.2165/00003088-199120020-00004

21. Lin MT, Beal MF. Mitochondrial dysfunction and oxidative stress in neurodegenerative diseases. *Nature* (2006) **443**:787–95. doi:10.1038/nature05292

22. Kamboj SS, Sandhir R. Protective effect of N-acetylcysteine supplementation on mitochondrial oxidative stress and mitochondrial enzymes in cerebral cortex of streptozotocin-treated diabetic rats. *Mitochondrion* (2011) **11**:214–22. doi:10.1016/j.mito.2010.09.014

23. Cocco T, Sgobbo P, Clemente M, Lopriore B, Grattagliano I, Di Paola M, et al. Tissue-specific changes of mitochondrial functions in aged rats: effect of a long-term dietary treatment with N-acetylcysteine. *Free Radic Biol Med* (2005) **38**: 796–805. doi:10.1016/j.freeradbiomed.2004.11.034

24. Douiev L, Soiferman D, Alban C, Saada A. The effects of ascorbate, N-acetylcysteine, and resveratrol on fibroblasts from patients with mitochondrial disorders. *J Clin Med* (2016) **6**:1. doi:10.3390/jcm6010001

25. Wright DJ, Renoir T, Smith ZM, Frazier AE, Francis PS, Thorburn DR, et al. N-Acetylcysteine improves mitochondrial function and ameliorates behavioral deficits in the R6/1 mouse model of Huntington's disease. *Transl Psychiatry* (2015) **5**:e492. doi:10.1038/tp.2014.131

26. Burr SP, Chinnery PF. Origins of tissue and cell-type specificity in mitochondrial DNA (mtDNA) disease. *Hum Mol Genet* (2024) **33**:R3–R11. doi:10.1093/hmg/ddae059

27. Herbers E, Kekäläinen NJ, Hangas A, Pohjoismäki JL, Goffart S. Tissue specific differences in mitochondrial DNA maintenance and expression. *Mitochondrion* (2019) **44**:85–92. doi:10.1016/j.mito.2018.01.004

28. Chen L, Zhou M, Li H, Liu D, Liao P, Zong Y, et al. Mitochondrial heterogeneity in diseases. *Signal Transduction Targeted Ther* (2023) **8**:311–27. doi:10.1038/s41392-023-01546-w

29. Johnson DT, Harris RA, French S, Blair PV, You J, Bemis KG, et al. Tissue heterogeneity of the mammalian mitochondrial proteome. *Am J Physiology-Cell Physiol* (2007) **292**:C689–C697. doi:10.1152/ajpcell.00108.2006

EBM Experimental Biology and Medicine

TYPE Original Research
PUBLISHED 22 May 2025
DOI 10.3389/ebm.2025.10585

OPEN ACCESS

*CORRESPONDENCE
Douglas J. Perkins,
dperkins@salud.unm.edu

RECEIVED 19 March 2025
ACCEPTED 06 May 2025
PUBLISHED 22 May 2025

CITATION
Wasena SA, Onyango CO, Osata SW, Anyona SB, Raballah E, Hurwitz I, Seidenberg PD, Ouma C, Cheng Q, Schneider KA and Perkins DJ (2025) Diagnostic accuracy of *Pf*HRP2-based malaria rapid diagnostic tests and antigenemia persistence in Kenyan children from a holoendemic region: implications for case management and surveillance.
Exp. Biol. Med. 250:10585.
doi: 10.3389/ebm.2025.10585

Diagnostic accuracy of *Pf*HRP2-based malaria rapid diagnostic tests and antigenemia persistence in Kenyan children from a holoendemic region: implications for case management and surveillance

Sharley A. Wasena[1,2], Clinton O. Onyango[1,2], Shamim W. Osata[1,2], Samuel B. Anyona[1,3], Evans Raballah[1,4], Ivy Hurwitz[5], Philip D. Seidenberg[5,6], Collins Ouma[1,2], Qiuying Cheng[5], Kristan A. Schneider[5] and Douglas J. Perkins[1,5]*

[1]University of New Mexico-Kenya Global Health Programs, Kisumu, Kenya, [2]Department of Biomedical Sciences and Technology, School of Public Health and Community Development, Maseno University, Maseno, Kenya, [3]Department of Medical Biochemistry, School of Medicine, Maseno University, Maseno, Kenya, [4]Department of Medical Laboratory Sciences, School of Public Health, Biomedical Sciences and Technology, Masinde Muliro University of Science and Technology, Kakamega, Kenya, [5]Center for Global Health, Department of Internal Medicine, University of New Mexico, Albuquerque, NM, United States, [6]Department of Emergency Medicine, School of Medicine, University of New Mexico, Albuquerque, NM, United States

Abstract

Malaria remains a significant cause of childhood morbidity and mortality, with *Plasmodium falciparum* Histidine-Rich Protein 2 (*Pf*HRP2)-based malaria rapid diagnostic tests (mRDTs) widely used in endemic regions where microscopy is sometimes not feasible. While these tests offer high sensitivity, persistent *Pf*HRP2 antigenemia and gene deletions can cause false-positive and false-negative results, compromising their accuracy for malaria case management and surveillance. This study evaluated the diagnostic performance and antigen persistence of *Pf*HRP2-mRDTs using data from a longitudinal birth cohort of 750 children followed monthly from birth to 36 months in a holoendemic region of Kenya. Malaria diagnosis was performed using both microscopy and mRDTs, with a total of 15,006 clinical events recorded from 573 children between 2017 and 2023. Data from an independent acute febrile cohort of 937 children (<5 years) followed for 14 days was analyzed to validate the findings. The mRDT showed a high sensitivity of 97.27% but a moderate specificity of 65.00% in acute febrile illness, indicating frequent false-positive results. The positive predictive value was low (35.10%), suggesting that confirmatory testing is needed, while the negative predictive value was high (98.89%), reinforcing the reliability of mRDTs in ruling out malaria. Persistent *Pf*HRP2 antigenemia was observed, with a median antigen clearance time of

51.14 days, respectively. Higher initial parasite densities (>50,000/μL) were associated with a slower antigen decay rate (p = 0.001), highlighting the challenge of interpreting positive mRDT results after treatment. Validation using the acute febrile cohort showed that mRDT specificity exceeded 95% at initial diagnosis and follow-up. Overall, *Pf*HRP2-based mRDTs remain valuable for frontline malaria diagnosis but are limited by antigen persistence, leading to false positives in follow-up testing. Where feasible, integration of confirmatory diagnostic methods, such as microscopy or molecular assays, could improve the performance of malaria case management and clinical decision making, particularly in high-transmission settings.

KEYWORDS

malaria diagnosis, *Plasmodium falciparum*, histidine rich protein, *Pf*HRP2, mRDT

Impact statement

The findings from this study provide critical insights into the diagnostic performance and antigen persistence of PfHRP2-based malaria rapid diagnostic tests (mRDTs) in a holoendemic region, highlighting their strengths and limitations in clinical and surveillance settings. The study advances the field by demonstrating that while mRDTs have high sensitivity and reliability in ruling out malaria, their specificity is compromised due to prolonged antigenemia, leading to false positives during follow-up assessments. This work presents novel longitudinal data showing that antigen persistence extends beyond two months post-treatment, with higher initial parasite densities slowing clearance. These findings have significant implications for malaria case management, emphasizing the need for confirmatory diagnostic strategies to improve accuracy and treatment decisions. By identifying antigenemia persistence as a key challenge, this study informs malaria control programs and underscores the necessity for improved diagnostic algorithms to enhance surveillance, reduce overtreatment, and guide policy development in high-transmission regions.

Introduction

Malaria continues to pose a major global public health threat, with 263 million cases of illness and 597,000 deaths annually [1]. In the World Health Organization (WHO) African Region, *Plasmodium falciparum*, the deadliest malaria species, accounts for the majority of the cases (247 million, 94%) and mortality (567,000, 95%) [1]. Children under five are the most vulnerable group, accounting for 76% of the malaria-related fatalities (432,400) in this region [1–3]. Kenya faces a substantial challenge, with ~3.29 million cases and 1,060 deaths annually, primarily in this susceptible age group [1]. In western Kenya, the highest-burden area, malaria prevalence is exceptionally high in Siaya County, where the microscopy positivity rate among children under five was reported to be 54.9% [4]. Another survey in western Kenya found a positivity rate of 32.8% among children under five, with prevalence increasing with age [5]. These findings highlight the disproportionate impact of malaria on young children in western Kenya, emphasizing the need for targeted interventions and prevention measures to reduce morbidity and mortality in this high-risk population.

Achieving these goals requires accurate diagnosis and timely treatment, which are critical for effective malaria management [6]. Misdiagnosis or delays in treatment can result in severe complications and increased mortality rates [3, 6]. To address this, the WHO recommends the use of parasite-based diagnostic methods, such as microscopy and/or malaria rapid diagnostic tests (mRDTs) before administering antimalarial treatment [7]. Moreover, residual drug concentrations in misdiagnosed individuals can shape a selective environment facilitating the evolution of drug resistance [8, 9].

Microscopy is the gold standard for malaria diagnosis, providing highly sensitive and specific detection of malaria parasites, allowing for quantifying parasitemia and identifying the infecting *Plasmodium* species, which is crucial for determining appropriate treatment strategies [3, 7, 10]. Despite these advantages, microscopy faces significant challenges in resource-limited settings. The method requires personnel with expertise in preparing and interpreting blood smears, along with access to specialized equipment, high-quality reagents, and a reliable electricity supply. These infrastructure and resource constraints limit microscopy's availability and consistent application in many endemic regions [10, 11].

Consequently, alternative diagnostic tools, such as mRDTs have become essential for improving access to cost-effective malaria diagnosis in resource-limited settings [12, 13]. The mRDTs are immuno-chromatographic tests that detect parasite-specific antigens in peripheral blood, typically using a finger-prick blood sample [7]. Compared to microscopy, mRDTs

are relatively simple to perform and interpret, overcoming the challenges of infrastructure limitations and making them valuable in resource-constrained areas [7, 14]. The mRDTs vary in their ability to detect different malaria species (e.g., *P. falciparum*, *P. vivax*, *P. ovale*, and *P. malariae*) by targeting specific antigens produced by the malaria parasites, enabling the differentiation of species or confirming the presence of *Plasmodium* parasites in mixed infections [7, 10]. For *P. falciparum*, the commonly targeted antigen is histidine-rich protein 2 (*Pf*HRP2) with some cross-reactivity with *Pf*HRP3 [10, 15]. Other mRDTs detect the enzyme *Plasmodium* lactate dehydrogenase (*P*LDH), which is expressed by all *Plasmodium* species but can be species-specific depending on the test [10]. Additionally, aldolase, another enzyme involved in the parasite's glycolytic pathway, may be targeted for broader detection of non-*P. falciparum* species [10].

However, challenges such as *Pf*HRP2 gene deletions can impact the reliability of mRDTs in diagnosing *P. falciparum* infections and provide false negative results [3, 15]. Such deletions have been reported in multiple malaria-endemic areas, including Kenya, although with a low prevalence [16–18]. Infection caused by non-falciparum species can also result in false negatives since *Pf*HRP2-based mRDT is designed to detect *P. falciparum*-specific antigens [19]. In addition, low-density parasitemia below the detection threshold (100-200 parasites/μL) [20] of mRDTs can decrease the sensitivity of *Pf*HRP2-specific tests and generate false negative results [21, 22].

The widespread use of *Pf*HRP2-based mRDTs for detecting *P. falciparum* in holoendemic regions (e.g., western Kenya) presents both advantages and disadvantages. While these tests offer a viable tool for prompt diagnosis in resource-constrained settings, the thermostable *Pf*HRP2 antigens can persist in the bloodstream after parasite clearance, leading to false-positive results in individuals who have cleared the parasite [23–25]. This persistent antigenemia complicates the detection of new infections after antimalarial treatment, reducing the effectiveness of mRDTs for post-treatment follow-up, particularly in high-transmission areas where recurrent malaria infections are common. Collectively, both false-negative and false-positive results can impact treatment decisions and potentially contribute to the misinterpretation and mismanagement of malaria cases.

Treating a child with antimalarials when the individual is aparasitemic can contribute to the selection and spread of drug-resistant malaria strains by exerting unnecessary drug pressure, potentially eliminating susceptible parasites while allowing resistant ones to survive and propagate [26]. In addition, treating a child for malaria when they do not have the infection can result in missing the actual cause of their symptoms, such as bacterial or viral infections that are common co-morbidities in malaria-endemic settings and require different treatments [27–29]. This can result in potentially delaying appropriate care and lead to worsening of the child's condition or complications from the untreated underlying illness. Antimalarial drugs can also have side effects, including gastrointestinal symptoms and allergic reactions and, in rare cases, severe adverse effects like neurotoxicity or cardiac issues [30, 31]. Unnecessary administration of these drugs exposes the child to these risks without any therapeutic benefit.

In the current study, we utilized concurrent microscopy and mRDTs for diagnosis of malaria infection in a mother-child birth cohort followed for 36 months (mos.), aimed at improving malaria management in affected cases. The longitudinal design provided valuable insights into the sensitivity and specificity of these diagnostic tools in detecting malaria in a highly vulnerable population of young children. Repeated longitudinal measurements allowed for the evaluation of diagnostic methods during early childhood when children are most vulnerable to malaria, as their immunity develops through repeated infections with varying parasite levels. Additionally, the study enabled an assessment of the persistence of antigenemia detected by the *Pf*HRP2 based mRDT across multiple infection events (n = 9,958). Collectively, these findings present a comprehensive evaluation of mRDT performance in children during their first 3 years of life in a high *P. falciparum* transmission setting.

Materials and methods

Mother-child pair longitudinal birth cohort

To evaluate the performance of mRDTs (i.e., CareStart Malaria HRP2, *Pf*) in a holoendemic *P. falciparum* setting, we first utilized data collected from a prospective birth cohort that enrolled 750 mother/child pairs between July 2017 and February 2023 at the Siaya County Referral Hospital (SCRH). Details of the study area have previously been described [32]. The mother/child cohort study was designed to investigate the pathogenesis of severe malaria anemia [SMA (hemoglobin, Hb) <6.0 g/dL] during the development of naturally acquired malarial immunity over the first 36 mos. of life in HIV-negative children. Data utilized for the current investigation included measures collected from the mothers at delivery and from the children across the follow-up period. Pregnant women received an explanation of the research protocol and were provided with HIV counseling, with the understanding that enrollment decisions would be made following HIV screening using rapid serological tests. HIV-negative women, regardless of malaria status, who met the following criteria were enrolled: ≥16 years of age, capable and willing to sign informed consent, willing to enroll their child in the study, committed to attending scheduled appointments and study visits over 36 mos., able to provide two contacts familiar with

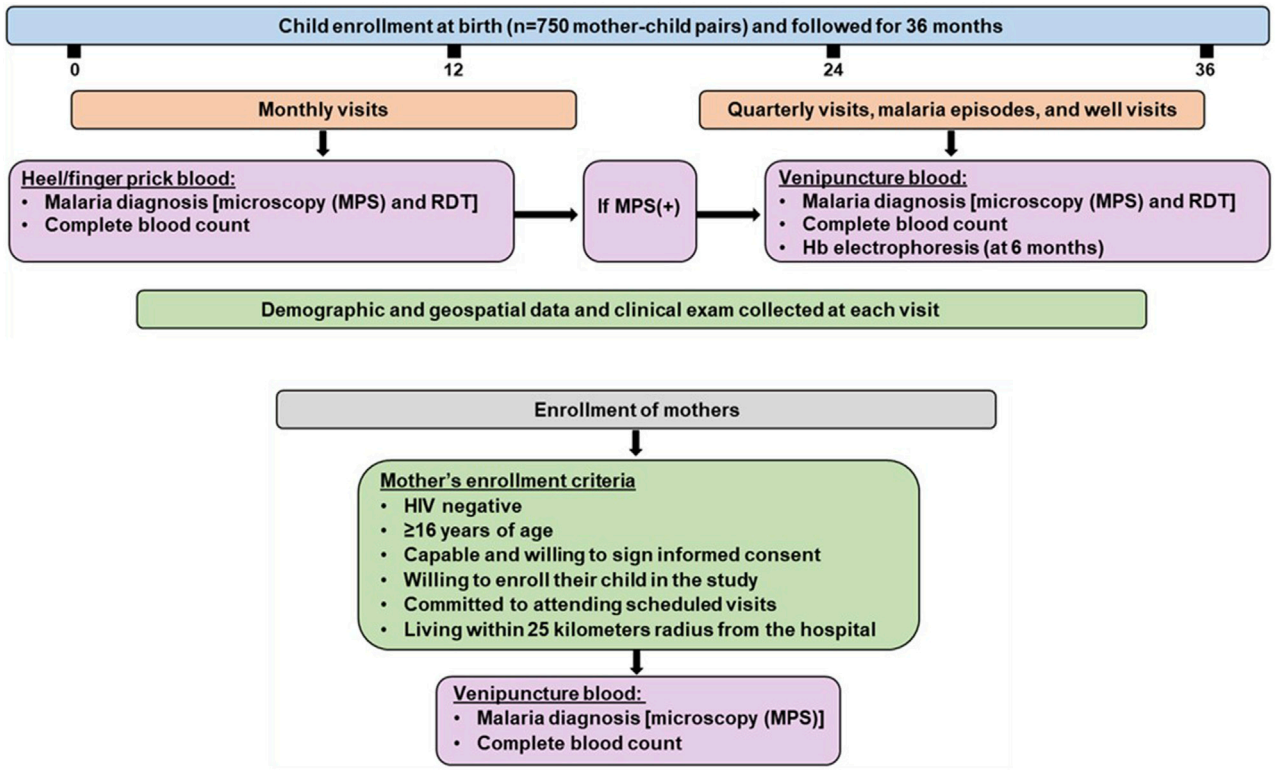

FIGURE 1
Mother-child longitudinal cohort study design. The study was conducted at Siaya County Referral Hospital, a holoendemic *P. falciparum* transmission region. Infants were enrolled at birth (n = 750) and followed for 36 months. Malaria and other endemic infections were monitored monthly and at acute febrile episodes throughout the study. Monthly testing for malaria was performed using microscopy and mRDT in heel/finger prick blood samples. Quarterly testing for malaria was conducted using microscopy and mRDT in venipuncture blood. Venipuncture was also performed on children found to have malaria at monthly or acute febrile visits and a 14-day follow-up (well-visit). Demographic and geospatial data were collected at each visit and a complete physical exam was performed. The study included HIV-negative mothers who met the inclusion criteria, regardless of malaria status. MPS: Malaria parasite, mRDT: malaria rapid diagnostic test, (+): positive, (–): negative.

the child's whereabouts, and living within a 25-km radius from the hospital. The study was approved by the Institutional Review Board of the University of New Mexico, United States, and the Maseno University Scientific and Ethics Review Committee, Kenya.

Follow-up of children in the longitudinal birth cohort

Children were followed monthly for 36 months. Comprehensive demographic data was collected, and a complete physical exam was performed at each scheduled and non-scheduled (acute) visit. If parents/guardians missed a scheduled visit, study staff visited the residence to check the child's health status (including mortality). Children were readily located through our geospatial surveillance system, which captured the participants' location at enrollment when mothers/guardians were provided transport to their residences/homesteads. To monitor infections and hematological parameters, heel/finger-prick blood (<100 μL) was collected monthly, while venipuncture blood (2-3 mL) was obtained quarterly, during malaria episodes, and 14 days after a documented illness (well-check). To monitor health status, parents/guardians were provided with a thermometer (Vive Precision®) and asked to bring their child to the hospital when febrile (>37.5°C). To ensure comprehensive documentation of all malaria episodes and other pediatric infectious diseases during the study, all participants underwent comprehensive laboratory testing for proper diagnosis, followed by clinical management according to the Kenya Ministry of Health guidelines. The study design and information captured at the visits are presented in Figure 1.

Acute febrile validation cohort

A prospective cohort study of children with acute febrile illness was also conducted at SCRH, enrolling 937 children aged 1–59 months between March 2017 and January 2024. Children presenting at SCRH with symptoms of infectious diseases were eligible if they met the following criteria: temporal temperature of ≥37.5°C, in-patient admission residence within 25 km of the

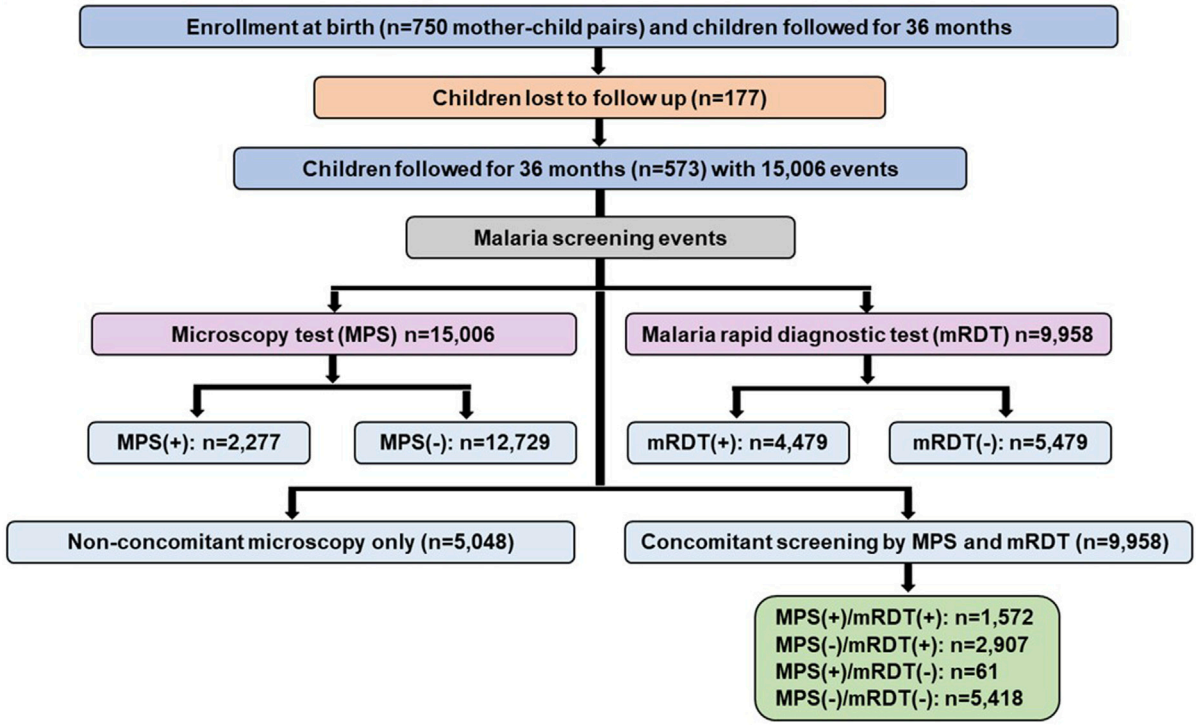

FIGURE 2
Data selection strategy for mother-child longitudinal cohort. The study enrolled 750 mother-child pairs in the longitudinal birth cohort. Based on relocation of study participants during the COVID-19 pandemic, 573 children had comprehensive follow-up information over 36 months, contributing to 15,006 clinical events. Malaria screening was performed using microscopy in all events, with 2,277 positive cases and 12,729 negatives. Malaria rapid diagnostic tests (mRDTs) were conducted for 9,958 events, with 4,479 positive and 5,479 negative results. A subset of 9,958 events had concomitant microscopy and mRDT results, classified as MPS (+)/mRDT (+) (n = 1,572), MPS (–)/mRDT (+) (n = 2,907), MPS (+)/mRDT (–) (n = 61), and MPS (–)/mRDT (–) (n = 5,418). An additional 5,048 events underwent microscopy-only screening since mRDT was introduced later in the study. MPS: Malaria parasite, mRDT: malaria rapid diagnostic test, (+): positive, (–): negative.

hospital, and the parent/guardian willing to sign an informed consent and commit to a day-14 follow-up. Children with non-infectious diseases or a history of prior hospitalization were excluded from the study. Demographic and clinical data were collected at enrollment, and each child underwent a comprehensive physical examination. Peripheral blood (3–4 mL) was drawn via venipuncture before starting antimalarial treatment for hematological parameters, as well as malaria diagnosis using microscopy and an mRDT (CareStart Malaria HRP2, *Pf*).

Laboratory procedures for longitudinal birth and acute febrile validation cohort

Complete blood counts (CBCs) were performed using a DxH 500 hematology analyzer (Beckman-Coulter; Miami, FL, United States). The mRDT (CareStart Malaria HRP2, *Pf*) was used to screen for malaria infection following the manufacturer's protocol [33]. Briefly, 5 µL of whole blood was placed on a sample well, and two drops of buffer were added to the buffer well. The results were determined after 15–20 min at room temperature. Malaria parasite densities were determined using light microscopy as previously described [32]. Briefly, Giemsa-stained thick and thin blood smears were prepared and examined for asexual malaria parasites in 200 high-power fields under oil immersion at ×1,000 magnification (i.e., a ×100 objective lens with a ×10 eyepiece). Parasite density was determined per 300 leukocytes and estimated using the total leukocyte count for each patient as determined by the hematology analyzer. For quality control, a second well-trained laboratory personnel read and independently confirmed the malaria microscopy results. Thick blood smears were considered negative if no parasites were observed in 200 high-power fields. The thresholds of low (≤999 parasites/µL), medium (1,000–49,999 parasites/µL), and high parasitemia (≥50,000 parasites/µL) were defined by a combination of nominal and prior field studies in holoendemic transmission settings. For example, mRDTs can perform less favorably at <1,000 parasites/µL (~0.02% parasitemia, assuming a standard RBC count of 5 M cells), whereas more severe malaria cases in our studies and others are commonly

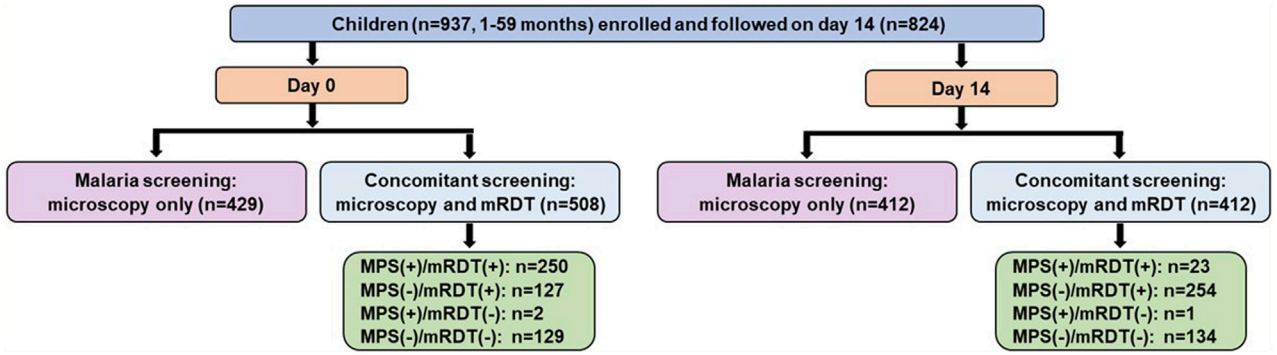

FIGURE 3
Data selection strategy for the short-term febrile cohort. Malaria screening outcomes among 937 febrile children (aged 1–59 months) enrolled in an acute febrile illness cohort and followed up on Day 14 (well-visit). At Day 0 (acute presentation, pre-treatment), malaria screening was performed using microscopy alone (n = 429) or concomitant microscopy and malaria rapid diagnostic tests (mRDT) (n = 508). Among those with concomitant screening, 250 children were positive by both microscopy and mRDT [MPS (+)/mRDT (+)], 127 were negative by microscopy but positive by mRDT [MPS (–)/mRDT (+)], 2 were positive by microscopy but negative by mRDT [MPS (+)/mRDT (–)], and 129 were negative by both tests [MPS (–)/mRDT (–)]. At the Day 14 follow-up visit, 824 children returned, with 412 undergoing microscopy-only screening and 412 receiving concomitant microscopy and mRDT testing. Among the concomitant testing group, 23 children were positive by both microscopy and mRDT, 254 were negative by microscopy but positive by mRDT, 1 was positive by microscopy but negative by mRDT, and 134 were negative by both tests. MPS: Malaria parasite, mRDT: malaria rapid diagnostic test, (+): Positive, (–): Negative.

associated with parasite densities above 50,000 parasites/μL (~1.0% parasitemia) [24, 34–38]. Sickle-cell trait status was determined by alkaline cellulose acetate electrophoresis (Helena Laboratories, Beaumont, TX, United States). In the acute febrile cohort, HIV-1 status was determined by two rapid serological antibody tests (Unigold™ Trinity Biotech, Jamestown, NY, United States and Determine™). For cases with single or concordant positive results, an HIV-1 proviral DNA PCR test was used to confirm infection [39]. Bacteremia was diagnosed by performing bacterial cultures on ~1.0 mL of venipuncture blood collected aseptically, inoculated into BD BACTEC™ PEDS Plus PRIME Medium Culture Vials (Becton-Dickinson, Franklin Lakes, NJ, United States), and incubated in an automated BACTEC 9050 system (Becton-Dickinson) for 5 days. Positive alerts were then examined by Gram staining and sub-cultured on blood agar, chocolate agar or MacConkey agar plate (Hardy Diagnostics, Santa Maria, CA, United States) [27].

Data selection for evaluating diagnostic accuracy and antigenemia persistence of the *PfHRP2*-mRDT in the longitudinal cohort

The mother-child cohort study enrolled 750 mother-child pairs with children followed longitudinally for 36 mos. after delivery (Figure 2). Due to the COVID-19 pandemic, there was a substantial relocation of study participants and subsequent loss to follow-up of 177 children. As such, 573 children remained in the cohort with comprehensive data for the scheduled longitudinal follow-up and acute visits, totaling 15,006 events. Of these, 2,277 were microscopy positive for malaria (MPS+) and 12,729 were microscopy negative (MPS-). From the 15,006 events for which microscopy was performed, there were 9,958 events with concomitant mRDT results. The mRDT (+) events were 4,479, while the mRDT (–) events were 5,479. All analyses presented are based on the 9,958 events with concomitant microscopy and mRDT results, enabling a direct comparison of mRDT performance against microscopy as the gold standard.

Data selection to validate the mRDT specificities and sensitivities in an acute febrile cohort

The short-term cohort enrolled 937 children on day 0 (acute episode) and had 824 individuals return for the follow-up (well-visit) on day 14 (Figure 3). Concomitant microscopy and mRDT results were available for 508 children on day 0 and 412 on day 14.

Statistical analysis

The demographic and clinical characteristics for concomitant microscopy and mRDT measures were analyzed using SPSS (version 23.0, SPSS Inc., Chicago, IL, United States) and R (version 4.3.0). To compare the distributions of categorical variables to null distributions, χ^2 goodness of fit test was used.

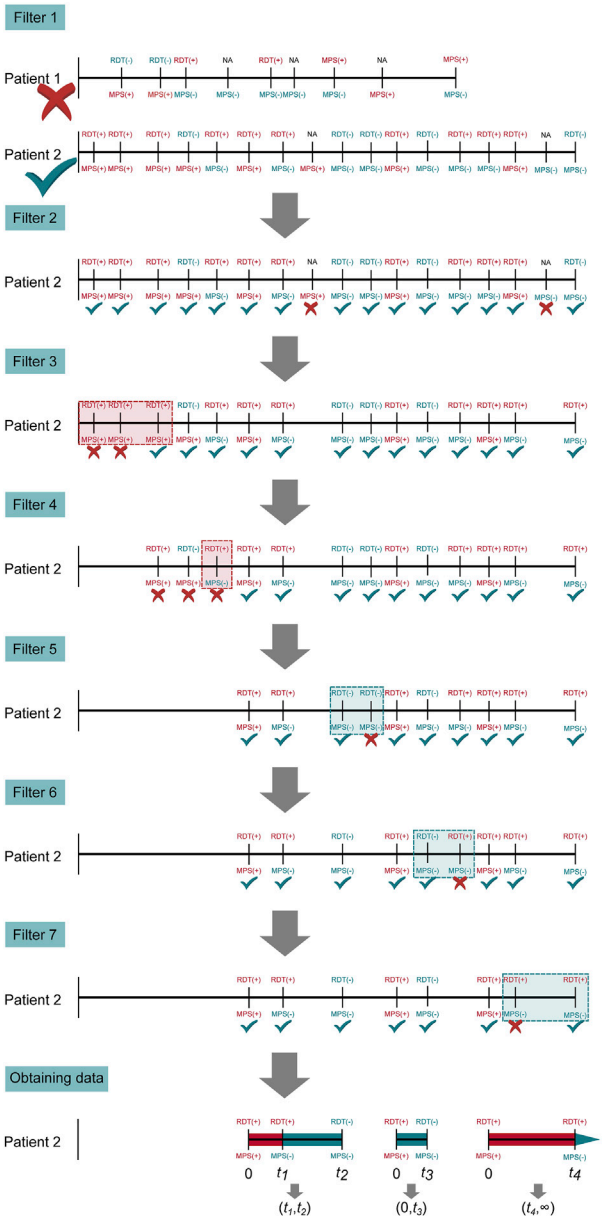

FIGURE 4
Steps of pre-processing to obtain interval-censored data. Illustrated are the seven filtering steps applied to patient visits to obtain interval-censored time-to-event data to ensure accurate evaluation of PfHRP2 antigen persistence. Filter 1: Excludes patients without both mRDT and microscopy results; Filter 2: Retains only patients with at least one positive malaria microscopy (MPS+) and mRDT (+) event; Filter 3: Removes redundant consecutive positive MPS(+) events, selecting only the last occurrence in each sequence; Filter 4: Eliminates inconsistent mRDT (−) results within an MPS(+) sequence to ensure HRP2 decay tracking; Filter 5: Retains only the first microscopy-negative (MPS-) visit following the last positive malaria episode; Filter 6: Removes intermittent mRDT-positive results in sequences where microscopy was negative; Filter 7: Final refinement ensures consistent representation of diagnostic results. The final data set captures distinct malaria infection episodes and HRP2 antigen

(*Continued*)

FIGURE 4 (Continued)
persistence to evaluate mRDT accuracy and antigen clearance over time. Horizontal lines correspond to longitudinal follow-up periods past the enrollment date (i.e., birth). Vertical lines indicate patient visits, with MPS and mRDT results. For example, patient 1 was eliminated by the first filter since the patient had no MPS (+) and mRDT (+) result. Patient 2 has three interval-censored events, which are treated as independent observations in the parametric Cox proportional hazard model.

Continuous variables across groups were compared using Kruskal-Wallis test. In contrast, the Mann-Whitney U test was utilized for pairwise comparisons, particularly when the parasitemia variable had a median of zero. The sensitivity, specificity, and predictive values of the mRDT were calculated using the two-by-two contingency tables [40]. The Wilson score method was used to calculate the 95% confidence intervals for the sensitivity, specificity, Positive Predictive Value (PPV), and Negative Predictive Value (NPV) [41]. A parametric, interval-censored Cox proportional hazards model with a gamma distribution was used to evaluate *Pf*HRP2 antigenemia persistence. This distribution offers flexibility and accounts for variability in antigen clearance, allowing for non-constant hazard rates by modeling antigen decay as a multi-step process with a non-constant hazard function capturing individual heterogeneity and providing a biologically relevant estimation of antigen persistence. To obtain interval censored data, all observations need to be pre-processed by applying seven filters to the dataset to accurately analyze definitive malaria events (MPS+) in HRP2 decay across time (Figure 4). (Filter 1) Inclusion Criteria: Inclusion of subjects who were (MPS+) and mRDT (+) at least once. From these data, all visits before the first (MPS+) and mRDT (+) visit were disregarded. This approach focused the analysis on the period following the initial confirmed malaria episode. (Filter 2) Data Refinement: Only cases where an mRDT result was available were selected to ensure that the analysis was based on consistent diagnostic criteria across all participants (microscopy results were available for all visits). (Filter 3) Sequential Data Selection: To analyze HRP decay, only the last visit in sequences of consecutive MPS (+) visits was used. This strategy was used to avoid over-representation of repeated positive results, which could bias the decay analysis. (Filter 4) Consistency in Diagnostic Results: If a visit was MPS (+) but mRDT (−), the mRDT result was considered false negative. Since such outcomes cannot be used for the decay of malaria antigens, all visits from the preceding MPS (+) and RDT (+) visit to the next were excluded. This ensured that only sequences of visits with consistent positive results across both diagnostic methods were considered. (Filter 5) Handling Negative Results: For subjects who were negative by both microscopy and mRDT in consecutive visits, only the first of these visits was retained. This eliminated redundant negative visits, focusing on the first

TABLE 1 Child and maternal characteristics in the mother-child cohort study.

Characteristic		*p*-value
Maternal Factors		
Number of mothers, n (%)	573 (100)	
Age (years)	23.3 (7.8)	N/A
Gravidity, n (%)		
Primigravidae Secundigravidae Multigravida (≥3)	232 (40.5) 126 (22.0) 215 (37.5)	**3.067E-51**[a]
Type of delivery, n (%)		
Normal birth Cesarian birth	529 (92.3) 44 (7.7)	**≤2.200E-16**[a]
Twins, n (%)	12 (2.1)	N/A
Preterm labor (<37 weeks), n (%)	114 (19.9)	N/A
Childhood Factors		
Number of children, n (%)	573 (100)	
Sex, n (%)		
Female Male	255 (44.5) 318 (55.5)	**0.010**[b]
Sickle cell genotypes, n (%)		
HbAA HbAS HbSS	367 (82.7) 72 (16.2) 5 (1.1)	0.492[c]
Number of events in children, n (%)	15,006 (100)	
Temperature, °C Afebrile, <37.5 Febrile, ≥37.5	36.5 (0.6) 13,704 (91.3) 1,302 (8.7)	N/A **≤2.200E-16**[a]
Hemoglobin, (g/dL)	10.58 (1.99)	N/A
Parasite density, MPS/μL Low (≤999), n (%) Medium (1,000–49,999), n (%) High (≥50,000), n (%)	7,980 (33,881) 399 (17.5) 1,496 (65.7) 382 (16.8)	N/A **1.972E-260**[a]
Geomean parasite density	7,303.6	N/A
Total *Plasmodium* cases, n (%)	2,277 (15.2)	
Plasmodium falciparum troph	2,261 (99.3)	**≤2.200E-16**[a]
Plasmodium malariae troph	13 (0.6)	
Mixed infection (*Pf/Pm*)	3 (0.1)	
mRDT measurements, n (%)	9,958 (66.4)	N/A

Demographic and clinical characteristics of mother-child pairs (n = 573). Data are presented as median (interquartile range; IQR) unless stated otherwise. Statistical significance was determined using the

[a]Chi-square goodness of fit.

[b]Proportions test (binomial test for equal frequencies), and

[c]Hardy Weinberg equilibrium. Bold indicates a statistically significant *p*-value after multiple test corrections using the Bonferroni-Holm method (familywise error rate, significance level at 0.050). MPS: malaria parasites, mRDT: malaria rapid diagnostic test, *troph* = trophozoites, *Pf/Pm; Plasmodium falciparum/Plasmodium malariae*.

occurrence of a negative result in each sequence. (Filter 6) Addressing Inconsistent mRDT Results: In cases where a subject was intermittently mRDT (−) and MPS (−) between two mRDT (+) but MPS (−) visits, only the visits up to (including) the first mRDT (−) result were considered. Subsequent visits in such sequences were excluded to maintain the focus on initial malaria clearance. (Filter 7) Selecting the Relevant Endpoint in a Sequence: If a sequence began with an mRDT (+) and MPS (+) visit, and was followed by consecutive mRDT (+) and MPS (−) visits, only the final mRDT (+) and MPS (−) visit in the sequence was retained. This approach focused on the period directly associated with *Pf*HRP decay and malaria clearance. After applying these filters, it was possible to define intervals in which the parasite antigen decayed. As such, an mRDT (+) and MPS (+) visit at time t_0 is either followed by (i) an mRDT (−) and MPS (−) event at time t_1, in which case the antigen decayed in the interval (t_0, t_1); first an mRDT (+) and MPS (−) and second an mRDT (−) and MPS (−) visit at times t_1 and t_2, in which case the antigen decayed in the interval (t_1, t_2); or (iii) and first an mRDT (+) and MPS (−) and second an mRDT (+) and MPS (+) visit at times t_1 and t_2, in which case the antigen decayed in the interval (t_1, ∞). Antigen decays between malaria episodes of the same patient were considered independent, as the analysis focused on the decay rather than the patient. The model was fitted separately: (i) without covariates, (ii) with stratification based on initial parasite densities, and (iii) sickle cell genotypes. All *p*-values ≤0.05 were deemed statistically significant.

Results

Maternal and child characteristics in the longitudinal cohort

The demographic characteristics of individuals in the mother-child birth cohort (n = 573 mothers and n = 573 children) are presented in Table 1. The median age for the mothers was 23.3 years, with gravidity differing among the women (p = 3.067E-51). The majority of the cohort had normal vaginal (92.3%) and singleton (97.9%) deliveries with 19.9% of the women experiencing preterm labor (<37 weeks). There was a higher proportion of male (55.5%) offspring than female (44.5%) in the cohort (p = 0.010). HbS genotypes were found to be in Hardy-Weinberg equilibrium in the study population (p = 0.492), but the prevalence of sickle cell trait [HbAS (16.2%)] and sickle cell disease [HbSS (1.1%)] was higher and significantly different from populations in other high-transmission regions in central and western Africa [42–45]. Throughout the 36 mos. follow-up, there were 15,006 child contact visits, the majority of which were afebrile (91.3%, n = 13,704), with 8.7% (n = 1,302) being febrile ($p \leq$ 2.200E-16). The median Hb concentration across the follow-up period was 10.58 g/dL. During the contact visits, 15.2% (n = 2,277) were malaria-positive based on light microscopy on thick and thin blood smears. The overall distribution of low (17.5%, n = 399), medium (65.7%, n = 1,496), and high (16.8%, n = 382) density parasitemia was not uniform (p = 1.972E-260), with the majority of the 2,277 microscopy-positive events being of medium density. The geometric mean parasite density for positive blood smears was 7,303.6 MPS/μL. Nearly all microscopy-confirmed cases had single-species infections with *P. falciparum* (99.3%, n = 2,261), followed by *P. malariae* (0.6%, n = 13). Mixed-species infections with *P. falciparum* and *P. malariae* (0.1%, n = 3) were rare, and the distribution of infections was not uniform ($p \leq$ 2.200E-16). *P. falciparum* specific HRP2 based malaria rapid diagnostic test (mRDT) results were performed for 66.4% (n = 9,958) of the total events.

Demographic and clinical characteristics for concomitant microscopy (MPS) and mRDT events

The primary objective of this study was to assess the performance characteristics and antigenemia persistence associated with *Pf*HRP2-mRDT, using microscopy as the reference standard. To achieve this objective, only events that included both microscopy and mRDT were utilized (n = 9,958). Based on concomitant MPS/mRDT measures, events were stratified into four groups: MPS (+)/mRDT (+) [15.8%, n = 1,572], MPS (−)/mRDT (+) [29.2%, n = 2,907], MPS (+)/mRDT (−) [0.6%, n = 61], and MPS (−)/mRDT (−) [54.4%, n = 5,418]. The demographic and clinical characteristics for each category are shown in Table 2. The distribution of females and males was comparable across the groups (p = 0.176). Temporal temperatures at visits varied across the groups (p = 3.280E-86) with more febrile events (≥37.50°C) in the MPS (+)/mRDT (+) groups (p = 7.537E-129). Consistent with microscopy accurately detecting acute malaria infections, Hb levels differed across the groups (p = 7.525E-155) and were lower in the MPS (+)/mRDT (+) and MPS (+)/mRDT (−) categories. Comparison of the two MPS (+) groups revealed higher parasite and geometric mean densities in MPS (+)/mRDT (+) than MPS (+)/mRDT (−) group (p = 9.513E-09, and p = 0.018, respectively) with a higher percentage of low-density parasitemia (≤999 μL) in the MPS (+)/mRDT (−) group (p = 6.097E-08). Among the total MPS (+) events (n = 1,633), there were 1,620 infections due to *P. falciparum* and 13 attributable to *P. malariae*. The distribution of sickle cell genotypes differed across the groups (p = 2.048E-22), with a higher percentage of HbAS in MPS (−)/mRDT (+) and MPS (−)/mRDT (−), consistent with the protective nature in HbAS carriers [46, 47].

TABLE 2 Demographic and Clinical Characteristics for Concomitant Microscopy (MPS) and mRDT Events.

Concomitant Microscopy (MPS) and mRDT Events						
Characteristic	**Total**	**MPS (+)/mRDT (+)**	**MPS (−)/mRDT (+)**	**MPS (+)/mRDT (−)**	**MPS (−)/mRDT (−)**	***p*-value**
No of events, n (%)	9,958 (100)	1,572 (15.8)	2,907 (29.2)	61 (0.6)	5,418 (54.4)	
Sex, n (%) Female Male	4,439 (44.58) 5,519 (55.12)	686 (43.6) 886 (56.4)	1,260 (43.3) 1,647 (56.7)	31 (50.8) 30 (49.2)	2,462 (45.4) 2,956 (54.6)	0.176[a]
Temperature, (^{0}C) Afebrile, <37.5°C Febrile ≥37.5°C	36.5 (0.5) 9,071 (91.09) 887 (8.91)	36.6 (1.20) 1,125 (71.6) 447 (28.4)	36.5 (0.4) 2,759 (94.9) 148 (5.1)	36.8 (1.4) 37 (60.7) 24 (39.3)	36.5 (0.5) 5,150 (95.1) 268 (4.9)	**3.280E-86**[b] **7.537E-129**[a]
Hematological Parameter						
Hemoglobin, (g/dL)	10.6 (2.0)	9.9 (2.1)	10.2 (1.9)	9.7 (2.5)	10.9 (1.8)	**7.525E-155**[b]
Parasitological Indices						
Parasite density, (MPS/μL)	6,607.8 (30,476.3)	7,030 (30,826.7)	-	957.0 (3,397.6)	-	**9.513E-09**[c]
Low (≤999/μL), n (%)	319 (19.5)	288 (15.6)	-	31 (50.8)	-	**6.079E-08**[a]
Medium (1,000–49,999/μL), n (%)	1,063 (65.1)	1,038 (66.1)	-	25 (41.0)	-	
High (≥50,000/μL), n (%)	251 (15.4)	246 (18.3)	-	5 (8.2)	-	
Geometric mean parasite density	3,526.7	21,886.2	-	11,708.7	-	**0.018**[d]
Plasmodium falciparum troph	1,620 (16.3)	1,572 (100.0)	-	48 (78.7)	-	N/A
Plasmodium malariae troph	13 (0.1)	0.0	-	13 (21.3)	-	N/A
Genetic Variants						
Sickle cell genotype, n (%) HbAA HbAS HbSS	9,621 (100) 7,906 (82.2) 1,607 (16.7) 108 (1.1)	1,333 (87.0) 183 (12.0) 16 (1.0)	2,435 (86.0) 381 (13.5) 16 (0.5)	54 (90.0) 6 (10.0) 0 (0.0)	4,082 (78.6) 1,035 (19.9) 76 (1.5)	**2.048E-22**[e]

Data are presented as counts, median (interquartile range; IQR), or mean (standard error of the mean; SEM). Statistical significance was determined using
[a]Chi-square homogeneity test.
[b]Kuskal-Wallis rank test.
[c]Mann-Whitney U test (pairwise comparison).
[d]Two-sample *t*-test, with equal variance, and
[e]Fisher's exact test. Bold indicates a statistically significant *p*-value at 0.05 after multiple test corrections using the Bonferroni-Holm method (familywise error rate). MPS: malaria parasites, mRDT: malaria rapid diagnostic test, *troph*: trophozoites.

High sensitivities and moderate specificities of the mRDT

The sensitivities, specificities, and predictive values of mRDTs can vary based on geographical regions, parasite genetic diversity, and levels of parasitemia [47]. Therefore, the diagnostic characteristics were evaluated in a high transmission region in western Kenya. Using microscopy as the reference standard, there were 1,572 true positives (TP), 2,907 false positives (FP), 61 false negatives (FN), and 5,418 true negatives (TN) for the combined *P. falciparum* and *P. malariae* infections (p < 2.20E-16, k = 0.361, Figure 5A). The mRDT demonstrated a high sensitivity of 96.27% (95%CI: 95.23–97.08) and a moderate specificity of 65.07% (95%CI: 64.04–66.09). The PPV was low at 35.10% (95%CI: 33.71–36.51), whereas the NPV was high at 98.89% (95%CI: 98.57–99.13). When considering only *P. falciparum* cases (Figure 5B), sensitivity showed a slight increase to 97.04% (95%CI: 96.10–97.76) and NPV to 99.12% (95%CI: 98.84–99.34), while specificity and PPV remained unchanged.

Performance characteristics were further evaluated by stratifying events based on visit type (i.e., acute *vs.* scheduled follow-up), excluding *P. malariae* cases. During acute visits, the mRDT demonstrated a sensitivity of 97.27% (95%CI: 95.75–98.28) and specificity of 71.29% (95%CI: 68.77–73.68), with a PPV of 65.00% (95%CI: 62.09–67.77) (Figure 5C). In contrast, for scheduled follow-up visits, while sensitivity remained high at 96.83% (95%CI: 95.39–97.84), specificity decreased to 63.87% (95%CI: 62.73–64.99), resulting in a lower PPV of 25.37% (95%CI:

A *P. falciparum/ P. malariae* only

mRDT	Microscopy Positive	Microscopy Negative	
	(TP)	(FP)	k=0.361
Positive	1,572	2,907	p≤2.200E-16
Negative	(FN)	(TN)	
	61	5,418	
Total	1,633	8,325	

mRDT Performance		
Indicators	%	95% CI
Sensitivity	96.27	95.23-97.08
Specificity	65.07	64.04-66.09
PPV	35.10	33.71-36.51
NPV	98.89	98.57-99.13

B *P. falciparum* only

mRDT	Microscopy Positive	Microscopy Negative	
	(TP)	(FP)	k=0.363
Positive	1,572	2,907	p≤2.200E-16
Negative	(FN)	(TN)	
	48	5,418	
Total	1,620	8,325	

mRDT Performance		
Indicators	%	95% CI
Sensitivity	97.04	96.10-97.76
Specificity	65.07	64.04-66.09
PPV	35.10	33.71-36.51
NPV	99.12	98.84-99.34

C *P. falciparum* Acute Visits

mRDT	Microscopy Positive	Microscopy Negative	
	(TP)	(FP)	k=0.620
Positive	715	387	p≤2.200E-16
Negative	(FN)	(TN)	
	20	961	
Total	735	1,348	

mRDT performance		
Indicators	%	95% CI
Sensitivity	97.27	95.75-98.28
Specificity	71.29	68.77-73.68
PPV%	65.00	62.09-67.77
NPV%	97.96	97.07-98.84

D *P. falciparum* Scheduled Visits

mRDT	Microscopy Positive	Microscopy Negative	
	(TP)	(FP)	k=0.270
Positive	857	2,520	p≤2.200E-16
Negative	(FN)	(TN)	
	28	4.457	
Total	885	6,977	

mRDT performance		
Indicators	%	95% CI
Sensitivity	96.83	95.39-97.84
Specificity	63.87	62.73-64.99
PPV%	25.37	23.90-26.83
NPV%	99.37	98.14-99.66

FIGURE 5
Sensitivity, specificity, and predictive values for mRDT measurements. Sensitivity, specificity, and predictive values for concomitant mRDT events (n = 9,958), using microscopy test (MPS) as the reference standard. Diagnostic measures are reported for four different scenarios: **(A)** *P. falciparum* (n = 1,620) and/or *P. malariae* (n = 13). **(B)** *P. falciparum* only. **(C)** *P. falciparum* only at acute visits. **(D)** *P. falciparum* only at scheduled follow-up visits. Statistical significance was determined using a Chi-square homogeneity test with a significance level of $p \leq 0.050$. Inter-rater agreement was calculated using Cohen's Kappa (k). TP: True positives, FP: False positives, FN: False negatives, TN: True negatives, PPV: Positive predictive value, NPV: Negative predictive value.

23.90–26.83) (Figure 5D). These results are supported by the 2.3-fold higher Cohen's kappa value (k) observed during acute visits, indicating a more substantial agreement between the mRDT and microscopy than in scheduled follow-ups. Importantly, the NPV remained consistently high, exceeding 97% for both visit types, demonstrating the mRDTs reliability in ruling out malaria infections regardless of visit type.

Longitudinal measures indicate prolonged HRP2 antigenemia

The rate of *Pf*HRP2 antigen decay following parasite clearance significantly impacts mRDT performance, influencing the sensitivity, specificity, and overall efficiency of the test [47]. A Cox proportional hazards model for ordered events was utilized to evaluate the decay kinetics in the longitudinal cohort. To ensure accurate analysis of malaria episodes [MPS (+)] and *Pf*HRP2 decay, the dataset was filtered to include only cases where microscopy and mRDT were consistently positive at least once. Visits before the first confirmed malaria episode and those with inconsistent diagnostic results were excluded. Intermittent positive results focused only on visits relevant to malaria progression and resolution. This approach ensured the analysis reflected the actual dynamics of malaria infection and *Pf*HRP2 persistence in the pediatric cohort. After rigorous filtering steps, the data included 291 children with 1,294 events. The positivity rate of *Pf*HRP2 antigenemia remained high (80–100%) within the first month and declined significantly over time ($p \leq 2.200E-16$). The time for the positivity rate of *Pf*HRP2 antigenemia to reach 0.5 (i.e., 50% of

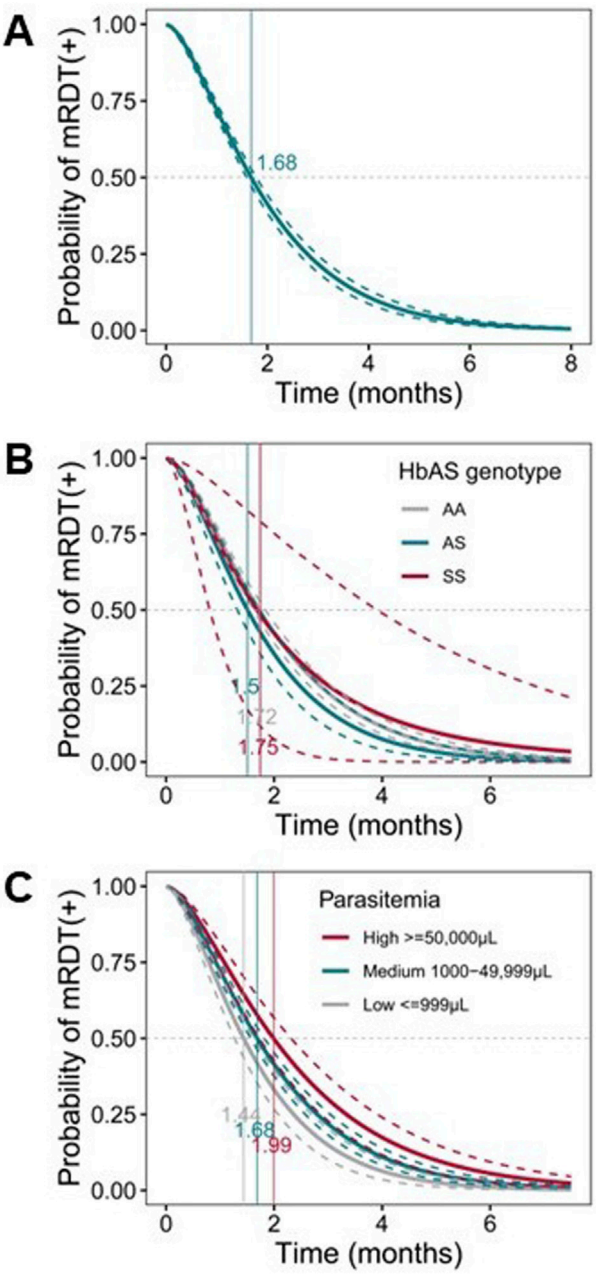

FIGURE 6
Probability of mRDT positive post-infection. Parametric, interval-censored Cox proportional hazards models with a gamma-exponential distribution were used to evaluate *Pf*HRP2 antigenemia persistence. The dataset used for this analysis was pre-processed to include only cases where both microscopy and mRDT were consistently positive at least once (n = 291 children; 1,294 events). The x-axis represents the time in months, and the y-axis shows the probability of mRDT remaining positive after parasite clearance. The curved dotted lines represent upper and lower confidence bounds, and the solid lines depict the decay probabilities of each group. Dotted gray lines at y = 0.50 represent the 50% probability. Vertical lines depict the median time to mRDT negative. **(A)** Survival curve representing the probability of mRDT (+) post-infection. **(B)** Survival curve representing the probability of mRDT (+) post-infection with parasitemia levels as covariates [≤999/µL (grey); medium [mid, 1,000–49,999/µL (turquoise)]; and high [≥50,000/µL (maroon)]. **(C)** Survival curve representing the probability of mRDT (+) post-infection with HbS genotypes as covariates: AA (grey), AS (turquoise), and SS (maroon).

*Pf*HRP2 decay) was 1.68 months (51.14 days), respectively (Figure 6A), indicating the persistence of *Pf*HRP2 in the bloodstream of the pediatric cohort. Stratification of children with initial parasite levels revealed that those with low parasite densities had a significantly faster *Pf*HRP2 antigen decay compared to those with either high initial parasite densities (p = 0.001) or medium parasite densities (p = 0.001). The 50% of *Pf*HRP2 decay for the three groups were 1.44 mos. (43.83 days), 1.99 mos. (60.58 days) and 1.68 mos. (51.14 days) respectively (Figure 6B).

Additional analyses revealed that sickle cell genotypes partially influence *Pf*HRP2 antigen decay rates (Figure 6C). Specifically, 50% of *Pf*HRP2 decay takes 1.72 mos. (51.75 days), 1.51 mos. (45.66 days) and 1.75 mos. (53.27 days) for malaria patients with HbAA, HbAS, and HbSS genotypes, respectively. Relative to the HbAA reference group, carriers of the HbAS genotype had a non-significantly shorter decay rate (p = 0.088), but no difference was observed for carriers of the HbSS genotype (p = 0.991). These analyses reveal that antigenemia persists for a prolonged period and is influenced by the initial parasite density and potentially, sickle cell genotypes.

Validation of mRDT performance in a short-term (14-day) febrile cohort

To further explore the performance of the mRDT, we utilized an independent dataset from a prospective febrile cohort with concomitant microscopy and mRDT results on day 0 (acute illness, n = 508) and day 14 (well-visit, n = 412). The demographic and clinical characteristics of the children at enrollment (day 0) are presented in Table 3. As expected during acute or recent malaria infections, Hb concentrations differed across the four groups (p = 0.025) and were highest in the MPS (−)/mRDT (−) group. The distribution of sickle cell genotypes also significantly differed (p = 1.000E-05) with the highest percentage of HbAS carriers in the MPS (−)/mRDT (−) group. Comparison of mRDT performance at days 0 and 14 revealed that acute disease (day 0) was characterized by higher sensitivity [99.21% (95%CI: 96.40–99.70) vs. 95.83% (95%CI: 84.68–99.27)], specificity [50.47% (95%CI: 44.10–56.05) vs. 34.54% (95%CI: 28.28–41.01)], and PPV [66.34% (95%CI: 60.75–71.53) vs. 8.30% (95%CI: 4.98–12.73%) (Figures 7A,B). The NPV remained high on both visit days (>98%). These results indicate that the mRDT

TABLE 3 Demographic and Clinical Characteristics for Concomitant Microscopy (MPS) and mRDT Categories in the Febrile Cohort.

Concomitant Microscopy (MPS) and mRDT Measures						
Characteristic	**Total**	**MPS (+)/mRDT (+)**	**MPS (−)/mRDT (+)**	**MPS (+)/mRDT (−)**	**MPS (−)/mRDT (−)**	***p*-value**
Sample size, n (%)	508 (100)	250 (49.2)	127 (25.0)	2 (0.4)	129 (25.4)	
Sex, n (%) Female Male	237 (46.7) 271 (53.3)	116 (46.4) 134 (53.6)	61 (48.0) 66 (52.0)	2 (100.0) 0.0	58 (45.0) 71 (55.0)	0.581[a]
Age at enrollment (months)	21.7 (26.6)	20.8 (22.73)	25.2 (30.1)	10.5 (N/A)	16.1 (26.7)	0.004[b]
Temperature, (^{0}C) Afebrile, <37.5°C Febrile, ≥37.5°C	38 (0.7) 37 (7.3) 471 (92.7)	38.0 (0.6) 16 (6.4) 234 (93.6)	38.0 (0.6) 10 (7.9) 117 (92.1)	39.2 (N/A) 0.0 2 (100.0)	38.0 (0.8) 11 (95.1) 118 (4.9)	0.137[b] 0.756[a]
Hematological Parameter						
Hemoglobin, (g/dL)	7.6 (4.4)	7.3 (3.8)	7.0 (4.5)	7.1 (N/A)	8.9 (5.2)	**0.025**[b]
Parasitological Indices						
Parasite density, (MPS/μL) Low (≤999/μL), n (%) Medium (1,000–49,999/μL), n (%) High (≥50,000/μL), n (%)	5,514 (39,714) 65 (25.8) 132 (52.4) 55 (21.8)	5,514 (39,506) 65 (25.8) 131 (52.4) 54 (21.8)	- - - -	77,886 (N/A) 0.0 1 (50.0) 1 (50.0)	- - - -	**3.256E-94**[c] N/A N/A N/A
Geometric mean parasite density	0.0	6,147	-	14,580	-	N/A
Plasmodium falciparum troph	250 (99.6)	250 (100)	-	0 (0.0)	-	N/A
Plasmodium malariae troph Mixed Infection (*Pm/Pf*)	1 (0.2) 1 (0.2)	0 (0.0) 0.0	- -	1 (50.0) 1 (50.0)	- -	N/A N/A
Genetic Variants						
Sickle cell genotypes, n (%) HbAA HbAS HbSS	492 (100) 377 (76.6) 56 (11.4) 59 (12.0)	208 (84.9) 22 (9.0) 15 (6.1)	96 (79.3) 11 (9.1) 14 (11.6)	2 (100.0) 0.0 0.0	71 (57.2) 23 (18.5) 30 (24.3)	**1.000E-05**[a]

Data are presented as median (interquartile range; IQR), unless otherwise indicated. Statistical significance was determined using
[a]Fisher's exact test.
[b]Kruskal-Walli's rank test, or
[c]Mann-Whitney U test (pairwise comparison). The boldface indicates a statistically significant *p*-value at a 0.05 threshold after multiple test corrections using the Bonferroni-Holm method (familywise error rate). MPS: malaria parasites, mRDT: malaria rapid diagnostic test, *troph*: trophozoites, *Pm/Pf*: *Plasmodium falciparum/Plasmodium malariae*.

is more effective at detecting and ruling out a malaria infection during acute disease (day 0) and follow-up visits, respectively.

Next, a direct comparison was made of the mRDT performance between days 0 and 14 (Figure 7C). Although higher on day 0, sensitivity did not differ between days 0 and 14 ($p = 0.234$), whereas specificity was significantly higher on day 0 than day 14 ($p < 0.0001$). The PPV was higher on day 0 compared to day 14 ($p < 0.0001$), highlighting the mRDT's reliability in detecting true malaria cases at initial diagnosis. However, the NPV remained consistently high on both days ($p = 0.618$), exceeding 98%, demonstrating the test's continued reliability in ruling out malaria infection when test results are negative. These results illustrate the utility of the mRDT's diagnostic performance during acute malaria episodes and the potential for increased false positives during short-term follow-up assessments.

Discussion

Rapid and reliable diagnostic methods are crucial for effective disease management in malaria-endemic regions, especially where *P. falciparum* transmission is high. Accurate and timely diagnosis is critical to guide appropriate treatment, especially in

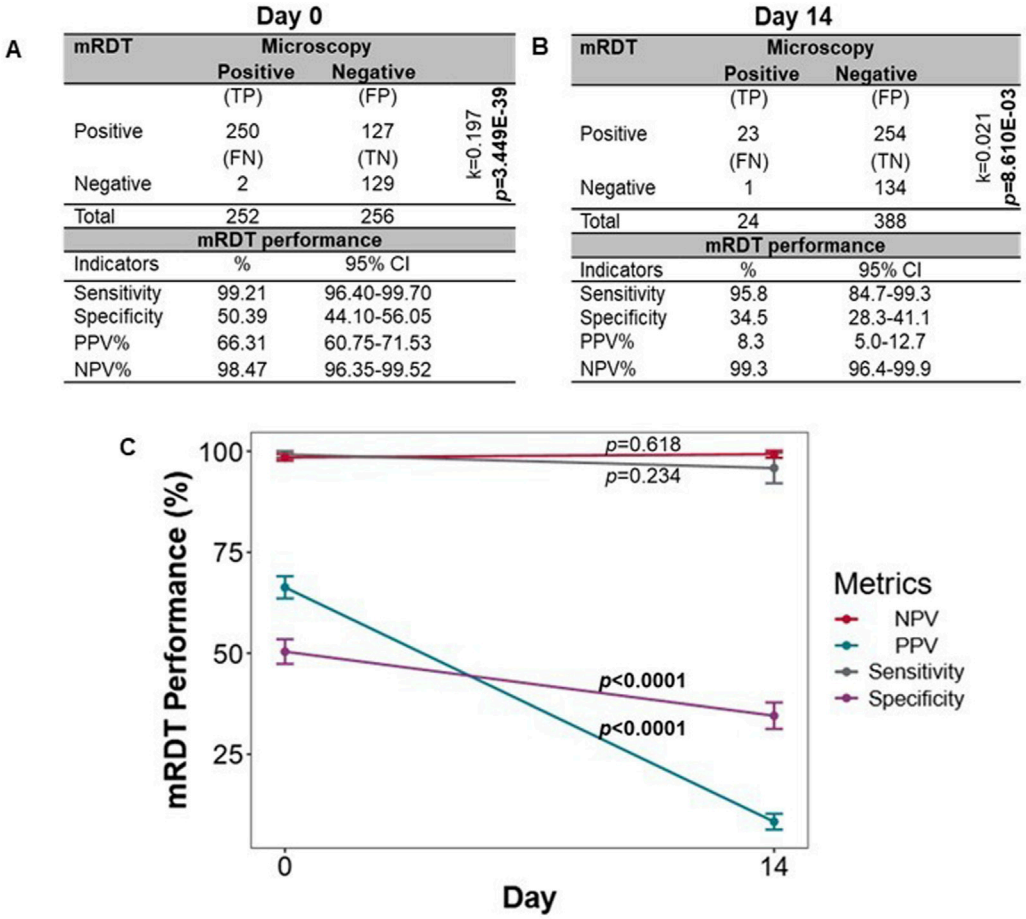

FIGURE 7
Sensitivity, specificity, and predictive values for mRDT measurements on day 0 and day 14. The mRDT performance was evaluated using microscopy as the reference standard. **(A)** Sensitivity, specificity, and predictive values for mRDT measurements on day 0 (n = 508 children). **(B)** Sensitivity, specificity, and predictive values for mRDT measurements on day 14 (412 events). For A and B, statistical significance was determined using Fisher's exact test, and the level of agreement between the two diagnostic tests was computed using Cohen's Kappa statistics (k). **(C)** Comparison metric of the sensitivities, specificities, and predictive values between day 0 and day 14. Statistical significance was determined using Fisher's exact test. TP: True positives, FP: False positives, FN: False negatives, TN: True negatives, PPV: Positive predictive values, NPV: Negative predictive value.

children under five, who are most vulnerable to severe malaria complications [3, 10]. In resource-limited settings where microscopy is sometimes not available, mRDTs have become essential tools, enabling timely diagnosis and treatment decisions [3, 7, 10, 11]. Our study provides a comprehensive evaluation of the diagnostic performance of *Pf*HRP2-based mRDTs and antigenemia persistence of *Pf*HRP2 in a *P. falciparum* holoendemic region of Kenya, contributing to a better understanding of their strengths and limitations in both acute and follow-up scenarios.

Findings from this study confirmed the high sensitivity (97.04%) and negative predictive value (NPV >99%) of the mRDTs in patients with *P. falciparum*, reinforcing their utility as frontline diagnostic tools in resource-constrained settings [48–50]. Our results are consistent with previous studies demonstrating their reliability in detecting *P. falciparum* infections, even in cases of low parasitemia [6, 15, 35]. However, the moderate specificity (65.07%), particularly during longitudinal follow-up visits, represents significant limitations, illustrating that mRDTs are not useful diagnostic tools for following the patients' malaria status after initial diagnosis. Reduced specificity is likely attributed to the persistence of *Pf*HRP2 antigen in the bloodstream after parasite clearance [37, 47, 51–53].

The performance of mRDTs can vary depending on parasite species, the target gene(s) deletion, and the timing of persistent antigenemia [47, 54]. Our study expands current knowledge in real-world settings by demonstrating how the type of patient visits influences mRDT performance. Performance varied significantly by visit type, with better specificity and positive

predictive value (PPV 65.00%) during acute visits when patients presented with higher parasitemia and clinical symptoms in the longitudinal study and validation cohort. These findings align with evidence showing that higher parasite densities improve the accuracy of mRDTs [18, 55, 56]. Conversely, during scheduled follow-up visits after administration of antimalarial therapy, specificity and PPV declined substantially, likely because *Pf*HRP2 antigens persisted from prior infections. This highlights the challenge of using mRDTs for post-treatment monitoring, particularly in high-transmission areas with persistent exposure, since positive results may not necessarily indicate active infection but rather residual antigenemia.

Notably, the mRDT specificities in the longitudinal mother-child and validation (acute febrile) cohorts were lower than the sensitivities, potentially due to recent antimalarial treatment that could reduce detectable parasites by microscopy but have little influence on the persistence of circulating antigens measured by the mRDT. While microscopy remains the gold standard for malaria diagnosis, the mRDT's utility lies in its rapid and accessible nature, particularly in resource-limited settings [12]. This moderate agreement between mRDTs and microscopy highlighted the need for confirmatory testing to improve malaria control and patient outcomes in endemic regions.

The sensitivity and specificity were validated by comparing results from the mother-child longitudinal birth cohort to those of an independent acute febrile cohort enrolled on day 0 (n = 508) and followed up on day 14 (n = 412) in the identical community. The mRDT demonstrated better sensitivity and specificity on day 0 than on day 14 (well-visit), confirming the trends observed in the mother-child cohort during acute and follow-up visits. For clinical relevance, the diagnostic performance of mRDTs should be interpreted in the context for which they are most aptly applied: evaluating febrile illness in symptomatic individuals. To address this, we conducted targeted performance analyses of mRDTs at acute pre-treatment visits in symptomatic children in both the longitudinal and the short-term febrile cohorts. These analyses reflect real-world clinical application. Sensitivity was high in both settings, 97.27% in the longitudinal cohort and 99.21% in the short-term cohort, while specificity was lower, at 71.29% and 50.39%, respectively. Factors that may account for lower specificity include submicroscopic infections undetected by microscopy that yield a positive mRDT (apparent false positives). Moreover, residual *Pf*HRP2 antigenemia from recent infections may persist in holoendemic settings despite parasite clearance, yielding discordant results. The acute febrile cohort's even lower specificity may be due to the likelihood of this cohort having a broader range of severe, non-malarial conditions and more recent treatment since they came directly from the community and were not part of a longitudinal study. The Cohen's kappa value observed during acute visits was 2.3 times higher than at scheduled follow-ups, indicating substantially greater agreement between mRDT and microscopy when used in symptomatic, pre-treatment cases. The consistency of findings across both studies strengthens the generalizability of our observations.

The longitudinal study design of the mother-child cohort with 36 mos. of follow-up allowed for a thorough evaluation of *Pf*HRP2 antigen decay kinetics. We found the time for positivity rate of *Pf*HRP2 antigenemia to reach 0.5 after parasite clearance was 1.68 months (i.e., 51.14 days). A comprehensive analysis using a Bayesian survival model, which aggregated data from multiple published studies, predicted the clearance time of the *Pf*HRP2 antigen following malaria treatment. The model estimated that 95% of *Pf*HRP2 tests are negative within 36 days (95%CI: 21–61 days) after treatment [23]. Our findings fall within the upper limit of this range, suggesting a similar, albeit slightly prolonged, antigen clearance timeline in our cohort. This could be explained by the rigorous study design and filters employed during this analysis, which enabled detailed tracking of antigen decay kinetics in the current study.

Stratification of the cohort by initial *P. falciparum* parasite density revealed that higher parasite densities were associated with prolonged antigen persistence, consistent with findings from previous studies in Uganda [60]. This prolonged persistence underscores the challenge of using mRDTs in high-transmission settings, where high parasite burdens are more frequent [19]. In addition, we explored the impact of sickle cell status on antigen decay. Although not statistically significant, results suggested trends of slower *Pf*HRP2 antigen decay rates in individuals with HbAS and HbSS compared to those with the HbAA genotype. These findings suggest a potential influence of host genetics on antigen clearance and require further investigation, particularly in regions where the sickle cell trait is prevalent.

The issue of *Pf*HRP2 gene deletions presents an additional diagnostic challenge that can lead to false-negative mRDT results. Such gene deletions have been increasingly reported in malaria-endemic regions; however, the prevalence is relatively low in Kenya compared to other countries such as Eritrea and Djibouti [17, 54, 58–61]. However, we are currently investigating deletions of the target gene in the false negatives detected in this study. The false negative results in this study are likely due to low parasite densities (957 MPS/μL) in the MPS (+)/MPS (−) group in which the mRDT failed to detect the antigen. Additional reasons for false-negative results in the MPS (+)/mRDT (−) group may be due to the timing of infection, in which very early infections were detected by microscopy, but before *Pf*HRP2 is secreted at detectable levels. It is unlikely that false negatives were due to a prozone effect (highly excessive antigen) since children with very high parasite densities fell withing the MPS (+)/mRDT (+) group.

In conclusion, our findings emphasize the utility of *Pf*HRP2-based mRDTs as a valuable tool for diagnosing acute malaria in children under five, where sensitivity and

NPV were high. However, reduced specificity during follow-up visits, due to *Pf*HRP2 antigen persistence, poses significant challenges for ongoing patient monitoring. This can result in overtreatment and misdiagnosis, underscoring the importance of integrating confirmatory diagnostics, such as microscopy or molecular tests, to improve diagnostic accuracy and patient outcomes. The strengths of this study include the extensive follow-up of children, which allows for an unbiased assessment of *Pf*HRP2 antigen decay rates and the validation of the results using an independent cohort. A potential limitation of the study is the use of microscopy as the reference standard for evaluating mRDT performance, since submicroscopic infections would go undetected. Future studies incorporating molecular diagnostics could provide more precise estimates of mRDT performance. Another potential limitation is that we did not directly measure *Pf*HRP2 protein levels using ELISA or Western Blot due to limited sample volume. However, our transcriptomic profiling of *P. falciparum* in a subset of patients provided indirect evidence of the antigenemia detected by the mRDT. *Pf*HRP2 was among the most highly expressed *P. falciparum* genes in Day 0 (pre-treatment) samples and was absent at Day 14 (well visit) in aparasitemic children. This suggests that persistent mRDT positivity reflects residual circulating antigen rather than active infection. Collectively, *Pf*HRP2-based mRDTs are valuable diagnostic tools at initial presentation, where sensitivity and specificity are optimal, but antigen persistence limits their effectiveness in follow-up assessments. Understanding these limitations in the context of confirmatory testing is crucial for optimal patient management and malaria control efforts to reduce the disease burden in high-transmission regions.

Author contributions

Conceptualization: DP; methodology: SW, CO, SO, QC, KS, and DP; investigation: SW, CO, SO, SA, ER, QC, IH, PS, CO, and DP; data curation: SW, CO, QC, KS, and DP; writing of manuscript: SW, CO, SO, SA, and DP; editing of manuscript: SW, CO, SO, SA, ER, IH, PS, CO, QC, KS, and DP; supervision: SA, ER, IH, CO, KS, and DP; funding acquisition: DP. All authors contributed to the article and approved the submitted version.

Data availability

The raw data supporting the conclusions of this article will be made available by the authors, without undue reservation.

Ethics statement

The study was approved by the University of New Mexico Institutional Review Board (United States) and Maseno University Ethics Review Committee (Kenya). Written informed consent in the language of choice (i.e., English, Swahili, or Dholuo) was provided by the parent or legal guardian of all children participating in the studies.

Funding

The author(s) declare that financial support was received for the research and/or publication of this article. This work was supported by funding from the National Institutes of Health: R01 AI130473 (DP and SA), D43 TW005884 (DP), and D43 TW010543 (DP).

Acknowledgments

We are grateful to the entire University of New Mexico team for clinical support. We thank the parents/legal guardians of the study participants and children who participated in the study.

Conflict of interest

The author(s) declared no potential conflicts of interest with respect to the research, authorship, and/or publication of this article.

Generative AI statement

The authors declare that no Generative AI was used in the creation of this manuscript.

References

1. WHO. World malaria report (2024). Available online at: https://www.who.int/teams/global-malaria-programme/reports/world-malaria-report-2024 (Accessed 25 April 2025).

2. WHO. World malaria report (2022). Available online at: https://www.who.int/teams/global-malaria-programme/reports/world-malaria-report-2022 (Accessed 25 April 2025).

3. WHO. World malaria report (2023). Available online at: https://www.who.int/teams/global-malaria-programme/reports/world-malaria-report-2023 (Accessed 25 April 2025).

4. Okoyo C, Githinji E, Muia RW, Masaku J, Mwai J, Nyandieka L, et al. Assessment of malaria infection among pregnant women and children below five years of age attending rural health facilities of Kenya: a cross-sectional survey in two counties of Kenya. *PLoS One* (2021) **16**(9):e0257276. doi:10.1371/journal.pone.0257276

5. Awuor SO, O Eric O, Musyoki S, I Daud I. Confirmed malaria cases among under five children with fever and history of fever in masogo sub-county, kisumu county-Kenya. *J Clin Images Med Case Rep* (2021) **2**. doi:10.52768/2766-7820/1274

6. Landier J, Parker DM, Thu AM, Carrara VI, Lwin KM, Bonnington CA, et al. The role of early detection and treatment in malaria elimination. *Malar J* (2016) **15**(1):363. doi:10.1186/s12936-016-1399-y

7. WHO. Guidelines for the treatment of malaria (2010). Available online at: https://www.paho.org/en/documents/guidelines-treatment-malaria-second-edition-2010 (Accessed 25 April 2025).

8. Rosenthal PJ. The interplay between drug resistance and fitness in malaria parasites. *Mol Microbiol* (2013) **89**(6):1025–38. doi:10.1111/mmi.12349

9. Romphosri S, Changruenngam S, Chookajorn T, Modchang C. Role of a concentration gradient in malaria drug resistance evolution: a combined within- and between-hosts modelling approach. *Scientific Rep* (2020) **10**(1):6219. doi:10.1038/s41598-020-63283-2

10. Wongsrichanalai C, Barcus MJ, Muth S, Sutamihardja A, Wernsdorfer WH. A Review of malaria diagnostic tools: microscopy and rapid diagnostic test (rdt). *Am J Trop Med Hyg* (2007) **77**(6 Suppl. l):119–27. doi:10.4269/ajtmh.2007.77.119

11. Dahal P, Khanal B, Rai K, Kattel V, Yadav S, Bhattarai NR. Challenges in laboratory diagnosis of malaria in a low-resource country at tertiary care in eastern Nepal: a comparative study of conventional vs. Molecular methodologies. *J Trop Med* (2021) **2021**:1–9. doi:10.1155/2021/3811318

12. Bruxvoort KJ, Leurent B, Chandler CIR, Ansah EK, Baiden F, Björkman A, et al. The impact of introducing malaria rapid diagnostic tests on fever case management: a synthesis of ten studies from the act consortium. *The Am J Trop Med Hyg* (2017) **97**(4):1170–9. doi:10.4269/ajtmh.16-0955

13. Allen EN, Wiyeh AB, McCaul M. Adding rapid diagnostic tests to community-based programmes for treating malaria. *Cochrane Database Syst Rev* (2022) **9**(9):Cd009527. doi:10.1002/14651858.CD009527.pub3

14. WHO. *The use of malaria rapid diagnostic tests*. Geneva, Switzerland: WHO Library Cataloguing in Publication Data (2004). Available online at: https://iris.who.int/bitstream/handle/10665/207715/9290610883_eng.pdf?sequence=1&isAllowed=y (Accessed 25 April 2025).

15. Gamboa D, Ho M-F, Bendezu J, Torres K, Chiodini PL, Barnwell JW, et al. A large proportion of P. Falciparum isolates in the amazon region of Peru lack Pfhrp2 and Pfhrp3: implications for malaria rapid diagnostic tests. *PLOS ONE* (2010) **5**(1):e8091. doi:10.1371/journal.pone.0008091

16. Agaba BB, Yeka A, Nsobya S, Arinaitwe E, Nankabirwa J, Opigo J, et al. Systematic Review of the status of Pfhrp2 and Pfhrp3 gene deletion, approaches and methods used for its estimation and reporting in *Plasmodium falciparum* populations in Africa: Review of published studies 2010–2019. *Malar J* (2019) **18**:355–10. doi:10.1186/s12936-019-2987-4

17. Rogier E, McCaffery JN, Nace D, Svigel SS, Assefa A, Hwang J, et al. *Plasmodium falciparum* Pfhrp2 and Pfhrp3 gene deletions from persons with symptomatic malaria infection in Ethiopia, Kenya, Madagascar, and Rwanda. *Emerg Infect Dis* (2022) **28**(3):608–16. doi:10.3201/eid2803.211499

18. Okanda D, Ndwiga L, Osoti V, Achieng N, Wambua J, Ngetsa C, et al. Low frequency of *Plasmodium falciparum* hrp2/3 deletions from symptomatic infections at a primary healthcare facility in kilifi, Kenya. *Front Epidemiol* (2023) **3**:1083114. doi:10.3389/fepid.2023.1083114

19. Bosco AB, Nankabirwa JI, Yeka A, Nsobya S, Gresty K, Anderson K, et al. Limitations of rapid diagnostic tests in malaria surveys in areas with varied transmission intensity in Uganda 2017-2019: implications for selection and use of Hrp2 rdts. *PLoS One* (2020) **15**(12):e0244457. doi:10.1371/journal.pone.0244457

20. WHO. Technical consultation on research requirements to support policy recommendations on highly sensitive point-of-care diagnostics for *P. Falciparum* malaria (2018). Available online at: https://www.who.int/publications/m/item/WHO-CDS-GMP-MPAC-2018.17. (Accessed 25 April 2025).

21. Hartley M-A, Hofmann N, Keitel K, Kagoro F, Antunes Moniz C, Mlaganile T, et al. Clinical relevance of low-density *Plasmodium falciparum* parasitemia in untreated febrile children: a cohort study. *Plos Med* (2020) **17**(9):e1003318. doi:10.1371/journal.pmed.1003318

22. Kozycki CT, Umulisa N, Rulisa S, Mwikarago EI, Musabyimana JP, Habimana JP, et al. False-negative malaria rapid diagnostic tests in Rwanda: impact of *Plasmodium falciparum* isolates lacking Hrp2 and declining malaria transmission. *Malar J* (2017) **16**(1):123. doi:10.1186/s12936-017-1768-1

23. Dalrymple U, Arambepola R, Gething PW, Cameron E. How long do rapid diagnostic tests remain positive after anti-malarial treatment? *Malar J* (2018) **17**(1):228. doi:10.1186/s12936-018-2371-9

24. Hendriksen IC, Mtove G, Pedro AJ, Gomes E, Silamut K, Lee SJ, et al. Evaluation of a Pfhrp2 and a pldh-based rapid diagnostic test for the diagnosis of severe malaria in 2 populations of african children. *Clin Infect Dis* (2011) **52**(9):1100–7. doi:10.1093/cid/cir143

25. Lee JH, Jang JW, Cho CH, Kim JY, Han ET, Yun SG, et al. False-positive results for rapid diagnostic tests for malaria in patients with rheumatoid factor. *J Clin Microbiol* (2014) **52**(10):3784–7. doi:10.1128/jcm.01797-14

26. Plowe CV. Malaria chemoprevention and drug resistance: a Review of the literature and policy implications. *Malar J* (2022) **21**(1):104. doi:10.1186/s12936-022-04115-8

27. Were T, Davenport G, Hittner J, Ouma C, Vulule J, Ong'Echa J, et al. Bacteremia in Kenyan children presenting with malaria. *J Clin Microbiol* (2011) **49**(2):671–6. doi:10.1128/jcm.01864-10

28. Davenport GC, Hittner JB, Otieno V, Karim Z, Mukundan H, Fenimore PW, et al. Reduced parasite burden in children with falciparum malaria and bacteremia coinfections: role of mediators of inflammation. *Mediators Inflamm* (2016) **2016**(1):1–14. doi:10.1155/2016/4286576

29. Nshakira N, Kristensen M, Ssali F, Reynolds Whyte S. Appropriate treatment of malaria? Use of antimalarial drugs for children's fevers in district medical units, drug shops and homes in eastern Uganda. *Trop Med & Int Health* (2002) **7**(4):309–16. doi:10.1046/j.1365-3156.2002.00858.x

30. AlKadi HO. Antimalarial drug toxicity: a Review. *Chemotherapy* (2007) **53**(6):385–91. doi:10.1159/000109767

31. National Academies of Sciences E. In: Savitz DA, Styka AN, editors. *Medicine. Assessment of long-term health effects of antimalarial drugs when used for prophylaxis*. Washington, DC: The National Academies Press (2020). p. 426.

32. Ong'echa JM, Keller CC, Were T, Ouma C, Otieno RO, Landis-Lewis Z, et al. Parasitemia, anemia, and malarial anemia in infants and young children in a rural holoendemic *Plasmodium falciparum* transmission area. *Am J Trop Med Hyg* (2006) **74**(3):376–85. doi:10.4269/ajtmh.2006.74.376

33. CareStartTM. Carestart Hrp2 diagnostic protocol. (2016).

34. Bousema T, Okell L, Felger I, Drakeley C. Asymptomatic malaria infections: detectability, transmissibility and public health relevance. *Nat Rev Microbiol* (2014) **12**(12):833–40. doi:10.1038/nrmicro3364

35. WHO. *Guidelines for the treatment of malaria*. Geneva, Switzerland: World Health Organization (2015). Available online at: https://www.who.int/malaria/publications/atoz/9789241549127/en/ (Accessed 25 April 2025).

36. Anyona SB, Cheng Q, Wasena SA, Osata SW, Guo Y, Raballah E, et al. Entire expressed peripheral blood transcriptome in pediatric severe malarial anemia. *Nat Commun* (2024) **15**(1):5037. doi:10.1038/s41467-024-48259-4

37. Kyabayinze DJ, Tibenderana JK, Odong GW, Rwakimari JB, Counihan H. Operational accuracy and comparative persistent antigenicity of Hrp2 rapid diagnostic tests for *Plasmodium falciparum* malaria in a hyperendemic region of Uganda. *Malar J* (2008) **7**:221. doi:10.1186/1475-2875-7-221

38. Chipwaza B, Sumaye RD. High malaria parasitemia among outpatient febrile children in low endemic area, east-Central Tanzania in 2013. *BMC Res Notes* (2020) **13**(1):251. doi:10.1186/s13104-020-05092-4

39. Otieno RO, Ouma C, Ong'echa JM, Keller CC, Were T, Waindi EN, et al. Increased severe anemia in hiv-1-exposed and hiv-1-positive infants and children during acute malaria. *Aids* (2006) **20**(2):275–80. doi:10.1097/01.aids.0000200533.56490.b7

40. Baratloo A, Hosseini M, Negida A, El Ashal G. Part 1: simple definition and calculation of accuracy, sensitivity and specificity. *Emerg (Tehran)* (2015) **3**(2):48–9.

41. Mercaldo ND, Lau KF, Zhou XH. Confidence intervals for predictive values with an emphasis to case-control studies. *Stat Med* (2007) **26**(10):2170–83. doi:10.1002/sim.2677

42. Masmas TN, Garly ML, Lisse IM, Rodriques A, Petersen PT, Birgens H. Inherited hemoglobin disorders in Guinea-bissau, west Africa: a population study. *Hemoglobin* (2006) **30**(3):355–64. doi:10.1080/03630260600755385

43. Grosse SD, Odame I, Atrash HK, Amendah DD, Piel FB, Williams TN. Sickle cell disease in Africa: a neglected cause of early childhood mortality. *Am J Prev Med* (2011) **41**(6 Suppl. 4):S398–405. doi:10.1016/j.amepre.2011.09.013

44. Thomson AM, McHugh TA, Oron AP, Teply C, Lonberg N, Vilchis Tella V, et al. Global, regional, and national prevalence and mortality burden of sickle cell disease, 2000–2021: a systematic analysis from the global burden of disease study 2021. *The Lancet Haematol* (2023) **10**(8):e585–e599. doi:10.1016/s2352-3026(23)00118-7

45. Piel FB, Patil AP, Howes RE, Nyangiri OA, Gething PW, Williams TN, et al. Global distribution of the sickle cell gene and geographical confirmation of the malaria hypothesis. *Nat Commun* (2010) **1**:104. doi:10.1038/ncomms1104

46. Eridani S. Hbs protection from *P. Falciparum* infection. *Br J Med Med Res* (2013) **3**(4):790–801. doi:10.9734/bjmmr/2013/2427

47. Martiáñez-Vendrell X, Skjefte M, Sikka R, Gupta H. Factors affecting the performance of hrp2-based malaria rapid diagnostic tests. *Trop Med Infect Dis* (2022) **7**(10):265. doi:10.3390/tropicalmed7100265

48. Ogunfowokan O, Ogunfowokan BA, Nwajei AI. Sensitivity and specificity of malaria rapid diagnostic test (mrdt carestattm) compared with microscopy amongst under five children attending a primary care clinic in southern Nigeria. *Afr J Prim Health Care Fam Med* (2020) **12**(1):1–8. doi:10.4102/phcfm.v12i1.2212

49. Natama HM, Traoré TE, Rouamba T, Somé MA, Zango SH, Rovira-Vallbona E, et al. Performance of pfhrp2-rdt for malaria diagnosis during the first year of life in a high malaria transmission area in Burkina Faso. *J Parasit Dis* (2023) **47**(2):280–9. doi:10.1007/s12639-023-01566-x

50. Bonko MD, Tahita MC, Kiemde F, Lompo P, Mens PF, Tinto H, et al. Diagnostic performance of *Plasmodium falciparum* histidine-rich protein-2 antigen-specific rapid diagnostic test in children at the peripheral health care level in nanoro (Burkina Faso). *Trop Med Infect Dis* (2022) **7**(12):440. doi:10.3390/tropicalmed7120440

51. Rosanas-Urgell A, Mueller D, Betuela I, Barnadas C, Iga J, Zimmerman PA, et al. Comparison of diagnostic methods for the detection and quantification of the four sympatric *Plasmodium* species in field samples from Papua New Guinea. *Malar J* (2010) **9**:361. doi:10.1186/1475-2875-9-361

52. Das S, Jang IK, Barney B, Peck R, Rek JC, Arinaitwe E, et al. Performance of a high-sensitivity rapid diagnostic test for *Plasmodium falciparum* malaria in asymptomatic individuals from Uganda and Myanmar and naive human challenge infections. *The Am J Trop Med Hyg* (2017) **97**(5):1540–50. doi:10.4269/ajtmh.17-0245

53. Apinjoh TO, Tangi LN, Oriero EC, Drammeh S, Ntui-Njock VN, Etoketim B, et al. Histidine-rich protein (hrp) 2-based rdt false-negatives and *Plasmodium falciparum* hrp 2 and 3 gene deletions in low, seasonal and intense perennial transmission zones in Cameroon: a cross–sectional study. *BMC Infect Dis* (2024) **24**(1):1080–14. doi:10.1186/s12879-024-09935-4

54. Berhane A, Anderson K, Mihreteab S, Gresty K, Rogier E, Mohamed S, et al. Major threat to malaria control programs by *Plasmodium falciparum* lacking histidine-rich protein 2, Eritrea. *Emerg Infect Dis* (2018) **24**(3):462–70. doi:10.3201/eid2403.171723

55 Apinjoh TO, Ntasin VN, Tataw PCC, Ntui VN, Njimoh DL, Cho-Ngwa F, et al. Comparison of conventional and non-invasive diagnostic tools for detecting *Plasmodium falciparum* infection in southwestern Cameroon: a cross-sectional study. *Infect Dis Poverty* (2021) **10**(1):75. doi:10.1186/s40249-021-00859-8

56. Kaaya RD, Matowo J, Kajeguka D, Tenu F, Shirima B, Mosha F, et al. The impact of submicroscopic parasitemia on malaria rapid diagnosis in northeastern Tanzania, an area with diverse transmission patterns. *Infect Dis Rep* (2022) **14**(6):798–809. doi:10.3390/idr14060082

57. Grandesso F, Nabasumba C, Nyehangane D, Page A-L, Bastard M, De Smet M, et al. Performance and time to become negative after treatment of three malaria rapid diagnostic tests in low and high malaria transmission settings. *Malar J* (2016) **15**:496–12. doi:10.1186/s12936-016-1529-6

58. Beshir KB, Sepúlveda N, Bharmal J, Robinson A, Mwanguzi J, Busula AO, et al. *Plasmodium falciparum* parasites with histidine-rich protein 2 (Pfhrp2) and Pfhrp3 gene deletions in two endemic regions of Kenya. *Sci Rep* (2017) **7**(1):14718. doi:10.1038/s41598-017-15031-2

59. Gatton ML, Chaudhry A, Glenn J, Wilson S, Ah Y, Kong A, et al. Impact of *Plasmodium falciparum* gene deletions on malaria rapid diagnostic test performance. *Malar J* (2020) **19**(1):392. doi:10.1186/s12936-020-03460-w

60. Prosser C, Gresty K, Ellis J, Meyer W, Anderson K, Lee R, et al. *Plasmodium falciparum* histidine-rich protein 2 and 3 gene deletions in strains from Nigeria, Sudan, and south Sudan. *Emerg Infect Dis* (2021) **27**(2):471–9. doi:10.3201/eid2702.191410

61. Vera-Arias CA, Holzschuh A, Oduma CO, Badu K, Abdul-Hakim M, Yukich J, et al. High-throughput *Plasmodium falciparum* Hrp2 and Hrp3 gene deletion typing by digital PCR to monitor malaria rapid diagnostic test efficacy. *eLife* (2022) **11**:e72083. doi:10.7554/elife.72083

Scope

Experimental Biology and Medicine (EBM) is a global, peer-reviewed journal dedicated to the publication of multidisciplinary and interdisciplinary research in the biomedical sciences. The journal covers the spectrum of translational research from T0, basic research, to T4, population health. Articles in EBM represent cutting edge research at the overlapping junctions of the biological, physical and engineering sciences that impact upon the health and welfare of the world's population. EBM is particularly appropriate for publication of papers that are multidisciplinary in nature, are of potential interest to a wide audience, and represent experimental medicine in the broadest sense of the term. However, manuscripts reporting novel findings on any topic in the realm of experimental biology and medicine are most welcome.

EBM publishes Research, Reviews, Mini Reviews, and Brief Communications in the following categories.

- Anatomy/Pathology
- Artificial Intelligence/ Machine Learning Applications to Biomedical Research
- Biochemistry and Molecular Biology
- Bioimaging
- Biomedical Engineering
- Bionanoscience
- Cell and Developmental Biology
- Clinical Trials
- Endocrinology and Nutrition
- Environmental Health/Biomarkers/ Precision Medicine
- Genomics, Proteomics, and Bioinformatics
- Immunology/Microbiology/Virology
- Mechanisms of Aging
- Neuroscience
- Pharmacology and Toxicology
- Physiology and Pathophysiology
- Population Health
- Stem Cell Biology
- Structural Biology
- Synthetic Biology
- Systems Biology and Microphysiological Systems
- Translational Research

EBM Experimental Biology and Medicine

EBM is the official journal of the Society for Experimental Biology and Medicine

Experimental Biology and Medicine (EBM) is a global, peer-reviewed journal dedicated to the publication of multidisciplinary and interdisciplinary research in the biomedical sciences.

Discover more of our Special Issues

See more →

Contact

development@ebm-journal.org

See more

ebm-journal.org

publishingpartnerships.frontiersin.org/our-partners